Chemical looping water splitting for hydrogen production, decarbonised steel production and energy storage/generation in-situ with CO_2 capture

Husain Bahzad

2019

Supervised by Prof. Paul S. Fennell and Prof. Nilay Shah

This dissertation is submitted for the degree of Doctor of Philosophy
at the Department of Chemical Engineering
at the Imperial College London of Science, Technology and Medicine

Abstract

In the research described in this thesis, a novel hydrogen production process *via* integrated chemical looping water splitting technology (ICLWS) was developed. In addition, a state-of-the-art process for production of decarbonised iron through a four-stage chemical looping water splitting technology (CLWSFe) was proposed. Both processes were simulated using the Aspen Plus simulator. Heat integration analysis was applied to the two processes, utilising pinch-point analysis in order to minimise utility usage and optimise their thermodynamic performance. Furthermore, sensitivity analysis was performed for the ICLWS process to detect the optimum operating conditions. Both processes were thermodynamically and economically assessed to determine their viability by comparing them with benchmark processes, *i.e.* the steam methane reforming process (SMR) that was developed earlier in this work and other competitive chemical looping processes described in the literature. The thermodynamic results showed that the ICLWS and the CLWSFe processes exhibited improved effective efficiency by 12.3% and 20.8% compared with the SMR process. Regarding the efficiency of hydrogen production, the ICLWS process exhibited 11.7% higher efficiency than the SMR process; however, the efficiency of hydrogen production by the CLWSFe process was 1.6% lower than that of the SMR process. For the economic assessment, CAPEX, OPEX and the hydrogen production cost were evaluated for both processes. Results indicated that the hydrogen production cost through the ICLWS process with $MgAl_2O_4$ as support material was 17.5% lower than that through the SMR process, and was 26.3% lower through use of the CLWSFe process than through use of the SMR when iron as a saleable product was considered. In addition, a one-dimensional steady-state model was developed to obtain the conversion and temperature profiles for all the reactors involved in the ICLWS and CLWSFe processes. Consequently, the size of each reactor was determined. Furthermore, a system of integrated pumped heat-energy storage (IPHES) was developed by integrating pumped-energy storage with the ICLWS process. Then, an open-cycle gas turbine was merged with this system to form another novel energy-storage system called OIPHES. The transient behaviour of the temperature of the solid inside the storage tanks and the daily energy generation for a selected days in the year in both systems were investigated. Based on that, both systems were assessed thermodynamically and economically. Also, an economic sensitivity analysis was performed for the OIPHES process and a feasibility equation was derived showing the conditions required to enhance the feasibility of the OIPHES system. As a case study, the influence of the hydrogen fuel feed rate on the system's daily profits was studied. Therefore, the optimum hydrogen fuel feed rate to maximise the daily profits of the OIPHES system was selected.

Declaration of originality

Herewith I declare that the content of this thesis is primarily my own work and work of others is appropriately referenced. I declare that I am the primary person responsible for the design, construction and preparation of this manuscript including the development of processes and the analysis of the data. Any work carried out as part of a collaborative work have been explicitly stated in the text.

Husain Bahzad, March 2020.

Copyright declaration

Acknowledgements

I would like to thank my supervisors Professor Paul S. Fennell and Professor Nilay Shah for their excellent guidance and support throughout my PhD project; it wouldn't have been possible without them. Also, I would like to thank Dr. Matthew Boot-Handford, who replaced Prof. Fennell during Prof. Fennell’s sabbatical period, for his patience, exceptional guidance and assistance. Furthermore, I have to thank the public authority of applied education and training for providing me with this scholarship to study in one of the best chemical engineering departments on the globe. Finally, I would like to thank my wife, family and friends for their continuous support and help.

Table of Contents

Chapter 3 : Development and thermodynamic evaluation of a novel chemical looping water splitting process *35*

Chapter 4 : Decarbonised iron production process via chemical looping water splitting technology *70*

List of Figures

List of Tables

Chapter 1 : Introduction

1.1 Statement of the problem

Global warming and climate change have become important subjects to tackle due to the implications they have for the global ecosystem and human quality of life [1]. Emissions of greenhouse gases (GHG), predominantly carbon dioxide (CO$_2$), are targets of the Intergovernmental Panel on Climate Change (IPCC) as the major precursors of global warming [2]. Efforts are underway to reduce anthropogenic emissions of GHG in order to restrict the associated rise in the worldwide temperature for this century to 1.5-2℃ above pre-industrial levels. These figures were enshrined in the Paris Agreement of the parties to the United Nations Framework Convention on Climate Change in 2015 [2]. To achieve this restriction in temperature rise, deep decarbonisation of all the major sources of CO$_2$ emissions, including power generation, transportation and industries such as cement and steel production, is essential.

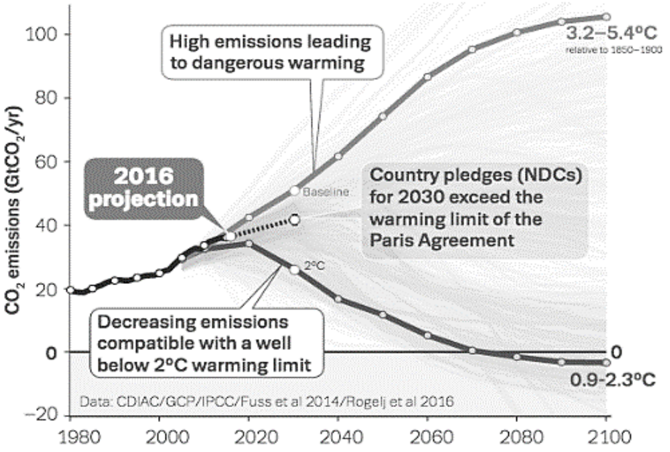

Figure 1.1: Global CO$_2$ emissions: historical emissions, country pledges, and emission scenarios

One strategy for decarbonisationg strategy is carbon capture and storage (CCS). CCS technologies are categorised into: i) pre-combustion, ii) post-combustion and iii) oxy-fuel combustion. In pre-combustion, the fuel is reformed or gasified with pure oxygen stream to produce a mixture of carbon monoxide (CO), CO$_2$ and hydrogen, or synthesis gas (syngas). The CO$_2$ is captured by physical absorption while the syngas is combusted with oxygen and fed to a gas turbine where power is generated [3]. In the post-combustion process, the CO$_2$ is captured after fuel combustion using a unit such as an amine scrubber. In the oxy-fuel technique, the fuel is combusted in pure oxygen separated from air. Combustion in this nitrogen-free system produces flue gases mainly composed of CO_2 and water, so the CO_2 is produced as a concentrated stream that can be captured efficiently [4]. Of these three techniques, pre-combustion, which involves a shift from carbon-intensive fossil fuel to a decarbonised fuel such as hydrogen, has drawn much research interest [5].

Hydrogen (H_2) is an environmentally benign fuel (zero carbon at the use point) that has multiple applications. It can be used in many ways: as fuel for transportation; as fuel for electricity generation through fuel cells and gas turbines; as a precursor in many industries such as fertiliser and pharmaceutical manufacture; in petroleum refining through hydro-treating and hydro-cracking units; and it can be used in domestic and industrial heating [6]. The main route of hydrogen production is the steam methane reforming process (SMR) [7]. This process is economically attractive; the hydrogen production cost through SMR is US$2.31/kg H_2 produced, which is considered the lowest among all hydrogen production methods [8]. However, this process produces approximately 3% of total global industrial-sector CO_2 emissions, as 7kg of CO_2 is emitted per kilogram of H_2 produced [9]. Therefore, an integration of this process with use of efficient carbon capture and storage (CCS) technology is mandatory to mitigate against global warming and climate change. The SMR process produces hydrogen through multi-units from a reformer through a water gas shift reactor and amine scrubber to pressure swing adsorbers or membrane separators [10]. These units are intensive users of energy,, which result in a high energy penalty that reflects on the overall thermal efficiency of the process [11]. Studies have shown that the thermal efficiency of the SMR process is between 68% and 70% [8, 12]. Hence, the deployment of an environmentally friendly and economically attractive process with a low energy-penalty H_2 production method is of huge interest to researchers.

Another important source of industrial CO_2 emissions is iron and steel production, which accounts for 30% (2.6 Gigatonnes (Gt) of CO_2 per year) of overall industrial emissions. Other emission sources are shown in Figure 1.2. Iron and steel are mainly produced via blast furnaces, each of which emits 1-1.5 Gt CO_2 per tonne (t) of iron produced. Oxy-fuel technology is employed normally to reduce CO_2 emissions from blast furnaces. However, only 75% of the CO_2 is captured using this technology, due to the emission of CO_2 from other units in steel production plants such as coke ovens and the sintering process [9]. Deep decarbonisation of steel and iron manufacturing results in a high cost of about 20-25 euros (about US$25) per tonne of CO_2 captured [13]. A lower cost substitute is direct reduced iron (DRI) technology. However, it is used only on a small-scale around the world and is mainly concentrated in the Middle East [9]. Based on these facts and the need for substitutes to the SMR process and blast furnaces in order to fulfil the Paris agreement, chemical looping water splitting (CLWS) technology is among the hydrogen production techniques that have caught attention. This technology has inherent CO_2 capture that results in a low energy-penalty compared with SMR.

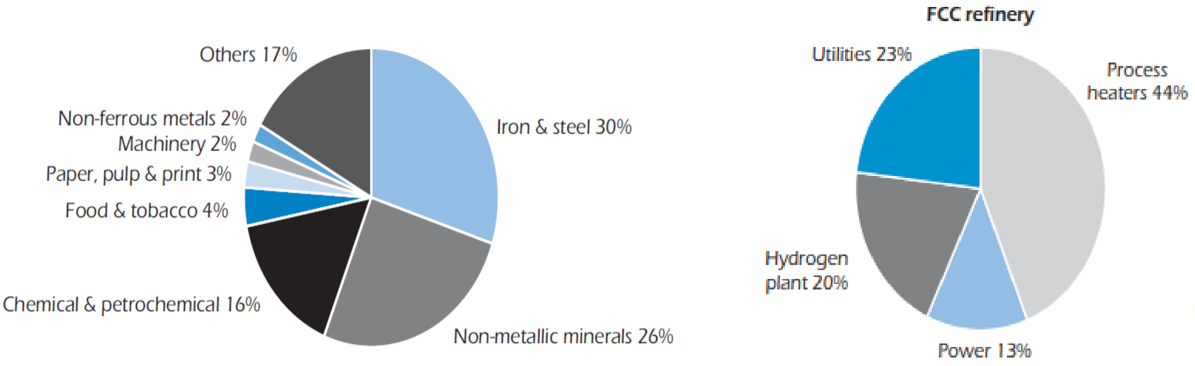

(a) (b)

Figure 1.2: (a) Industrial direct CO_2 emissions by sector; (b) CO_2 emission sources at refineries [9]

In the CLWS process, carbonaceous fuel is indirectly fully combusted with oxygen through an oxygen carrier. Carbon dioxide is captured through steam condensation [10]. Hydrogen is produced via the thermal splitting of steam with the reduced oxygen carrier. Hence, a pure hydrogen stream is formed through steam condensation without the need for any additional energy-intensive unit [14]. In addition, CLWS configuration can be adjusted towards the manufacturing of pig iron with almost 100% CO_2 capture . Also, due to the vast amount of excess thermal energy, steam generation or combined cycle can be integrated with the CLWS to generate/store electricity in-situ with CO_2 capture [15]. The scope of the work described in this thesis is to develop decarbonised processes that can be a promising substitute in the near future for the major methods currently employed for hydrogen energy and steel and iron production, as well as energy generation.

1.2 Aims and objectives of the research project

To evaluate the feasibility of alternative processes for the production of hydrogen, iron or electricity and to decide whether they can be effective substitutes for the current benchmark processes for these products, the following procedures were conducted:

- A novel chemical looping process was developed for the production of stand-alone targeted products, i.e. hydrogen, iron and electricity, or the three combined in one process.
- The developed process was optimised thermodynamically to find the highest possible efficiency. This was performed by minimising the heating utility usage through pinch-point analysis.
- The processes developed were evaluated thermodynamically by determining their energy and exergy efficiency, and economically by determining their capital expenditure, operating expenses and the production cost of the process measured against the amount of product obtained. In order to study the quality of the processes developed, they were compared with their alternative benchmark processes.

1.3 Structure of the thesis

This thesis is comprised of eight chapters with the following content:

(i) The first chapter describes the scope of the research. First it defines the problem, i.e. climate change and global warming. Then, the chapter discusses the main cause of the problem's existence, which is the emission of greenhouse gases and predominantly CO_2. Finally, it considers approaches to overcome the problem, by use of decarbonised fuel and development of a decarbonised process that leads to near-zero carbon emissions.

(ii) The second chapter presents a literature review about hydrogen production technologies and briefly discusses their advantages and disadvantages. It introduces chemical-looping technologies and specifically those used for hydrogen production, i.e. chemical looping water splitting (CLWS) and chemical looping reforming. Also, it contains a brief overview of chemical looping processes that have been developed in earlier studies.

(iii) The third chapter discusses the development of the baseline CLWS process and describes in detail how this process is optimised thermally using pinch-point analysis. The optimised process is called integrated chemical looping water splitting (ICLWS). In addition, sensitivity of process output parameters such as gas and solids conversion due to the manipulation of the process input parameters such as the oxygen-carrier flow rate, temperature or gas temperature is analysed. Finally, the process is assessed thermodynamically by determining its thermal and effective efficiencies, and it is compared with other similar chemical looping processes which have been previously developed, as well as the SMR process, which is considered the benchmark process for H_2 production.

(iv) The fourth chapter presents the development of a novel chemical-looping process (CLWSFe) for the production of hydrogen with direct reduced iron (DRI) as co-product, as well as electricity generation *in-situ* with CO_2 capture. The chapter includes descriptions of the process and its development, then its optimisation through the minimisation of utilities usage and finally the thermodynamic evaluation of the process by determining its thermal energy and exergy efficiencies.

(v) Chapter Five starts with an overview of the process reaction kinetics. Then it discusses the modelling of the reactors involved in both the ICLWS and CLWSFe processes. It shows the equations that govern the mass balances of the components involved in the reactions that occur during both processes, and the energy balances in both the gas and solid phases. Moreover, the gas and solids conversion profiles as well as the temperature profiles are presented.

(vi) In Chapter Six, the economic methodology followed to assess the ICLWS and CLWSFe processes are introduced. Then, both processes are evaluated economically based on the methodology presented, and are compared with both the SMR process and other competitive chemical looping processes.

(vii) Chapter Seven describes an energy storage system called "Pumped thermal energy storage" and considers previous studies evaluating this system. The chapter explains the integration of this energy storage system into the ICLWS process for further study. The energy storage tanks are modelled for the integrated process and then the process is evaluated thermodynamically and economically. An open-cycle gas turbine is added to the system and its effect on the process efficiencies and feasibility are investigated.

(viii) Finally, Chapter Eight summarises all findings and conclusions.

Chapter 2 : Chemical looping and competing processes for hydrogen production

In this chapter, hydrogen production processes including chemical looping are introduced. The chapter is divided into two parts. The first part presents a description of hydrogen production processes. The section focuses on the steam methane reforming process, as this is the dominant method used in industry. It provides an overview of the other methods used for hydrogen production, such as partial oxidation of fuels, electrolysis, water pyrolysis using photo-catalysts and biological techniques. The second part of the chapter introduces the chemical looping technologies specialised in hydrogen production. It describes the technology through process flow diagrams, showing its advantages and disadvantages, and it mentions previous studies conducted on the development of processes for hydrogen production via this technology. Furthermore, parameters such as thermal efficiency and hydrogen production cost discussed in these studies are evaluated to compare chemical looping technology with other competitive processes of hydrogen production.

2.1 Steam methane reforming

Steam methane reforming is currently the most favoured process for hydrogen production. Overall, 75% of worldwide hydrogen production is via this technology. The reason for this is economic: depending on the amount of carbon capture and storage (CCS) and whether or not the process is coupled with the power generation cycle, the hydrogen production cost has been quoted to be as low as US$1.64-1.7/kg H_2 produced, which is cheaper than other H_2 production processes [16]. In steam methane reforming, methane is reacted with steam and passed into a reformer, which is a set of metallic tubes filled with nickel catalyst. Eqs. (2.1-2.2) show the endothermic reactions that occur [12]. Heat is radiated to the metallic tubes in the reformer by combusting the flue gas that is exhausted from the hydrogen separation units and mixed with natural gas, as shown in Figure 2.1. This step is required to ensure the reaction continuity. According to the International Energy Agency's Greenhouse Gas (IEAGHG) research programme, the endothermic reactions (2.1-2.2) are thermodynamically limited; in order to improve the equilibrium conversions, the reformer temperature or the steam to natural gas ratio is altered [16]. The syngas discharged from the reformer is fed to the water gas shift reactor (WGS) to convert most of the CO to CO_2 (i.e. 97% conversion) according to reaction (2.3). This reaction usually takes place in several stages, each at a different temperature, to maintain the required CO conversion. In most SMR processes this step is accomplished through two reactors: the high and low temperature water gas shift reactors. In the high water gas shift reactor (HTS), reaction 2.3 usually occurs at temperatures of 310-350 ºC which achieves 70-80% conversion of CO to CO_2. Since this reaction is exothermic and equilibrium constrained, another stage of WGS is needed at a lower temperature of 250-290 ºC in the low temperature water gas shift reactor to increase the CO overall conversion to 97%. The catalysts used in WGS reactors are iron, nickel or copper based [12].

$$CH_4 + H_2O = CO + 3H_2 \qquad \Delta H_{298} = 205 \text{ kJ/mol} \qquad (2.1)$$

$$CH_4 + 2H_2O = CO_2 + 4H_2 \qquad \Delta H_{298} = 165 \text{ kJ/mol} \qquad (2.2)$$

$$CO + H_2O = CO_2 + H_2 \qquad \Delta H_{298} = -42 \text{ kJ/mol} \qquad (2.3)$$

To obtain hydrogen of 99% purity, separation units that comprise an amine scrubbing unit followed by either a pressure swing adsorber (PSA) or a membrane are required [12, 17]. The block flow diagram of the conventional SMR process is shown in Figure 2.2.

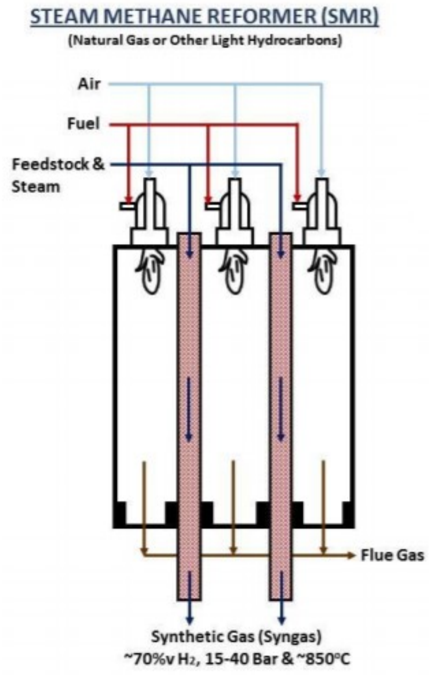

Figure 2.1:Schematic representation of a steam methane reformer [16]

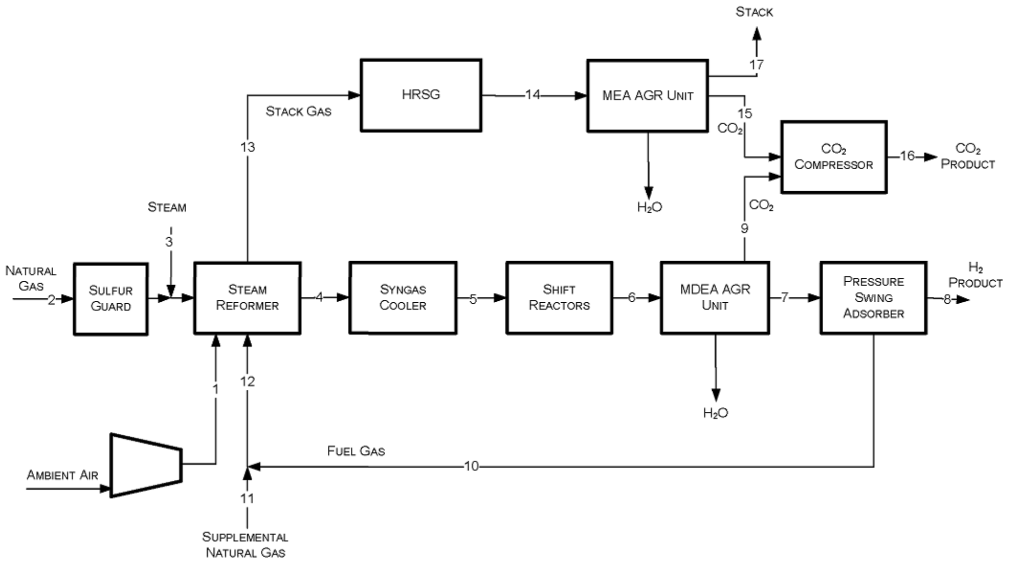

Figure 2.2: Steam methane reforming block-flow diagram, AGR = acid gas removal [12]

Despite the economic attraction of SMR for hydrogen production, the energy penalty is high due to the vast amount of thermal energy utilised in the separation units [11]. As a consequence, the thermal efficiency of the process is low, ranging between 68% and 70%, according to the literature [8]. In modern SMR processes, only PSA or a membrane system is used for hydrogen purification [16], and this leads to a reduction in the total energy consumption of the process. Consequently, the overall energy efficiency of the process is increased to 74 - 85% [18] and the total energy consumption for such a process is 12.4 – 16.3 GJ/Nm^3 of H_2 produced [16]. The block flow diagram for the modern SMR process is represented in Figure 2.3.

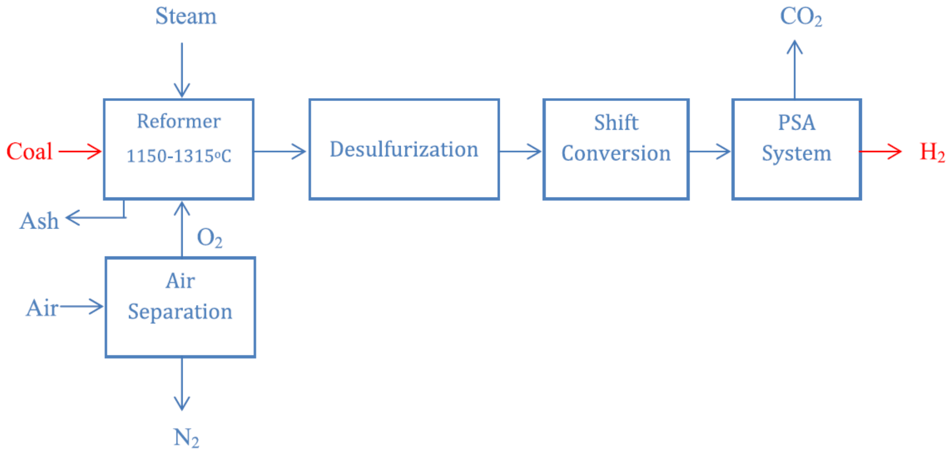

Figure 2.3: The block flow diagram of the modern SMR process [19]

2.2 Hydrocarbon partial oxidation

Hydrogen can be generated through the partial oxidation (POX) of hydrocarbons with steam according to reactions (2.4) and (2.5) under moderate to high pressure depending on the hydrocarbon used [20].

$$2C_nH_m + H_2O + 11.5O_2 \rightarrow nCO + nCO_2 + (m+1)H_2 \qquad (2.4)$$

$$\mathrm{Coal} + 0.6O_2 + 0.7H_2O \rightarrow CO_2 + H_2 \qquad (2.5)$$

Many hydrocarbons are suitable for this process, from gaseous fuels through heavy-liquid fuels, such as heavy oil or petroleum residual oil, to charcoal. Depending on the fuel used, certain undesired components are produced in combination with CO and CO_2 such as hydrogen sulphide (H_2S), sulphurous oxides (SO_x), mercaptans, ash and metals [20]. Consequently, sulphur-treatment units, wastewater treatment units, solids deposition treatment units, and hydrogen purification units such as a pressure swing adsorber are required downstream. Process flow diagrams for heavy hydrocarbon partial oxidation and coal partial oxidation are shown in Figures 2.4 &2.5 respectively.

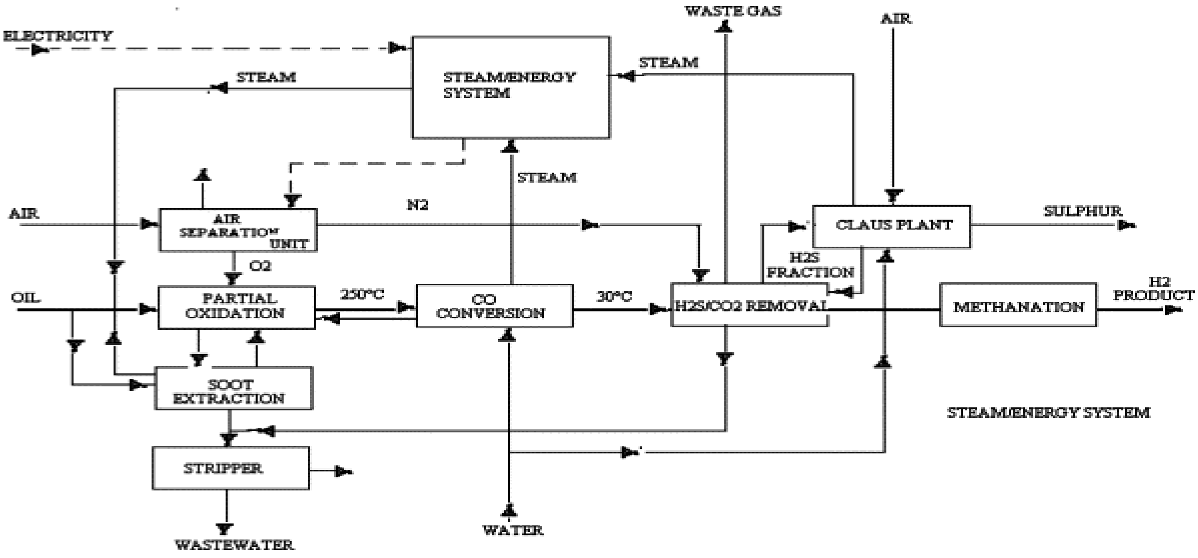

Figure 2.4: Hydrogen production via heavy hydrocarbon partial oxidation [20]

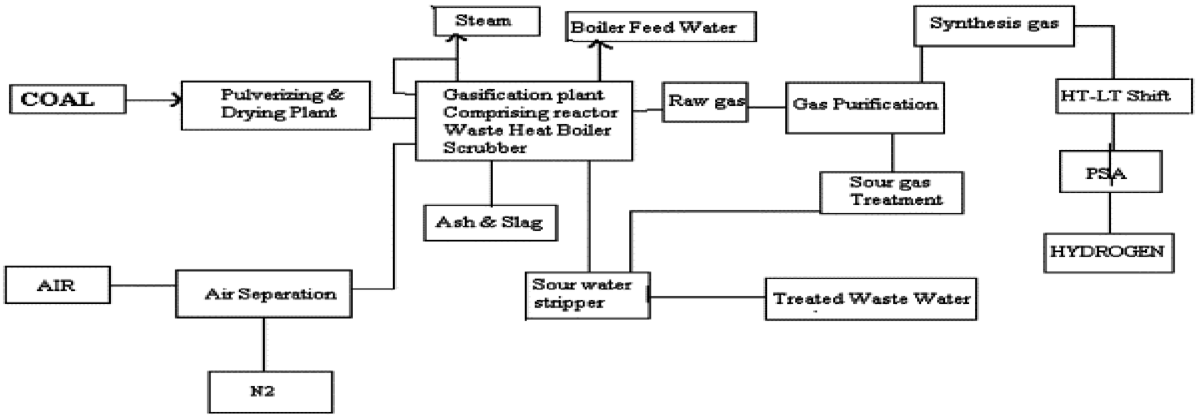

Figure 2.5: Hydrogen production by coal gasification [20]

2.3 Auto-thermal reforming

The auto-thermal reforming (ATR) process is a synergy between the steam methane reforming and partial oxidation processes. In ATR, heat that is exhausted from the partial oxidation reaction of the fuel is utilised in the endothermic reaction of steam reforming. Thus, the hydrogen production and the thermal efficiency of the process are improved [16]. Fuel (natural gas) with steam and air/O_2 are fed to the auto-thermal reformer. If pure oxygen is fed to the reformer, an air separation unit must be integrated into the process upstream, as shown in Figure 2.6 [19]. In the auto-thermal reformer, two reaction zones occur: a) the combustion zone; and b) the reforming zone. The following combustion reactions take place at the combustion zone [16]:

$$\mathrm{CH_4} + 0.5\,\mathrm{O_2} \rightarrow \mathrm{CO} + 2\mathrm{H_2} \quad (2.6)$$

$$\mathrm{H_2/CO} + 0.5\,\mathrm{O_2} \rightarrow \mathrm{H_2O/CO_2} \quad (2.7)$$

Then the gases pass to the lower section of the ATR, which is filled with nickel catalyst and is where the steam reforming reactions (2.1-2.3) takes place. A schematic diagram of the auto-thermal reformer is shown in Figure 2.7 [16]. After the reformer the syngas is fed to the gas shift convertor to convert the CO into CO_2, as represented by reaction 2.3. If the natural gas contains impurities, such as sulphur or heavy metals, these must be removed either before or after the reformer, as shown in Figure 2.6 [19]. The gas that emerges from the shift convertor passes to the H_2 recovery and purification unit in a similar way to its passage in the modern SMR process. The ATR process has thermodynamic efficiency of 60 – 74% [19].

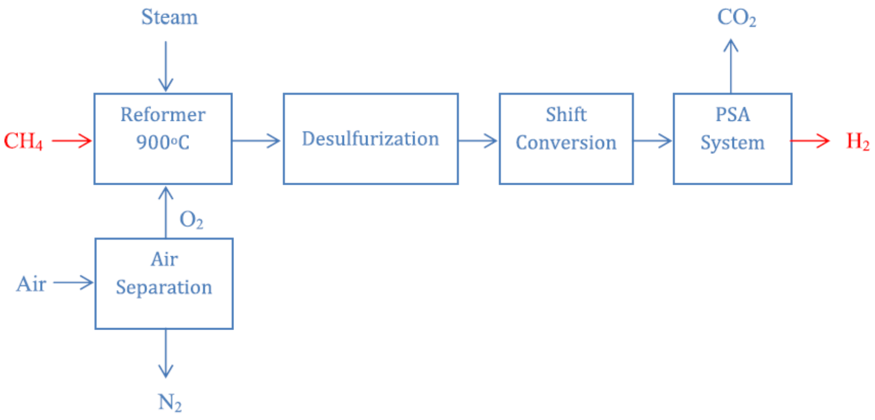

Figure 2.6: Simplified process-flow diagram of auto-thermal reforming [19]

In addition, the energy consumption here is 9.2 - 10.5 GJ/Nm^3, which is 25.8 - 35.5% lower than that found with SMR [16]. This is attributed to the absence of an external energy source, i.e. additional natural gas used for heating. Therefore, less fuel is consumed in this case than in SMR. The ATR process has the most economic hydrogen production cost of $1.48-2.0/kg [18].

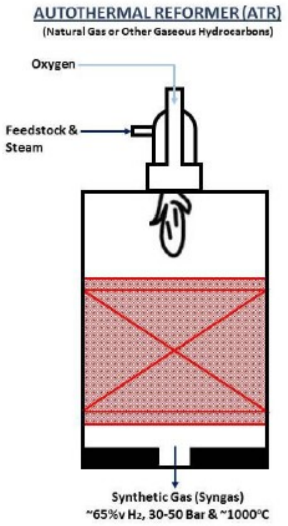

Figure 2.7: Schematic diagram of auto-thermal reformer[16]

2.4 Hydrocarbon pyrolysis

Hydrogen can be formed through the decomposition of hydrocarbons via the following reaction [19]:

$$C_nH_m \rightarrow nC + {}^{m}/_{2}\, H_2 \qquad (2.8)$$

For light hydrocarbons with normal boiling point of 50-200 ºC, reaction (2.8) is carried out catalytically, forming only elemental carbon and hydrogen. However, for heavier hydrocarbons, hydrogen is produced through the two-stage reaction represented by:

Hydro-gasification: $\mathrm{CH_{1.6} + 1.2H_2 \rightarrow CH_4}$ (2.9)

Methane cracking: $\mathrm{CH_4 \rightarrow C + 2H_2}$ (2.10)

When methane is used for this process, the decomposition takes place at 980ºC and atmospheric pressure. Carbon is separated from the product gas comprised of hydrogen and unconverted methane, and then it is fed to a membrane separation unit to decarbonise the hydrogen product. The catalyst is detached from the deposited carbon and recycled to the decomposer reactor, whereas the carbon is stored as the process by-product. The block flow diagram of the methane pyrolysis is shown in Figure 2.8 [19].

This process offers an advantage over SMR in its lower energy requirement per mole of H_2 produced, at 37.6 kJ/mol compared with 63.3 kJ/mol for SMR. The amount of energy necessary for hydrocarbon pyrolysis can be obtained from the combustion of 15-20% of the hydrogen produced [21]. Furthermore, this process does not require the water gas shift (WGS) or CCS units for hydrogen decarbonisation. Therefore for large-scale plants, the capital cost and the hydrogen production cost are lower compared with those of SMR or POX. [22].

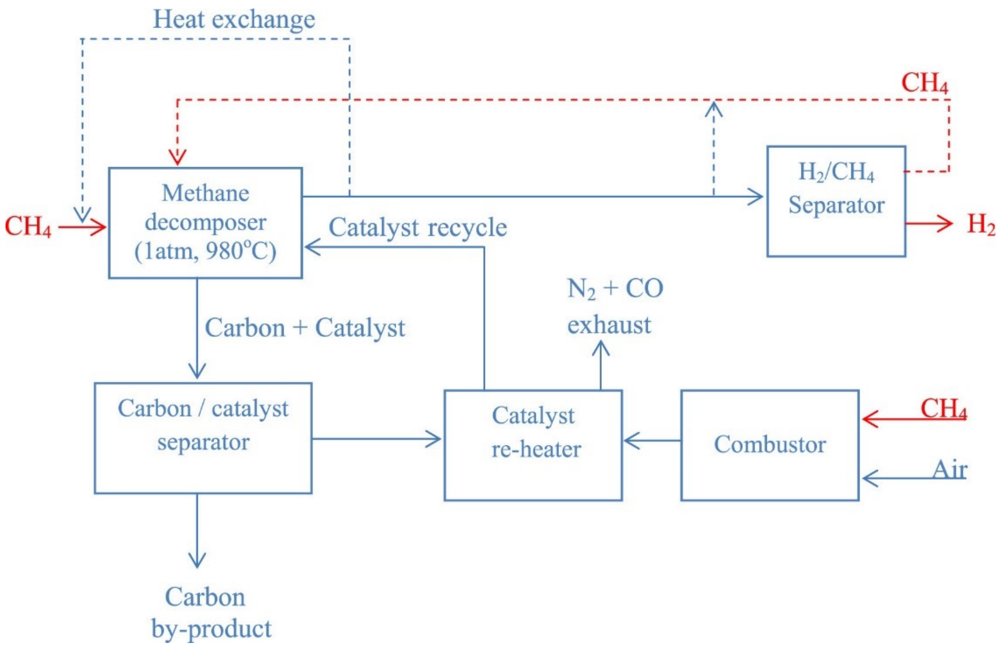

Figure 2.8: Block-flow diagram of methane pyrolysis process [19]

In contrast, the complexity of H_2/CH_4 separation is considered the main disadvantage of the process. Membrane durability is the main problem; the high operating temperature needed to overcome the equilibrium constraints reduces the membrane's lifetime.

2.5 Water electrolysis

Water electrolysis was first discovered in 1789 by Troostwijk and Diemann, and was defined as the electrochemical splitting of water into hydrogen and oxygen according to reaction 2.11 [23].This technology was reported to produce hydrogen of purity 100%.

$$H_2O_{(l)} + \underbrace{237.2\ \mathrm{kJ/mol}}_{\text{Electricity}} + \underbrace{48.6\ \mathrm{kJ/mol}}_{\text{Heat}} \rightarrow H_2 + {}^{1}\!/_{2}\, O_2 \qquad (2.11)$$

Several technologies have been developed under the umbrella term of water electrolysis. The most important are: i) alkaline electrolysis, and ii) proton exchange membrane (PEM) electrolysis.

2.5.1 Alkaline Electrolysis (AE)

Alkaline electrolysis is the most mature water electrolysis technology. Commercial hydrogen production facilities that use this technology consume megawatts of energy worldwide [24]. An electrolysis cell comprises an anode, a cathode, a power supply and electrolyte [25]. An electric current is applied to the electrodes, resulting in decomposition of the water molecule into hydrogen gas and hydroxide ion that is drawn to the cathode, as shown by reaction (2.12). Hydroxide ions from the electrolyte solution (potassium hydroxide, KOH) pass through a membrane to the anode, which releases the electrons back to the power supply to close the circuit and maintain the charge balance according to reaction (2.13) [23].

Cathode: $2H_2O + 2e^- \rightarrow H_2 + 2OH^-$ (2.12)

Anode: $2OH^- \rightarrow \frac{1}{2} O_2 + H_2O + 2e^-$ (2.13)

Overall: $H_2O \rightarrow H_2 + \frac{1}{2} O_2$ (2.14)

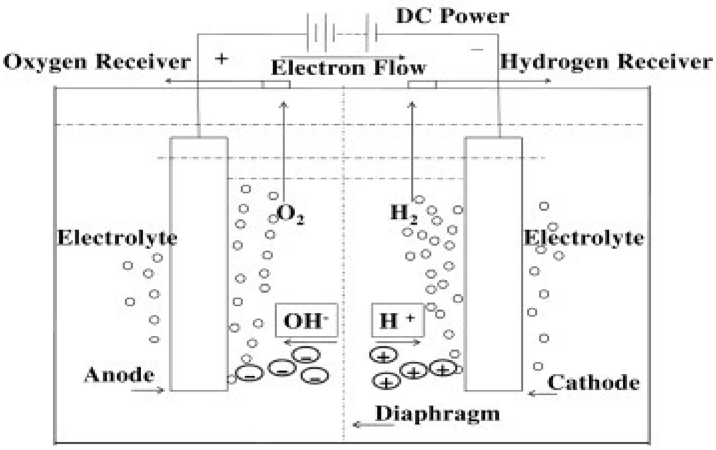

Figure 2.9: Schematic of basic alkaline electrolysis cell [20].

Gas scrubbing and cooling are required to separate hydrogen from water and oxygen. The result is +99%-pure hydrogen [25].

This technology offers long-term operational stability and relatively low cost compared with PEM. The main disadvantages of this method are the requirements for limited current density (0.2-0.4 mA/cm^2), low operating pressure, and the occurrence of gas cross diffusion through the membrane, which lead to a reduction in the hydrogen production rate and in the cell's overall efficiency. [23].

2.5.2 PEM electrolysis

This technology was first developed by General Electric to overcome the disadvantages of alkaline water electrolysis [26]. In this technology, a solid polymer membrane was used as an electrolyte as opposed to the alkaline solution in the alkaline electrolysis. For the PEM electrolysis, a hydrogen proton H+ and an electron are released as a result of the electrochemical split of water at the anode. Both are transported through the polysulphonated membrane to the cathode, where they are recombined to form hydrogen. This is represented by the schematic shown in Figure 2.10 [27].

PEM electrolysis has several advantages over alkaline water electrolysis, one of which is the use of high current density (2 A/cm^2). This feature decreases the operational cost of the electrolysis operation [23]. High proton conductivity is also achievable (0.1± 0.02 S/cm) due to the thin membrane electrolyte used (Σ20-300 μm). Also, reduced gas crossover was detected in PEM electrolysis compared with alkaline electrolysis and, as a consequence, higher purity of hydrogen product [28].

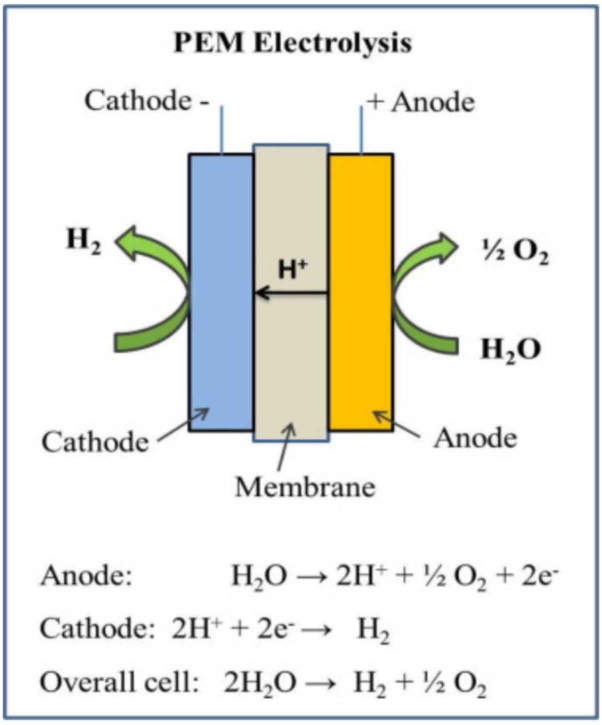

Figure 2.10: Schematic diagram of PEM electrolysis cell [23]

In contrast with alkaline electrolysis, PEM electrolysis can be operated at high pressure due to the use of solid electrolytes, which enables the cells to be placed in a stacking design [29]. High-pressure operation can improve the electrolysis in multiple ways, such as: provision of hydrogen product at elevated pressure for the end user, thus reducing the cost of energy required to pressurise it; minimisation of the expansion and dehydration of the membrane polymer, which results in preservation of the catalytic layer and extension of its lifetime; and improvement of the diffusion of the hydrogen gas product from the cell [30].

2.6 Water photolysis

In this method, water is split by the application of ultraviolet (UV) radiation rather than electricity, in photochemical cells analogous to the electrolysis cell. The splitting of water occurs when the molecules absorb at least 285.6 kJ/mol of energy from the UV radiation [20]. Some photo-catalysts such as semi-conductors or salts are used to promote the rate of absorption and transmission to the water molecule of the UV radiation. As a consequence, the water molecule at the anode splits into an H+ ion and O_2, releasing electrons. The oxygen gas remains in the water at the anode while the H+ ion and electrons travel to the cathode through the electrolyte to form H_2. The reactions taking place in a photo-electrolysis cell are listed below [31].

Anode: $2P^+ + H_2O \rightarrow 2H^+ + \frac{1}{2}O_2$ (2.15)

Cathode: $2e^- + 2H^+ \rightarrow H_2$ (2.16)

In these equations, P^+ is the photo-catalyst.

2.7 Biological methods

The production of hydrogen is possible through biological methods such as fermentation. For example, two moles of hydrogen can be produced per mole of glucose via glycolysis using Escherichia coli [32]. The use of this technology is still limited to laboratory scale and more research is needed to adapt it for large-scale production of hydrogen [33].

The final method of hydrogen production discussed in this study is the thermochemical combustion technology, chemical looping. It is explained in the next section.

2.8 Chemical looping combustion (CLC)

Basic chemical looping refers to a process in which a solid oxygen carrier, typically a transition metal oxide, is utilised to transport oxygen to the "fuel reactor" where it oxidises fuel to produce steam and carbon dioxide. Then, the reduced solid is transferred to another reactor called an "air reactor", in which the solid particles are re-oxidised (regenerated) in air and re-circulated to the fuel reactor, as shown in Figure 2.11 [6]. This process is considered as an inherent CO_2 generation process, because only steam condensation is required to capture CO_2 for sequestration. In the air reactor, heat is released and supplied to the fuel reactor where the reactions are endothermic. Hence, the energy penalty for this process of CO_2 capture is 3-5% [11, 14] . If steam is used to regenerate the oxygen carriers instead of air, both heat and hydrogen are produced in this reactor. Furthermore, the substantial amount of heat produced through this process enables its integration with a steam generation cycle or steam methane reforming. Therefore, in addition to its lower energy penalty, this process can be easily adapted toward the production of valuable components such as hydrogen or electricity. In the upcoming sections, two chemical looping processes for hydrogen production are discussed.

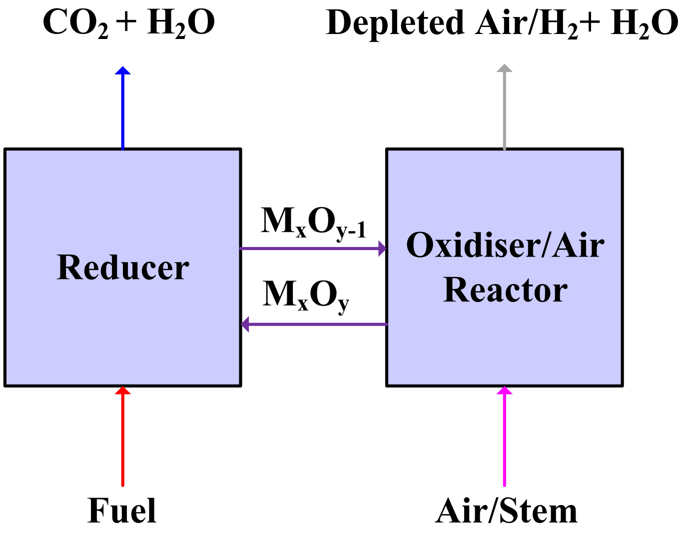

Figure 2.11: The general chemical looping combustion scheme [11].

2.8.1 Chemical looping reforming (CLR)

In chemical looping reforming, air is substituted as an oxygen source for fuel combustion with metal oxides performing the same function as in chemical looping combustion. Hence there is no direct contact between oxygen and fuel [34]. Chemical looping reforming has three subcategories:

i) Chemical looping reforming for syngas (CLRa)

ii) Chemical looping reforming integrated with oxidation for hydrogen and syngas (CLRw)

iii) Steam reforming integrated with chemical looping (CLRS).

Chemical looping reforming for syngas is the baseline model for chemical looping reforming. For CLRa, the fuel, normally methane, is partially oxidised to syngas via its reaction with an oxygen carrier in the reducer [35]. A nickel-based oxygen carrier is the most applicable metal oxide for this process, since research has shown that it has a high capability for hydrocarbon partial oxidation to syngas due to its catalytic activity in the conversion of CO_2 to CO and H_2 [10, 36]. However, the toxicity of material based on nickel (Ni) is considered a major drawback of its use in the CLR process. The reduced Ni oxide is regenerated by air in the air reactor. The reactions followed in this process are shown in equations (2.17-2.20). To attain the required purity level of hydrogen product (>99%), a WGS reactor followed by a PSA process is necessary, and therefore this method offers limited improvement over the conventional SMR process. However, one of the main advantages of the process besides its intrinsic CO_2 capture is the ability to integrate it with a steam cycle for power generation. Both gaseous streams exiting from the fuel and the air reactor contain thermal energy that can be employed in a steam cycle for power generation. Net electricity production of 27 kJ/mol CH_4 has been obtained when the CLR process has been integrated with a steam generation cycle [10, 37] :

$$\mathrm{CH_4 + Me_xO_y \rightarrow CO + 2H_2 + Me_xO_{y-1}} \quad (2.17)$$

$$\mathrm{CH_4 + 4Me_xO_y \rightarrow CO_2 + 2H_2O + 4Me_xO_{y-1}} \quad (2.18)$$

$$\mathrm{CH_4 + CO_2 \overset{N_i}{\rightarrow} 2CO + 2H_2} \quad (2.19)$$

$$\mathrm{CH_4 + H_2O \overset{N_i}{\rightarrow} CO + 3H_2} \quad (2.20)$$

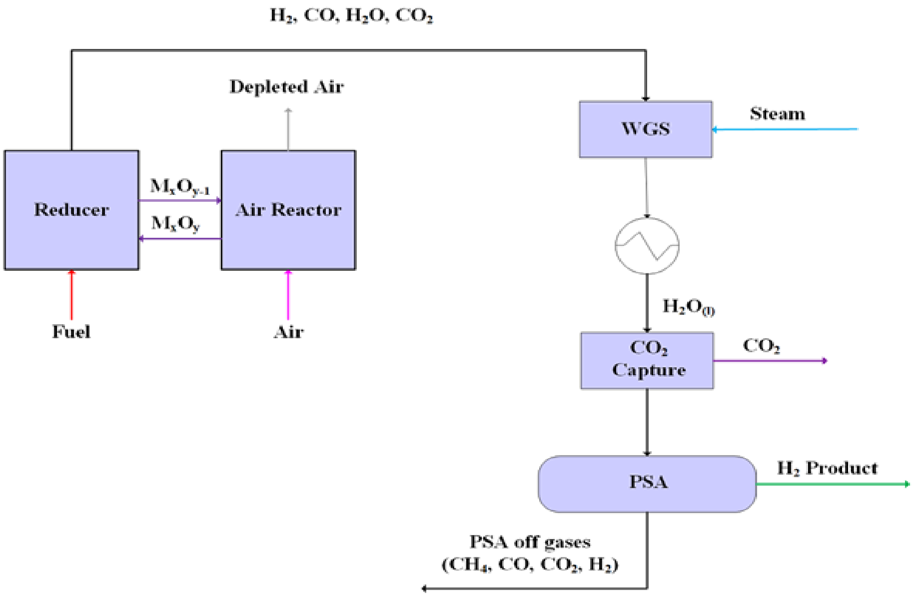

Figure 2.12: The hydrogen production process by steam reforming integrated with CLR [37]

In CLRw, syngas is produced in the fuel reactor in a similar way to the method in CLRa. However, unlike CLRa, the reduced oxygen carrier from the fuel reactor is partially oxidised in a steam reactor, producing a pure hydrogen stream that is easily purified by condensing the steam as illustrated by equation (2.21). The oxygen carrier is then fully regenerated in the air reactor. Therefore, use of this process produces syngas alongside the main product H_2 [38].

$$H_2O + M \leftrightarrow H_2 + MO \quad \text{(Oxidiser)} \tag{2.21}$$

In CLRS, methane is fed with steam into the steam reforming tubes (SR) where part of the steam and methane are converted to H_2, CO and CO_2 as explained earlier in section 2.1. The reactions in the steam reformer do not differ from those of the conventional SMR process; however, the reformer product gas is used as the fuel for the fuel reactor. The heat required for the steam methane reforming reactions is supplied from the hot oxygen carriers circulated from the air reactor. Further purification of hydrogen is achieved by the use of a WGS reactor and a PSA unit, which results in a high-purity hydrogen stream similar to that obtained in a CLRa process. The PSA off-gases comprise significant amounts of unconverted CH_4 and CO with some H_2.

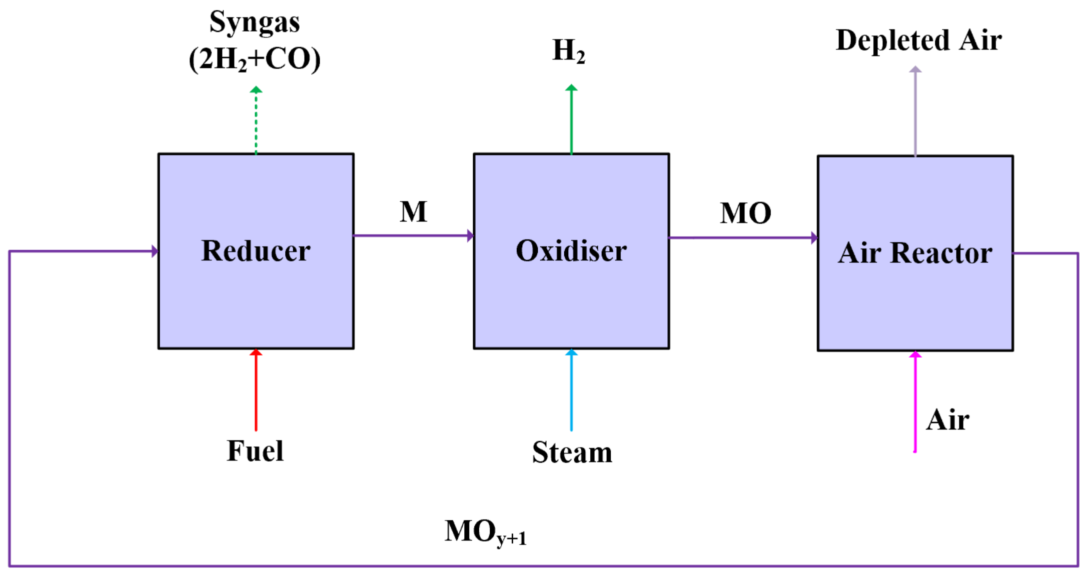

Figure 2.13: Process flow diagram for the CLRw process [10].

This gas stream is used as the feed for the fuel reactor where it is combusted using the metal oxides from the air reactor, resulting in an inherent CO_2 capture [10]. The main advantages of the CLR process compared with SMR are: 1) no external source of heat is needed for the reformer; 2) no CO_2 is emitted from an external combustion source; 3) less catalyst and steam is required per unit of fuel feed; 4) the reaction rate is high since no limitations are imposed by heat transfer [38].

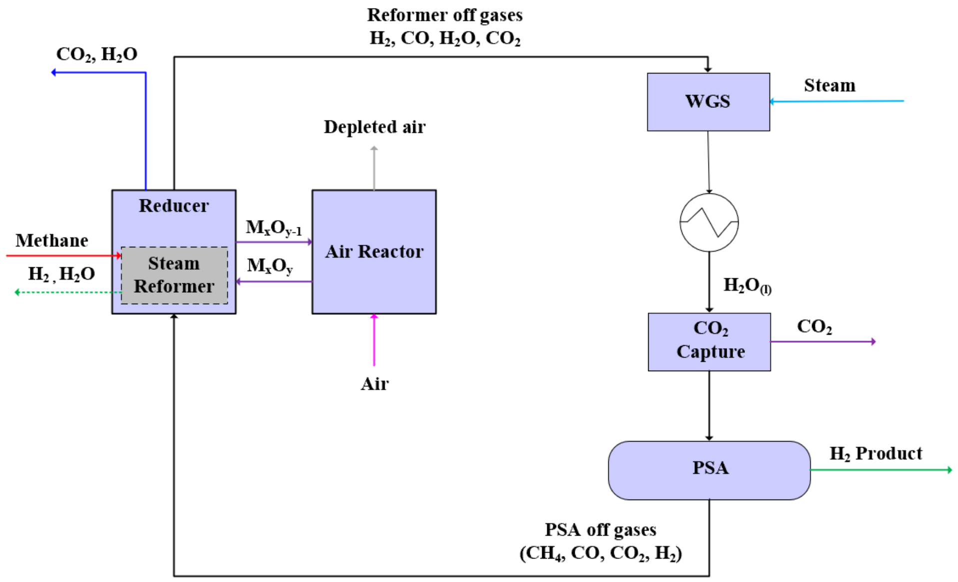

Figure 2.14: CLSR process flow diagram[10, 38]

However, CLR processes still require WGS and separation units such as PSA to achieve a high purity H_2 product, which increases the capital expenditure of the process [38]. Several studies have been conducted to find ideal oxygen carriers for the CLR process. In addition, a number of projects have been performed to investigate reaction-rate kinetics, thermodynamic properties of the oxygen carrier, the main parameters that affect the H_2 production rate, and process performance and feasibility. These have been summarised in the literature [35]. Furthermore, the CLRS process has been modified by adding a sorbent to overcome the WGS equilibrium limitations and reduce the reforming temperature to achieve high H_2 yield in addition to CO_2 capture. This sorbent-enhanced method (SE-CLSR) reduces the energy penalty of CLRS as well as the process expenditure, since fewer additional separating units are required to produce a high purity H_2 product with in-situ CO_2 capture [39, 40]. In addition to the reforming and WGS reactions (Eqs 2.1 and 2.3) the sorption reaction is represented as follows [35]:

$$\mathrm{MeO} + \mathrm{CO_2} \leftrightarrow \mathrm{MeCO_3} \quad \text{(Me: CaO, Li}_2\text{ZrO}_3\text{)} \tag{2.22}$$

SE-CLSR has also been tested with liquid fuel (ethanol), and showed high hydrogen selectivity with low energy demand [39].

2.8.2 Chemical looping with water splitting (CLWS)

The major difference between the CLWS and the CLC processes is the use of a steam reactor instead of an air reactor for the regeneration of the oxygen carriers [14]. In the fuel reactor, fuel is fully combusted to carbon dioxide and steam as shown in reaction (2.23). Then, the reduced oxygen carriers are transferred to the steam reactor where the steam is used to split to hydrogen and oxygen according to reaction (2.24) [8, 41, 42]. CLWS can be fuelled with solid fuels such as coal, liquid fuels or gaseous fuels such as methane [41]. Coal can be used directly as fuel in the fuel reactor, as in “coal direct chemical looping” (CDCL), or it is gasified first to syngas and then used as fuel in the “syngas chemical looping” (SCL) process [6]. If methane is used as the fuel, the reactions that take place in the fuel reactor are highly endothermic, so an external heating source is necessary to sustain the operation. However, this process produces CO_2 and H_2 streams without the necessity for any additional gas separation, hence it results in a lower energy penalty and cost compared with CLR [41]. Therefore, it is considered a promising process for hydrogen generation in future. Further insights about the process thermodynamics and the choice of oxygen carrier follow in upcoming sections.

$$CH_4 + 4Me_xO_y \rightarrow 2H_2O + CO_2 + 4Me_xO_{y-1} \tag{2.23}$$

$$H_2O + Me_xO_{y-1} \leftrightarrow H_2 + Me_xO_y \tag{2.24}$$

CLR and CLWS are two related technologies that have been proposed for combined hydrogen production with CO_2 capture [10, 43]. CLWS is an alternative approach, producing separate, high-purity streams of H_2 and CO_2 [14, 41]. In this process, the separation method for CO_2 is simply a steam condenser [44, 45]. As a result, the corresponding energy penalty is low. The thermal efficiency of the CLWS process is higher than that for SMR [6, 8]. CLWS utilises a reducer, an oxidiser and an air reactor. In the reducer, the oxygen carrier (*e.g.* a metal oxide) is reduced to provide the oxygen required to combust the fuel and thereby produce steam and carbon dioxide. In the oxidiser, the reduced metal oxide is partially oxidised by steam to produce H_2. Finally, the partially oxidised metal oxide is regenerated via full oxidation with air in a third "air" reactor [10, 41]. A schematic diagram of a three-reactor CLWS process is shown in Figure 2.15.

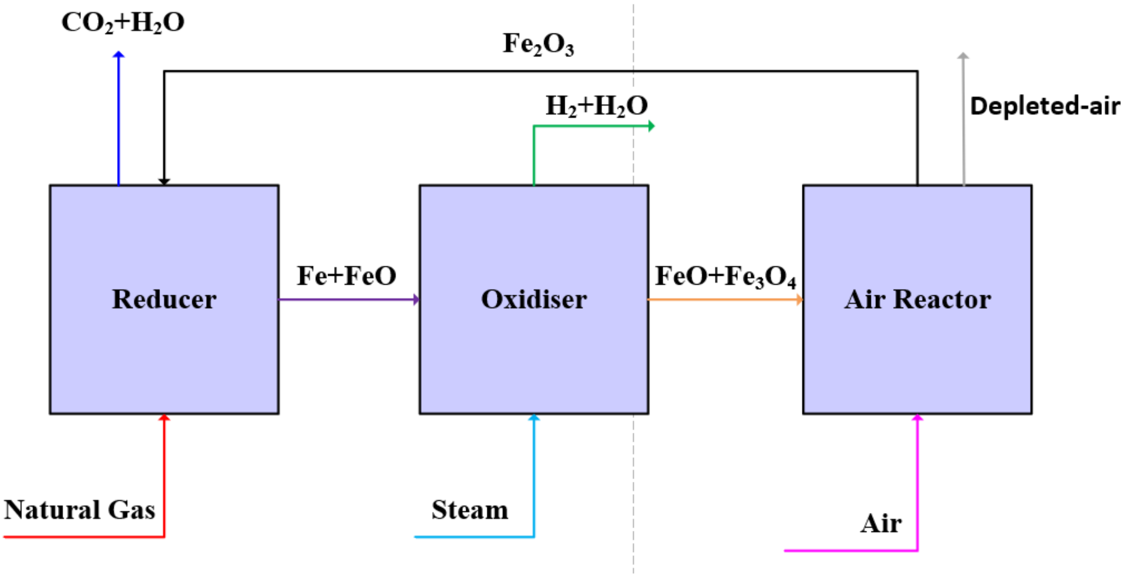

Figure 2.15: Scheme of hydrogen production by chemical looping water splitting [42]

A number of studies have been carried out to model CLWS with gaseous fuels: [11] (syngas chemical looping process (SCL) integrated with gas turbines for power generation); [8, 41] (iron oxide chemical looping with natural gas fuel); [41, 46] (iron oxide chemical looping in three moving bed reactors with natural gas as fuel together with a study of oxygen carrier selection); [47] (iron oxide chemical looping integrated with combined cycle power generation using natural gas or syngas); [41, 48, 49] (chemical looping with iron oxide oxygen carrier integrated with combined cycle using natural gas fuel). Additionally, solid fuels have been tested: [50] (coal direct chemical looping (CDLC) for H_2 and power production using an iron oxide oxygen carrier); [51](iron oxide chemical looping using biomass (sawdust) and coal fuel coupled with combined cycle for power generation); [52] (comparison between SCL and CDCL processes using iron oxide oxygen carrier); [53] (iron oxide chemical looping of biomass integrated with another chemical looping combustion process which uses a copper-based oxygen carrier, and this study proposes calcium oxide looping of biomass); [54] (iron oxide chemical looping with brown coal fuel integrated with the power cycle); [55] (CDCL with iron and copper bi-metallic oxygen carrier); and [56] liquid fuels. These studies have focused on process modelling and thermodynamic evaluation, aimed at providing insight into the effect of key variables on the gas and solid conversions, product efficiencies and overall thermal efficiencies of the process. They indicate that the hydrogen production efficiency in the CLWS process using a gaseous feedstock ranges from 71.3% [49] to 80.3% [48], while the highest overall process efficiency observed was 80.2% [48]. For CLWS with solid fuels, the hydrogen production efficiency values were between 65.3% [51] and 72% [50]; the overall process efficiency for some recent studies has achieved 90.3% by employing high operating pressure utilising a combined power generation cycle [54]. However, little is known about the techno-economic aspects and feasibility of the CLWS process [49, 51].

2.9 Development of kinetic models for the gas-solid reactions involved in the chemical looping water splitting process

Clear understanding and description of the reaction kinetics take a primary role in designing any reactor. The concentration and temperature profiles are all affected by the reaction kinetics of a reactor. Therefore, knowledge of the reaction rate expressions is the first step toward production of an appropriate design of a reactor to conduct any of the reactions or reaction schemes above. Efforts have been conducted to describe the gas-solid oxidation-reduction reactions. All the reactor models fall into two major categories:

a) Unreacted shrinking core model [57]

b) Nuclei and nucleation growth [58]

In the unreacted shrinking core model, determination of the reaction rate depends on the particle size and morphology of the starting materials. However, for the nucleation model, only the gas-solid reaction mechanism is considered and the particle structure is ignored. Recently, more models have been derived that combine both categories to obtain the oxidation-reduction rate parameters [59].

2.9.1 Unreacted shrinking core model

This model was developed by Yagi and Kunii in 1956 and 1961. It expresses the mechanism of the reactions carried out between the gas and the solids in five steps [60]:

1- The gaseous reactant A diffuses through the gas film to the solid particle surface.
2- Gaseous reactant A diffuses through the ash layer that surrounds the surface of the particle to reach its unreacted core.
3- The gaseous reactant A reacts with the solid particles at its unreacted core.
4- The product gas B back diffuses through the ash layer to the outer surface of the solid particle.
5- The gaseous product B diffuses from the gas film to the bulk part of the reactor.

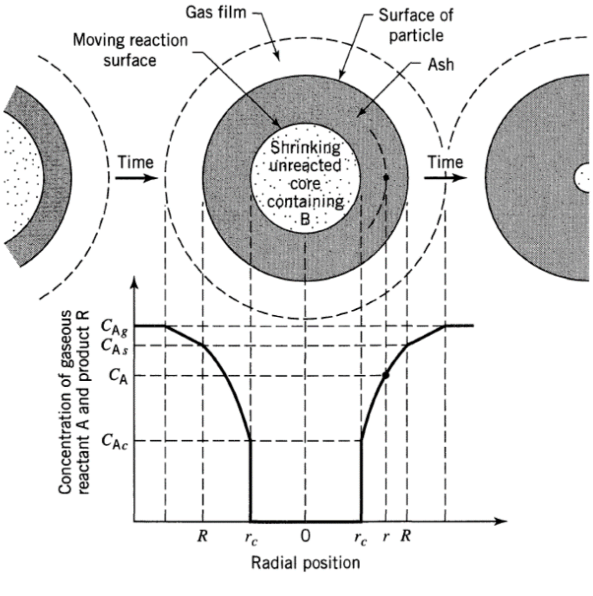

Figure 2.16: Representation of the concentration profile of a reaction $A_{(g)} + S \rightarrow B_{(g)} + S_2$ *in the unreacted shrinking core model [60]*

For a reaction in which no gaseous product is formed, steps 4 and 5 are ignored. Also, the resistance at each step varies according to the reaction conditions and species reacted. The step with high resistance is considered as the rate-controlling step.

Gas film diffusion is controlling step

In the irreversible gas-solid reaction represented by Eq. (2.25), the concentration profile of gaseous reactant A when the gas-film resistance is the controlling step is shown in Figure 2.17.

$$A_{(g)} + B_{(s)} \rightarrow C_{(g)} + D_{(s)} \qquad (2.25)$$

For this case the diffusion of reactant A through the ash layer is fast. Hence, no gaseous reactant A is present at the surface of the solid particle, as can be observed from Figure 2.17. Therefore, concentration of A at the solid surface (C_{As}) is negligible, thus the driving force, which is the concentration gradient, becomes C_{Ag}. Using the stoichiometry of Eq. (2.25), the rate of change of solid B with respect to time is shown in Eq. (2.26):

$$\frac{1}{4\pi R^2}\frac{dN_B}{dt} = \frac{-b}{4\pi R^2}\frac{dN_A}{dt} = bk_g C_{Ag} \qquad (2.26)$$

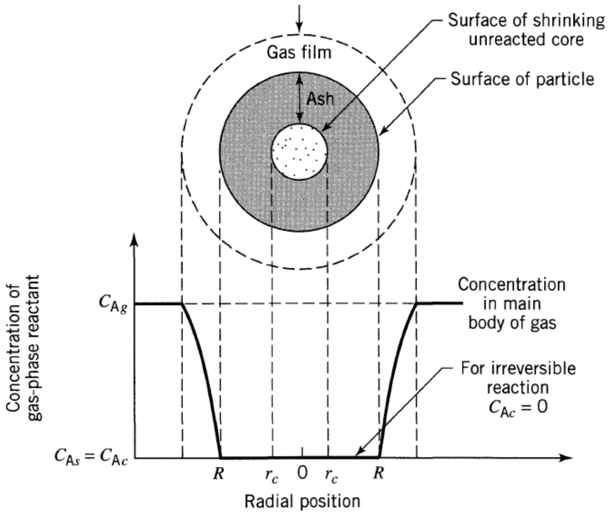

Figure 2.17: Representation of a reacting particle when diffusion through the gas film represents the rate controlling step

When the moles of A are represented in terms of density and molar volume and the molar volume is represented in terms of unreacted core radius, the unreacted core shrinkage and the time for complete reaction can be represented by Eqs. (2.27) and (2.28) as follows:

$$t = \frac{\rho_B R}{3bk_g C_{Ag}}\left[1 - \left(\frac{r_c}{R}\right)^3\right] \tag{2.27}$$

$$\tau = \frac{\rho_B R}{3bk_g C_{Ag}} \tag{2.28}$$

The radius of unreacted core is related with the fraction conversion of B according to Eq. (2.29):

$$\frac{t}{\tau} = X_B = 1 - \left(\frac{r_c}{R}\right)^3 \tag{2.29}$$

In these equations:

R = radius of the solid particle S (m^2).

b = stoichiometric parameter of solid B.

k_g = mass transfer coefficient through the gas film (m/s).

C_{Ag} = concentration of gaseous reactant A in the bulk gas (mol/m^3)

ρ_B = molar density of solid particle B (mol/m^3)

r_c = radius of the unreacted core of the solid particle B (m).

τ= time for complete conversion (s).

X_B = fractional conversion of solid particle B.

Diffusion through ash layer as controlling step

For the same reaction shown in Eq. (2.25), the concentration profile for the case when the diffusion through the ash layer is the controlling step is represented by Figure 2.18.

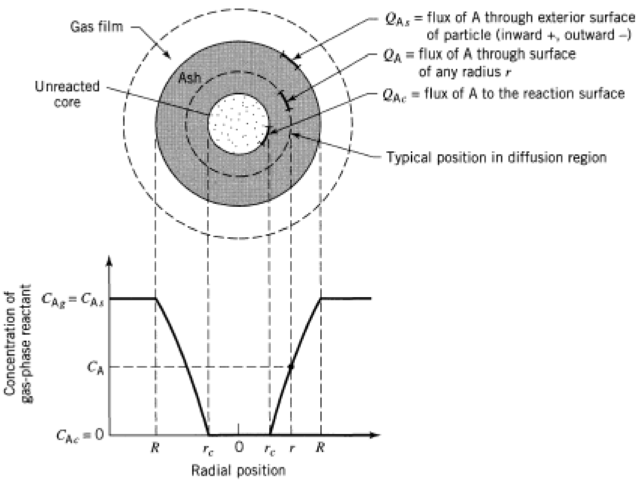

Figure 2.18: Representation of a reacting particle when diffusion through the ash layer is the controlling step of the reaction

The unreacted core is assumed to be stationary. This assumption is sensible, based on the fact that the shrinkage of the unreacted core is 1000 times slower than the molar flow rate of reactant A through the surface of the core. Therefore, the rate of reaction of A can be represented by the rate of diffusion of A via the ash layer as follows:

$$-\frac{dN_A}{dt} = 4\pi R^2 Q_{As} \tag{2.30}$$

In this equation, Q_{As} is the flux of A within the ash layer (in mol/m^2.s) and can be expressed by Fick's law as follows:

$$Q_{As} = D_e \frac{dC_A}{dr} \tag{2.31}$$

D_e = effective diffusivity of reactant A in the ash layer (in m^2/s). Substitution of Eq. (2.31) into Eq. (2.30), and integration from $r=R$ to $r=r_c$, the rate of reaction of A with respect to time can be represented as:

$$-\frac{dN_A}{dt}\left(\frac{1}{r_c} - \frac{1}{R}\right) = 4\pi D_e C_{Ag} \tag{2.32}$$

Now, an expression for the size of the unreacted core over time is derived. This can be achieved by integration of Eq. (2.32). However, this equation contains three variables N_A, t, r_c. Thus, one variable should be represented as a function of the other two. N_A is written as a function of r_c according to the following formula:

$$-b\frac{dN_A}{dt} = 4\pi {r_c}^2 \rho_B dr_c \tag{2.33}$$

Consequently, the reaction time in terms of the size of the unreacted core and the time required to achieve a complete conversion are represented by Eqs. (2.34) and (2.35), respectively:

$$t = \frac{\rho_B R^2}{6bDC_{Ag}}\left[1 - 3\left(\frac{r_c}{R}\right)^2 + 2\left(\frac{r_c}{R}\right)^3\right] \tag{2.34}$$

$$\tau = \frac{\rho_B R^2}{6bDC_{Ag}} \tag{2.35}$$

The reaction progression as a function of fractional conversion of the particle is:

$$\frac{t}{\tau} = 1 - -3(1 - x_B)^{2/3} + 2(1 - x_B) \tag{2.36}$$

Chemical reaction as the controlling step

The concentration profile when surface reaction rate is the controlling step is shown in Figure 2.19. As observed in this figure, the reaction does not progress until the reactant reaches the surface of the unreacted core. Therefore, the rate of reaction as a function of the size of the unreacted core is expressed by:

$$\frac{-b}{4\pi {r_c}^2}\frac{dN_A}{dt} = bk'C_{Ag} \tag{2.37}$$

In this equation, k′ is the surface reaction rate constant. If N_A is represented as a function of unreacted core radius, separation and integration leads to:

$$t = \frac{\rho_B R}{bk'C_{Ag}}(R - r_c) \tag{2.38}$$

Setting $r_c = 0$, yields to the time needed for complete conversion, the change in the fractional conversion in terms of τ is written as:

$$\frac{t}{\tau} = 1 - (1 - x_B)^{1/3} \tag{2.39}$$

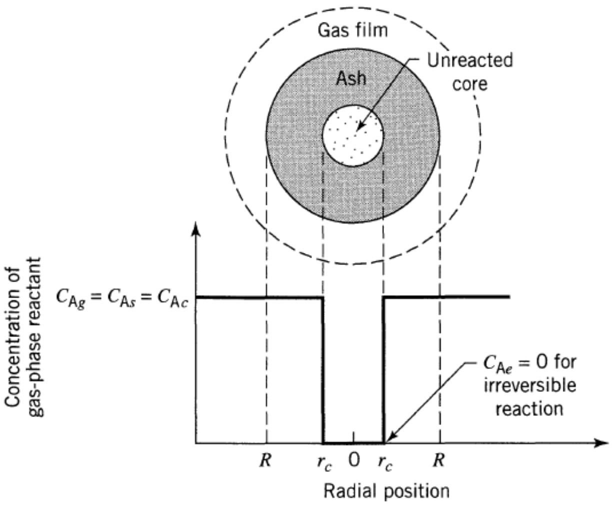

Figure 2.19: Representation of a reacting particle when the chemical reaction is the controlling step.

2.9.2 Nucleation growth

The nucleation growth model does not consider the morphology of the particles in the determination of the overall reaction rate. In this model, the gas-solid reaction mechanism is described in five steps as shown in Figure 2.20 [59, 61]:

1) The induction period: the solid particles are prepared (activated) to form nuclei. The induction period depends on the reaction temperature.
2) Nuclei formation: the reaction starts when the first nucleus is generated.
3) Growth and further nuclei formation: during this period, the reaction progresses. The nuclei grow due to the overlap of newly formed nuclei with the existing nucleus.
4) End of the growth: nuclei cease growing and hence, the reaction achieves the required conversion.

The rate of reaction can be expressed generally according to the following formula [42]:

$$r = \frac{-d\alpha}{dt} = k(T)f(\alpha)f(C_i) \qquad (2.40)$$

In this equation:

α is the degree of solid reduction, i.e. conversion.

k = is the intrinsic reaction rate constant.

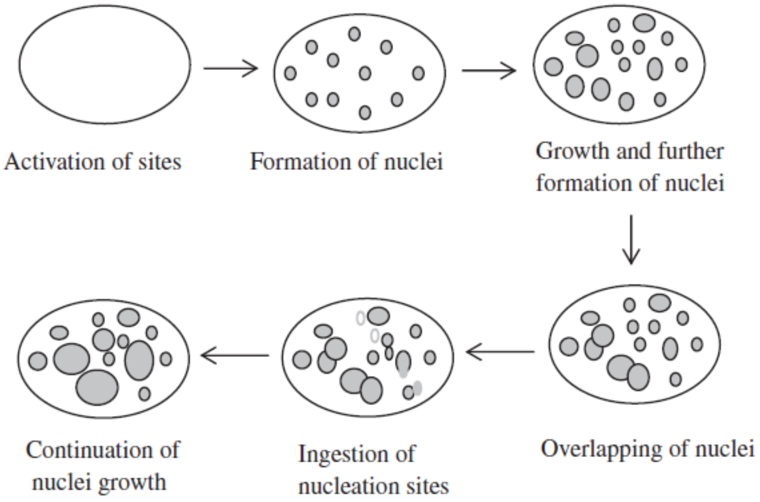

Figure 2.20: Formation and growth of nuclei of product during the reduction/oxidation reactions in the nucleation growth model [62]

The overall conversion and the reaction rate both rely on the nucleation or nuclei growth, or the combination of both [62]. At least one of these steps could be the rate controlling step of the reaction. Generally, experimental procedure is conducted to obtain the functions of conversion $f(\alpha)$ and concentration $f(C_i)$, and the parameters of the reaction rate constant, which is represented by the Arrhenius equation as follows:

$$k(T) = Ae^{\left(\frac{-E_a}{RT}\right)} \tag{2.41}$$

Here A is the pre-exponential factor and E_a is the activation energy. The conversion function is obtained by analysis of the conversion-time plot. The Avrami-Erofeev model represented by Eq. (2.42) describes the conversion function and can be used to calculate the rate-controlling step [63].

$$f\ (\alpha)\ =\ n(1-\alpha)[-\ln(1-\alpha)]^{(n-1)/n} \tag{2.42}$$

Here n is an Avrami-exponent which indicates the reaction mechanism.

2.9.3 General screening method to derive the reaction-rate expression model

General approaches are proposed in the literature to identify the reaction mechanism, and the correct kinetic model with conversion function is selected based on these approaches [59, 64]. All these methods are based on a general formula related to the illustration of the nucleation as follows [42, 64]:

$$ln[-ln(1 - X)] = m\, ln(t) + ln(n) \tag{2.43}$$

In this equation X is the solids conversion rate, n is a constant that depends on the nucleation frequency and m is a constant that indicates the reaction mechanism. The classification of the kinetics models are categorised according to the value of m as listed in Table 2.1.

Table 2.1: Reaction models and the represented expressions [42]

Kinetic model	**Conversion function of the kinetic model $f(X)$**	**Integral form of the kinetic model function $g(X)$**	**m**
One-dimensional diffusion (D1)	${}^{1}/_{2}X$	$X^2 = kt$	0.62
Two-dimensional diffusion (D2)	$\frac{1}{[-ln(1-X)]}$	$(1 - X)\, ln(1 - X) = kt$	0.57
Three-dimensional diffusion (D3)	$\frac{3(1-X)^{2/3}}{2\left[1 - ln\,(1-X)^{1/3}\right]}$	$\left[1 - \ln\,(1-\mathrm{X})^{1/3}\right]^2 = kt$	0.54
First-order reaction (AE1)	$(1 - X)$	$-ln(1 - X) = kt$	1.00
Two-dimensional nuclei growth(AE2)	$2(1 - X)[-ln(1 - X)]^{1/2}$	$[-ln(1 - X)]^{1/2} = kt$	2.00
Three-dimensional nuclei growth(AE2)	$3(1 - X)[-ln(1 - X)]^{2/3}$	$[-ln(1 - X)]^{2/3} = kt$	3.00
Phase boundary (Infinite slab R_1)	1	$X = kt$	1.24
Phase boundary (contracting cylinder R_2)	$(1 - X)^{1/2}$	$1 - (1 - X)^{1/2} = kt$	1.11
Phase boundary (contracting sphere R_3)	$(1 - X)^{2/3}$	$1 - (1 - X)^{2/3} = kt$	1.07

2.10 Summary of proposed H_2 production routes

In order to decide which H_2 production process will be fully analysed and assessed in the upcoming chapters, a full comparison is carried out showing the potentials and the setback of each process discussed here, its thermodynamic efficiency, the current commercial status (laboratory scale, pilot plant or industrial-scale plant) and economic viability (hydrogen production cost). Tables 2.2-2.3 summarise these data [19].

Table 2.2: Comparison of hydrogen production processes (a) [19]

Process	**SMR**	**ATR**	**POX**	**CHs pyrolysis**
Thermal efficiency (%)	68-85	60-74	60-75	-
Advantages	Most developed tech, lowest cost	Proven technology	Proven technology	Emission-free
Disadvantages	CO_2 by-product, fossil-fuel dependent	CO_2 by-product, fossil-fuel dependent	CO_2 by-product, fossil-fuel dependent	Carbon by-product, fossil-fuel dependent
Current commercial status	Existing infrastructure	Existing infrastructure	Existing infrastructure	Pilot plant
Hydrogen production cost (\$/kg)	2.27 with CCS 2.08 without CCS	1.48 – 1.7	1.63 with CCS 1.34 without CCS	1.6 – 1.7

Table 2.3: Comparison of hydrogen production processes (b) [19]

Process	**Electrolysis**	**Photolysis**	**Chemical looping**
Thermal efficiency	40-60	0.06	65-90
Advantages	No pollution with renewable source, abundant feedstock, proven technology	Clean and sustainable, abundant feedstock	Inherent CO_2 capture, cost competitive, low energy penalty
Disadvantages	Low overall efficiency, high capital cost	Sunlight requirement, low efficiency, ineffective photo-catalytic material	Deactivation of the oxygen carriers, under-developed technology
Current commercial status	Lab scale (PEM) – well established technology (AE)	Lab scale	Pilot plant
Hydrogen production cost ($/kg)	4.15 - 23.3	10.63	1.43 - 1.67

Tables 2.2-2.3 indicate that hydrocarbon reforming is the dominant technology for hydrogen production owing to its thermodynamic and economic viabilities. It shows the lowest hydrogen production cost and highest thermal efficiency. Carbon dioxide emission is its only major disadvantage. Other renewable-energy dependent technologies such as electrolysis and photolysis have zero carbon emission, but their current thermodynamic and economic evaluation does not qualify them as promising technology. In contrast, the initial thermodynamic and economic evaluations of chemical looping mark it out as a main substitute for SMR, especially as it enables CO_2 capture with low energy penalty and low capital cost. The latter leads it to be cost competitive with SMR.

2.11 Concluding remarks

This chapter discusses the main routes toward the production of hydrogen, either from fossil fuels through steam reforming, partial oxidation, hydrocarbon pyrolysis or chemical looping, or through use of renewable sources via electrolysis, photolysis or biological methods. An overview of each process has been presented, describing the process, the main reactions involved, raw materials used and summaries of earlier studies that have assessed these processes thermodynamically and economically. Comparison of all the processes indicates that steam methane reforming shows high values of thermal efficiency (68-85%) with the lowest hydrogen production cost (US$1.6-2.34 /kg hydrogen produced), placing it at the top of the preferred hydrogen production processes list. However, its high intensity of CO_2 emissions and the high energy requirement associated with CO_2 capture (especially from the flue gas) is considered as a major drawback of the technology. High production cost and low efficiency are the main flaws that prevent the decarbonised hydrogen production technologies, i.e. electrolysis and photolysis, from becoming reliable sources of hydrogen in the near future, despite their non-pollutant by-products and feedstock abundance. Instead, chemical looping with its inherent CO_2 capture, thermodynamic efficiency and economic attractiveness can be considered a promising alternative for SMR in the near future.

Chapter 3 : Development and thermodynamic evaluation of a novel chemical looping water splitting process

This chapter describes the development and thermodynamic evaluation of a novel hydrogen production process via chemical looping water splitting technology. For any chemical looping process, selection of the most appropriate oxygen carrier is a critical step. Section 3.1 discusses the principles used for oxygen-carrier selection and provides an overview of the previous studies that have been conducted for that purpose. The thermodynamic limitations of the oxygen carriers and the reactions carried out in the process are illustrated in the second part of the chapter (section 3.2-3.4). Section 3.5 explains the baseline process that has been developed. It shows the methodology followed and describes the process in full detail. Section 3.6 includes the development and the heat integration of steam methane process. Sections 3.5 and 3.8 describe the application of the pinch-point method and sensitivity analysis to the baseline process in order to optimise both the energy requirement of the process and the hydrogen yield. Based on the results obtained from sections 3.5 and 3.8, section 3.7 explains the thermodynamic assessment of the chemical looping water splitting and steam methane reforming processes developed. Finally, section 3.9 concludes the chapter and offers a summary of its findings.

3.1 Oxygen-carrier selection

Oxygen carriers play a key role in CLC technology. Oxygen carriers are solid particles composed of an active metal that chemically binds the oxygen lattice, which takes part in the combustion reaction with the fuel. In the case of CLWS, oxygen is provided to the carrier by splitting the steam. Several studies in the last 15 years have been conducted to develop the most practical oxygen carriers for the CLC process. They have to fulfil the following criteria [10, 14]:

- High reactivity with fuel and oxygen, so that the carrier will fully convert the starting materials to CO_2 and H_2O, or in the case of CLWS, to split water to produce hydrogen.
- Low tendency for agglomeration and attrition (low deactivation rate).
- Low cost and high abundance.

- Low health and safety risk.
- Sufficient oxygen transfer capacity.

The reactivity of oxygen carriers and their ability to generate steam, CO_2 and H_2 are determined through a thermodynamic analysis of the materials. In the upcoming section this analysis is discussed together with the physical properties of the oxygen carriers.

3.2 Thermodynamic analysis of candidates to be oxygen carriers for CLWS process

Studies have been performed on a range of oxygen carriers to categorise them and provide an oxygen-carrier map that shows the best oxygen carriers for each chemical looping process [36, 65]. Further research by Kang et al. was designed to discover the most suitable oxygen carrier for hydrogen production in conjunction with CO_2 and H_2O via chemical looping through CLWS specifically [46]. These studies investigated the thermodynamic constraints for the studied oxygen-carrier reactions with fuel to produce hydrogen in-situ with CO_2 capture. To do so, the Gibbs free-energy values for the reactions between the oxygen carriers were determined with both steam and fuel and these are summarised in Tables 3.1 and 3.2. These values show whether the reaction is spontaneous ($\Delta G < -25$ kJ/mol), reversible (-25 kJ/mol $< \Delta G <25$ kJ/mol) or thermodynamically infeasible and results in low yield of hydrogen product ($\Delta G > 25$ kJ/mol). Based on the Gibbs free-energy criterion, the potential oxygen carriers to be used in the CLWS process for hydrogen production with CO_2 capture were selected. Furthermore, the durability and sustainability of the oxygen-carrier material was an important factor in the selection, since they would be required to operate under high-temperature conditions in the CLWS process. Therefore, the melting points for some of the oxygen carriers were also included in the study and some are shown in Table 3.3.

Table 3.1: Standard reaction Gibbs free-energy change of the candidate oxygen carriers with steam[46]

Reaction	**ΔG at 600 °C (kJ/mol)**
$Ni + H_2O_{(g)} \leftrightarrow NiO + H_{2\,(g)}$	40
$Cu + H_2O_{(g)} \leftrightarrow CuO + H_{2\,(g)}$	123
$2Cu + H_2O_{(g)} \leftrightarrow Cu_2O + H_{2\,(g)}$	95
$Cu_2O + H_2O_{(g)} \leftrightarrow 2CuO + H_{2\,(g)}$	150
$3FeO + H_2O_{(g)} \leftrightarrow Fe_3O_4 + H_{2\,(g)}$	-8
$3/4\,Fe + H_2O_{(g)} \leftrightarrow 1/4\,Fe_3O_4 + H_{2\,(g)}$	-8
$3.807Fe_{0.947}O + H_2O_{(g)} \leftrightarrow 1.202Fe_3O_4 + H_{2\,(g)}$	-12
$Mn + H_2O_{(g)} \leftrightarrow MnO + H_{2\,(g)}$	-121
$3MnO + H_2O_{(g)} \leftrightarrow Mn_3O_4 + H_{2\,(g)}$	78
$2Mn_3O_4 + H_2O_{(g)} \leftrightarrow 3Mn_2O_3 + H_{2\,(g)}$	175
$Co + H_2O_{(g)} \leftrightarrow CoO + H_{2\,(g)}$	27
$3CoO + H_2O_{(g)} \leftrightarrow Co_3O_4 + H_{2\,(g)}$	143
$Ce_2O_3 + H_2O_{(g)} \leftrightarrow 2CeO_2 + H_{2\,(g)}$	-56
$3.571CeO_{1.72} + H_2O_{(g)} \leftrightarrow 3.571CeO_2 + H_{2\,(g)}$	-29
$5.882CeO_{1.83} + H_2O_{(g)} \leftrightarrow 5.882CeO_2 + H_{2\,(g)}$	-18
$9.091CeO_{1.72} + H_2O_{(g)} \leftrightarrow 9.091CeO_{1.83} + H_{2\,(g)}$	-46
$WO_2 + H_2O_{(g)} \leftrightarrow WO_3 + H_{2\,(g)}$	12
$1.389WO_2 + H_2O_{(g)} \leftrightarrow 1.389WO_{2.72} + H_{2\,(g)}$	0
$1/2\,W + H_2O_{(g)} \leftrightarrow 1/2\,WO_2 + H_{2\,(g)}$	-15
$1/5\,Nb + H_2O_{(g)} \leftrightarrow 1/5\,Nb_2O_5 + H_{2\,(g)}$	-104
$2/3\,NbO + H_2O_{(g)} \leftrightarrow 1/3\,Nb_2O_5 + H_{2\,(g)}$	-79
$2NbO_2 + H_2O_{(g)} \leftrightarrow Nb_2O_5 + H_{2\,(g)}$	-46
$NbO + H_2O_{(g)} \leftrightarrow NbO_2 + H_{2\,(g)}$	-95
$2/3\,Cr + H_2O_{(g)} \leftrightarrow 1/3\,Cr_2O_3 + H_{2\,(g)}$	-101
$Cr_2O_3 + H_2O_{(g)} \leftrightarrow 2CrO_2 + H_{2\,(g)}$	252
$2/5\,Ta + H_2O_{(g)} \leftrightarrow 1/5\,Ta_2O_5 + H_{2\,(g)}$	-132

Table 3.2: Standard reaction Gibbs free energy change of methane and candidate oxygen carriers [46]

Reaction	**ΔG at 600 °C (kJ/mol)**
$4Fe_2O_3 + CH_{4\,(g)} \leftrightarrow 8FeO + CO_{2\,(g)} + 2H_2O_{(g)}$	-236
$Mn_3O_4 + CH_{4\,(g)} \leftrightarrow 3Mn + CO_{2\,(g)} + 2H_2O_{(g)}$	180
$4MnO + CH_{4\,(g)} \leftrightarrow 4Mn + CO_{2\,(g)} + 2H_2O_{(g)}$	393
$8CeO_2 + CH_{4\,(g)} \leftrightarrow 4Ce_2O_3 + CO_{2\,(g)} + 2H_2O_{(g)}$	60
$14.286CeO_2 + CH_{4\,(g)} \leftrightarrow 14.286CeO_{1.72} + CO_{2\,(g)} + 2H_2O_{(g)}$	-34
$4WO_3 + CH_{4\,(g)} \leftrightarrow 4WO_2 + CO_{2\,(g)} + 2H_2O_{(g)}$	-136
$4Nb_2O_5 + CH_{4\,(g)} \leftrightarrow 8NbO_2 + CO_{2\,(g)} + 2H_2O_{(g)}$	90
$1.33Cr_2O_3 + CH_{4\,(g)} \leftrightarrow 2.67Cr + CO_{2\,(g)} + 2H_2O_{(g)}$	303
$4/5\,Ta_2O_5 + CH_{4\,(g)} \leftrightarrow 8/5\,Ta + CO_{2\,(g)} + 2H_2O_{(g)}$	428

Table 3.3: Melting points of some common oxygen carriers [46]

Metal oxide and metal	**Melting point (°C)**
Ni/NiO	1455/1955
$Cu/Cu_2O/CuO$	1085/1235/1446
$Fe/FeO/Fe_{0.947}O/Fe_3O_4/Fe_2O_3$	1538/1377/1378/1597/1565
$Mn/MnO/Mn_3O_4/Mn_2O_3$	1246/1842/1562/1347
$Co/CoO/Co_3O_4$	1495/1830
$Ce_2O_3/CeO_{1.72}/CeO_{1.83}/CeO_2$	2230/-/-/2400
$Sn/SnO/SnO_2$	232/1042/1630
Zn/ZnO	420/1975
$W/WO_2/WO_{2.722}/\ WO_{2.96}/WO_3$	3407/1724/-/-/1472

The Gibbs free-energy change values in Tables 3.1 and 3.2 indicate that materials based on iron, tungsten and cerium (Fe, W and Ce) are the only suitable candidates for use in the CLWS process. Consideration of the melting points shows that tungsten-based materials have the highest melting points (greatest durability) followed by cerium-based materials, with iron-based materials showing the lowest melting points of the three, and therefore the lowest durability. However, iron usually produces the highest H_2 yield in the steam reactor. In addition, iron is highly abundant and low in cost. Therefore, it is highly preferable for this process.

3.3 Selection of support material

The active metals are mounted on a support material to reduce the attrition and agglomeration rate during the reaction and ensure that the oxygen carrier maintains its activity over a high number of reduction-oxidation (redox) cycles. In addition, the support material should have high heat capacity to store heat from the air reactor and transport it to the fuel reactor. Moreover, the support material should be chemically inert with the active metal, as any reaction between them would decrease the reactivity and capacity of the oxygen carrier to produce the required product [36, 46]. Magnesium aluminium oxide ($MgAl_2O_4$) and zirconium oxide (ZrO_2) showed high thermal and chemical stability when tested with a Fe_2O_3-based oxygen carrier [46, 65].

Table 3.4: Heat capacities of potential support materials [65]

Support material	Cp at 900 °C (kJ/kg.K)	Melting Point (K)
$MgAl_2O_4$	1.283	2408
Al_2O_3	1.254	2327
ZrO_2	0.633	2983
Nb_2O_5	0.672	1785
MgO	1.285	3105
SiO_2	1.187	1996
TiO_2	0.949	2116
La_2O_3	0.416	2586

3.4 Thermodynamic analysis of reactions in CLWS process reactors

The core reactions that take place in the CLWS process to generate hydrogen *in-situ* with CO_2 capture using iron-based oxygen carriers are listed in Table 3.5. Also, the phase equilibria of Fe-O-H and Fe-O-C bonds are shown in Figure 3.1.

Table 3.5: Core reactions in the CLWS process

Reactor	**Main reactions taking place**
Fuel Reactor	(3.1) $6Fe_2O_3 + 2CH_4 \leftrightarrow 4Fe_3O_4 + 2CO + 4H_2$
	(3.2) $2Fe_3O_4 + 2CH_4 \leftrightarrow 6FeO + 2CO + 4H_2$
	(3.3) $2FeO + 2CH_4 \leftrightarrow 2Fe + 2CO + 4\,H_2$
	(3.4) $6Fe_2O_3 + 2CO/2H_2 \leftrightarrow 4Fe_3O_4 + 2CO_2\,/2H_2O$
	(3.5) $2Fe_3O_4 + 2CO/2H_2 \leftrightarrow 6FeO + 2CO_2\,/\,2H_2O$
	(3.6) $2FeO + 2CO/2H_2 \leftrightarrow 2Fe + 2CO_2\,/\,2H_2O$
	(3.7) $CH_4 \leftrightarrow 2C + 4H_2$
Steam Reactor	(3.8) $Fe + H_2O \leftrightarrow FeO + H_2$
	(3.9) $3FeO + H_2O \leftrightarrow Fe_3O_4 + H_2$
Air reactor	(3.10) $6FeO + O_2 \leftrightarrow 2Fe_3O_4$
	(3.11) $4Fe_3O_4 + O_2 \leftrightarrow 6Fe_2O_3$

The phase equilibria indicate the suitable operating temperature range for the CLWS process. High conversion of CO to CO_2 can be achieved in the presence of Fe_2O_3 as an oxygen carrier. On the other hand, Fe^0 and FeO forms of oxygen carriers are favourable for the production of hydrogen as also indicated in reactions (3.8) and (3.9). Therefore, it is difficult to produce hydrogen and capture CO_2 in the same reactor. Thus, a three-reactor configuration has been developed to fulfil the main aim of the process, to enable the production of high-purity hydrogen product in situ with CO_2 capture. In the first reactor (fuel reactor), methane is fully combusted to CO_2 and steam via reaction with Fe_2O_3, which is reduced to a mixture of Fe and FeO as shown in reactions (3.1) to (3.7) in Table 3.5.

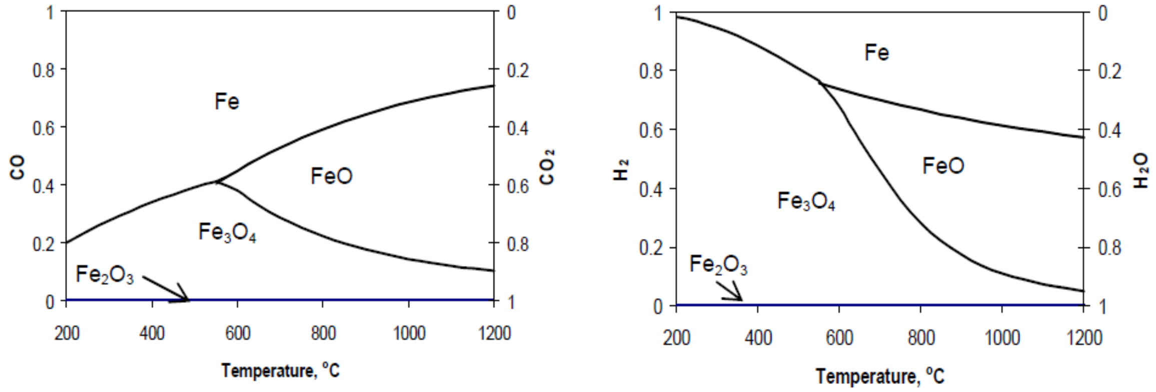

(a) *(b)*

Figure 3.1: Phase equilibria diagrams for: (a) Fe-O-C , (b) Fe-O-H at 1 atm pressure [50]

The discharged solid mixture is fed to the steam reactor, where steam is converted to H_2 and the Fe^0/FeO mixture is oxidised to Fe_3O_4. An air reactor is required to oxidise fully the oxygen carrier to Fe_2O_3 via air. It is then recycled to the fuel reactor, as shown in Figure 3.2. This configuration was developed and described in previous research.[8, 10, 45, 49].

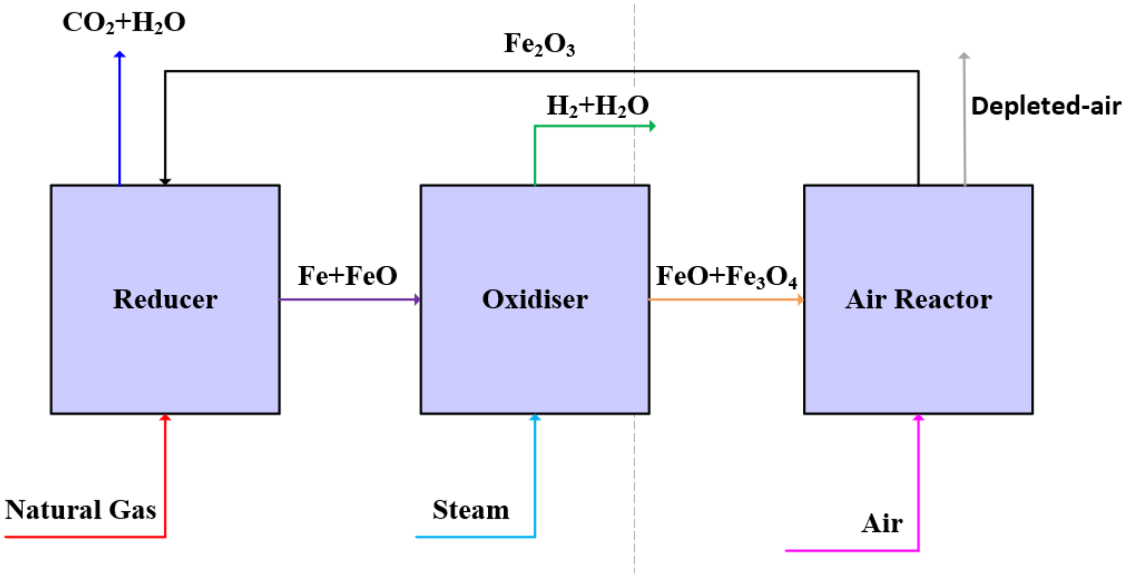

Figure 3.2: Three-reactor configuration for CLWS process

3.5 Baseline chemical looping water splitting process (BCLWS)

A research group led by L.S. Fan at Ohio State University (OSU) in the US developed a CLWS process that used methane as fuel with a reactor configuration similar to that shown in Figure 3.2 [8]. In the group's study, both the fuel and steam reactors were modelled and simulated as counter-current moving-bed reactors, while the air reactor was modelled as a riser. Counter-current moving-bed reactors proved to offer greater contact between the gas and solids and improved gas and solids conversion to product than fluidised-bed reactors [8]. In addition, sensitivity analysis was performed to study the effect of the oxygen carrier/steam flow on the gas and solids conversion and on the temperatures of the discharged gases in both the fuel and steam reactors. The influence of the mass percentage of the alumina (support material) on the discharged solids conversion was also investigated. Based on these analyses, the process was optimised and evaluated thermodynamically. Finally it was compared with the steam methane reforming process developed by the National Energy Technology Laboratory (NETL) in the US, to measure its feasibility [12]. The process-flow diagram for the process developed by the OSU group is presented in Figure 3.3.

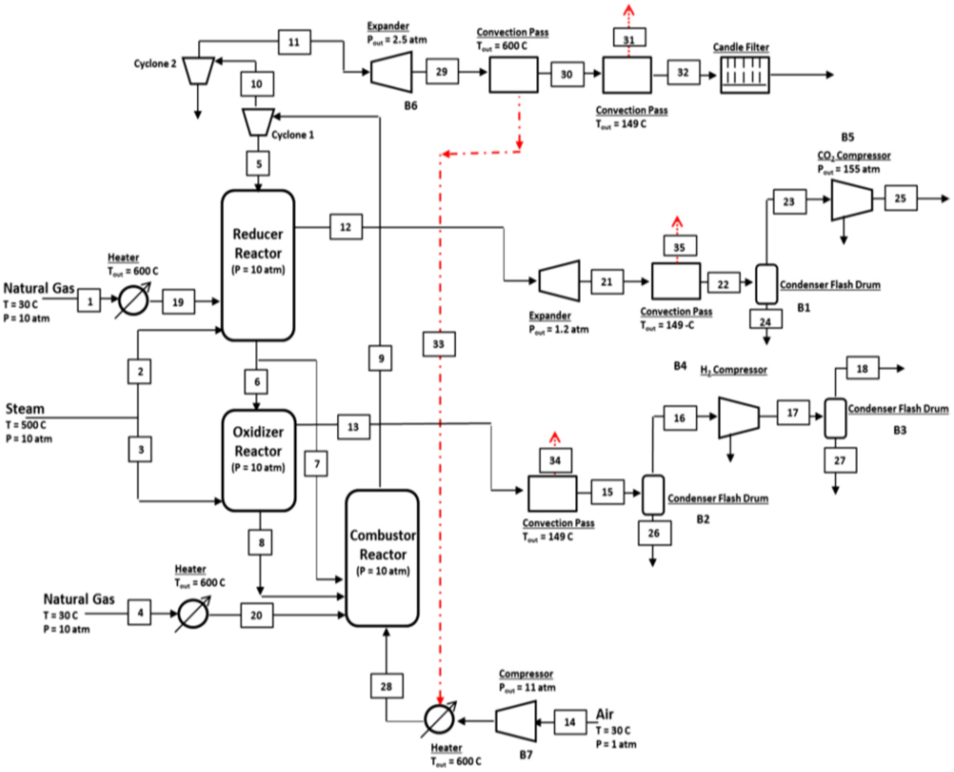

Figure 3.3: Process-flow diagram for CLWS process developed by Ohio State University researchers [8]

The baseline process used in the study described in this thesis was developed by adopting the CLWS process devised by OSU researchers. In this study, $MgAl_2O_4$ was utilised as support material as opposed to the alumina used in the OSU process due to the greater heat capacity of $MgAl_2O_4$ compared with alumina. This improved the energy storage by the oxygen carrier and therefore improved the energy efficiency of the process.

3.5.1 Process description for the BCLWS process

Natural gas is pre-heated and fed to the reducer, together with the regenerated oxygen carrier (47.3 mole% Fe_2O_3) from the air reactor, as shown in Figure 3.4. According to the operating parameters of the fuel reactor (reducer) as listed in Table 3.7, natural gas is combusted to carbon dioxide and steam, while haematite (Fe_2O_3) is reduced to a mixture of iron and wüstite ($Fe_{0.947}O$). Solids conversion of 67% is achieved in the fuel reactor. To maximise heat recovery, the reduced oxygen carrier is heated before being fed into the oxidiser. Using the pre-heated steam, the heated oxygen carrier is oxidised to magnetite (Fe_3O_4), while 65.9% of the steam is converted to H_2. This calculation was determined according to the sensitivity analysis performed on the process as will be described in section 3.8. The magnetite is then introduced to the air reactor with a pre-heated air stream. It is fully oxidised to haematite. To aid the heat recovery, a stream that contains unconverted haematite and magnetite (Fe_3O_4) at elevated temperature is fed to the air reactor.

In the configuration used for this study, as with the OSU process, moving-bed reactors were selected for their superior gas-solids contact characteristics, which enabled the achievement of greater gas and solids conversions in the reducer and oxidiser [8, 11, 47, 65]. All the reactors were operated at $P = 1.2$ bar. The mixture of CO_2 and steam was then cooled to 30 ºC in order to condense and separate the water. The dry CO_2 was then compressed to 110 bar. The H_2 and steam mixture was cooled to 30 ºC to condense the steam and separate the water. The target purity of the hydrogen stream was 99.4%, and this was met by compression of the H_2-steam mixture to 3 bar, hence removing more water via condensation. The corresponding process-flow diagram and its components are shown in Figure 3.4 and Table 3.6.

3.5.2 Heat integration in the BCLWS process

Heat integration is a vital part of process optimisation. It results in the minimisation of process heat going to waste [66]. One approach to integrate the heat produced is the use of heat exchangers to recover thermal energy from the process streams, leading to a minimisation in utility consumption [66, 67].

In this study, the pinch-point method was employed to minimise the use of process utilities. A minimum temperature difference of 10ºC between the hot and cold streams in the heat exchanger was assumed.

Table 3.6: List of the equipment illustrated on the BCLWS process-flow diagram

Notation on the figure	**Equipment**
H-i	Heater
E-i	Coolers
V-i	Separation vessel
VL-i	Valves
C-i	Compressors
Reducer, Oxidiser, Combuster	Moving-bed reactors

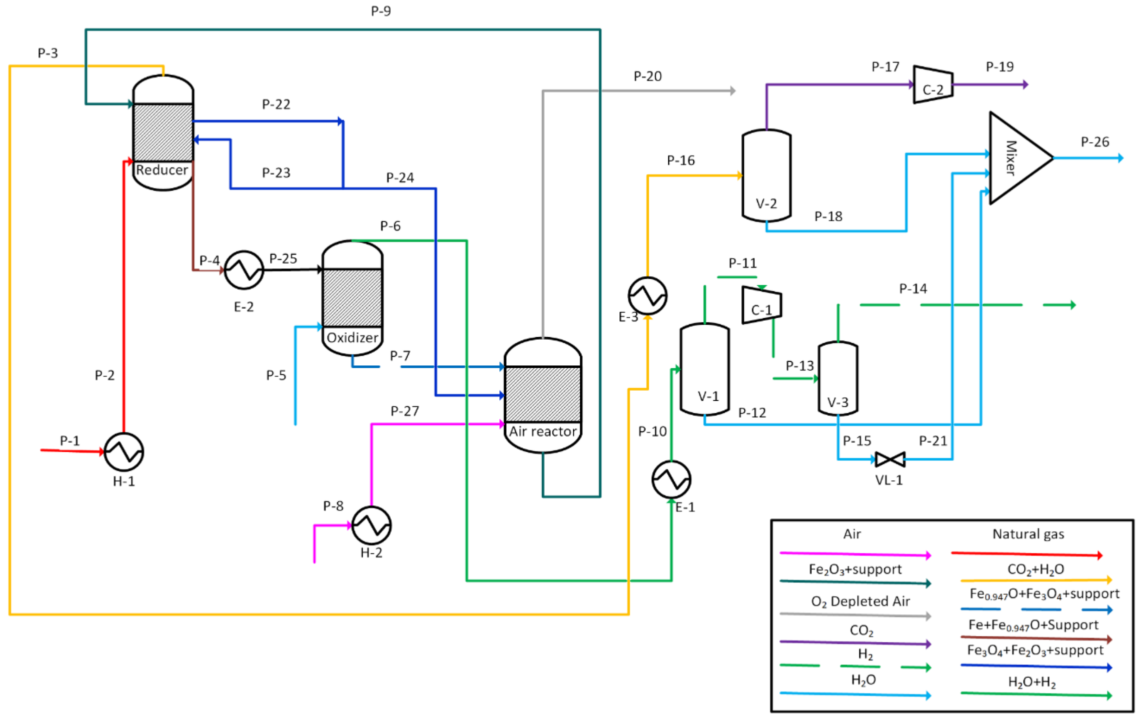

Figure 3.4: The BCLWS process-flow diagram

Table 3.7: List of operating parameters for the main units of the BCLWS process

Design specification	Specified value
Temperature of natural gas fed to the reducer (bottom)	600 ℃
Temperature of the solids fed to the reducer (top)	1050 ℃
Temperature of the gas mixture discharged from reducer (top)	1050 ℃
Temperature of the solids discharged from reducer (bottom)	651 ℃
Oxygen carrier to natural gas feed ratio	6.7
Temperature of the solids fed to the oxidiser	800 ℃
Temperature of the steam fed to the oxidiser	500 ℃
Temperature of the wet hydrogen discharged from oxidiser	680 ℃
Temperature of the solids discharged from oxidiser	820 ℃
Oxygen carrier to steam ratio	4.4
Air reactor temperature	1015 ℃
Separation vessel operating temperature	30 ℃
Reactors operating pressure	1.2 bar
Outlet pressure of CO_2 compressor	110 bar
Outlet pressure of H_2 compressor	3 bar

The hot and cold streams involved in the heat-integration analyses are shown in Figure 3.5. Temperature intervals were selected based on the inlet and outlet temperatures of the corresponding streams (Figure 3.5). The enthalpy associated with each stream in each of the intervals was then determined and summed. The total net enthalpy in interval 1 was then added to that corresponding to the interval 2. The resulting enthalpy was next added to the enthalpy in the subsequent interval. This procedure was applied to the rest of the intervals, forming the cascade heat duty for all the intervals as shown in Table 3.8. The cascade heat duty was then altered to obtain the interval through which no heat was transferred. The minimum temperature associated with this interval was the pinch-point temperature. The adjusted cascade heat duty is shown in Table 3.8. It can be seen from this table that the 12th interval corresponded to the pinch point *i.e.* 25 °C on the cold temperature scale. This suggested that utility heating of 71.5 MW was required for this particular interval.

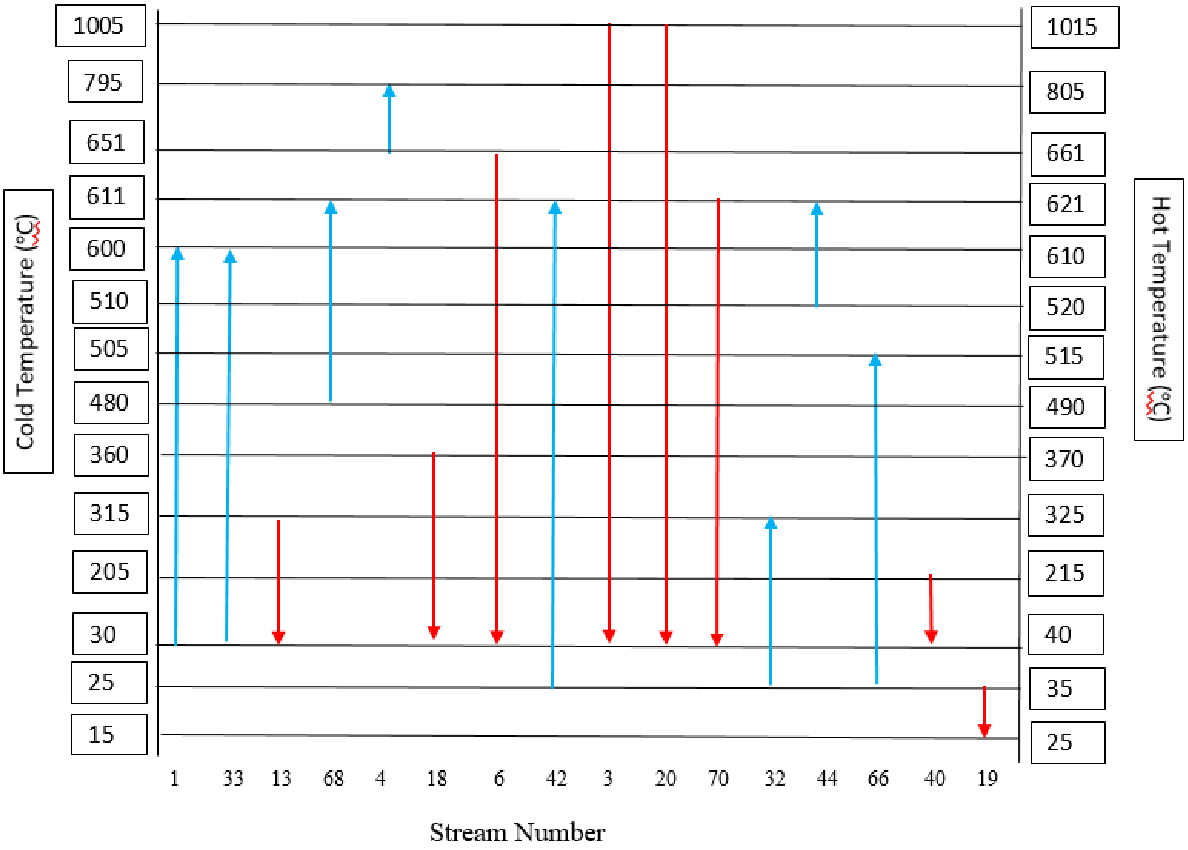

Figure 3.5: The temperature intervals of the streams involved in the pinch-point analysis for the BCLWS process

Table 3.8: The cascade and adjusted cascade heat duty for each interval in the pinch-point analysis

Temperature interval (^oC)	Cascade heat duty (MW)	Adjusted cascade heat duty (MW)
1+2 (1015 – 805) + (805 – 661)	12.4	83.9
3 (661– 621)	28.9	100.4
4 (621 – 610)	32.2	103.7
5 (610 – 520)	36.9	108.4
6 (520 – 515)	67.1	138.7
7 (515 – 490)	45.7	117.2
8 (490 – 370)	25.4	96.9
9 (370 – 325)	10.8	82.3
10 (325 – 215)	-9.5	62.0
11 (215 – 40)	-66.9	4.6
12 (40 – 35)	-71.5	0.0
13 (35 – 25)	-67.1	4.4

A minimum utility cooling (4.4 MW) was needed below this pinch-point interval. Accordingly, a heat exchanger network was designed (Figure A1) with the following considerations to enhance the thermal and exergy efficiency of the process:

1- The CO_2 compression to 110 bar was accomplished through use of five compressors with one inter-stage cooling system. This reduced the compression power consumption by 36 percentage points compared with the baseline process;

2- Considering water as the by-product of the process, and the large amount of heat released from the high temperature streams i.e. streams 73, 34, 39,70, 3 and 20, a water preheating unit (HE-(8-10)) followed by a heat-recovery steam generation

(HRSG-1) unit was added to vaporise the water and to generate power via the steam-generation cycle;

3- The steam required for the oxidiser was generated by two units, HRSG-2 and the fired heater (E-6) (Figure 3.6). HRSG-2 comprised four parallel evaporators which used the heat energy released from the streams 18, 40, 74 and 51. In the fired heater, 5% of the syngas - generated in the bottom of the reducer (stream 26) - was fully combusted via their reaction with the pre-heated air.

The detailed heat integration analysis performed in this study has improved the process beyond the state of the art that is published in the literature. This can be seen specifically in the third consideration made during the heat-exchanger network design. The splitting of a high-temperature gas stream (stream 26) from the reducer improves the process performance due to the reduction in fuel consumption. This technique was not discussed in previous studies that integrated a CLWS process [6, 8, 48-50].

This optimised heat integration process is termed integrated CLWS, or ICLWS, and the operating parameters for this process are shown in Table 3.9.

To show the effect of stream 26 on the process performance, an experiment was performed in which natural gas replaced stream 26 in the vessel E-6. This test is shown in Figure A3. This process was called CLWS(a). The thermodynamic evaluation of process CLWS(a) is shown with comparisons of evaluations of all processes in Table 3.13.

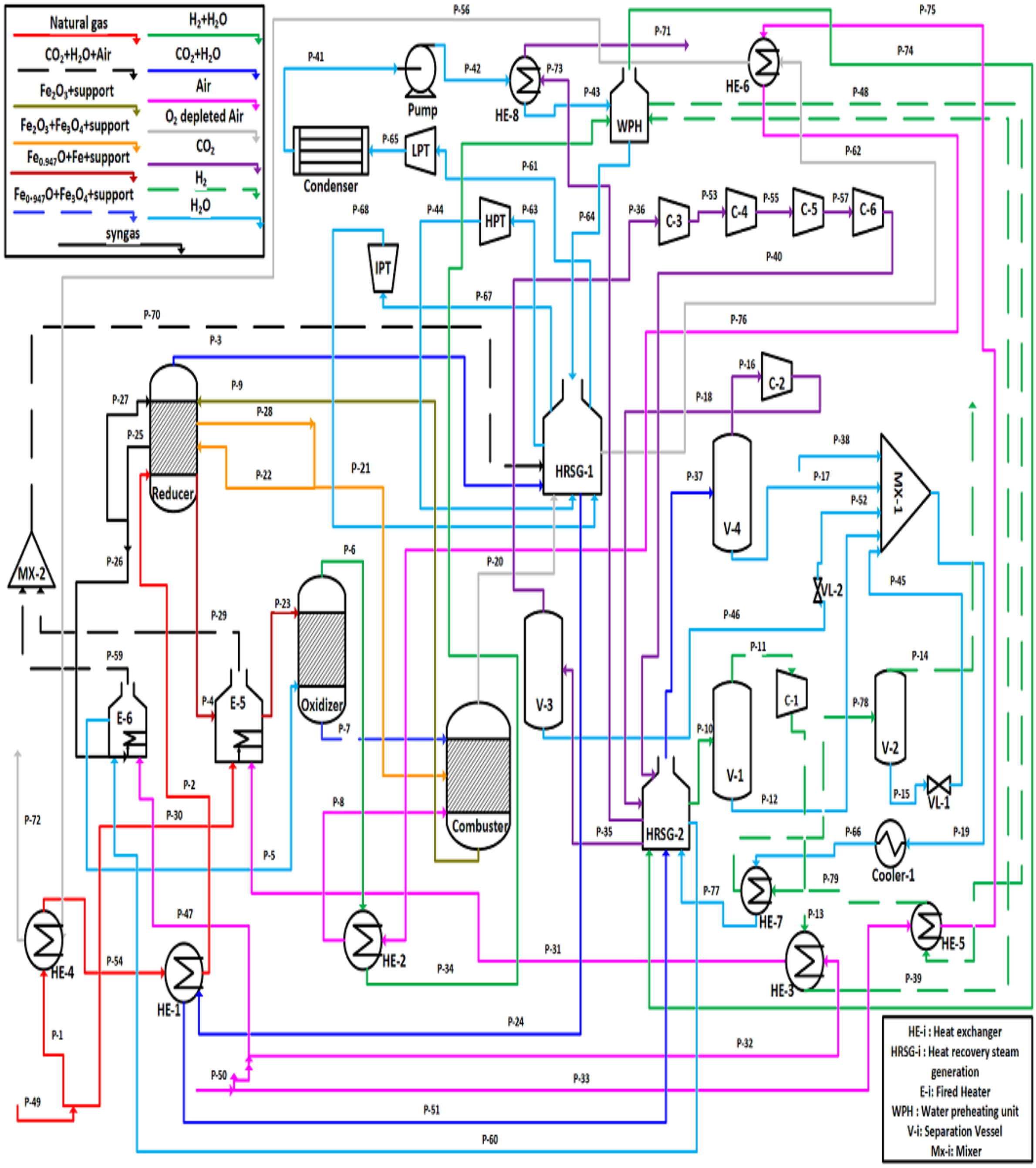

Figure 3.6: The process-flow diagram of the integrated CLWS process ICLWS

Table 3.9: List of the operating parameters of the main units in the ICLWS process

Design specification	**Specified value**
Reducer operating temperature	1015 ℃
Temperature of the solids fed to the reducer	1015 ℃
Temperature of the solids discharged from the reducer	651 ℃
Temperature of the natural gas fed to the reducer	600 ℃
Oxygen carrier to natural gas feed ratio	6.7
Temperature of the solids fed to the oxidiser	795 ℃
Temperature of the steam fed to the oxidiser	505 ℃
Operating temperature of the oxidiser	661 ℃
Temperature of the solids discharged from oxidiser	820 ℃
Oxygen carrier to steam ratio	4.4
Operating temperature of the air reactor	1015 ℃
Separation vessels temperature	40 ℃
Operating pressure for all the reactors	1.2 bar
Pressure of the CO_2 product	110 bar
Pressure of the H_2 product	10.0 bar
Isentropic efficiency of the compressors	0.90
Isentropic efficiency of the HP&IP turbines	0.90
Isentropic efficiency of the LP turbine	0.87
Designed vapour fraction of the LP turbine	0.9
Pump efficiency	0.85
Inlet temperature of the turbines	611 ℃
Pump outlet pressure	260 bar
HP outlet pressure	150 bar
IP outlet pressure	70 bar
LP outlet pressure	0.026 bar

3.5.3 Unconventional equipment used in the ICLWS process

Since ICLWS is a novel process, some non-standard pieces of equipment were included in the design of the chemical plant used for the process. These pieces of equipment were as follows:

a- Moving-bed reactor (reducer, oxidiser and air reactor);
b- Indirect gas-solid heater; and
c- Atmospheric pressure HRSG unit.

Moving-bed Reactor (MBR)

The moving-bed reactor (MBR) was first proposed by Andrew in 1890 [68]. The MBR involves a layer of granular solid that moves as a plug through the reactor length. The solid might be a reactant or a catalyst [69]. The MBR is used in the petrochemical industry in the separation of heavy-cut petroleum from metals that are present at concentrations of more than 250 ppm [70, 71]. It is also used as a catalyst regeneration unit in the continuous catalytic cracking process that is employed in production of DRI, as developed by MIDREX, or in the biofilm processes of municipal and waste-water treatment plants [69, 72]. Schematic diagrams of MBR designs are shown in Figure 3.7 [73]. The main benefit of using this technology lies in the lowering of the energy consumption because the pressure drop across the reactor is reduced. Thus, the overall plant performance and economics are improved [69].

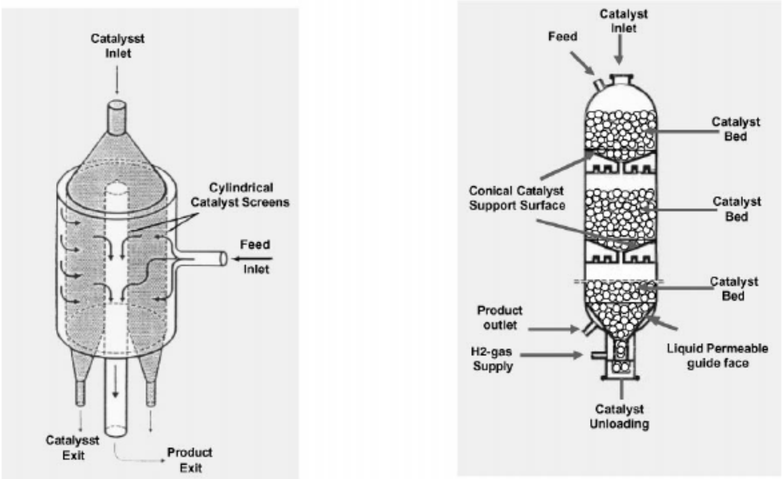

Moving-bed Reactor for Catalytic Reforming

Moving-bed Reactor for Residue Hydroprocessing

Figure 3.7: Schematic diagram of moving-bed reactors used in industry

In the area of chemical looping, most of the studies that have been conducted have considered the fuel, steam and air reactors as fluidised-bed reactors [25, 36, 37, 44, 52]. Few studies propose the moving-bed reactor as the main reactor type for use in the chemical looping process [8, 45, 49]. These researches have shown that the moving-bed reactor has a potential advantage over the fluidised-bed in terms of higher efficiencies of gas and solid conversion in both fuel and steam reactors [8]. Therefore, it was selected here. Several mathematical models have been proposed in the literature to describe the MBR. These models either employ computational fluid dynamics [74] or the mass, energy and kinetics technique [45, 75]. In Chapter 5, we employ the model based on mass, energy balance and kinetics to calculate the reactor's length and consequently the cost of the reactor based on its size. In addition, 30% is added to the calculated length to account for the section in which the gas distributor and the piping for the solids discharge are installed.

Indirect gas-solid heater

Recent technologies have been proposed in terms of indirect gas-solid heating. One of these was developed by Solex Thermal Science [76]. This company's device consists of several stacked hollow stainless-steel plates through which fluid flows to exchange heat with the solids that flow freely downward between these plates. This process is represented in the schematic shown in Figure 3.8. Conduction heat transfer takes place through the walls to the solids. In our case, the fuel and air mixture flows through the hollow pipes as wustite and metallic iron descends freely between these plates. Solex Thermal Science states that this technology consumes 90% less fuel than other gas-solid heat-exchanger technologies such as fluid-bed heater/coolers [76].

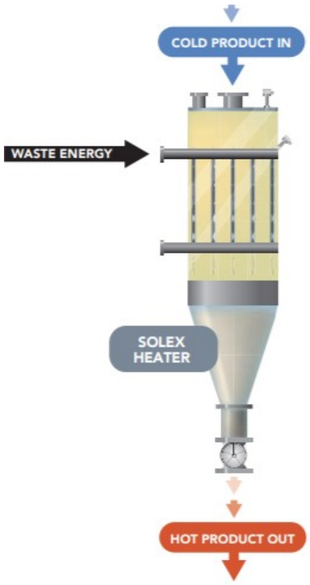

Figure 3.8: Schematic diagram of indirect gas-solid heater made by Solex Thermal Science [76]

Atmospheric heat recovery steam generation unit

Usually the HRSG unit operates at moderate to high pressure (50 - 260 bar) in order to minimise latent heat and therefore to reduce consumption of energy [77]. The HRSG-2 unit in the ICLWS process operates at P = 1.2 bar since the steam generated there is fed to the oxidiser, which operates at P = 1.2 bar. This unit is considered as the standard HRSG unit; however, the volume of the pipes through which the steam is discharged must be larger than those of the standard unit because the pressure is 50 - 100 times less, and therefore the gas volume is large due to the inverse relationship between pressure and gas volume. This fact is considered in the economic evaluation of the process that is explained in Chapter 6. The purpose of this thesis is not necessarily to develop a process that is “shovel-ready” but also to point to some areas for future development.

3.6 Steam methane reforming process (SMR)

In order to investigate the ICLWS process viability it has to be compared with the benchmark process for hydrogen production *i.e.* steam methane reforming. Therefore, a steam methane reforming process (SMR) adopted from the assessment study performed from the US department of energy was developed and simulated using Aspen V.9 [12]. The SMR process was illustrated earlier in section 2.1 and the block flow diagram of the process was represented in Figure 2.2. However, details about the thermal energy optimisation of the process was absent from adopted sources. Hence, heat integration analysis was performed on the basic SMR process represented by Figure 2.2 following the pinch point analysis similar to the ICLWS. Then, the optimised SMR process will be thermodynamically evaluated. The simulated SMR process is referred to “SMR1” whereas the process found in the literature is called “$\mathrm{SMR_r}$”[12].

3.6.1 Heat Integration analysis for SMR process

Following the methodology presented in section 3.5.2 for pinch point analysis, the thermal energy of the SMR1 process was optimised through the minimisation of the hot and cold utilities required by the process. The hot and cold streams involved in the pinch point analyses were represented by Figure 3.9.

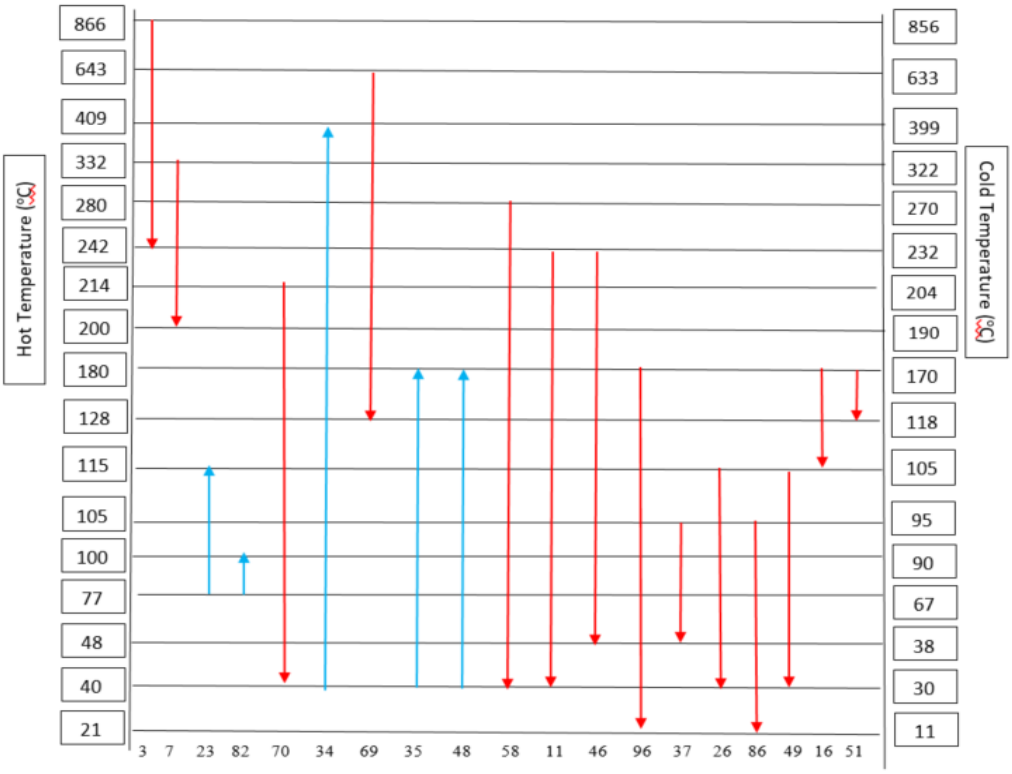

Figure 3.9: Temperature intervals for the streams involved in the pinch analysis for SMR1 process

Table 3.10 shows the cascaded enthalpy for each interval in the analysis. As mentioned previously in section 3.5.2, the interval at which the sign of cascaded enthalpy is changed from +ve to –ve is the interval that contains the pinch point temperature. Also, no heat transfer is taking place across the pinch point temperature. Thus, the cascade heat load is adjusted as shown in Table 3.10 so the heat load across the pinch point interval is zero.

Table 3.10: The cascade and the adjusted cascade heat duties for each interval in the pinch point analysis for SMR1 process

Temperature interval (ºC)	Cascade Heat duty (MW)	Adjusted Cascade Heat duty (MW)
1+2 (866 – 643) + (643 – 409)	230.6	237.2
3 (409– 332)	263.3	269.9
4 (332 – 280)	298.0	304.6
5 (280 – 242)	153.8	160.4
6 (242 – 214)	159.3	165.9
7 (214 – 200)	166.6	173.2
8 (200 – 180)	177.1	183.7
9 (180 – 128)	-6.6	0.0
10 (128 – 115)	217.3	223.9
11 (115 – 105)	108.2	114.8
12 (105 – 100)	103.9	110.5
13 (100 – 77)	137.8	144.4
14 (77 – 48)	243.4	250
15 (48 – 40)	227.6	234.2
16 (40 – 21)	229.4	236.0

Consequently, the pinch point temperature occurs on the 9th interval and equals 128 ºC (hot scale) or 118 ºC (cold scale). As a results in Table 3.10, the minimum heating utility is 6.6 MW while the minimum cooling utility is 236 MW.

Table 3.11: Identification of the units presented in the SMR1 process flow diagram

Unit abbreviation	**Identification of the unit**
HE-i	Heat exchanger
P-i	Pumps
HRSG-i	Heat recovery steam generation
A-i	Absorber
S-i	Stripper
VL-i	Valves
HTS	High shift reactor
LTS	Low shift reactor
C-i	Compressor
V-i	Flash drum
E-i	Cooler
H-i	Heater

The operating conditions for SMR1 process is listed in Table 3.12 and the process flow diagram is represented by Figure 3.10.

The next step following the determination of the minimum utility required, is the design of the heat exchanger network for the SMR1 process. The network is shown in the process flow diagram of the SMR1 process presented in Figure 3.10. The following points summarises the main steps conducted in the design of the heat exchanger network:

1- The steam required for the reformer is generated via two units: water pre-heating and HRSG-1.The water pre-heating is composed of four heat exchangers in series (HE1& HE-(7-9)). The excess heat exhausted from streams 37, 13, 7, 71 used in HE-1&HE-(7-9) respectively. The HRSG-1 unit is utilising the heat from the elevated temperature streams 3, 68 to vaporise the water and heat it to the inlet temperature of the steam fed to the reformer.

Table 3.12: The operating parameters used to simulate the SMR1 process

Parameter	Value
Temperature of the steam fed to the reformer tubes	399 ºC
Temperature of the syngas discharged from reformer tubes	866 ºC
Temperature of the flue gas discharged from the reformer shell	643 ºC
Pressure inside the reformer shell	1.1 bar
Pressure inside the reformer tubes	30 bar
Temperature of the syngas fed to the high shift reactor	242 ºC
Temperature of the syngas discharged from the high shift reactor	332 ºC
Temperature of the gas fed to the low shift reactor	200 ºC
CO conversion of the gas discharged from the low shift reactor	98.1%
Temperature of the syngas discharged from the low shift reactor	214 ºC
High and low shift reactor pressure	28 bar
Pressure of the steam fed to the reformer	30 bar
Pressure of the absorber A-1 used in MDEA unit	27 bar
Pressure of the stripper S-1 used in the MDEA unit	1.4 bar
Heat load required by the boiler B-1 in the MDEA unit	23 MW
MDEA solution to CO_2 ratio fed to MDEA unit	10.4 kg/kg
CO_2 Capture % from MDEA unit	95.2%
Pressure of the absorber A-2 used in the MEA unit	1.0 bar
Pressure of the stripper S-2 used in the MEA unit	1.4 bar
Heat load required by the boiler B-2 in the MEA unit	40 MW
MEA solution to CO_2 ratio fed to MEA unit	5.78 kg/kg
CO_2 Capture % from MEA unit	76 %
Temperature of the flash drum V-1	21 ºC
Pressure of the flash drum V-1	1.6 bar
Temperature of the flash drum V-2	48 ºC
Pressure of the flash drum V-2	1.4 bar
Temperature of the flash drum V-3	48 ºC
Pressure of the flash drum V-3	10 bar
Temperature of the flash drum V-4	21 ºC
Pressure of the flash drum V-4	10 bar
H_2 removal efficiency from the pressure swing adsorption unit	73.6%

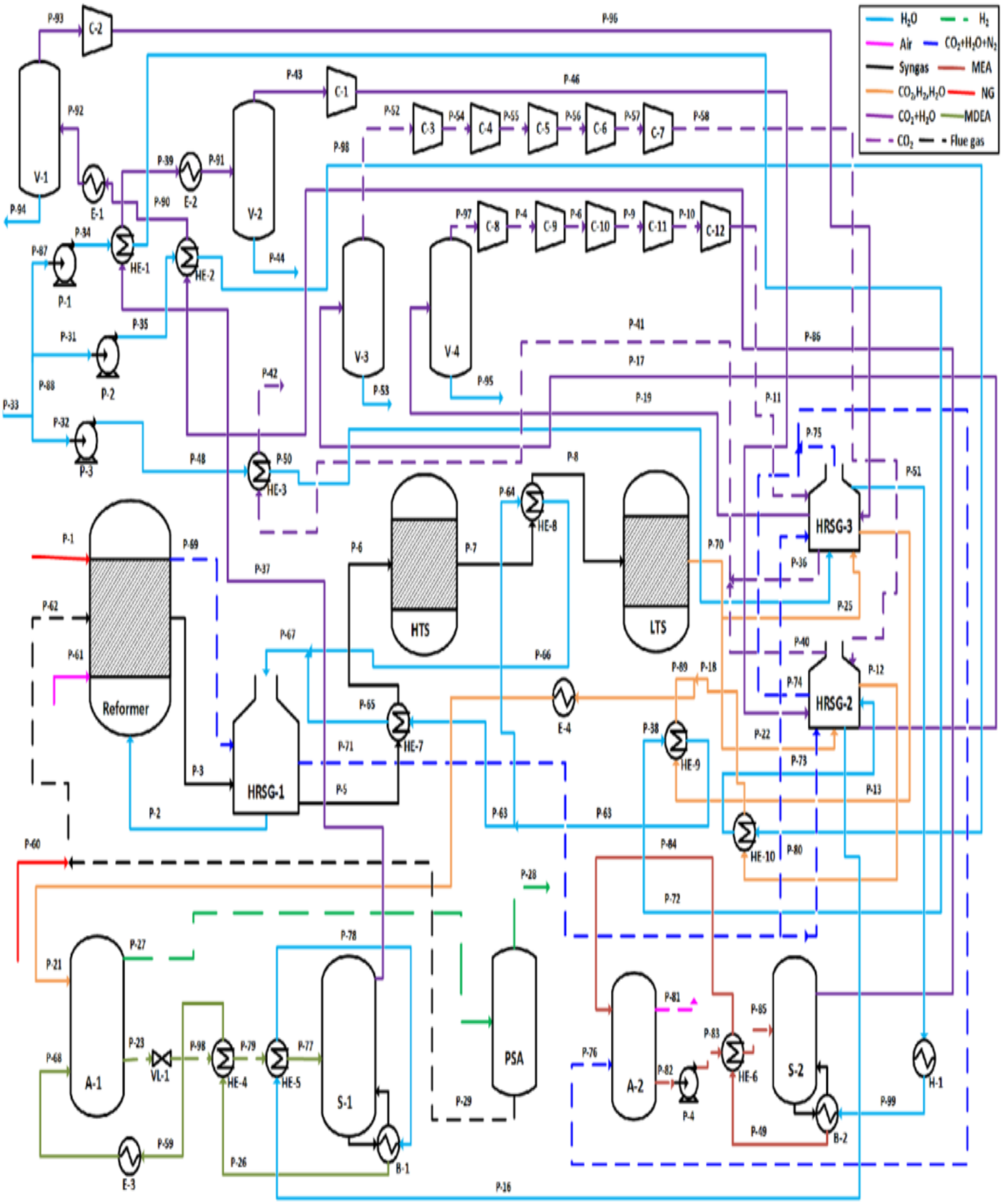

Figure 3.10: The process flow diagram for the SMR process developed

2- The heat associated with streams 86 and 12 employed to pre-heat the water *via* HE-2 & HE-10 respectively before it vaporises in HRSG-2. In addition, the heat related with stream 41 is utilised to pre-heat the water before it evaporates in HRSG-3.

3- HRSG-2 and HRSG-3 units were both used to generate the steam required for both strippers (S-1&S-2). The enthalpy associated with streams 11, 58, 5, 70, 46, 96 were mainly implemented for this purpose.

4- The hot lean MDEA amine discharged from stripper (S-1) in addition with the steam represented as stream 16 were used to heat up the rich MDEA amine *via* HE-(4-5) in order to recover it in S-1. Moreover, stream 49 (hot lean MEA solution) is utilised to heat the lean MEA solution *i.e* stream 83 to recover it in S-2.

3.7 Thermodynamic evaluation of the ICLWS process

The ICLWS process was thermodynamically analysed by assessing the thermal efficiency of the process and the hydrogen yield using Eqs. (3.12) to (3.17) [12]

$$\eta_{th} = \frac{\dot{Q}_o}{\dot{Q}_i} \qquad (3.12)$$

$$\eta_{H_2} = \frac{\dot{Q}_o}{\dot{Q}_f} \qquad (3.13)$$

$$\eta_{eff} = \frac{\dot{Q_o} - P_{c/g}}{\dot{Q_i}} \qquad (3.14)$$

$$\dot{Q}_o = \dot{m}_{H_2} HHV_{H_2} \qquad (3.15)$$

$$\dot{Q}_i = \dot{m}_{NG} HHV_{NG} + \dot{Q}_{MH} \qquad (3.16)$$

$$\dot{Q}_f = \dot{m}_{NG} HHV_{NG} \qquad (3.17)$$

In these equations:

$\dot{m}_{H_2}$ is the mass flow rate of H_2 produced from the process (kg/s).

$\dot{m}_{NG}$ is the mass flow rate of natural gas consumed by the process (kg/s).

F_{H_2} is the molar flow rate of H_2 produced (kmol/h).

F_{NG} is the molar flow rate of natural gas consumed by the process (kmol/h).

HHV is the higher heating value of the fuel (54.1 MJ/kg) [78, 79].

$P_{c/g}$ is the power generated (-ve) through turbines or consumed (+ve) through pumps and compressors in the process (MW).

$\dot{Q}_{MH}$ is the net heating utility supplied to the process (MW).

η_{eff} is the effective efficiency.

The corresponding values of all these parameters are summarised in Table 3.13. These parameters were identical for both support materials used in this work, i.e. $MgAl_2O_4$ and ZrO_2. It can be observed that use of the optimised process (ICLWS) has improved the use of thermal energy by 31.1 percentage points compared with the baseline process (BCLWS). The ICLWS process shows improvements in hydrogen production efficiency by 23.7 percentage points and 2.8 percentage points compared with the baseline process and the no-split process (CLWS(a)). Furthermore, the hydrogen production efficiency has been improved by 11.7 percentage points, 6.8 – 13.5 percentage points and 6.5 – 12.7 percentage points in comparison with conventional SMR1, modern SMR_m [18, 80] and ATR [18] processes respectively. However, the hydrogen production efficiency is 1.1 percentage points lower than that of the highest SMR hydrogen production efficiency reported in the literature [19]. Also, the hydrogen production efficiency for the ICLWS process is 6.3 percentage points and 13.4 percentage points higher than that of the OSU process [8] and the three-reactor chemical looping reforming (TRCLR) process proposed by Khan and Shamim of the Centre for Energy in Abu Dhabi [49], respectively.

Regarding the effective efficiency, the ICLWS process dominates over all the competitors considered in this study. The effective efficiency appears to be 12.3 percentage points, 2 – 11.1 percentage points and 4.1 – 10.8 percentage points higher than those reported for the conventional SMR, modern SMR_m and ATR processes, respectively. Also, it is improved by 6.5 percentage points and 10.8 percentage points compared with OSU and TRCLR processes, respectively. In addition, the effective efficiency is 41.3 percentage points higher than that observed in the baseline process. This is attributed to the amount of power generated by the steam generation cycle within this process. This cycle is absent from the conventional SMR, OSU and basic processes. Power is produced in the TRCLR, modern SMR_m and ATR systems but to a lesser degree than in the ICLWS process. Moreover, the effective efficiency of the ICLWS system is 4.1 percentage points higher than that of the no-split process CLWS(a). Use of 5% of the syngas in the split process improved the developed process performance by 2.8 percentage points, and by 4.1 percentage points in terms of the hydrogen production and effective efficiencies. However, it reduced the CO_2 capture efficiency by 1.5 percentage points.

Table 3.13: Comparison between the thermodynamic evaluations of the optimised ICLWS process and other published, methods(a)

Parameter	SMR_r[12]	SMR1	SMR_m[18, 80]	ATR[18]	BCLWS	CLWS(a)	ICLWS
CO_2 capture %	90.0	90.0	55.7-90	53.2-66.9	69.2	88.8	87.3
$\frac{F_{H_2}}{F_{NG}}$	2.30	2.36	2.3-2.5	2.3-2.5	1.96	2.63	2.72
$\dot{Q}_i$ (MW)	N/A	1411.0	455.6-503.4	457.7-500	2116.6	1354.4	1285.2
$\dot{Q}_o$ (MW)	1012.6	1013.3	351.1-354.5	354.5	1021.0	1021.0	1019.2
$\dot{Q}_f$ (MW)	1402.9	1404.4	455.6-503.4	457.7-500	1696.1	1258.2	1215.7
$P_{c/g}$ (MW)	34.2	34.0	-(0.3-11.8)	-(0.2-1.6)	78.6	-28.3	-29.5
η_{th}	-	71.8	-	-	48.2	75.2	79.3
η_{H_2}	72.2	72.2	70.4-77.1	71.2-77.4	60.2	81.1	83.9
η_{eff}	69.7	69.3	70.5-79.6	70.8-77.5	40.3	77.5	81.6

Table 3.14: Comparison between the thermodynamic evaluations of the optimised ICLWS process and other published methods(b)

Parameter	OSU[8]	TRCLR[49]	BCLWS	CLWS(a)	ICLWS
CO_2 capture %	90.0	100	69.2	88.8	87.3
$\frac{F_{H_2}}{F_{NG}}$	2.29	2.54	1.96	2.63	2.72
$\dot{Q}_i$ (MW)	N/A	-	2116.6	1354.4	1285.2
$\dot{Q}_o$ (MW)	1017.9	291.5	1021.0	1021.0	1019.2
$\dot{Q}_f$ (MW)	1309.4	413.3	1696.1	1258.2	1215.7
$P_{c/g}$ (MW)	33.4	1.6	78.6	-28.3	-29.5
η_{th}	-	-	48.2	75.2	79.3
η_{H_2}	77.6	70.5	60.2	81.1	83.9
η_{eff}	75.1	70.8	40.3	77.5	81.6

3.8 Sensitivity Analysis (Reducer and Oxidiser)

Sensitivity analysis is a paramount step toward the optimisation of any chemical process [8, 48, 49]. The output (dependent) and the input (independent) parameters involved in this analysis are summarised in Tables 3.15 and 3.16. The Aspen Plus V.8.8 simulator was employed to analyse the results. Based on the insights gained through the heat integration and sensitivity analysis, the BCLWS process was optimised to the ICLWS process shown in Figure 3.6.

Table 3.15: Output parameters analysed in this study

Output parameter	Symbol
Gas outlet conversion in the reducer	X_{gr}
Discharged solid conversion in the reducer	X_{sr}
Gas outlet conversion in the oxidiser	X_{go}
Discharged solid conversion in the oxidiser	X_{so}

Table 3.16: Input parameters analysed in this study

Input parameter	Symbol	Span	Step size
Oxygen carrier-to-methane feed ratio	$R_1=F_{oc}/F_{CH4i}$	1-7.6	0.2
Oxygen carrier-to-steam feed ratio	$R_2= F_{oc}/F_{sti}$	2-6	0.2
Temperature of reducer’s discharged gas	T_{gr}	700-1020	20
Temperature of reducer’s discharged solids	T_{sr}	600-900	20
Temperature of oxidiser’s discharged gas	T_{go}	620-900	20
Temperature of oxidiser’s discharged solids	T_{so}	620-900	20

3.8.1 Reducer sensitivity analyses

The effect of the oxygen carrier to methane feed ratio on the conversion of the discharged gas and solid is shown in Figure 3.11. The temperature and pressure of the gas discharged from the reducer were set at 1015 ºC and 1.2 bar, respectively. The gas conversion was observed to increase as the ratio of the oxygen carrier to the methane feed increased. Similar trends have been reported in the literature [8, 14] under similar operating conditions with different oxygen-carrier supports. This results from the extent of combustion that takes place in the reducer [14].

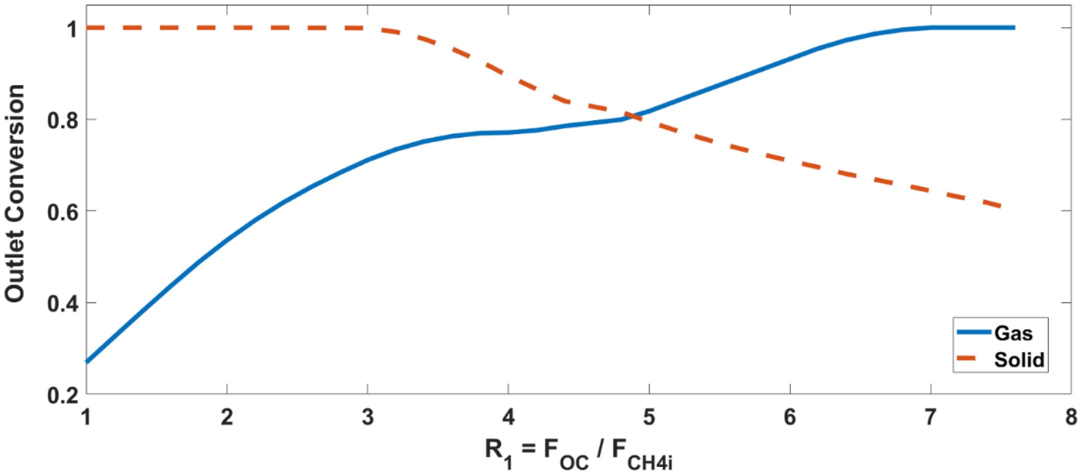

Figure 3.11: The effect of the oxygen carrier to methane feed ratio (R_1) on the conversion of the discharged gas and solids in the reducer

As R_1 increases, reactions (3.1) and (3.2) approach completion, moving the equilibrium state of reactions (3.4) and (3.5) toward complete combustion. The addition of a discharged solid stream (12% Fe_2O_3 and 28% Fe_3O_4) from the reducer leads to enhanced conversion of solid and enhanced heat recovery from the reactors. The amount of $Fe_{0.947}O$ generated via reaction (3.5) is influenced by the reduction in the amounts of Fe_2O_3 and Fe_3O_4. As a consequence, the amount of Fe^0 in the discharged solid increases. The conversion of solid is in contrast with that of the gas. For R_1 values below 3.4, solid conversion is at or near 100%, which indicates that metallic iron is the only form of oxygen carrier in the reduced state. For R_1>3.4, $Fe_{0.947}O$ is co-generated in addition to Fe^0. This consequently leads to a linear reduction in solid conversion rate [14].

The effect of the outlet temperature of the reducer on the gas conversion is shown in Figure 3.12, which shows that the outlet gas conversion improves with an increase in the outlet temperature until complete conversion is achieved at T_{gr} = 940 ºC. This is due to the endothermic nature of the reactions (3.1) to (3.3), which occur in the reducer. Similar results have been reported in the literature [8]. If T_{gr} is increased, the equilibrium state in reactions (3.1) and (3.2) moves to the right, towards the products, and therefore the equilibrium states in reactions (3.4) and (3.5) are also shifted to the right. This consequently results in complete combustion.

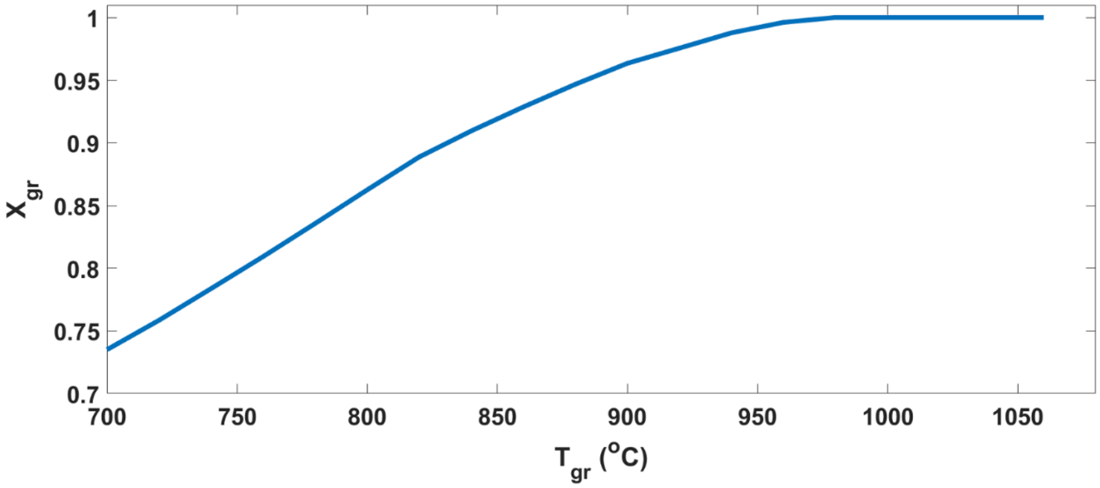

Figure 3.12: The effect of the outlet gas temperature of the reducer on the conversion (R_1 = 6.8 and T_{sr} = 651 ºC)

Figure 3.13 demonstrates the effect of the outlet temperature of the solids on their conversion. It can be seen that, as the discharge temperature increases, the solid conversion increases to a maximum value of 0.66 at T_{sr} = 651 ºC. This behaviour is linked to the amount of carbon deposited on the discharged solid (reaction (3.7) in Table 3.5). Raising the temperature of the discharged solid forces a reduction in the carbon deposition, which improves the conversion of the solid. A further increase in the discharged-solid temperature to above 651 ºC does not affect the conversion of the solid since carbon deposition is eliminated at these elevated temperatures.

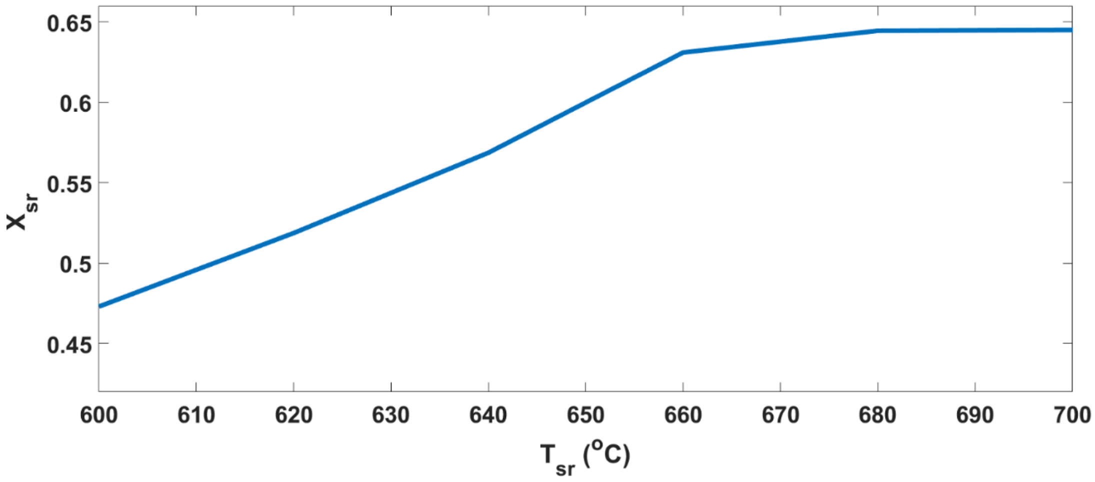

Figure 3.13: The effect of the temperature of the discharged solid on the conversion of the solid

3.8.2 Oxidiser sensitivity analyses

The variations of the discharged gas and solid conversion ratios as a function of steam-to-methane ratios are shown in Figure 3.14.

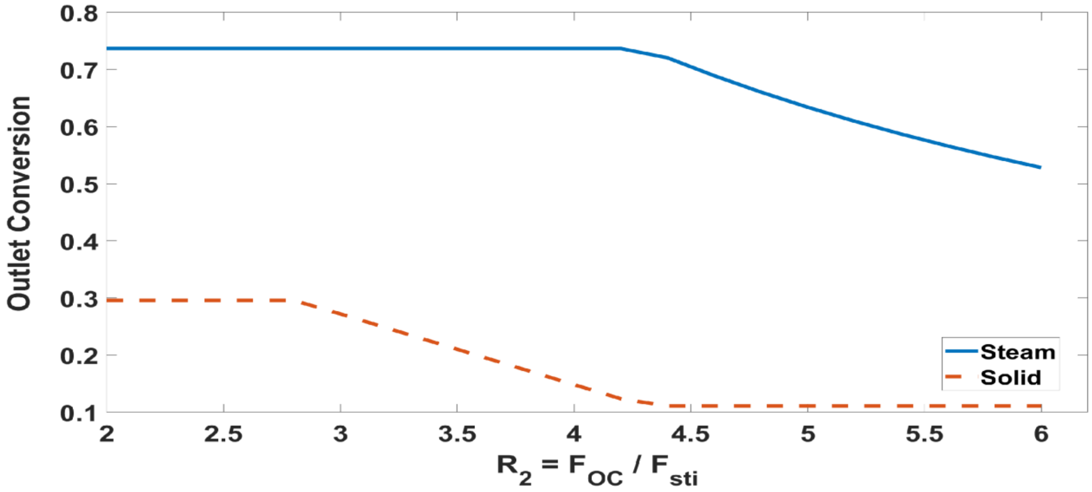

Figure 3.14: The effect of the steam-to-methane inlet flow ratio on the gas discharged from and solid converted in the oxidiser (T_{go} = 660 °C, T_{so} = 820 °C and X_{sr} = 0.66)

The discharged-gas conversion remains constant at 71% for $R_2 \leq 4.4$, but steadily declines as R_2 increases (Figure 3.14). For $2.8 \leq R_2 \leq 4.4$, the conversion ratio decreases almost linearly with an increase in R_2. For $R_2 \geq 4.4$, little variation is observed in the conversion ratio. Similar trends with alumina as support have been reported in the literature [8]. The results observed in Figure 3.14 can be illustrated via the thermodynamic analysis of the reactions that occur in the oxidiser and oxygen carrier (reactions (3.8) and (3.9) in Table 3.5). For $R_2 \leq 4.4$, the equilibrium of these reactions is shifted to the right, i.e. more hydrogen is generated. However, the amount of hydrogen produced is equivalent to the amount of steam fed. As a result, the steam conversion remains constant. For $R_2 \geq 4.4$, the value of the solid conversion is 11%. This conversion value corresponds to the presence of pure magnetite. Thermodynamically, $Fe_{0.947}O$ and metallic iron are the required forms of the iron-based oxygen carriers for hydrogen production, as explained earlier in section 3.4. The solid conversions exhibit different behaviour from that of the steam conversion. For $2 \leq R_2 \leq 2.8$, the quantity of steam fed to the oxidiser activates reaction (3.8) only, based on the stoichiometry of reactions (3.8) and (3.9). This suggests that the discharged solid is made up of $Fe_{0.947}O$ only. Reaction (3.8) indicates that 0.947 mole of Fe^0, when reacted with one mole of steam, produces a mole each of $Fe_{0.947}O$ and hydrogen. In reaction (3.9), each mole of steam requires 3.17 moles of $Fe_{0.947}O$ to produce one mole each of hydrogen and magnetite, and therefore, more $Fe_{0.947}O$ is required to activate reaction (3.8). For $2.8 < R_2 \leq 4.4$, the continuous generation of $Fe_{0.947}O$ via reaction (3.8) activates reaction (3.9). Therefore, the equilibrium state of reaction (3.9) moves to the right until all the $Fe_{0.947}O$ has been converted to magnetite at an R_2 value of 4.4.

The effects of the discharged gas and solid temperatures of the oxidiser on the oxidiser's discharged gas and solid conversions are shown in Figures 3.15 and 3.16.

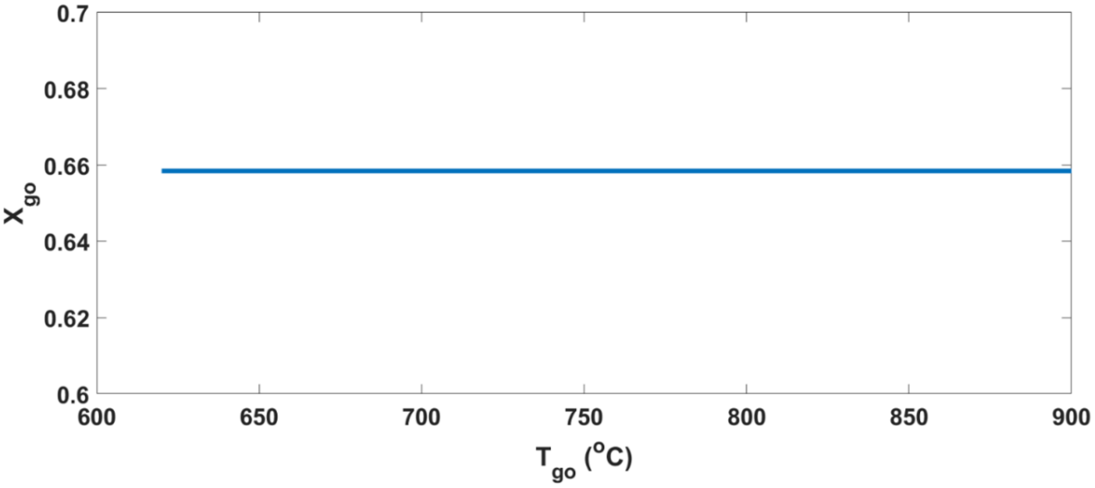

Figure 3.15: The effect of the oxidiser's outlet gas temperature on the oxidiser's outlet gas conversion (R_2 = 4.4 and X_{sr} = 0.66)

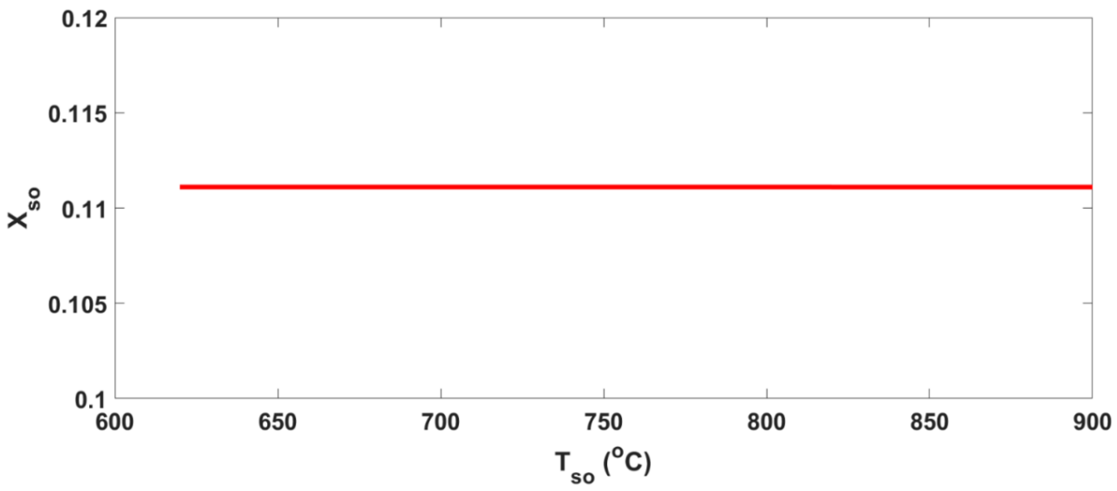

Figure 3.16: The effect of the oxidiser's outlet solid temperature on the oxidiser's outlet solid conversion ($R_2 = 4.4$ and $X_{sr} = 0.66$)

It can be seen that the discharged solid and gas temperatures have a negligible impact on the conversion in the oxidiser. Under these operating conditions, the discharged solid conversion is 11%, i.e. hydrogen is not produced in the oxidiser.

3.8 Concluding remarks

This chapter reveals the steps followed to develop a novel hydrogen production process via chemical looping water splitting (CLWS) technology. It discusses both the pinch-point and sensitivity analyses performed on the developed baseline CLWS process in order to optimise it. Finally the optimised process was assessed via the determination of its effective and hydrogen efficiency, and compared with the benchmark process for hydrogen production, SMR, and CLWS competitor processes. Heat integration into the CLWS process, called the ICLWS process, aided the minimisation of utility usage and resulted in a 23.7 percentage point and 41.3 percentage point improvement in hydrogen production and effective efficiency, respectively, compared with the baseline process. In addition, the hydrogen production efficiency for the optimised process (ICLWS) was improved by 11.7 percentage points, 6.8 – 13.5 percentage points and 6.5 – 12.7 percentage points compared with the conventional SMR1, modern SMR, and ATR processes. Moreover, it was 6.3 percentage points and 13.4 percentage points higher compared with the OSU and (TRCLR) processes. Furthermore, the ICLWS process showed the highest effective efficiency among all the comparable SMR/ATR processes considered in this study, at 12.3 percentage points, 2 – 11.1 percentage points and 4.1 – 10.8 percentage points higher than the conventional SMR, modern SMR and ATR processes, respectively. It offered the added benefit over SMR of simple production of a pure CO_2 stream as well. Yet, the hydrogen production and effective efficiencies of the ICLWS process were lower by 1.1 percentage points and 3.4 percentage points, respectively, than the highest of these that were reported by the literature.

The sensitivity analyses revealed a direct relation between the conversion of the discharged gas from the reducer and the ratio of the oxygen carrier to natural gas feed. The outlet conversion of the solid exhibited contrasting behaviour. At low oxygen carrier to natural gas ratio, it was observed to be at its maximum. However, it started to decline linearly when the $Fe_{0.947}O$ began to form in the discharged solid from the reducer. The conversion of the discharged gas from the reducer increased as its outlet temperature rose until complete conversion was achieved. This followed an expected trend due to the endothermic nature of the reactions carried out in the reducer. For the steam reactor, the steam to methane feed ratio showed negligible effect on the outlet steam conversion at low values. However, the conversion decreased as the ratio passed the value of 4.4. At this ratio, all discharged solid was in the form of magnetite. Lastly, the discharged gas and solid temperatures showed insignificant influence on the gas and solids conversions respectively.

Chapter 4 : ***Decarbonised iron production process via chemical looping water splitting technology***

Chemical looping with water splitting technology can be employed to improve iron and steel manufacture beyond the current state of the art. The technology presented in Chapter 3 and data from the literature for hydrogen production are adapted in this chapter to employ CLWS for iron co-production. The first section of this chapter reviews the thermodynamic limitations of use of an iron-based oxygen carrier in the production of metallic iron via the oxygen carrier's reaction with methane fuel. This information is supported by the results derived from Chapter 3 in the sensitivity analysis section. The second section describes the baseline process developed for the sensitivity analysis. Similarly, heat integration analysis following the methodology presented in section 3.5.2 of Chapter 3 is applied to the process described in this chapter to optimise it. The integrated process for iron manufacture is fully described. Finally, the optimised process for iron production is thermodynamically evaluated using the same parameters as those discussed in Chapter 3.

4.1 Review of the literature regarding steel production through the direct reduced iron process

Direct reduced iron (DRI) is an alternative method to blast furnaces for iron and steel production. In the DRI process, iron is produced as a solid of uniform density and shape [81]. The DRI product lacks the tramp elements that result from use of coal as a reducing agent in the regular blast-furnace process. Therefore, it is an acceptable substitute for the high-quality scrap that is fed to an electric arc furnace (EAF) for steel production [82]. In addition, the DRI process has gained more interest in recent years because of environmental concerns and limitations imposed on carbon emissions. The blast furnace, which is the primary method of iron and steel production, makes a significant contribution to global warming and climate change [2]. The DRI process is mainly a reduction of the iron ore to metallic iron in the solid state using a reducing agent. The reducing agent comprises hydrogen and carbon monoxide (syngas) that results from the reforming of natural gas or coal gasification. The DRI product has a degree of metallisation in the range of 85 – 95%, with a carbon content of 0.4 – 5% [81]. Cold/hot reduced iron (CDRI/HDRI) and hot briquetted iron are the forms of direct reduced iron that can be generated by this process. According to the technologies employed in the iron ore reduction reactor, the DRI processes are classified into the following types:

a- Shaft furnace;
b- Rotary kiln;
c- Rotary hearth furnace;
d- Fluidised bed reactor.

The most common DRI plants have been developed by MIDREX and HYL-ENERGOEN. Both use the shaft furnace reducing reactor [83]. The energy consumption of the DRI process is in the order of 10.4 GJ/t-DRI with CO_2 emission rates of 0.77-0.92 tCO_2/t-steel [81]. Since the MIDREX process accounts for 60% of the DRI production capacity worldwide, more explanation is presented on this process in the upcoming section [84]. Also, the thermodynamic evaluation of the iron-based chemical looping process for iron production, the development of which is described in this chapter, is compared with the values obtained from the MIDREX process.

4.1.1 MIDREX process for DRI production

This process depends on shaft-furnace technology. Natural gas, coke oven gas (COG) and coal have all been used as primary fuels of various configurations in this process [85]. Here, the natural-gas-fuelled process is discussed in more detail since the iron production process via chemical looping proposed in this chapter also utilises natural gas as the reducing agent. In the MIDREX process, natural gas is mixed with part of the process gas that is discharged from the shaft furnace, then the mixture is pre-heated and fed to the reformer. The syngas generated by the reformer is fed to the upper part of the shaft furnace. In the shaft furnace, the syngas reduces the iron ore that is fed in at the top of the shaft furnace in a counter-flow operation. As a result, iron ore is converted to metallic iron that contains some percentages of iron oxides and iron carbide, which is discharged at the reactor bottom [86, 87]. The DRI product comprises 83 – 89% Fe^0, 4 – 7% FeO and 1 – 3% C, according to the literature [81, 87]. Most of the syngas is combusted to a mixture of carbon dioxide and steam. All the reactions that take place in the shaft furnace are shown in Figure 4.1 [83]. Due to the endothermic nature of some reactions that occur in the shaft furnace, pure oxygen is fed with additional natural gas to the furnace in order to aid the sustainability of the reactions occurring there [88]. The heat associated with the flue gas effluent from the reformer is recovered in the pre-heating of the natural gas and process gas mixture [87]. The DRI product is either stored in the form of CDRI or HBI or fed to the EAF to produce steel [89]. In addition, a CO_2-capture unit is integrated with the process due to the environmental limitations imposed by the IPCC. The integration of this unit is shown in Figure 4.2. The specific gas consumption and level of CO_2 emission of this process is 9.4 – 9.6 GJ/t-DRI and 1.27 tCO_2/t of steel produced, respectively [87].

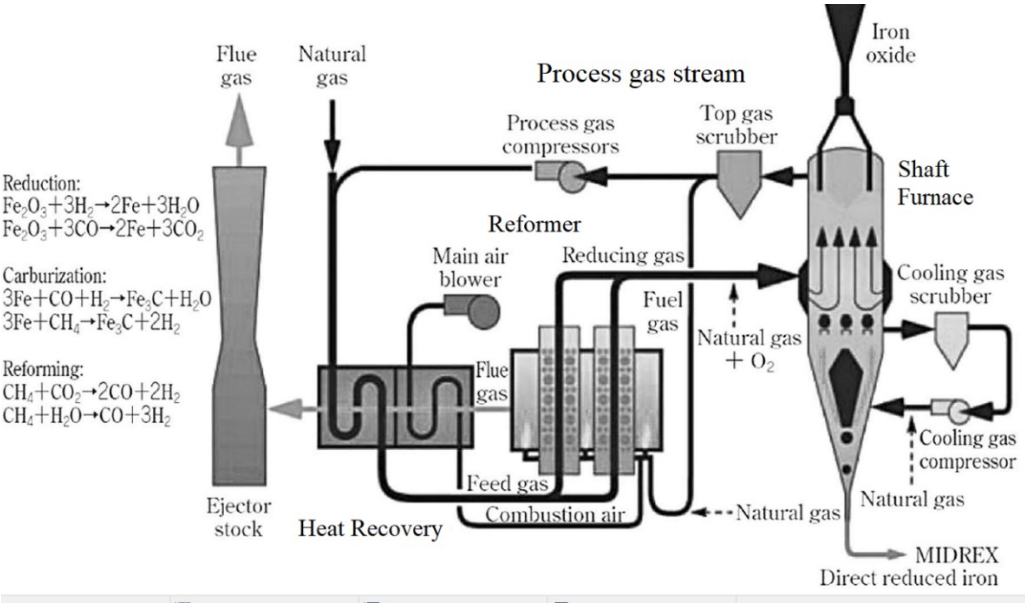

Figure 4.1: Process flow diagram of MIDREX process [87]

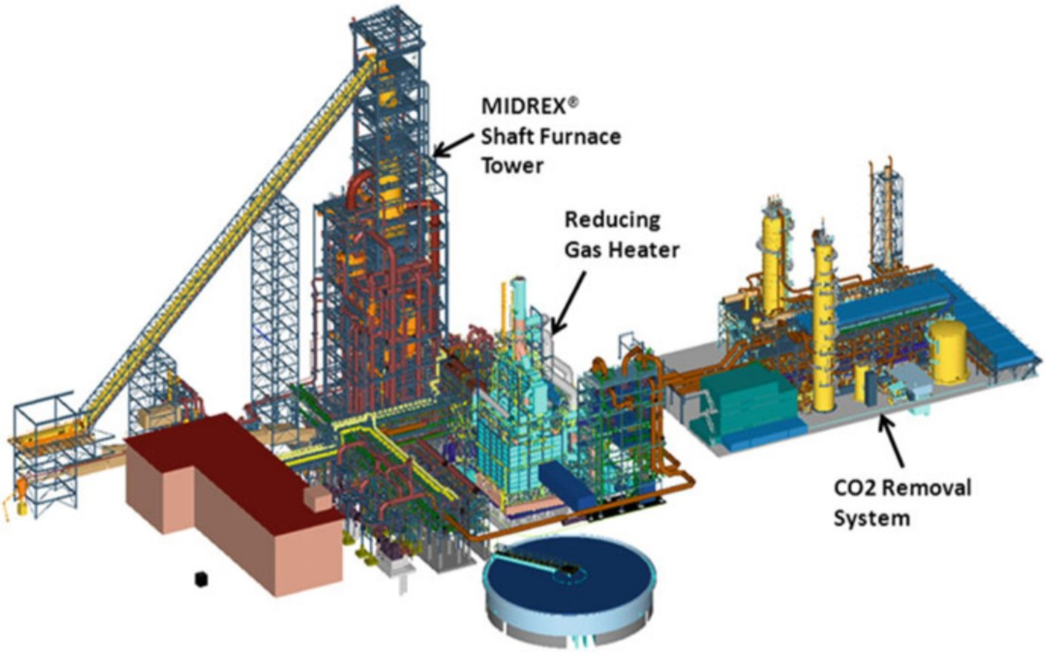

Figure 4.2: MIDREX plant with CO_2 capture [81]

4.2 Reaction of iron-based oxygen carriers with methane: thermodynamic limitations for iron production and theoretical background

In Chapter 3, the reduction of iron ore (Fe_2O_3) to metallic iron was discussed. The phase equilibria for Fe-O-C and Fe-O-H were presented in section 3.4 of that chapter. This reduction process can be exploited to produce decarbonised metallic iron. Furthermore, Figures 3.11 and 4.3 indicate that if a slow flow rate of oxygen carrier is employed, metallic iron can be discharged exclusively from the reducer of a CLWS system. Therefore, the superior ICLWS process, the development of which was described in Chapter 3, can be retrofitted toward the production of metallic iron.

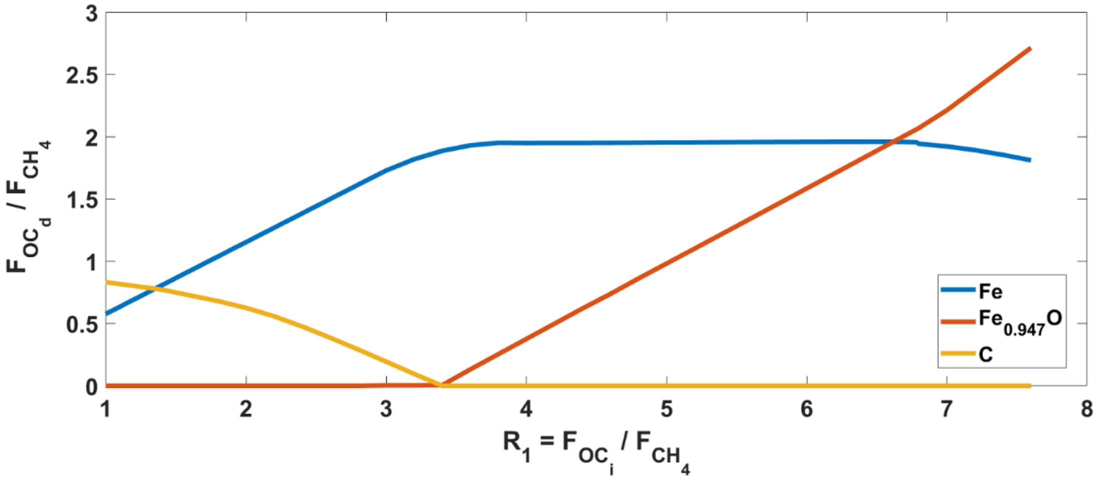

Figure 4.3: The flow rate of discharged oxygen carrier as the oxygen carrier to methane feed ratio increases

However, two obstacles can prevent the production of metallic iron though this approach. The first is related to the durability of the oxygen carrier particles, which affects the sustainability of the operation. This can be illustrated as follows: as the reaction progresses, the deep chemical reduction of the iron-based oxygen carrier enforces a severe and rapid deactivation rate of reaction of the solid particles during the first redox cycles. This is attributed to the significant chemical and physical stresses caused to the particles during the deep reduction (Fe_2O_3 to Fe). The chemical stress is represented by particle sintering, i.e. loss of particle surface area available for the reaction; while the physical stress is caused by the change (about 70%) in particle molar density, which leads to mechanical destabilisation and particle break up. Nevertheless, the added value of obtaining metallic iron as a saleable co-product from the process may compensate for the losses in the oxygen carrier due to sintering. The second obstacle is linked with the carbon capture and storage policy. As shown in the phase equilibria diagrams (Figure 3.1 in Chapter 3), during Fe_2O_3 reduction to Fe^0, achievement of a complete conversion of fuel to CO_2 and steam is not possible. Syngas is produced instead, and hence the percentage of CO_2 captured is affected significantly. To overcome this impediment, the reactor configuration described in section 3.4 of Chapter 3 is altered by adding a fourth reactor. The aim of this change is to combust fully the syngas produced in the fuel reactor as a result of partial oxidation. The modified reactor configuration is presented in Figure 4.4.

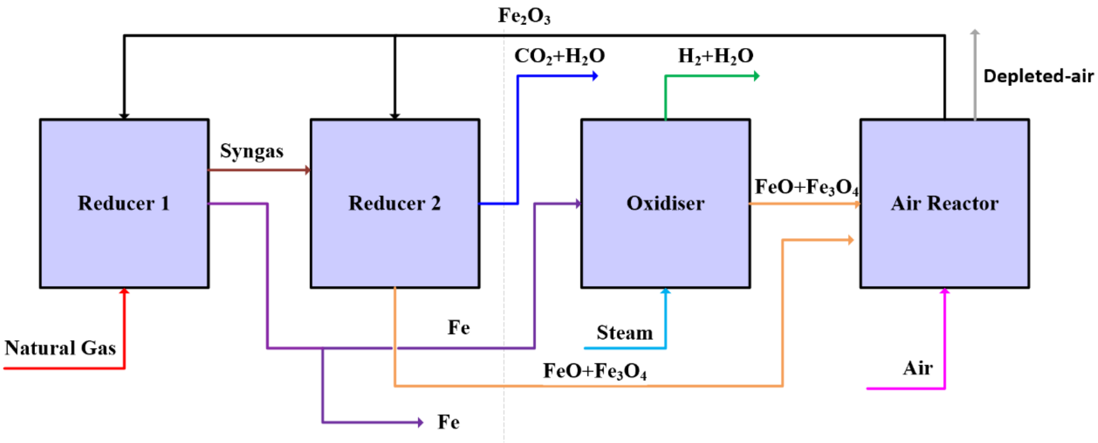

Figure 4.4: Schematic diagram of the proposed four-stage CLWS process to enable iron co-production

4.3 The baseline process for the production of hydrogen with iron co-product in situ with CO_2 capture

Unlike the conventional chemical looping water splitting process, this proposed process consists of four reactors as shown in Figure 4.5. Natural gas is pre-heated and fed to Reducer-1 where it is partially combusted to syngas via reaction with 31.7% of the hematite recycled from the air reactor. The hematite is fully reduced to metallic iron Fe^0. From this reaction, 13% of Fe^0 is stored as a final product, while the balance is introduced to the oxidiser to produce hydrogen at a comparable rate as is produced through the ICLWS process. In the oxidiser, metallic iron is partially oxidised by steam to form a mixture of $Fe_{0.947}O$ and magnetite Fe_3O_4, while steam is converted to hydrogen as shown in reaction 3.9 in Table 3.5, Chapter 3. The syngas produced from Reducer-1 is sent to

Reducer-2 to fully combust the syngas to a mixture of carbon dioxide and steam with the balance of the Fe_2O_3 generated in the air reactor, while the hematite is reduced to a mixture of $Fe_{0.947}O$ and Fe_3O_4. Both solid mixtures discharged from the oxidiser and Reducer-2 are fed to an air reactor to be fully regenerated through their reactions with pre-heated air. The wet CO_2 and hydrogen mixtures are cooled to 30 °C through coolers E-1 and E-2 to condense and separate the water. The dry CO_2 (stream 17) is compressed to 110 bar to prepare it for underground storage. Hydrogen in stream 11 is compressed further to 3 bar, and then cooled to 30 °C to condense and separate more water to achieve the desired 99.4% purity of the product.

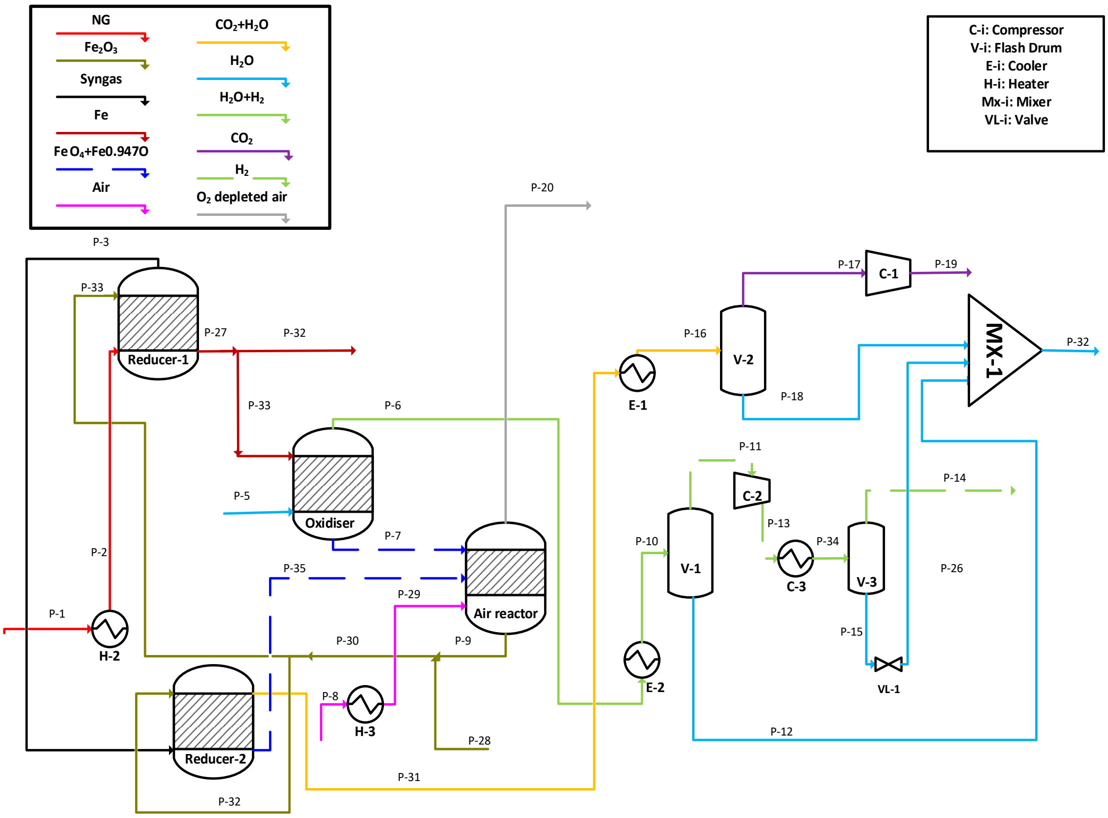

Figure 4.5: Process-flow diagram for the baseline process of chemical looping with iron co-production (BCLWSFe)

4.4 Heat integration in the hydrogen with iron co-product baseline process (BCLWSFe)

Heat was integrated into this process, following performance of the pinch-point analysis as in the ICLWS process presented in Chapter 3. The hot and cold streams involved in the analysis are presented in Figure 4.6, with 10 ºC selected as the minimum temperature difference between them. The temperature intervals were constructed based on the inlet and target temperatures of the hot and cold streams involved. Then, the enthalpy associated with each stream in each temperature interval was calculated and the net enthalpy for each interval was determined. The net enthalpy from interval 1 was added to the enthalpy of the subsequent interval (cascaded) to determine the interval at which no heat was transferred, i.e. the pinch-point interval. At this interval, the cascade enthalpy sign switched from positive (heat supply) to negative (heat demand). The lower bound temperature of this interval was the pinch-point temperature, as discussed in Chapter 3. The net enthalpy that was calculated for each interval, as well as the cascade heat, are summarised in Table 4.1. It is observed that no switch in cascade enthalpy occurred in this case, which is defined as a "threshold" case. For this case, the pinch-point temperature could not be obtained. In this case, it is clear that the excess heat liberated from the process is more than the heat required.

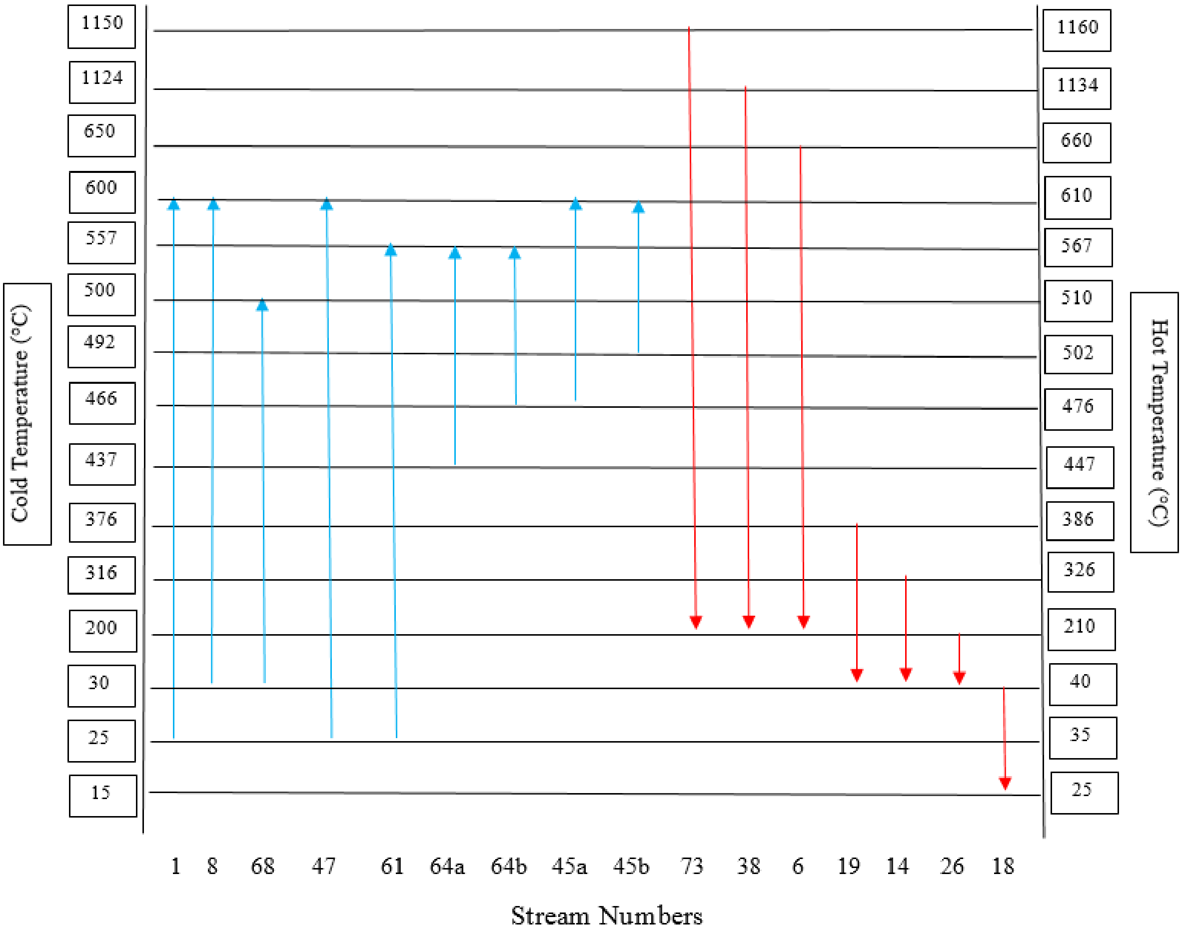

Figure 4.6: Streams involved in the heat integration analysis for the CLWSFe process

Table 4.1: The cascade and the adjusted-cascade heat duty for each interval in the pinch-point analysis

Temperature interval (ºC)	Cascade heat duty (MW)
1+2 (1160 – 1134) + (1134 – 660)	227.2
3 (660 – 610)	258.8
4 (610 – 567)	254.0
5 (567 – 510)	220.6
6 (510 – 502)	214.4
7 (502 – 476)	194.9
8 (476 – 447)	179.3
9 (447 – 386)	99.1
10 (386 – 326)	52.1
11 (326 – 210)	19.6
12 (210 – 40)	1.0
13 (40 – 35)	0.5
14 (35 – 25)	3.4

Therefore, based on the values presented in Table 4.1, only 3.4 MW of cooling utility is needed. In addition, the minimum enthalpy difference was 2.5 MW between the hot and cold cumulative curves obtained at temperature 25 ºC (cold scale) and 35 ºC (hot scale), as shown in Figure 4.7. This indicates that this temperature is considered as “nearly pinch-point temperature” as defined for similar case studies in the literature [90].

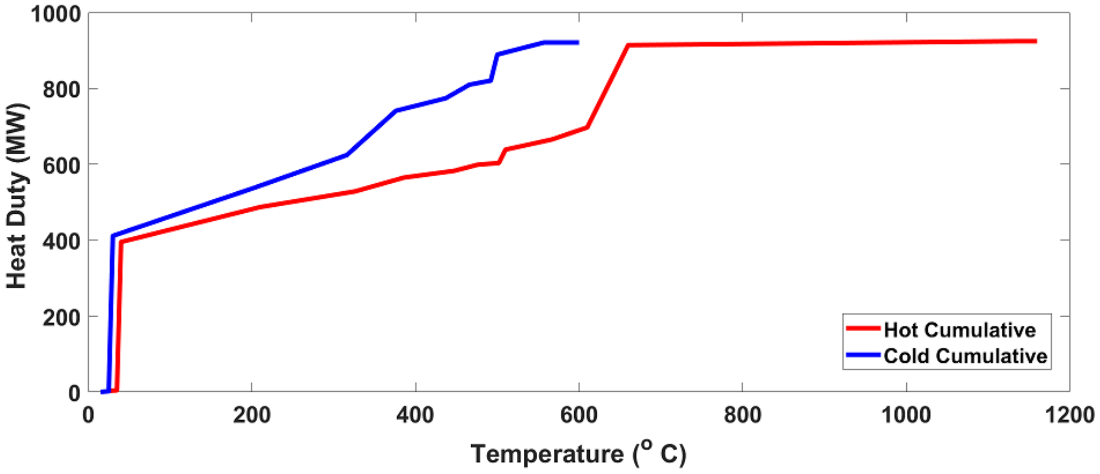

Figure 4.7: Hot and cold composite curves based on the pinch-point analyses performed for the CLWSFe process

The design of the heat-exchanger network starts at the "non-utility end", i.e. the hot side, at approaching the nearly pinch-point temperature, whereas the cooling takes place below it. The following points summarise the heat integration performed on the process and represented by the heat-exchanger network. The process-flow diagram for the optimised CLWSFe process and the operating conditions for the main units in the process are shown in Figure 4.8 and Table 4.2, respectively.

1- Heat exchangers HE-1 and HE-4 use the heat released from streams 75 and 60 with temperatures of 660 °C and 800 °C respectively to pre-heat natural gas to 600 °C, while the indirect solid-gas heater H-1, heat exchanger HE-2 and heat exchanger HE-7 use the heat released from streams 30 (T = 660 °C), 71 (T = 210 °C) and (T = 750 °C) respectively to pre-heat air to 600 °C for the air reactor.

2- The large amount of heat released from the high-temperature streams, i.e. streams 38, 74, 18 and 60, are used to heat two steam generation cycles for power generation. In the first cycle, a unit for heat recovery steam generation (HRSG-1) is comprised of two parallel evaporators that recover the heat from streams 38 and 70 to vaporise water, while HE-3 and HRSG-4 use the heat from streams 18 and 60, respectively, in the second cycle.

3- The steam required in the oxidiser is generated via two units (HRSG-2 and HRSG-3). HRSG-2 is made up of two parallel evaporators to raise steam using the heat from streams 19 and 43.

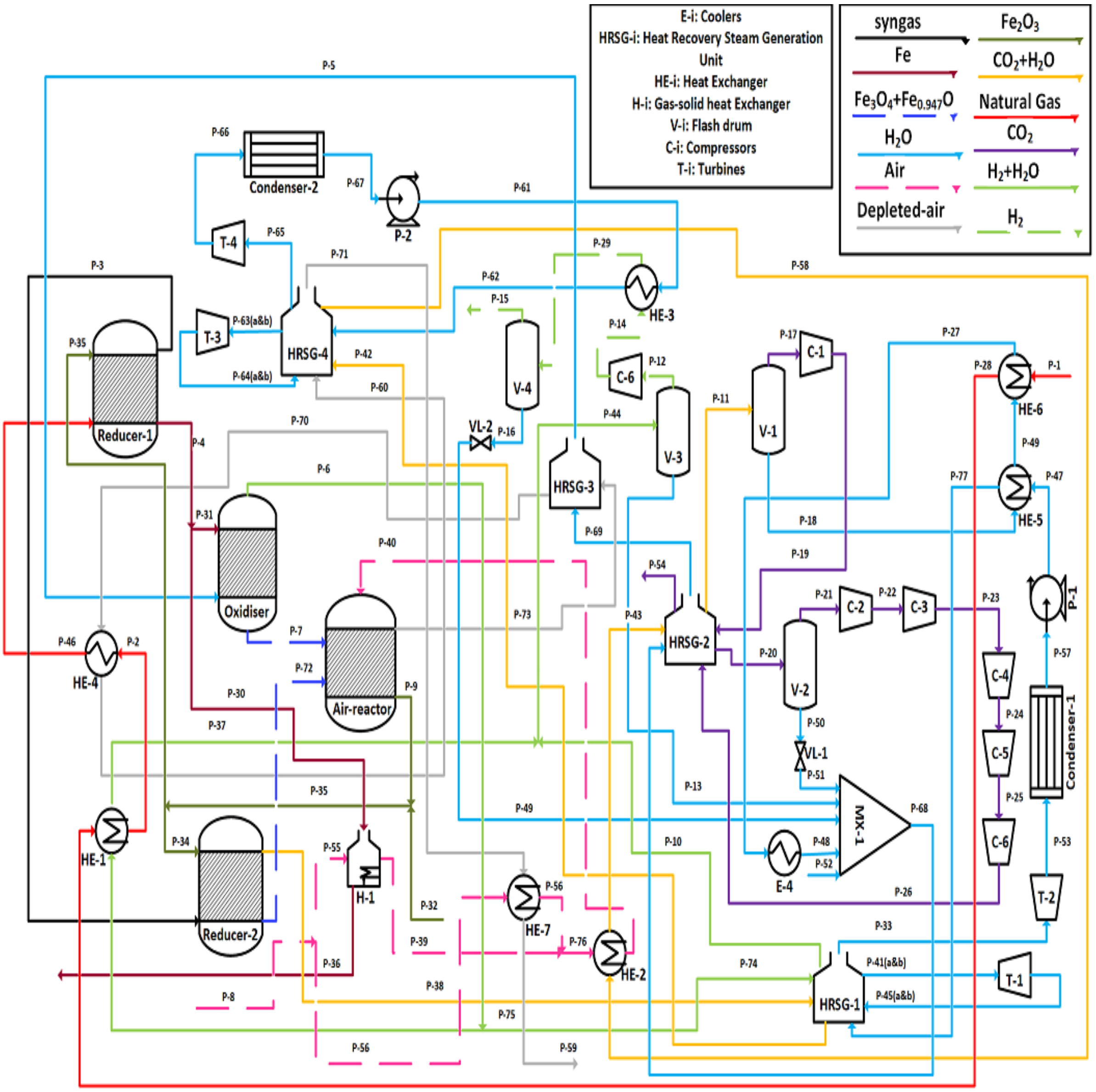

Figure 4.8: Process-flow diagram for the optimised hydrogen and iron co-product chemical looping process CLWSFe

HRSG-3 recovers the heat released from stream 73 to boost the steam temperature from 237˚C to 500 ˚C.

Similar to ICLWS process, the CLWSFe has a non-conventional equipment since it is a state-of-the-art process. These units are listed as follows:

a- Moving bed reactors (Reducer-1&2, oxidiser, air reactor)

b- HRSG-2

c- Indirect gas-solid cooler.

These equipment are similar to the non-conventional equipment described in section 3.5.3.

Table 4.2: List of the operating parameters of the main units in the ICLWS process

Design specification	**Specified value**
Reducer-1 operating temperature	972 ℃
Temperature of the solids fed to the reducer-1	1139 ℃
Temperature of the solids discharged from the reducer-1	660 ℃
Temperature of the natural gas fed to the reducer-1	600 ℃
Oxygen carrier (Fe_2O_3) to natural gas feed ratio	0.9 mol/mol
Fraction of hematite fed to reducer-1	31.7%
Reducer-2 operating temperature	1134 ℃
Oxygen carrier (Fe_2O_3) to syngas feed ratio	0.66 mol/mol
Temperature of the steam fed to the oxidiser	500 ℃
Operating temperature of the oxidiser	660 ℃
Temperature of the solids discharged from oxidiser	820 ℃
Oxygen carrier (Fe_2O_3) to steam ratio	1.0
Operating temperature of the air reactor	1160 ℃
Separation vessels temperature	40 ℃
Operating pressure for all the reactors	1.2 bar
Pressure of the CO_2 product	110 bar
Pressure of the H_2 product	10.0 bar
Isentropic efficiency of the compressors	0.90
Isentropic efficiency of the HP&IP turbines	0.90
Isentropic efficiency of the LP turbine	0.88
Designed vapour fraction of the LP turbine	0.9
Pump efficiency	0.85
Inlet temperature of the Turbines	610 ℃
Pump outlet pressure	260 bar
HP outlet pressure	150 bar
IP outlet Pressure	70 bar

4.5 Thermodynamic evaluation of the process

Thermodynamic analysis of the system was performed to determine the effective thermal efficiency, hydrogen production efficiency, hydrogen yield, iron yield and CO_2 capture efficiency as defined by the equations shown below [8, 12, 41].

$$\eta_{H_2} = \frac{\dot{Q}_0}{\dot{Q}_f} \tag{3.12}$$

$$\eta_{eff} = \frac{\dot{Q}_0 - P_{c/g}}{\dot{Q}_\iota} \tag{3.13}$$

$$\dot{Q}_0 = \dot{m}_{H_2} HHV_{H_2} + \dot{m}_{Fe} \Delta H_{cFe} \tag{4.1}$$

$$\dot{Q}_\iota = \dot{m}_{CH_4} HHV_{CH_4} + \dot{Q}_{MH} \tag{3.16}$$

$$\dot{Q}_f = \dot{m}_{CH_4} HHV_{CH_4} \tag{3.17}$$

$$y_{H_2} = \frac{F_{H_2}}{F_{CH_4}} \tag{4.2}$$

$$y_{Fe} = \frac{F_{Fe}}{F_{CH_4}} \tag{4.3}$$

$$Q_{0s} = \frac{\dot{Q}_0}{\dot{m}_{Fe}} \tag{4.4}$$

$$Q_{Is} = \frac{\dot{Q}_I}{\dot{m}_{Fe}} \tag{4.5}$$

$$Q_{fs} = \frac{\dot{Q}_f}{\dot{m}_{Fe}} \tag{4.6}$$

$$\eta_{Ieff} = \frac{Q_{0s} - \frac{P_{c/g}}{\dot{m}_{Fe}}}{Q_{Is}} \tag{4.7}$$

$$CO_2\,Capture\% = \frac{F_{CO_2}}{Ft_{CO_2}} \tag{4.8}$$

In these equations, η_{eff}, η_{Ieff} and η_{H_2} are the effective, iron effective and hydrogen production efficiencies, respectively; $\dot{m}_{H_2}$, $\dot{m}_{Fe}$, and $\dot{m}_{CH_4}$ are the mass flow rates of H_2 and Fe produced and of CH_4 consumed by the process, respectively; F_{H_2}, F_{Fe} and F_{CH_4} are the molar flow rates of H_2 and Fe produced, and of CH_4 consumed by the process; *HHV* is the higher heating value of the fuel (MJ/kg); $P_{c/g}$ is the power generated (-ve) through turbines or consumed (+ve) through pumps and compressors in the process; $\dot{Q}_{MH}$ is the net heating utility supplied to the process in MW; y_{H_2} and y_{Fe} are the hydrogen and iron yields, respectively; F_{CO2} is the molar flow rate of CO_2 captured; Ft_{CO2} is the total amount of CO_2 generated through the process; and ΔH_{cFe} is the heat associated with the oxidation of metallic iron, Fe^0 to Fe_2O_3, in kJ/kg according to: $4Fe_{(s)} + 3O_{2\,(g)} \rightarrow 2Fe_2O_{3(s)}$ under standard conditions. Q_{0s}, Q_{Is} and Q_{fs} are the specific rates of the total energy produced, total energy consumed and fuel consumed (GJ/tDRI), respectively.

A summary of the thermodynamic performance indicators calculated using these equations is provided in Table 4.3 and Table 4.4. Results from this study were benchmarked and compared against similar studies reported in the open literature that investigated a conventional SMR process (without CO_2 capture) [28], modern SMR_m/ATR [18] and the non-heat integrated, three-stage OSU process, which was used as the baseline process [29]. Also, the CLWSFe thermodynamic performance was compared with that of the benchmark process for DRI production, i.e. the MIDREX process [81].

Both CLWS processes that have been compared in this study demonstrated higher effective efficiencies than that found in the conventional SMR process with CO_2 capture. The CLWSFe process exhibited the highest effective efficiency at 90.5%, which was 20.8 percentage points and 10.9 – 20 percentage points higher than the effective efficiencies reported for the conventional SMR and modern SMR/ATR reference processes. In addition, the effective efficiency of the CLWSFe process was 15.4 percentage points higher than that of a chemical looping competitive process i.e. the OSU process.

Table 4.3: Comparison between the thermodynamic evaluations of the CLWSFe, SMR and OSU processes.

Parameter	**SMR [28]**	**SMR_m/ATR[18]**	**OSU [29]**	**CLWSFe**
CO_2 capture %	90	53.2-90	90	100
y_{H_2}	2.2	2.3-2.5	2.3	2.2
y_{Fe}	N/A	N/A	N/A	0.75
$\dot{Q}_i$ *(MW)*	N/A	457.7-503.4	N/A	1683.2
$\dot{Q}_o$ *(MW)*	1013	354.5	1018	1447.1
$\dot{Q}_f$ *(MW)*	1403	457.7-503.4	1309	1683.2
$P_{c/g}$*(MW)*	34	0.2-1.6	33	-77
η_{H_2}	72.2	70.4-77.4	77.6	70.6
η_{eff}	69.7	70.5-79.6	75.1	90.5

The higher effective efficiency of the CLWSFe process compared with those of the OSU and SMR processes was attributed to the additional power produced during the CLWSFe process, which was made possible through heat recovery by two steam generation cycles. The hydrogen production efficiency of the CLWSFe process, however, was 1.6 percentage points, 6.8 percentage points and 7.0 percentage points lower than the figures for the conventional SMR1, modern SMR/ATR and OSU processes respectively. The lower hydrogen production efficiency of the CLWSFe process was due to the large amount of metallic iron that was removed from the process as a DRI co-product that was therefore not available for H_2 production. The economic assessment of the process follows in Chapter 6 for this process and for the ICLWS process, the development of which was explained in Chapter 3.

Table 4.4: Comparison between the thermodynamic evaluation of the CLWSFe and MIDREX processes

Parameter	MIDREX[81]	CLWSFe
CO_2 sp.emission (tCO_2/ tNG)	0.638	0.0
y_{H_2}	-	2.2
y_{Fe}	1.44 – 1.54	0.75
Q_{0s} *(GJ/tDRI)*	8.6– 9.2	57.9
Q_{Is} *(GJ/tDRI)*	10.2 – 10.4	67.2
Q_{fs}*(GJ/tDRI)*	9.9 – 10.2	67.2
$P_{c/g}$*(MW)*	-	-77
η_{Ieff}	84.1 – 90.0	90.7

The CLWSFe process exhibited a higher level of specific output energy than the MIDREX process, by 53.2 GJ/tDRI, due to the amount of hydrogen fuel produced by the CLWSFe method. This has a high calorific value. In addition, the CLWSFe system has the potential to generate power. However, the total energy consumed by the MIDREX process and that consumed by natural gas were significantly lower than that used by the CLWSFe method. As a result, the CLWSFe process demonstrated higher iron production efficiency in the range of 0.7 – 6.6 percentage points compared with the MIDREX process.

4.6 Concluding remarks

A novel decarbonised iron and steel manufacturing process has been developed based on iron-based chemical looping technology (CLWSFe). The process is comprised of four stages. In the first, the aim is full reduction of the oxygen carrier, i.e. iron ore, to metallic iron through the partial combustion of fuel. The fuel is fully converted to steam and carbon dioxide and the latter is completely captured in the second stages. Another environmentally benign fuel (H_2) is produced in the third stage by thermal decomposition of steam using metallic iron. In the last stage the oxygen carrier is fully regenerated via its reaction with air. Heat integration is performed in the process to optimise the energy consumption.

The process has been assessed thermodynamically and compared with conventional and modern SMR, auto thermal reforming, CLWS and DRI competitor processes to calculate its viability. The thermodynamic evaluation of the developed CLWSFe process shows an effective efficiency of 90.5% which is 20.8 percentage points and 10.9 – 20.9 percentage points higher than the effective efficiencies of the conventional SMR and modern SMR_m/ATR processes. Also, it was 15.4 percentage points higher than that found with the three-stage chemical looping water splitting process developed by OSU. However, the hydrogen production efficiency for the SMR and OSU processes were 7.0 percentage points and 1.6 percentage points higher than that of the developed decarbonised iron process, due to the amount of iron stored as a by-product and therefore not utilised in the third stage of the process to produce hydrogen. Furthermore, the effective efficiency of iron production showed an improvement of 0.7 – 6.6 percentage points over the MIDREX process for DRI production. These values enable the developed process to be considered as a promising choice in the future to support the decarbonisation of the steel industry.

Chapter 5 : Kinetics and reactor modelling for both ICLWS and CLWSFe processes

This chapter is comprised of three parts. The first part discusses the kinetics derived from the earlier studies that describe the gas-solid reactions that take place in the chemical looping water splitting process. The second part contains a description of the moving-bed reactor model that was employed to size all the reactors involved in the process developed in this chapter. The explanation of the model includes the assumptions made, the boundary conditions and the methods that were used to solve the problems. The third section describes the conversion and temperature profiles for all the reactors in the ICLWS and CLWSFe processes that were obtained and plotted using the counter-current moving-bed reactor model. Finally, the major points are listed as the concluding remarks of the chapter.

5.1 Development of kinetic models for the iron-based oxygen-carrier oxidation-reduction reactions

Chapter 2 of this thesis discussed the use of chemical looping water splitting to produce hydrogen. It considered various reaction models, and stated that the reaction rate for iron-based oxygen carriers could be generally expressed as:

$$r = \frac{-dX}{dt} = k(T)f(X)f(C_i) \qquad (2.40)$$

In this equation, $k(T)$ is the intrinsic reaction rate constant and is represented by the Arrhenius equation; $f(X)$ is the solid conversion function, which depends on the reaction mechanism as mentioned in Table 2.1; and $f(C_i)$ is the concentration function, which depends on the power law.

Several studies have been conducted to identify the mechanism of iron-based oxidation-reduction reactions, i.e. to obtain the $f(X)$ in addition to the order of the reaction and Arrhenius equation parameters. A number of these studies are summarised in Table 5.1.

None of the studies listed in Table 5.1 were conducted on the oxygen carrier $Fe_2O_3/MgAl_2O_4$ used in our developed process ICLWS. Therefore, we assumed that the kinetics of reaction with Fe_2O_3/ZrO_2 studied by Kang et al. [42] would be applicable to Fe_2O_3 with magnesium aluminate spinel ($MgAl_2O_4$), since Kang's study was comprehensive and had covered all the reactions involved in the ICLWS process. Therefore, the model developed by Kang et al. was the most applicable model for the rest of the reactions involved in the ICLWS process. Note that reactions (5.4) to (5.6) result from the summation of reactions (3.1) to (3.2) and reactions (3.4) to (3.5) for both carbon monoxide and hydrogen reactants.

For the CLWSFe process, the kinetic models for the two-stage reduction of Fe_2O_3 to FeO and Fe with methane fuel were selected based on a study conducted by Prof. Paul Fennell research group at Imperial College London [15]. The kinetic models for the reactions carried out in the ICLWS and CLWSFe processes are summarised in Tables 5.2 to 5.4. The equations involved in the reduction of haematite to metallic iron in the CLWSFe process are listed in Table 5.5. The kinetics applied to the reactions in Reducer-2 of the CLWSFe process, in which haematite is reduced to a mixture of $Fe_{0.947}O$ and Fe_3O_4, were based on an earlier study published in the literature and are summarised in Table 5.6 [91].

Table 5.1: Summary of published data on the kinetics of oxidation-reduction reactions of iron oxides, gathered from a literature survey

Composition	**Reduction degree**	**Gas**	**Kinetic model**	n_i	E_a **(kJ/mol)**	**Ref**
Pure Fe_2O_3	Fe_2O_3 – FeO	H_2	R_3	-	72.7	[92]
Pure Fe_2O_3	Fe_2O_3 – FeO	H_2	R_3, AE_2	-	28.8	[93]
Pure Fe_2O_3	Fe_2O_3 – FeO	CO	R_3, AE_1	-	122.5	[93]
Pure Fe_2O_3	Fe_2O_3 – FeO	CO	R_3	1	93.3	[91]
Pure Fe_2O_3	Fe_2O_3 – FeO	H_2	R_3	1	28.0	[91]
Fe_2O_3	Fe_2O_3 – FeO	CH_4	D_3	-	271	[94]
Fe_2O_3	FeO – Fe_3O_4	H_2O	D_3	-	77.9	[94]
Fe_2O_3	Fe_2O_3 – FeO	CH_4	D_3	1.5	40 ± 18	[15]
Fe_2O_3	FeO – Fe	CH_4	R_3	1.0	110 ± 73	[15]
Fe_2O_3/Al_2O_3	Fe_2O_3 – FeO	H_2	R_3	0.85	22	[95]
Fe_2O_3/Al_2O_3	Fe_2O_3 – FeO	CO	R_3	1.0	19	[95]
Fe_2O_3/Al_2O_3	Fe_2O_3 – FeO	CH_4	R_3	0.2	25	[95]
Fe_2O_3/Al_2O_3	Fe_2O_3 – Fe_3O_4	CH_4	R_3	1.3	49	[65]
Fe_2O_3/Al_2O_3	Fe_2O_3 – Fe_3O_4	H_2	R_3	0.8	24	[65]
Fe_2O_3/Al_2O_3	Fe_2O_3 – Fe_3O_4	CO	R_3	1.0	20	[65]
Fe_2O_3/Al_2O_3	Fe_3O_4 – Fe_2O_3	O_2	R_3	1.0	14	[65]
Fe_2O_3/bentonite	Fe_2O_3 – Fe	CH_4	AE_1	-	28.8	[96]
Fe_2O_3/bentonite	Fe – Fe_2O_3	O_2	R_3	-	8.64	[96]
Fe_2O_3/ZrO_2	Fe_2O_3 – FeO	CH_4	R_1	-	219	[97]
Fe_2O_3/ZrO_2	FeO – Fe_2O_3	H_2O	R_1	-	238	[97]
Fe_2O_3/ZrO_2	Fe_3O_4 – Fe_2O_3	O_2	R_1	-	20	[97]
Fe_2O_3/ZrO_2	Fe_2O_3 – FeO	CH_4	R_3	0.56	251	[42]
Fe_2O_3/ZrO_2	FeO – Fe	CH_4	R_1	0.91	230	[42]
Fe_2O_3/ZrO_2	Fe_2O_3 – Fe	H_2	R_3	1.16	59	[42]

Fe_2O_3/ZrO_2	Fe_2O_3 – Fe	CO	R_3	1.0	37	[42]
Fe_2O_3/ZrO_2	Fe – Fe_2O_3	H_2O	R_3	0.75	27	[42]
Fe_2O_3/ZrO_2	FeO – Fe_2O_3	O_2	R_3	0.59	7	[42]
Fe	Fe – Fe_3O_4	H_2O	-	-	55-65	[98]

Table 5.2: Kinetic expressions for reactions in the reducer for the ICLWS process

Rxn No.	**Reaction**	**Kinetic model**	$f(C_i)$	***Ea***	***Ai***
5.1	$\mathrm{Fe_{0.947}O + CH_4 \leftrightarrow 0.947Fe + CO + 2H_2}$	R_1	${C_{CH_4}}^{0.91}$	193	6.6E7
5.2	$\mathrm{Fe_{0.947}O + H_2 \leftrightarrow 0.947Fe + H_2O}$	R_3	${C_{H_2}}^{1.16}$	59	2.24
5.3	$\mathrm{Fe_{0.947}O + CO \leftrightarrow 0.947Fe + CO_2}$	R_3	C_{CO}	37	0.24
5.4	$\mathrm{Fe_2O_3 + 0.89CH_4 \leftrightarrow 2.11Fe_{0.947}O + 0.89CO + 1.78H_2}$	R_3	${C_{CH_4}}^{0.6}$	251	1.1E9
5.5	$\mathrm{Fe_2O_3 + 0.89CO \leftrightarrow 2.11Fe_{0.947}O + 0.89CO_2}$	R_3	C_{CO}	37	0.24
5.6	$\mathrm{Fe_2O_3 + 0.89H_2 \leftrightarrow 2.11Fe_{0.947}O + 0.89H_2O}$	R_3	${C_{H_2}}^{1.16}$	59	2.24
5.7	$\mathrm{CH_4 \leftrightarrow C + 2H_2}$	R_1	C_{CH_4}	193	5.4E3
5.8	$\mathrm{CO_2 + C \leftrightarrow +CO}$	R_1	${P_{CO}}^{0.8}$	166	5.1E6
5.9	$\mathrm{H_2O + C \leftrightarrow +2CO + 2H_2}$	R_1	P_{H_2O}	156	6.6E3

Table 5.3: Kinetic expressions for the reactions in the oxidiser for the ICLWS and CLWSFe processes

Rxn No.	**Reaction**	**Kinetic model**	$f(C_i)$	***Ea***	***Ai***
5.10	$\mathrm{3.17Fe_{0.947}O + 0.83H_2O \leftrightarrow Fe_3O_4 + 0.83H_2}$	R_3	$\left(C_{H_2O} - \frac{C_{H_2}}{K_e}\right)^{0.75}$	27	0.122
5.11	$\mathrm{0.947Fe + H_2O \leftrightarrow Fe_{0.947}O + H_2}$	R_3	$\left(C_{H_2O} - \frac{C_{H_2}}{K_e}\right)^{0.75}$	27	0.122

Table 5.4: Kinetic expressions for the reactions in the air reactor for the ICLWS and CLWSFe processes

Rxn No.	**Reaction**	**Kinetic model**	$f(C_i)$	E_a	A_i
5.12	$3.17Fe_{0.947}O + 0.41O_2 \leftrightarrow Fe_3O_4$	R3	${C_{O_2}}^{0.59}$	7	0.07
5.13	$2Fe_3O_4 + 0.5O_2 \leftrightarrow 3Fe_2O_3$	R3	${C_{O_2}}^{0.59}$	7	0.07

Table 5.5: Kinetic expressions for reactions in Reducer-1 for the CLWSFe process

Rxn No.	**Reaction**	**Kinetic model**	$f(C_i)$	E_a	A_i
5.1	$Fe_{0.947}O + CH_4 \leftrightarrow 0.947Fe + CO + 2H_2$	R3	C_{CH_4}	113	2.7E3
5.4	$Fe_2O_3 + 0.89CH_4 \leftrightarrow 2.11Fe_{0.947}O + 0.89CO + 1.78H_2$	D3	${C_{CH_4}}^{1.5}$	49	0.07

Table 5.6: Kinetic expressions for the reactions in Reducer-2 for the CLWSFe process

Rxn No.	**Reaction**	**Kinetic model**	$f(C_i)$	E_a	A_i
5.14	$3Fe_2O_3 + CO \leftrightarrow 2Fe_3O_4 + CO_2$	R3	C_{CO}	93	790
5.15	$3Fe_2O_3 + H_2 \leftrightarrow 2Fe_3O_4 + H_2O$	R3	C_{H_2}	28	0.76
5.16	$Fe_3O_4 + 0.84CO \leftrightarrow 3.17Fe_{0.947}O + 0.84CO_2$	R3	C_{CO}	93	790
5.17	$Fe_3O_4 + 0.84H_2 \leftrightarrow 3.17Fe_{0.947}O + 0.84H_2O$	R3	C_{H_2}	28	0.76

5.2 Development of mathematical model for the moving-bed reactors employed in the ICLWS and CLWSFe processes

A one-dimensional steady-state model was formulated to investigate the progression of the gas-solid oxidation-reduction reactions in the ICLWS and CLWSFe processes in order to obtain the concentration and temperature profiles along the reactors’ lengths. Therefore, a primary design of the ICLWS and CLWSFe reactors was developed.

5.2.1 Model assumptions

To draw up any mathematical model, assumptions must first be made. The model assumptions in this case are denoted in the following points:

1- The model variables are independent of time, i.e. steady-state operation is reached.
2- The model variables consist of concentrations, flow rates and temperatures and are varied in the axial direction (along the reactors' lengths) only.
3- The physical properties of the solids, such as density and volume, remain constant throughout the reactors' lengths. However, the molar volume changes with the variation of solid phase, i.e. haematite (Fe_2O_3) to magnetite (Fe_3O_4), magnetite to wustite ($Fe_{0.947}O$) or wustite to metallic iron.
4- The physical and thermal properties of the gaseous components are arithmetically averaged between the reactor inlet and outlet temperatures.
5- The reactor diameter is constant.
6- The axial dispersion is neglected due to the high volumetric flow rate of the gaseous components in all the reactors in the ICLWS and CLWSFe processes [45].

5.2.2 Model derivation

The main reason for the development of this model was to obtain the flow, conversion and temperature profiles along the axial direction of the reactor. From this, the reactor size was determined. Consequently, the cost of the reactor was evaluated and employed for the economic analysis of both processes developed in Chapters 3 and 4.

Mass-balance equation for the gaseous and solid components:

To derive the model, mass and energy balances were performed on an arbitrary element with thickness ΔZ as shown in Figure 5.1 for the moving-bed reactor schematic.

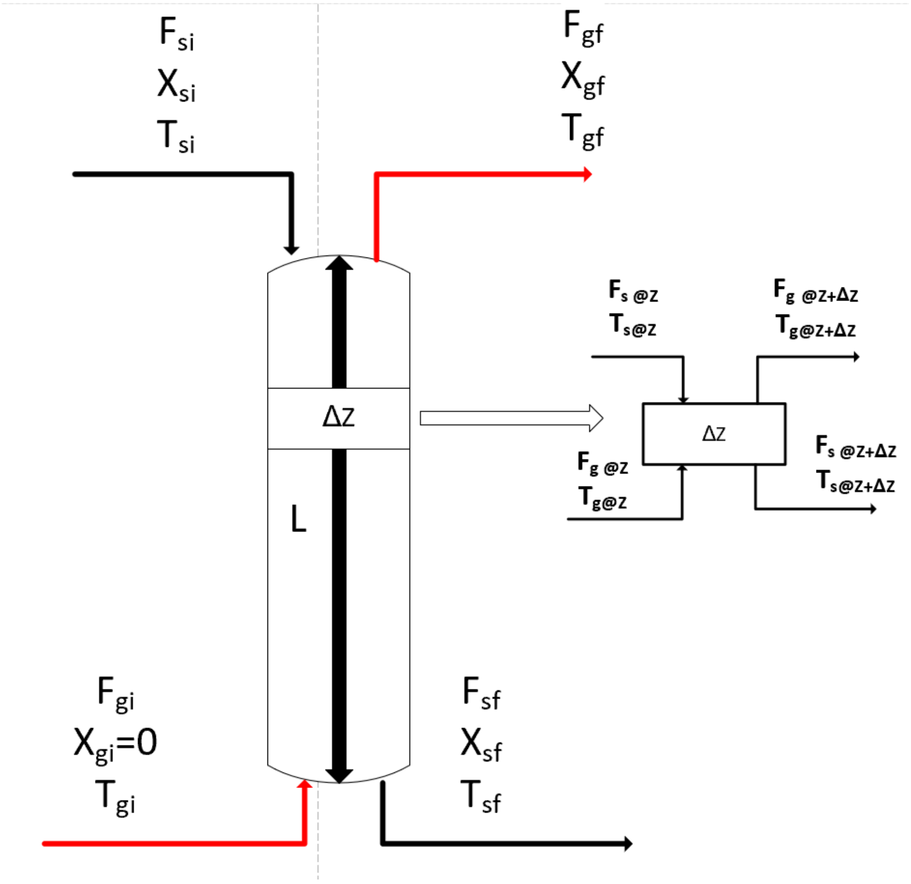

Figure 5.1: |Schematic of moving-bed reactor model

In this figure:

F_{gi} = is the inlet molar flow rate of the gas to the reactor (mol/time);

F_{gf}= is the outlet molar flow rate of the gas discharged from the reactor (mol/time);

X_{gi} = is the conversion of the gas at the reactor inlet;

X_{gf}= is the conversion of the discharged gas at the reactor outlet;

T_{gi} = the inlet temperature of the gaseous mixture to the reactor (K);

T_{gf} = the temperature of the gaseous mixture discharged from the reactor (K);

F_{si} = the inlet molar flow rate of the solid to the reactor (mol/time);

F_{sf} = the molar flow rate of the solid discharged from the reactor (mol/time);

X_{si} = the conversion of the solid at the reactor inlet;

X_{sf}= the conversion of the solid discharged from the reactor;

T_{si} = the inlet temperature of the solid mixture to the reactor (K);

T_{sf} = the temperature of the solid mixture discharged from the reactor (K).

L = the length of the reactor (m)

The general mole balance equation for the element with *ΔZ* is:

$$\begin{pmatrix} Moles\ of\ component\ A \\ into\ the\ element \\ due\ to\ the\ bulk\ flow\ @Z \end{pmatrix} + \begin{pmatrix} Moles\ of\ component\ A \\ into\ the\ element \\ due\ to\ the\ axial\ dispersion\ @Z \end{pmatrix} - \begin{pmatrix} Moles\ of\ component\ A\ discharged \\ from\ the\ element \\ due\ to\ the\ bulk\ flow\ @Z + \Delta Z \end{pmatrix} -$$
$$\begin{pmatrix} Moles\ of\ component\ A\ discharged \\ from\ the\ element \\ due\ to\ the\ bulk\ flow\ @Z + \Delta Z \end{pmatrix} \pm \begin{pmatrix} Moles\ of\ component\ A\ generated \\ or\ consumed\ as\ a \\ result\ of\ chemical\ reaction \end{pmatrix} =$$
$$\begin{pmatrix} Moles\ of\ component\ A\ accumulated \\ in\ the\ element \end{pmatrix} \qquad (5.18)$$

For a steady-state system neglecting the axial dispersion as assumed above, Eq. (5.18) becomes:

$$F_{A\,@Z} - F_{A\,@Z+\Delta Z} \pm r_A(A\Delta Z) = 0 \qquad (5.19)$$

where $F_{A\,@Z}$ and $F_{A\,@Z+\Delta Z}$ represent the bulk flow of moles of component A into and out of the elements, respectively; and

r_A is the reaction rate for component A (mole/vol.time), (-ve for reactant, +ve for products).

Dividing Eq. (5.19) on an infinitesimal thickness of the elements resolves to:

$$\boldsymbol{\frac{dF_A}{dZ} = -r_A A} \qquad (5.20)$$

Eq. (5.20) was also published in the literature as derived for plug-flow reactors in which multiple reactions occurred [75]. In addition, it can be re-written in terms of particle density if the rate is given as a function of particle density as follows:

$$\boldsymbol{\frac{dF_A}{dZ} = -r_A A \rho_s} \qquad (5.21)$$

Eqs. (5.20) and (5.21) can be applied to both gas and solid components in the reactor. The boundary condition for the latter equation is:

Gas: $\boldsymbol{F_A = F_{Ai}\ @\ Z = 0}$

Solids: $\boldsymbol{F_A = F_{si}\ @\ Z = L}$

Energy balance in the gas phase:

As in the case of the mass-balance equation, the energy balance in the moving-bed reactor can be obtained by applying the general energy balance equation on an element with thickness *ΔZ* as follows:

$$\begin{pmatrix}\text{The enthalpy associated with}\\ \text{gaseous bulk flow}\\ \text{into the element}\\ @Z\end{pmatrix}+\begin{pmatrix}\text{Energy associated with the axial}\\ \text{dispersion of gas}\\ \text{into the element}\\ @Z\end{pmatrix}-\begin{pmatrix}\text{The enthalpy discharged}\\ \text{from the element}\\ \text{due to the bulk}\\ \text{gaseous flow } @Z+\Delta Z\end{pmatrix}-$$

$$\begin{pmatrix}\text{Energy discharged}\\ \text{from the element}\\ \text{due to axial dispersion}\\ \text{of gas mixture } @Z+\Delta Z\end{pmatrix}\pm\begin{pmatrix}\text{Energy supplied to or removed}\\ \text{from element due to surroundings}\end{pmatrix}+\begin{pmatrix}\text{Enthalpy transferred}\\ \text{between gas and solids}\end{pmatrix}=$$

$$\begin{pmatrix}\text{Energy of gaseous}\\ \text{mixture}\\ \text{accumulated}\\ \text{in the element}\end{pmatrix} \qquad (5.22)$$

As mentioned above, the axial dispersion is neglected. Also, for a time-independent operation, Eq. (5.22) becomes:

$$\sum_{A=1}^{n}(F_A \cdot H_A)_{@Z} + \sum_{A=1}^{n}(F_A \cdot H_A)_{@Z+\Delta Z} \pm Q \cdot A\Delta Z + hAS_m(T_g - T_s)\Delta Z = 0 \quad (5.23)$$

For infinitesimal thickness of the element, the above equation yields to:

$$\frac{d}{dZ}\left(\sum_{A=1}^{n}(F_A \cdot H_A)\right) \pm Q + hAS_m(T_g - T_s)\Delta Z = 0$$

or $\sum_{A=1}^{n} H_A \frac{dF_A}{dZ} + \sum_{A=1}^{n} F_A \frac{dH_A}{dZ} \pm Q + hAS_m(T_g - T_s)\Delta Z = 0$ (5.24)

Substituting $\frac{dF_A}{dZ}$ with Eq. (5.20), taking into consideration that the reaction is taking place in the solid phase only and that the heat capacity is averaged over the reactor temperature range as assumed above, Eq. (5.24) can be represented as:

$$\sum_{A=1}^{n} F_A Cp_{\bar{A}} \frac{dT_g}{dZ} \pm Q + hAS_m(T_g - T_s) = 0 \quad (5.24a)$$

$$\boldsymbol{\frac{dT_g}{dZ} = \frac{hAS_m(T_s - T_g) \pm Q}{\sum_{A=1}^{n} F_A Cp_{\bar{A}}}} \quad (5.24b)$$

Eq. (5.24b) is the final form of the gas energy balance equation used later to determine the profiles through the axial direction of the moving-bed reactor. Similar equations have been published in the literature [45, 75]. The boundary condition for this equation is:

$$\boldsymbol{T_g = T_{gi} \ @ \ Z = 0}$$

where:

H_A = the enthalpy of component A (J/mol);

h = heat-transfer coefficient between the gas and solid mixtures (W/m^2.K);

S_m = surface area per volume of heat transfer related to solid particle (m^{-1});

T_g = the temperature of the gaseous mixture (K);

T_s = the temperature of the solid mixture (K); and

$Cp_{\bar{A}}$ = average heat capacity of component A over the reactor temperature range (J/mol.K).

Energy balance in the solid phase:

For the solid phase, Eq. (5.22) can be applied. Since the assumptions made in section 5.2.1 are applicable for both phases, Eq. (5.25) is derived as follows:

$$\sum_{A=1}^{n} H_{As}\frac{dF_{As}}{dZ} + \sum_{A=1}^{n} F_{As}\frac{dH_{As}}{dZ} \pm Q + hAS_m\left(T_g - T_s\right)\Delta Z = 0$$

For this case, the enthalpies and the flow rate represent the components for the solids denoted by the subscripts. In addition, here $\frac{dF_{As}}{dZ} \neq 0$, because the reaction is taking place in the solid phase. Thus substituting for this term with Eq. (5.24) resolves to:

$$\sum_{A=1}^{n} H_{As}(-r_A A) + \sum_{A=1}^{n} F_A\frac{dH_A}{dZ} \pm Q + hAS_m\left(T_g - T_s\right)\Delta Z = 0 \qquad (5.25)$$

From chemical reaction engineering principles, $r_A = \upsilon_A r_L$ [60], therefore, $\sum_{A=1}^{n} H_{As}\upsilon_{As}(-r_L)A$ or $\sum_{A=1}^{n} \Delta H_{rxi}(-r_L)A$. Substitution of these terms and representation of the second term as a function of the temperature of the solid mixture similar to Eq.(5.24) into Eq. (5.25) leads to:

$$\sum_{A=1}^{n} \Delta H_{rxA}(-r_L)A + \sum_{A=1}^{n} F_{As}Cp_{\overline{As}}\frac{dT_s}{dZ} \pm Q + hAS_m\left(T_g - T_s\right) = 0 \qquad (5.26)$$

For the solid phase, no heat will be supplied from the surroundings or removed to it. Therefore, the final form for the solid energy balance will be:

$$\frac{dT_s}{dZ} = \frac{hAS_m(T_s - T_g) + \sum_{A=1}^{n} \Delta H_{rxi}(-r_L)A}{\sum_{As=1}^{n} F_{As} Cp_{\overline{As}}} \tag{5.27}$$

where:

υ_{As} = stoichiometric coefficient of component A as the solid phase;

$(-r_L)$ = reaction rate for the limiting reactant in reaction *i* (mol/time.vol);

ΔH_{rxi} = heat of reaction *i* taking place in the solid phase (J/mol); and

T_s = temperature of the solid mixture throughout the reactor length (K).

The boundary condition for Eq. (5.27) is represented as:

$$\boldsymbol{T_s = T_{si} \ @ \ Z = L}$$

5.2.3 Solution methods for equations

The moving-bed reactor model is comprised of n number of ordinary differential equations (ODEs) that represent the mass balance of each component in the reactor. Moreover, two ODEs each demonstrate the energy balance for the gas and solid phases. In addition, the model involves algebraic equations that contain variables that depend on either temperature or mass. These algebraic equations are listed in Table 5.7.

Polymath is a user-friendly software program which is often used to solve ODEs. It has been utilised in some engineering texts such as Chemical reaction engineering by Scott Fogler [75]. For this reason, it was employed to solve this model using the boundary conditions mentioned for the mass and energy balance ODEs.

Important note here for polymath should be mentioned about the boundary conditions. Polymath's nature is to solve the ODE system from *Z=0* to *Z=L* where *L* must be specified. The reactor is counter-current, so the solids are fed to the reactor at $Z = L$ and discharged at $Z = 0$. However, its unable to insert the conditions of the solids at $Z= L$ as mentioned above. Therefore, the discharged conditions for solids at *Z = 0* from Aspen Plus simulator were inserted, the model was iterated until the solids inlet parameters from the Aspen Plus model required, such as conversion and temperature were approximately achieved.

Table 5.7: Summary of all equations involved in the moving-bed reactor model

Parameter	**Status**	**Equation**	**Source**
F_A	Variable	$\frac{dF_A}{dZ} = -r_A A \rho_s$	Derived
T_g	Variable	$\boldsymbol{\frac{dT_g}{dZ} = \frac{hAS_m(T_s - T_g) \pm Q}{\sum_{A=1}^{n} F_A Cp_{\overline{A}}}}$	Derived
T_s	Variable	$\boldsymbol{\frac{dT_s}{dZ} = \frac{hAS_m(T_s - T_g) + \sum_{A=1}^{n} \Delta H_{rxi}(-r_L)A}{\sum_{As=1}^{n} F_{As} Cp_{\overline{As}}}}$	Derived
ρ_{sm}	Constant	$\rho_{sm} = \frac{x_p \rho_b}{M_{wt}}$	[45]
S_m	Constant	$S_m = \frac{\rho_b}{V_P \rho_P} A_P$	[45]
ρ_b	Constant	$\rho_b = 2200\ {}^{kg}/_{m^3}$	[45]
V_P	Constant	$V_P = \frac{1}{6} \pi {d_P}^3$	[75]
ρ_P	Constant	$\rho_P = 4000\ {}^{kg}/_{m^3}$	[45]
A_P	Constant	$A_P = \pi {d_P}^2$	[99]
d_P	Constant	75 µm	[42]
h	Variable	$h = \frac{\left(\frac{1}{3}\right) Re^{1/3} k_g}{d_P}$	[99]
Re	Variable	$Re = \frac{\rho_g u_g d_P}{\mu_g}$	[75]
ΔH_{rxi}	Variable	$\Delta H_{rxi} = \sum_{A=1}^{n} \upsilon_A H_A +$ $\sum_{A=1}^{n} \upsilon_A \overline{Cp}_A \cdot (T_s - T_R)$	[75]
T_R	Constant	298 K	Assumption
$\overline{Cp}_A$	Variable	Depend on the component	Aspen Plus

C_A	Variable	$C_A = \frac{F_A}{\dot{v}}$	[75]
$\dot{v}$	Variable	$\dot{v} = \frac{F_T R T_g}{P}$	[75]
P	Constant	1.2 bar	Aspen Plus
F_T	Variable	$\sum_{A=1}^{n} F_A$	[75]
K_e	Variable	$K_e = exp\left(\frac{\Delta G}{R T_s}\right)$	[79]
ΔG	Variable	$\Delta G = \sum_{A=1}^{n} v_A G_A$	[79]
Q	Constant	Depend on the reactor	Aspen Plus

5.3 Profiles for the ICLWS process reactors

5.3.1 Fuel reactor

Based on the moving-bed reactor model derived in section 5.2 and for the fuel reactor conditions listed in Table 5.8, the flow profiles for the reactants and products are expressed through Figures 5.2 and 5.3. In addition, the conversion rates and temperatures for both the gas and solid phases through the reactor length were determined and are represented in Figures 5.4 and 5.5.

Table 5.8: Operating parameters used for reducer model in ICLWS process

Parameter	**Value**
Temperature of the gas fed to the fuel reactor	873 K
Molar flow of the gas fed to the fuel reactor	1126 mol/s
Temperature of the solid fed to the fuel reactor	1278.3 K
Molar flow of the haematite fed to the fuel reactor	3671.7 mol/s
Fuel reactor pressure	1.2 bar
Amount of heat load supplied to the fuel reactor	103 MW

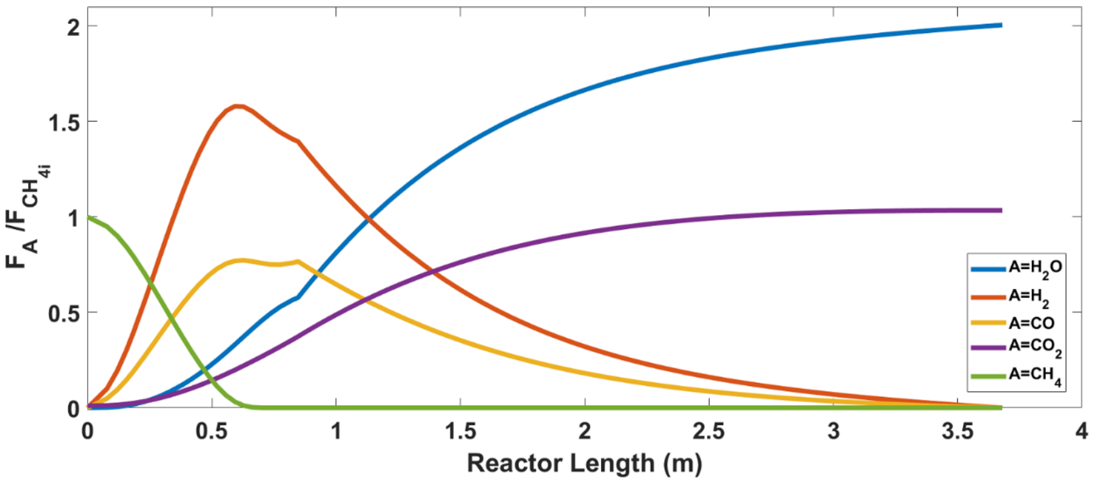

Figure 5.2: Gas flow profiles through the fuel reactor

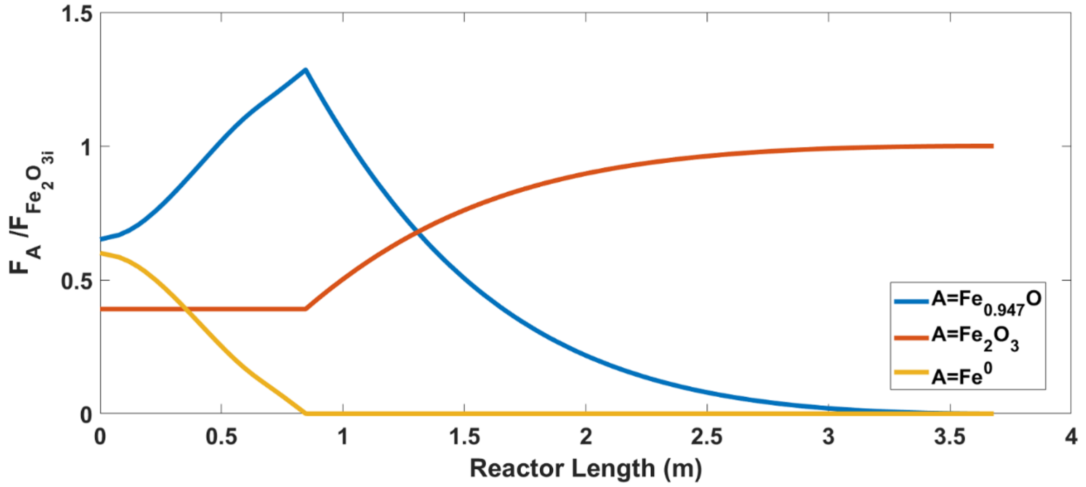

Figure 5.3: Solids flow profiles through the fuel reactor

For the gas-flow profiles shown in Figure 5.2, the molar flows for the gaseous reactants and products were normalised based on the inlet flow rate of the methane feed. It can be observed that the methane is completely converted to syngas at 0.8 m distance from the bottom of the fuel reactor. Through this reactor zone, reactions 5.1 to 5.3 take place, converting the methane to syngas. Also, metallic iron Fe^0 is formed from the reduction of wustite $Fe_{0.947}O$ in this region, as indicated by reactions (5.1) to (5.3) and shown in Figure 5.3.

In addition, the conversion of syngas to carbon dioxide and steam follows a linear behaviour in the region between 0.6m and 0.8 m of the reactor length. This is attributed to the reduced amount of methane present in this region. Reactions 5.2 and 5.3, which govern the generation of carbon dioxide and steam through use of the $Fe_{0.947}O$ oxygen carrier, depend on reaction 5.1, which governs the reaction of methane with the $Fe_{0.947}O$ oxygen carrier. Therefore, generation of CO_2 and steam is reduced as the quantity of methane falls. Also, side reactions 5.7 to 5.9, by which carbon dioxide and steam are consumed to generate syngas, take place in this region. Therefore, the consumption of syngas is slower in this region comparable with the rest of the reactor.

In addition, the hematite Fe_2O_3 in this zone, represented in Figure 5.3, is stripped out and fed to the air reactor to enhance heat recovery, as mentioned earlier in Chapter 3. For $L >$ 0.8 m, metallic iron is not present in the solid phase. Therefore, it can be deduced that reactions 5.5 and 5.6 take over at distances more than 0.8 m along the reactor length, since all the methane has been consumed before this zone. As a consequence, the syngas is fully combusted to a mixture of CO_2 and steam at the top of the fuel reactor as indicated in Figure 5.2. In contrast, Fe_2O_3 at L =3.8 begin to reduce to $Fe_{0.947}O$ until it is completely reduced at L = 0.8 m.

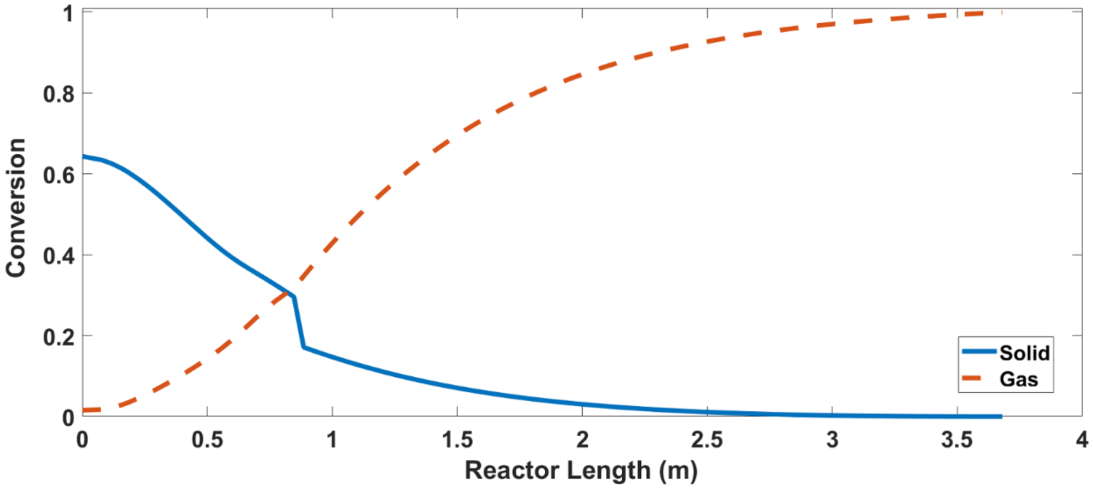

Figure 5.4: Conversion profile through the fuel reactor

The conversion profile for the fuel reactor is represented by Figure 5.4. It can be seen that for $L<$ 2 m, the gas conversion increases rapidly. It then increases linearly until a complete conversion is achieved at the top of the fuel reactor, where all the natural gas is converted to a mixture of CO_2 and steam. Solid conversion becomes zero through the reactor length, i.e. Fe_2O_3 is the only oxygen carrier present from the top of the fuel reactor to a point where L= 3 m. As we move downward from this point, wustite generation increases and the solid conversion increases gradually until L=0.8 m, where metallic iron begins to form as mentioned earlier. From this point downwards, the solid conversion increases steeply to achieve 64% at the bottom of the fuel reactor.

The temperature profile through the reactor is shown in Figure 5.5. From the fuel reactor bottom to a distance 0.8 m upward, it is observed that the gas temperature increases steeply to reach 1300 K. However, the temperature of the solid particles drops significantly due to the endothermic reaction 5.1, which takes place in this region of the reactor. The temperature of the solids is maintained at 924K through the supply of excess heat from the other reactors in the process. For the same reason, the gas temperature increases in this zone.

Moving upward through the reactor until L = 2 m, the gases and solids reach an approximate thermal equilibrium. Their temperature increases by 30 K since the exothermic reactions 5.5 and 5.6 occur in this region. After this region, the temperature remains constant. For $2 < L < 3.7$ m, the temperature decreases slightly by 55 K because of the endothermic reaction 5.4, which occurs there.

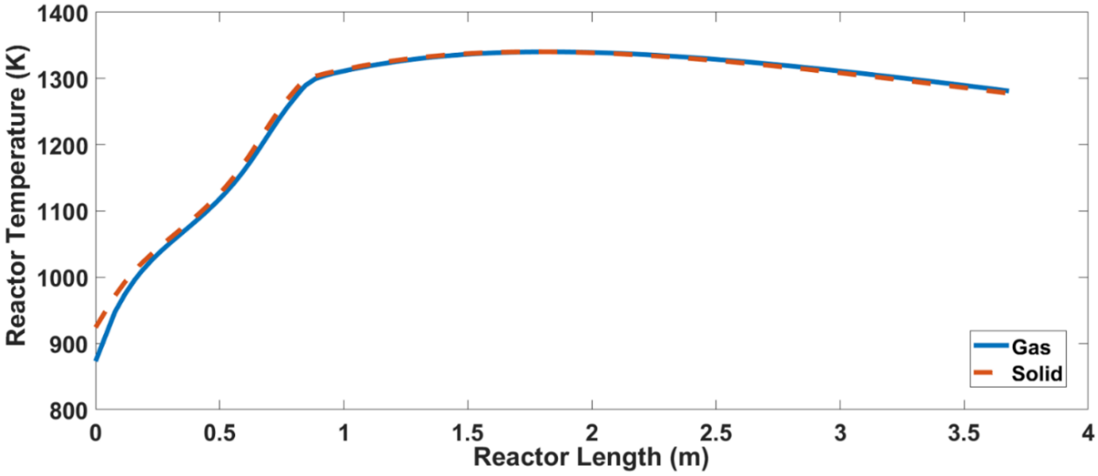

Figure 5.5: Temperature profile through the fuel reactor

5.3.2 Oxidiser profiles

The conversion and temperature profiles for the oxidiser are expressed through Figures 5.6 and 5.7 for the conditions listed in Table 5.9.

The gas conversion increases extremley rapidly through the first 3 m from the start of the oxidiser. At this point conversion reaches 0.53, which corresponds to 80% of the outlet gas conversion. Moving upward, the gas conversion increases linearly until it reaches 90% of the outlet conversion at L = 4.3 m. After this point, reactions 5.10 and 5.11, which govern the conversion of steam to hydrogen through use of wustite and metallic iron, are approximately at equilibrium, therefore the gas conversion increases gradually to the target outlet conversion i.e. 0.65 at L = 9.45 m.

For the solids conversion, the top of the reactor contains Fe^0 and wustite with conversion of 0.65. As the solids move downward, conversion decreases slightly due to the equilibrium limitation achieved for reaction 5.11 as Fe^0 is converted to $Fe_{0.947}O$. This is in the region 9.45 > L > 4.3 m. Below this point, the solids conversion reduces dramatically as the wustite is oxidised to magnetite until it is oxidised completely at the bottom of the reactor.

Table 5.9: Operating parameters used for the oxidiser model in the ICLWS process

Parameter	Value
Temperature of the gas fed to the oxidiser	780 K
Temperature of the solids fed to the oxidiser	1093 K
Molar flow of the steam fed to the oxidiser	5422 mol/s
Molar flow of the solids fed to the oxidiser	4599 mol/s
Excess heat from the oxidiser to the surroundings	43.7 MW
Oxidiser pressure	1.2 bar

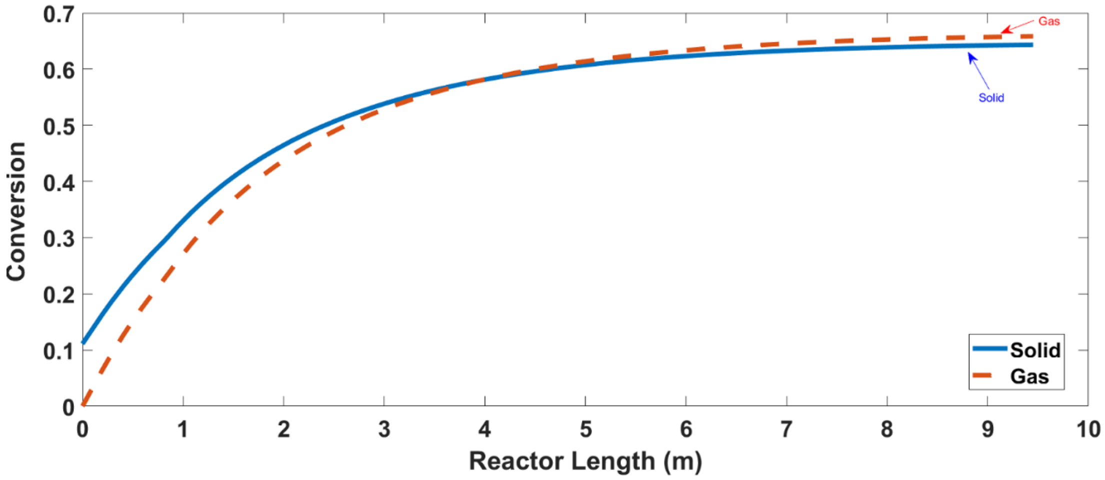

Figure 5.6: Conversion profile of the oxidiser

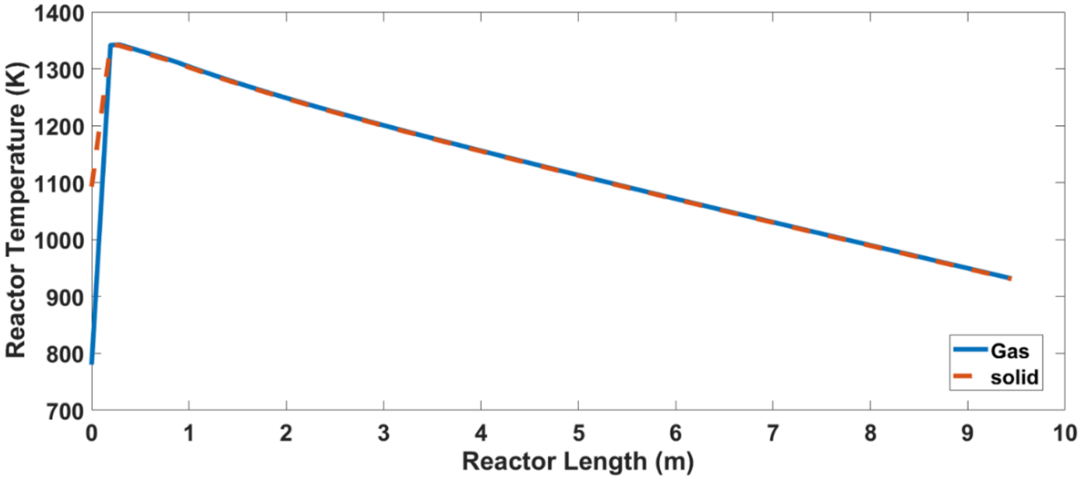

Figure 5.7: Temperature profile of the oxidiser

To explain the temperature profile, the gas temperature increases steeply over the first half metre above the bottom of the oxidiser as a result of the exothermic reaction 5.11, which converts steam and Fe^0 to hydrogen and $Fe_{0.947}O$, occurs in this region. Therefore, heat is transferred from the solids to the gas. Furthermore, both phases reach thermal equilibrium at this point. Above this point, the temperature of both phases decreases linearly as the excess heat from the slightly exothermic reactions 5.10 and 5.11 is extracted to the environment, since both reactions favour low temperature to overcome the equilibrium limitations.

5.3.3 Air reactor profiles

The conversion and temperature profiles for both the gas and solid phases are represented in Figures 5.8 and 5.9 for the air-reactor conditions listed in Table 5.10.

Table 5.10: Operating parameters used for the air-reactor model in the ICLWS process

Parameter	Value
Temperature of the gas fed to the air reactor	780 K
Temperature of the solids fed to the air reactor	1093 K
Molar flow of the steam fed to the air reactor	5422 mol/s
Molar flow of the solids fed to the air reactor	4599 mol/s
Excess heat from the oxidiser to the surroundings	43.7 MW
Air reactor pressure	1.2 bar

The gas conversion increases exponentially as the gas is elevated in the air reactor. This behaviour is expected due to the activation energy value of the kinetic expression of reaction 5.12. On the other hand, the solids conversion starts at 10.1%, which corresponds to magnetite mixture with hematite split from fuel reactor to aid the heat recoverey as mentioned in chapter 3. It decreases significantly in this zone to attain 0% at the bottom of the reactor. This conversion corresponds to pure hematite. From $L = 2$ m to the top of the reactor the incremental rate of the gas conversion is slower until the outlet gas conversion of 96% is achieved. Also, the solid conversion rate is slow in this region since most of the oxygen is consumed at the bottom region of the reactor ($L < 1$ m) to oxidise the magnetite to hematite.

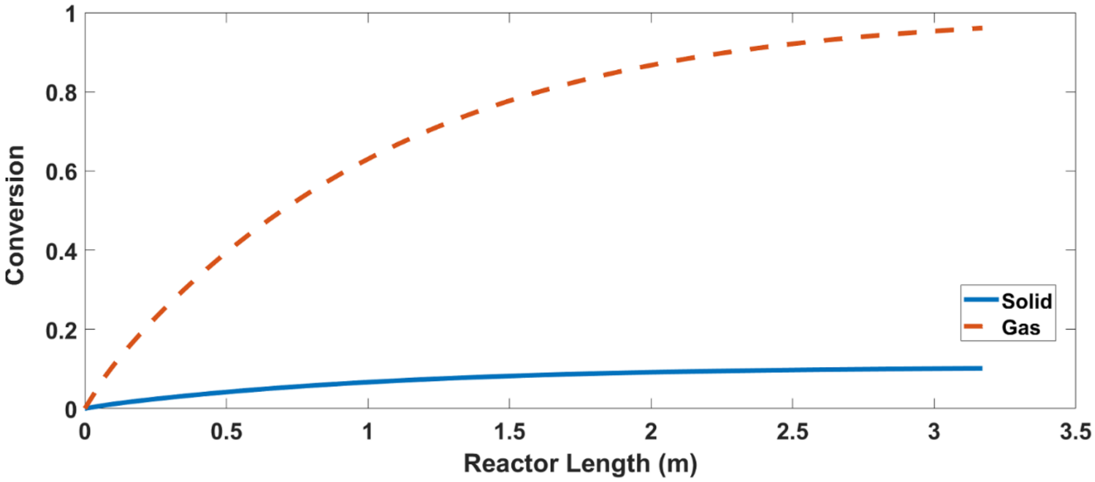

Figure 5.8: Conversion profile for the air reactor

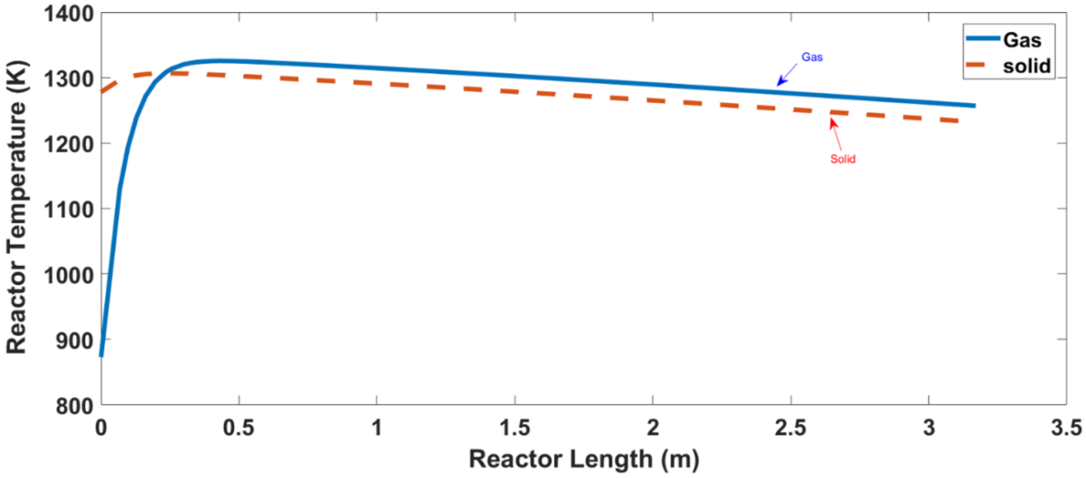

Figure 5.9: Temperature profile for the air reactor

The temperature profile shows that the gas temperature increases steeply between 0 m and 0.5 m, since reaction 5.13, which governs the conversion of Fe_3O_4 to Fe_2O_3 is highly exothermic and the temperature difference between the gas and the solid is great. Ascending upward from this point, the temperature difference between both phases is relatively smaller. Since reaction 5.13 is highly exothermic, controlling the temperature by removing the excess heat is necessary. Thus beyond this point, the heat removed from the reactor is slightly higher than the generated via reaction 5.13. Consequently, the temperature of both phases decreases at a constant rate at achieve 1256 K and 1232 K for gas and solid phases, respectively.

5.4 Profiles for CLWSFe process reactors

5.4.1 Reducer-1 profiles

The flow profiles for gas and solid for reducer-1 are illustrated in Figures 5.10 and 5.11. Aslo, conversion and temperature profiles are illustrated in Figures 5.12 and 5.13. The operating parameters ised for reducer-1 model are summaries in Table 5.11

Table 5.11: Operating parameters used for the reducer-1 model in the CLWSFe process

Parameter	Value
Temperature of the gas fed to reducer-1	873 K
Temperature of the solids fed to reducer-1	1412 K
Molar flow of the natural gas fed to reducer-1	1855 mol/s
Molar flow of the circulating solids fed to reducer-1	1725 mol/s
heat required for reducer-1 from the surroundings	65 MW
Reducer-1 pressure	1.2 bar

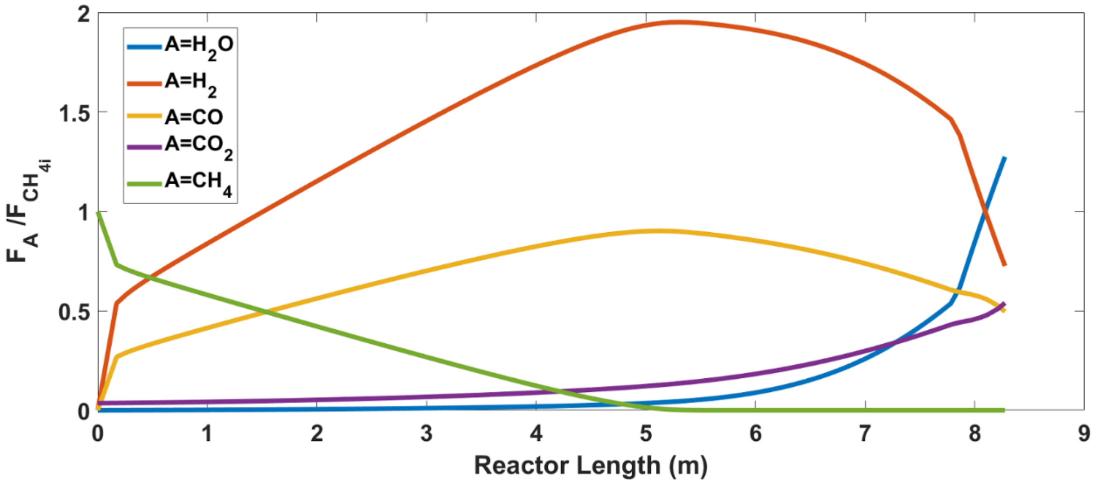

Figure 5.10: Flow profile for gaseous components in reducer-1 of CLWSFe process

Similarly to ICLWS process, the flow profiles for the gaseous component were normalised based on the inlet flow of methane. As observed by Figure 5.10, methane decreases linearly at the reactors bottom until it is completely converted to CO and H_2 via reaction 5.1 at $L = 5.2$ m.

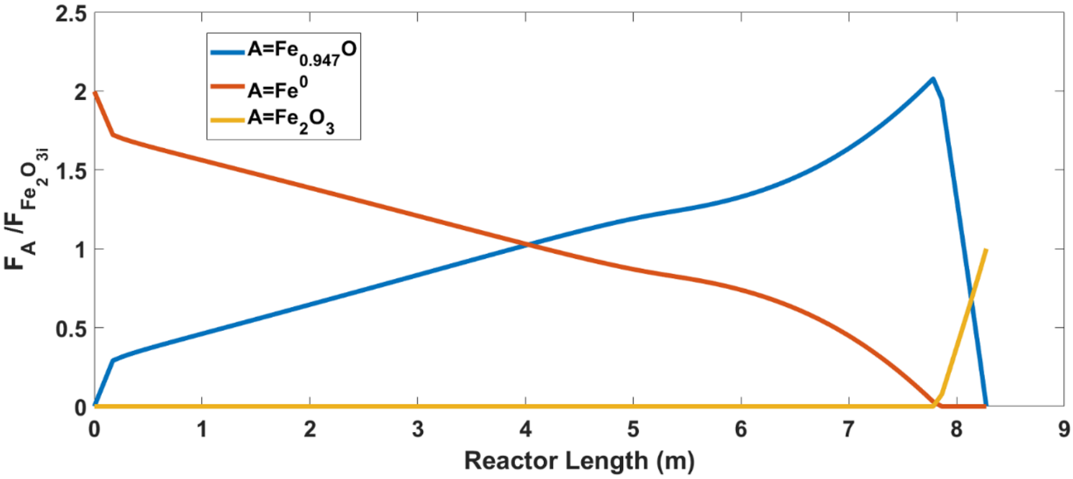

Figure 5.11: Flow profiles for the solids components in the reducer-1 of CLWSFe process

In addition, iron flow rate is increased gradually until all of the $Fe_{0.947}O$ is reduced to pure iron at the reactor bottom (Figure 5.11). The rate here is slower than the case for the ICLWS process as can be seen from the activation energy and frequency factor values. Also, at this zone, H_2 and CO are continuously increasing up to the point where they reach their maximum flow at $L = 5.2$ m. For $5 < L < 7.8$ m, reaction (5.2-5.3) takes place at a faster rate than reaction (5.1) leading to a significant decrease in both CO and H_2. Meanwhile, CO_2 and steam increases at a much higher rate compared with $L< 5$m. For the solids, metallic iron will form at $L = 7.8$ m. moving downward from this point, countinuous reduction of $Fe_{0.947}O$ to iron occurs, leading to a rapid growth in Fe^0 flow rate. From $L = 7.8$ m to the reactor top, reactions (5.14-5.17) are carried out at a much higher rate than reactions (5.2-5.3) as mentioned in Table 5.6. As a result, the rate of CO and H_2 conversion to CO_2 and H_2O, respectively is increased significantly causing a steep increase in both carbon dioxide and steam flow rate. In addition, hematite is reduced until it is fully converted to $Fe_{0.947}O$ at $L = 7.8$ m.

As mentioned above, the conversion rate of CO and H_2 to CO_2 and H_2O is very slow for $L < 5.2$ m, leading to an approximately constant gas conversion in this region (Figure 5.12).

In contrast, the solid conversion gradually increases until complete conversion is achieved at the bottom of reducer-1 where $Fe_{0.947}O$ is fully converted to Fe^0 . For $5.2 < L < 7.7$ m , CO_2 and H_2O are generated at a higher rate, as illustrated before via reactions (5.2-5.3). As a result, an exponential growth in gas conversions occurs in this region. However, the solid conversion decreases as the rate of wustite formation via reactions (5.2-5.3) increases. For $L = 7.8$ to the top of reducer-1, reactions (5.14-5.17) were carried out at fast rate leading to a steep increase in both gas conversion. In contrast, the solid conversion decreases to achieve zero at the top of the reactor as all the wustite is converted to hematite.

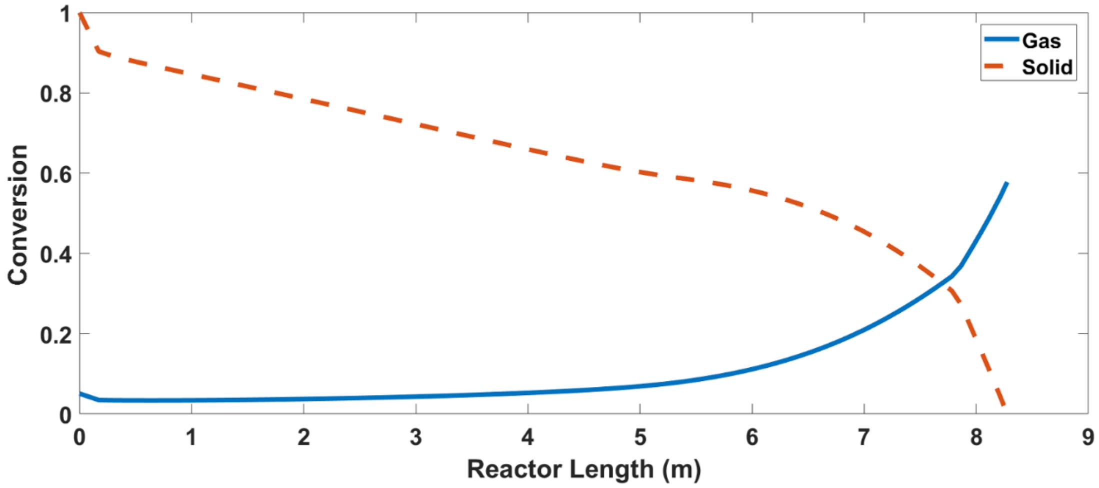

Figure 5.12: Conversion profile for reducer-1 in the CLWSFe process

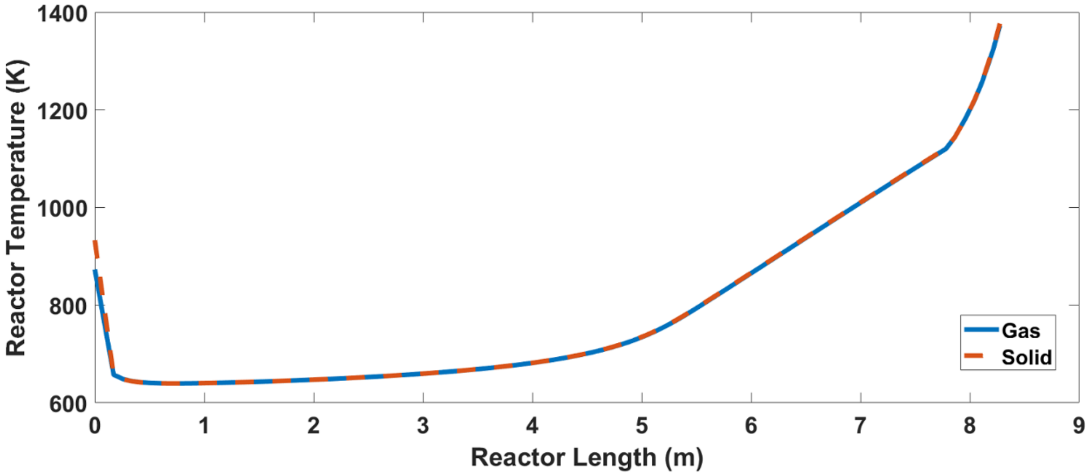

Figure 5.13: Temperature profile for reducer-1 in the CLWSFe profile

The temperatures in both gas and solid phases decrease significantly and reaches a thermal equilibrium for $L < 0.78$ m as a result of the endothermic reaction 5.1, which takes place there (Figure 5.13). For $0.78 < L < 3$ m the temperature in both phases remained constant. For L between 3 m to 5 m as the exothermic reactions (5.2-5.3) were carried out, the temperature in both phases increases. For $5 < L < 7.7$ m, rapid rate of reactions (5.2-5.3) are obtained causing the temperature in both phases to grow exponentially. From $L = 7.8$ m upward reactions (5.14-5.17) occur, with a much higher rate compared with the ones occurring downward leading to a steep increase in the temperature for both phases until they reach 1372 K at the reactor top.

5.4.2 Reducer-2 profiles

The conversion and temperature profiles for reducer-2 are illustrated in Figures 5.14 and 5.15. The operating parameters used for the reducer-2 model are listed in Table 5.12.

Table 5.12: Operating parameters used for reducer-2 model in CLWSFe process

Parameter	**Value**
Temperature of the gas fed to reducer-2	1245 K
Temperature of the solids fed to reducer-2	1331 K
Molar flow of the syngas fed to reducer-2	5616 mol/s
Molar flow of the circulating solids fed to reducer-2	3534 mol/s
Make-up solids fed to reducer-2	186 mol/s
Excess heat from reducer-2 to the surroundings	0 MW
Reducer-2 pressure	1.2 bar

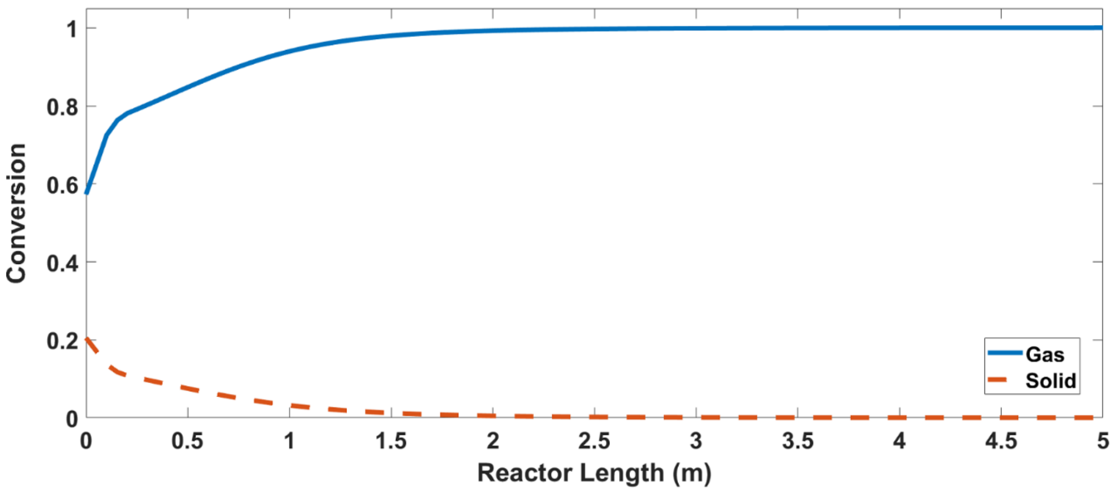

Figure 5.14: Reducer-2 conversion profile

The gas conversion shown in Figure 5.14 experiences a rapid increase for $0 < L < 0.12$ m. This is due to the generation of wustite in this region as represented by reactions 5.16 and 5.17. Since both reactions are endothermic and the solids have elevated temperatures in this reactor zone, as shown by Figure 5.15, high values for the rates of reactions 5.16 and 5.17 are recorded. As a result, the temperature drops significantly to a minimum value of 1085 K at $L = 0.2$ m (Figure 5.15).

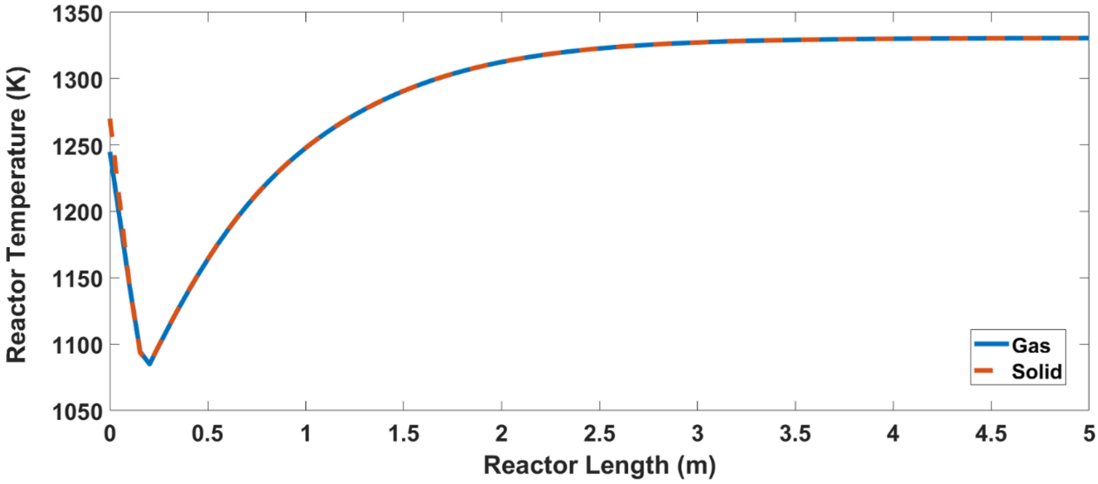

Figure 5.15: Reducer-2 temperature profile

As shown by the stoichiometry of reactions 5.16 and 5.17, 1 mole of magnetite results in the generation of 0.84 moles of carbon dioxide and steam. However, the same amount of moles of Fe_2O_3, when reacted, yields ⅓ mole each of CO_2 and H_2O as represented by reactions 5.14 and 5.15. As a consequence, the gas conversion increases more steeply at the reactor bottom as opposed to in this area *i.e* 1.5 < *L* < 0.2 m . From this point onward (*L* >1.5 m), the gas conversion increases gradually until complete gas conversion is attained at the top of the reducer-2. The temperature of both phases increases rapidly as a result of the exothermic nature of reaction 5.15 to achieve 1330 K at the top of the reactor.

The solids conversion remains approximately zero from the top of the reactor to a point 3.5 m downward where large-scale generation of magnetite begins. At 1.5 < *L* < 0.1 m the solids conversion increases as more magnetite is produced in this region. At *L* = 0.1 m, the hematite is fully replaced. From *L* = 0.1 m downward, wustite production commences as the conversion increases from 0.11 (pure magnetite) to 0.21 at the reactor bottom.

5.4.3 Oxidiser profiles

The conversion and temperature profiles for both gas and solids in the oxidiser of the CLSWFe process are shown in Figures 5.16 and 5.17 for the oxidiser conditions listed in Table 5.13.

Table 5.13: Operating conditions for the oxidiser in the CLWSFe process

Parameter	**Value**
Temperature of the gas fed to the oxidiser	773 K
Temperature of the solids fed to the oxidiser	973 K
Molar flow of the steam fed to the oxidiser	5458 mol/s
Molar flow of the circulating solids fed to the oxidiser	2996 mol/s
Excess heat from oxidiser to the surroundings	3.2 MW
Oxidiser operating pressure	1.2 bar
Oxidiser diameter	2.8 m

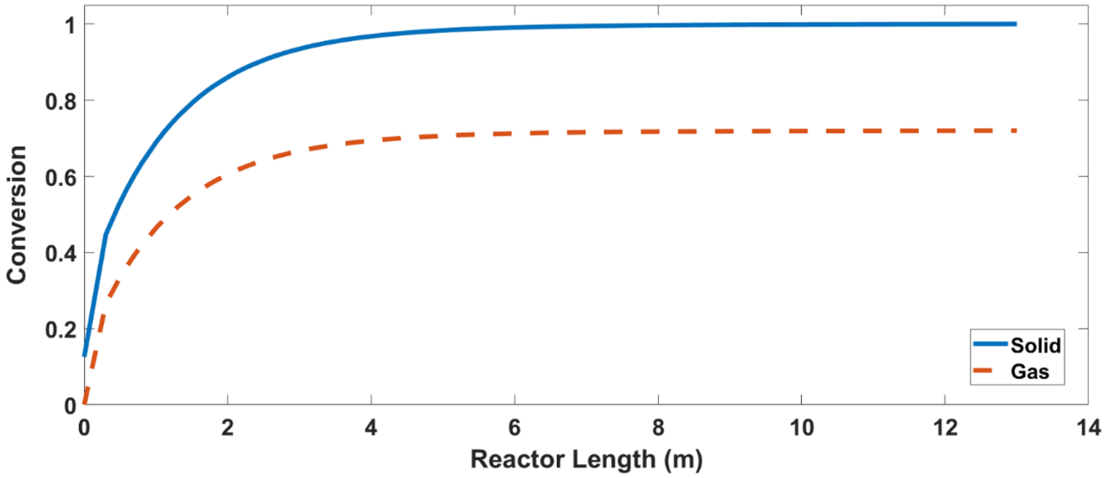

Figure 5.16: Conversion profile for the oxidiser in the CLWSFe process

Gas conversion increases exponentially from the bottom of the oxidiser to a point 4 m upward. The reason of this behaviour is the fast kinetics of reactions 5.10 and 5.11 that take place in the oxidiser. Reaction 5.10 occurs in the region $L< 0.2$ m, while reaction 5.11 is carried out in the rest of the oxidiser. For $L > 4$ m, it can be seen in Figure 5.16 that the gas conversion increases by only 2% due to the equilibrium limitation of reaction 5.11 to attain the final 72% conversion at the top of the reactor. The solid conversion is 100% at the top of the oxidiser, since metallic iron is the only form of oxygen carrier fed to the oxidiser.

Moving downward, the solid conversion changes gradually, as the generation of wustite is insignificant due to the equilibrium limitation that governs reaction 5.11 in this region of the oxidiser, as mentioned earlier. From $L = 4$ m downward, the mass production of wustite commences and the solid conversion decreases rapidly. For $0 < L < 0.2$ m, magnetite begins to form, resulting in a linear decrease of the solid conversion to achieve 12.5% at the bottom of the oxidiser.

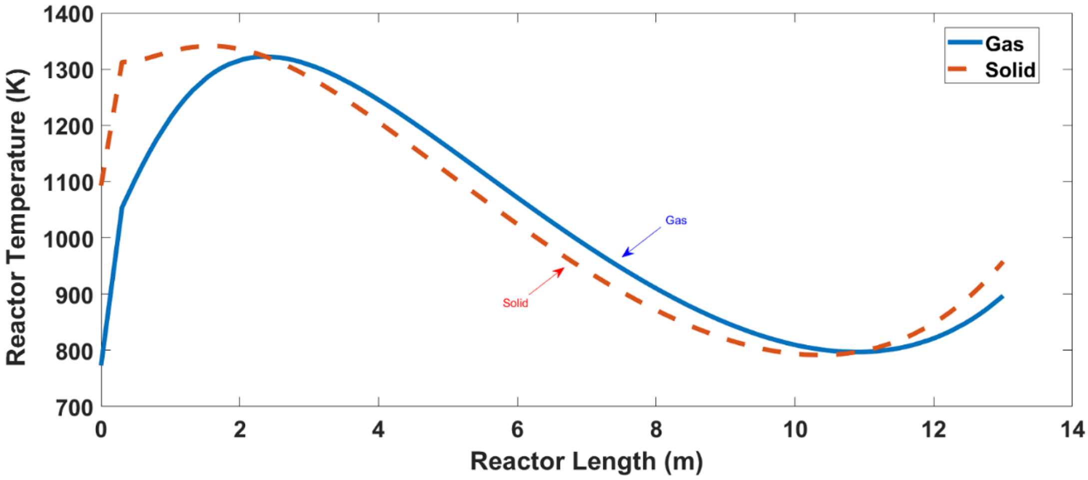

Figure 5.17: Temperature profile for the oxidiser in the CLWSFe process

The gas temperature profile represented by Figure 5.17 shows an increase in temperature for $0 < L < 3$ m. Although the excess heat from the oxidiser is exhausted to the surroundings, the gas temperature continues to rise due to the strong heat generation caused by the exothermic reactions 5.10 and 5.11 that occur at elevated solids temperatures in this region. From $L = 3$ m to $L = 11.5$ m, the gas temperature exhibits a curvature decrease as the reactions approximate to equilibrium. Therefore, the rate of reaction 5.11 and its associated heat decreases. As a consequence, the heat removed from the reactor approaches the level of heat generated. For $11.5 < L < 13$ m, the temperatures of the gas and solids start to rise again as the amount of wustite, which has high heat capacity, becomes insignificant. Thus, the heat liberated from reaction 5.11 is greater than the heat removed to the surroundings.

The temperature profile of the solids exhibits similar behaviour to that of the gas at the bottom of the reactor, where both increase steeply. However, the temperature of the solids begins to drop at $L = 2$ m, as the heat generated from reaction 5.11 is transferred to the gas. The temperature then decreases in the same manner as that of the gas until $L = 11.5$ m. After that, it rises again, as the amount of wustite present in the oxidiser becomes negligible compared with the amount of metallic iron. More heat is created within the reactor than is exhausted to the surroundings.

5.4.4 Air reactor profiles

Finally, the conversion and temperature profiles for both gas and solid phases in the air reactor were obtained and are illustrated in Figures 5.18 and 5.19 for the conditions listed in Table 5.14.

Table 5.14: Operating conditions for the air reactor in the CLWSFe process

Parameter	**Value**
Temperature of the gas fed to the air reactor	890 K
Temperature of the solids fed to the air reactor	1413 K
Molar flow of the steam fed to the air reactor	7082 mol/s
Molar flow of the circulating solids fed to the air reactor	6381 mol/s
Excess heat from air reactor to the surroundings	25 MW
Air reactor operating pressure	1.2 bar
Air reactor diameter	1.5 m

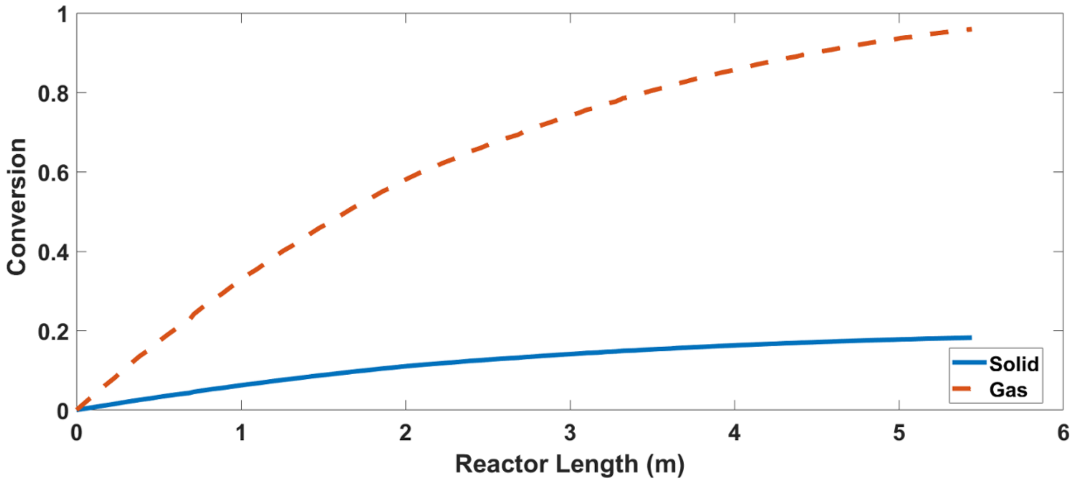

Figure 5.18: Conversion profile for the air reactor in the CLWSFe process

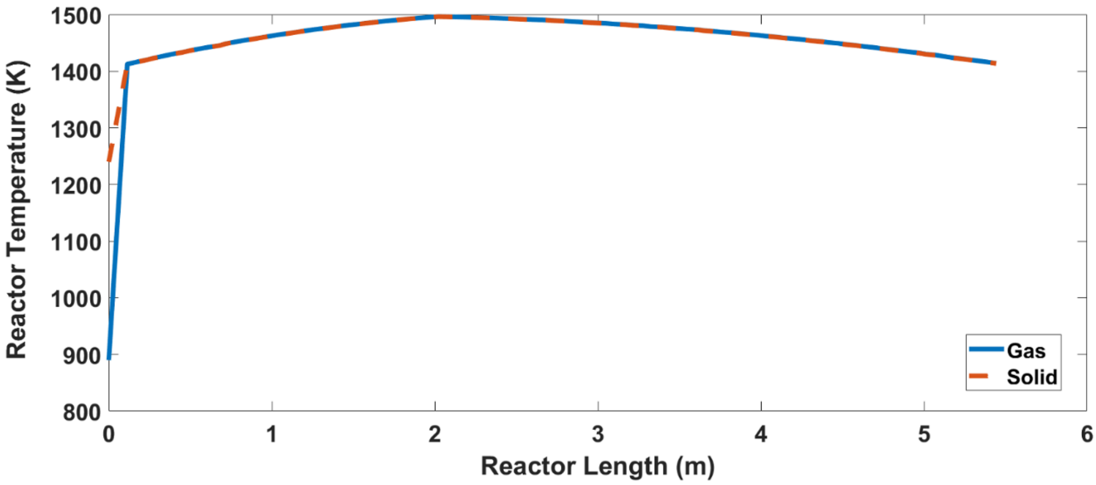

Figure 5.19: Temperature profile for the air reactor in the CLWSFe process

The gas conversion increases steadily over the length of the air reactor from the bottom to $L = 2$ m, as shown in Figure 5.18. In this zone, reaction 5.13 takes place to oxidise the magnetite to hematite by oxygen. Therefore, the solids conversion in this region drops from 0.11 to zero at the air reactor bottom. For $2 < L < 5$ m, oxygen is consumed, thus the gas conversion increases to 96% at the reactor top. This means that 96% of the oxygen in the air is used to regenerate the oxygen carrier feed. In this zone, reaction 5.12 takes place, converting the wustite in the solid-feed mixture to pure magnetite at $L = 2$ m. Consequently, the solids conversion decreases from 12.8% at the top of the reactor to 11% at $L = 2$ m.

Both the gas and the solids temperatures increase steeply at the bottom of the air reactor as a result of highly exothermic reaction 5.13, which occurs over the length of the reactor from the bottom to $L = 2$ m. They both reach thermal equilibrium approximately 0.1m above the reactor bottom. Above that height, the temperature of both phases continues to rise gradually to attain a peak temperature of 1485 K at $L = 2$ m. This temperature is very high and in reality a proper heat recovery system should be installed for this reactor to recover the excess heat to the reducer-1 reactor. The gas and solids temperature falls from there to the reactor top, despite the exothermic reaction 5.12 that takes place in this region. The reason for this is the slower reaction rate that occurs in this zone compared with the rate of reaction 5.13, which is predominant below 2m in the reactor. Therefore, the heat liberated from the exothermic reaction 5.12 is lower than the heat exhausted to the surroundings.

5.5 Comparision of the obtained profiles with Aspen Plus results

The conversions and the temperatures of the discharged gas obtained from this model were compared with ones determined from the Aspen plus simulation developed for ICLWS and CLWSFe processes in chapters 3 and 4 , respectively. For solids, we will compare the conversion and the temperature of the solids fed to the reactors since these are the values obtained from the model as mentioned earlier in section 5.2.3. The differences in the parameters mentioned above are summaried through Tables 5.15-5.17 for the ICLWS reactors. Tables 5.18-5.21 represent the differences in the conversion and temperature values for the discharged gas and the solid feed between Aspen plus results and the model for CLWSFe reactors.

The values from Tables 5.15-5.21 showed a good agreement between the simulation and the polymath with the largest error of 4.8% obtained in the temperature of the solid fed to reducer-2. All the percentage errors calculated either for conversion or temperature for both gas and solid phases in all the reactors modelled were less than 5%.

Table 5.15: Comparison for the conversions and temperatures between Aspen simulation and polymath model for fuel reactor in ICLWS process

Parameter	X_{gf}(%)	X_{si} (%)	$T_{gf}(K)$	T_{si} (K)
Polymath model	99.9	0.0	1281.2	1277.5
Aspen Plus model	100.0	0.0	1278.0	1288
Error %	0.06	0.0	0.25	0.82

Table 5.16: Comparison for the conversions and temperatures between Aspen simulation and polymath model for oxidiser in ICLWS process

Parameter	X_{gf}(%)	X_{si} (%)	$T_{gf}(K)$	T_{si} (K)
Polymath model	65.8	64.3	931.5	930.7
Aspen Plus model	65.6	64.9	933.0	924
Error %	0.37	0.87	0.16	0.72

Table 5.17: Comparison for the conversions and temperatures between Aspen simulation and polymath model for air reactor in ICLWS process

Parameter	X_{gf} **(%)**	X_{si} **(%)**	$T_{gf}(K)$	T_{si} **(K)**
Polymath model	96.0	10.1	1244.6	1185
Aspen Plus model	97.5	10.3	1288.0	1190
Error %	1.5	1.5	3.5	0.42

Table 5.18: Comparison for the conversions and temperatures between Aspen simulation and polymath model for reducer-1 in CLWSFe process

Parameter	X_{gf} **(%)**	X_{si} **(%)**	$T_{gf}(K)$	T_{si} **(K)**
Polymath model	0.572	1.0	1304.0	1374.0
Aspen Plus model	0.572	1.0	1245.0	1412.0
Error %	0.0	0.0	4.7	2.7

Table 5.19: Comparison for the conversions and temperatures between Aspen simulation and polymath model for reducer-2 in CLWSFe process

Parameter	X_{gf} **(%)**	X_{si} **(%)**	$T_{gf}(K)$	T_{si} **(K)**
Polymath model	100.0	0.0	1341.6	1341.7
Aspen Plus model	100.0	0.0	1407.0	1410.0
Error %	0.0	0.0	4.3	4.8

Table 5.20: Comparison for the conversions and temperatures between Aspen simulation and polymath model for oxidiser in CLWSFe process

Parameter	X_{gf} **(%)**	X_{si} **(%)**	$T_{gf}(K)$	T_{si} **(K)**
Polymath model	72.0	99.9	897.0	957.9
Aspen Plus model	72.0	100.0	933.0	933.0
Error %	0.0	0.01	3.8	2.7

Table 5.21:Comparison for the conversions and temperatures between Aspen simulation and polymath model for air reactor in ICLWS process

Parameter	X_{gf} **(%)**	X_{si} **(%)**	$T_{gf}(K)$	T_{si} **(K)**
Polymath model	95.9	18.2	1413	1413
Aspen Plus model	96.2	18.4	1433	1435
Error %	0.3	1.1	1.3	1.5

5.5 Concluding remarks

A steady-state one-dimensional mathematical model was derived for all the moving-bed reactors involved in the ICLWS and CLWSFe processes, the development of which was described in Chapters 3 and 4, respectively. The aim of the development of the model was to determine the conversion and temperature profiles through each reactor for each process. Also, both rates of conversion and temperatures for the gases and solids fed into and discharged from the reactor were compared with those obtained from the Aspen Plus simulator to verify the model, since no model has been reported in the literature that used the same fuel and conditions, nor is there published experimental data with which our model can be validated. The model developed for this study showed good agreement with the Aspen model. The greatest error of 4.8 percentage points was observed in the temperature of the solids discharged from the second reducer in the CLWSFe process. The errors in gas and solid conversions and temperatures were less than 5 percentage points for the rest of the reactors modelled.

Chapter 6 : Economic assessments of the developed chemical looping processes and their comparison with steam methane reforming

To determine the viability of the chemical looping processes described in the previous chapters, the processes must be assessed economically. The assessment methodology is defined in the first section of this chapter. In the next three sections, this methodology is applied to determine the total investment, operating and hydrogen production costs which are considered to be the essential parameters in our economic study. These parameters are calculated for the integrated chemical looping water splitting (ICLWS), chemical looping with iron co-production (CLWSFe) and the steam methane reforming (SMR) processes explained in Chapters 3 and 4. A comparison of the results obtained from this study with those published in the literature were included as well. The last section summarises the chapter findings.

6.1 Economic evaluation methodology for processes

Hydrogen production cost is the essential parameter used to evaluate the feasibility of any hydrogen production process. In order to determine this parameter, the total investment cost and the operating cost of the process should be calculated beforehand.

The "Lang method" is an approach that is intended to gather the total investment cost, or capital expenditure (CAPEX), of a chemical plant. It was employed in this research to deduce the total investment cost of the developed chemical looping process as well as of the steam methane reforming process. The Lang method relies on knowledge of the purchased cost of the equipment involved in the process to obtain the total investment cost. The total cost of purchases is multiplied by a factor which accounts for installation, instrumentation, labour to fit the equipment, and many others, as listed in Table 6.1. Finally, the total investment cost is escalated to current (2018) prices using the chemical engineering plant index factor mentioned in Eq. (6.2).

Table 6.1: Important factors used to calculate the total investment cost

Cost type	% equipment delivered cost
Direct costs (equipment installation, instrumentation, piping, electrical system, buildings, labour and service facilities)	302
Indirect costs (engineering supervision, construction, legal expenses, contractor's fee, contingency)	126
Working capital (15% of the total capital investment)	75
Total capital investment	503

To determine the purchased cost of the equipment required for the processes, the specific size of each piece of equipment must be known. Volume is the major parameter required to find the purchased cost of a reactor, towers i.e. absorber/stripper and a flush drum. However, for the heat exchanger and fired heaters, the heat transfer area is the parameter required for the cost calculation. For boilers, the parameters required to calculate their costs are either the heat required to generate the steam or the capacity of the equipment based on the quantity of steam to be generated. For pressure-change equipment, i.e. compressors, turbines and pumps, figures for the amount of work required or generated are needed to obtain their costs. In addition, 60% value has been added on the purchased cost for the unconventional equipment used in both ICLWS and CLWSFe processes developed and mentioned in chapters 3&4. Table 6.2 reviews the main parameters needed for the determination of the details of each piece of equipment involved in the process and the methods used to obtain the data.

Table 6.2: Methods used to calculate purchased costs for each piece of equipment required in the developed processes

Equipment	Parameter	Method to obtain the main parameter	Reference
Reactor	Volume	Reactor sizing based on mass and energy balance aided by the reaction kinetics (Chapter 5 discusses the sizing of each reactor in the developed process)	[45, 75]
Towers	Volume	Aspen Plus simulation	-
Flash drum	Volume	Vessel sizing based on the gas-liquid densities and terminal velocity	[99]
Heat exchanger	Heat transfer area	Aspen Plus simulation	-
Fired heater	Heat load	Aspen Plus simulation	-
Boilers	Amount of steam generated	Aspen Plus simulation	-
Compressors	Work consumed	Aspen Plus simulation	-
Pumps	Work consumed	Aspen Plus simulation	-
Turbines	Work delivered	Aspen Plus simulation	-

Once these methods had been decided, equations to calculate embedded purchased costs taken from the Couper et al. and Garrett references [100, 101] were utilised, and the total investment cost was multiplied by the chemical engineering cost index to adjust the figures to a 2018 basis to take into account inflation since 2007, which was the date on which most of the equipment purchased cost was based [102].

Calculations of the operating cost (OPEX) require knowledge of the time-dependent costs. The price of raw materials, which comprise the fuel, the oxygen carrier required for chemical looping, and the solvent make-up for SMR, are essential for the OPEX calculation. The oxygen carrier make-up cost was based on the Abad and Adanez equation [65]. In addition, the cost of utilities such as power usage to cool water and heat steam must be included in the calculation. The prices for the raw materials and the utilities along with other parameters required for the OPEX calculation are listed in Table 6.4 for the SMR process, Table 6.7 for ICLWS process and Table 6.11 for CLWSFe process.

The next step performed to obtain the hydrogen production cost is the calculation of the annual value of the total investment cost, based on the project's lifetime and the annual interest rate, by applying the following equation:

$$A_c = CAPEX \times (1+i)^n \left[\frac{i}{(1+i)^n - 1}\right] \qquad (6.1)$$

In this equation:

A_c = annual value of the total investment cost of the plant (US$/yr);

$CAPEX$ = total investment cost of the plant (US$);

$$= Total\ purchased\ cost\ of\ equipment\ \times total\ capital\ investment\ factor\ \times plant\ cost\ index \qquad (6.2)$$

i = interest rate (%); and

n = project lifetime (years).

This equation (6.2) takes into account the present value of the CAPEX payment as well as the interest payment. Finally, the hydrogen production cost is calculated using Eq. (6.3) as follows:

$$P_C = \frac{A + OPEX}{\dot{m}_{H_2 y}} \qquad (6.3)$$

In this equation:

P_C = production cost of hydrogen product (US$/kg);

$OPEX$ = operating cost of the plant (US$/yr); and

$\dot{m}_{H_2 y}$ = annual production rate of the hydrogen product (ton/yr).

6.2 Economic evaluation of the steam methane reforming process

Following the methodology presented in section 6.1, the economics of the SMR process developed in Chapter 3 were determined. This process offered the benchmark against which the viabilities of the chemical looping processes (ICLWS and CLWSFe) developed in Chapters 3 and 4, respectively, were investigated. The purchased costs of the units contained in the SMR process are listed in Table 6.3, while Tables 6.4 and 6.5 show the operating parameters used to calculate the OPEX and the calculations of OPEX for the SMR process.

Table 6.3: Purchase cost of the equipment used in the SMR process

Equipment	Purchased cost (US$, M)
Reformer	16.5
Shift reactors	4.0
Heat exchangers	14.1
Condensers	4.8
Coolers	2.2
Vapour-liquid separation vessels	2.4
Heat recovery steam generation units	39.5
Air compressor	1.1
CO_2 compressors	19.6
MDEA absorber	4.1
MDEA stripper	3.3
MEA absorber	1.7
MEA stripper	1.3
PSA unit	11.9
Pumps	0.17
Initial catalyst load	1.0
Initial adsorbent load	0.26
Total	128.3

Table 6.4: Operating parameters used to calculate OPEX for SMR process

Parameter	Value	Reference
Electricity	US$0.07 /kWh	[103]
Cooling water	US$1.03 /$m^3$	[104]
Fuel (natural gas)	US$0.13 /kg	[78]
$NiAl_2O_4$ catalyst	US$17.90 /kg	[12]
Zeolite 5A	US$1.65 /kg	[105]
MDEA solvent	US$8.70 /gal	[12]
MEA solvent	US$0.52 /kg	[105]

Table 6.5: Operating cost parameter calculations for SMR

Operating cost parameters	Total consumption	Cost ($/year, M)
Electricity	-28.8 MW	15.9
Cooling water	140 Mm^3/yr	138.5
Fuel	0.74 Mt/yr	122.1
$NiAl_2O_4$ catalyst make-up	125.1 t/yr	2.2
Zeolite 5A make-up	86.6 t/yr	0.14
MDEA solvent make-up	0.21 Mgal/yr	4.1
MEA solvent make-up	1.56 kg/yr	4.7
Total		287.6

The CAPEX, OPEX, total annual cost and the hydrogen production cost for the developed SMR process with and without CCS were compared with values obtained from the literature [12]. To ensure clarity of the comparison, the developed and simulated SMR process is referred to as SMR1, whereas the literature process is called SMR_r.

In Table 6.6, differences can be noted between the economic parameters shown for the simulated SMR process SMR1 and the values obtained from the literature denoted as SMR_r. The total investment cost for the process developed in this study was 4.8 percentage points lower than the cost obtained from the literature. In contrast, the operating cost for the simulated SMR was 9.3 percentage points higher than that reported for the reference process [12]. These values led to a 4.9 percentage point difference between the H_2 production cost according to the simulated process SMR1 and the cost according to the reference process SMR_r. Note that the fuel prices for the reference process SMR_r were adjusted to 2018 prices. Moreover, the total investment cost was modified to 2018 prices by multiplying it by the Chemical Engineering Plant Cost Index (CEPCI) for 2018. These differences in the economic evaluation are attributed to the different methodology followed for the determination of the economic parameters. The reference process was based on real plant data, whereas our simulated process was evaluated economically using the methodology mentioned in section 6.1.

Table 6.6: Summary of the economic evaluation of the SMR process

Parameter	**Developed model (SMR1)**	**Developed (SMR1) without CCS**	**SMR_r [12]**
Total investment cost (M$)	749.0	656.8	786.6
Total operating cost (M$/yr)	265.4	257.2	242.8
Hydrogen produced (Mt/yr)	0.20	0.20	0.20
Interest rate (%)	10	10	10
Plant lifetime (yr)	25	25	25
Total annual cost (M$)	347.9	329.6	329.5
H_2 production cost ($/kg H_2)	1.71	1.62	1.63

6.3 Economic evaluation of the ICLWS process

Techno-economic assessments of the chemical looping processes were conducted, first for the ICLWS process, the development of which was described in Chapter 3. The methodology illustrated above was applied to the ICLWS as with SMR to determine the CAPEX, OPEX and P_C for the ICLWS process. The results are summarised in Tables 6.7 to 6.10. To investigate the feasibility of the method, these values were compared with those obtained for the SMR process in section 6.2.

The results indicate that the calculated production cost of hydrogen ($/kg) for the simulated SMR process is 17.5% higher using $MgAl_2O_4$ as support material to the oxygen carrier (a) and 5.3% higher using ZrO_2 as support material (b) than the production cost via the ICLWS process. In addition, it is 12.9% lower for ICLWS (a) compared with the modern SMR_m process. However, the difference in hydrogen production cost is negligible between ICLWS (b) and modern SMR_m/ATR [18, 80]. Also, the hydrogen production cost for the ICLWS process is 16.1% (a) and 3.6% (b) lower than the cost of the TRCLR process [49].

The capacity of the ICLWS plant developed in this study is 3.5 and 2.9 times that of the TRCLR and modern SMR_m/ATR methods, respectively. Hence, the rates of fuel consumption and of water generated are greater in this process. Consequently, the amount of cooling water used in the condenser is greater. In addition, the equipment is larger and the labour requirement is greater. All these factors lead to larger operating and capital costs compared with those of the TRCLR and SMR_m/ATR processes. To compare the CAPEX and the OPEX for the ICLWS process with these processes, they linearly scaled up to the similar capacity of the ICLWS process. Considering the data collected for the SMR_m/ATR and the TRCLR processes are for one train in a hydrogen production plant. scaling up results in a CAPEX equivalent to 440.6 – 1152.2 US$,M for the modern SMR/ATR and 628.2 US$,M for TRCLR processes. These figures indicate that the CAPEX for ICLWS process is 11.8 – 65.8% lower compared with the scaled up SMR_m/ATR process. Also, it is 37.3% lower compared with the TRCLR process. The OPEX is 263.4 – 297.1 US$,M/yr and for 317.6 for the scaled up SMR_m/ATR and TRCLR processes, respectively. Therefore, the OPEX for ICLWS (a) process is 6.4 – 17% and 22.4% lower compared with SMR_m/ATR and TRCLR, respectively. As a result, the ICLWS process has a lower hydrogen production cost per unit mass. Note that the CAPEX and the OPEX values for the SMR_m/ATR actual plant with similar capacity as the simulated ICLWS process is lower.

Table 6.7: Operating parameters assumed in this study

Parameter	**Value**	**Reference**
Fuel (natural gas)	US$0.17 /kg	[78]
Iron oxide	US$0.072 /kg	[106]
$MgAl_2O_4$	US$0.63 /kg	[106]
ZrO_2	US$4.68 /kg	[106]
Iron oxide makeup percentage required	1%/15h	[50]
Power consumption of Iron oxide manufacturing	22 kWh/t	[106]
Plant operating time in a year	328 days	[12]
Electricity (selling price)	US$0.07 /kWh	[103]
Cooling water	US$1.03 /$m^3$	[104]

Table 6.8: Operating cost parameter calculations

Operating cost parameters	**Total consumption**	**Cost (US$/year, M)**
Electricity	-29.5 MW	-16.4
Cooling water	130 Mm^3/yr	136.3
Fuel	0.64 Mt/yr	105.9
Iron oxide and support make-up ($MgAl_2O_4$)	0.022 Mt/yr	23.1
Iron oxide and support make-up (ZrO_2)	0.02 Mt/yr	65.3
Total ($MgAl_2O_4$)		246.5
Total (ZrO_2)		289.0

Ignoring the cost of CO_2 capture, the SMR operating cost is 4.2% higher than that of the ICLWS process with oxygen carrier (a), whereas it is 12.3% lower than that of the ICLWS using oxygen carrier (b). However, when CO_2 capture is considered, the ICLWS process with its inherent CO_2 capture functionality becomes the cheaper option at a capital cost that is 47.4% lower than that of SMR with CO_2 capture. The hydrogen production cost ($/kg) for the ICLWS (a) process with the $MgAl_2O_4$-Fe_2O_3 oxygen carrier is therefore the lowest cost option.

Table 6.9: The list of equipment unit prices as estimated in this work

Equipment	Purchase price (US$, M)
Reducer	0.512
Oxidiser	1.952
Air reactor	0.544
Heat exchangers	1.04
HRSGs	14.5
Fired heater (E-6)	1.77
Indirect solid-gas heater (E-5)	1.152
LP + IP + HP turbines	11.46
CO_2 compressors	8.01
H_2 compressors	7.63
Coolers	0.24
Separation vessels	12.34
Water preheater	3.84
Surface condenser	2.52
Pump	0.014
Total	**67.52**

Table 6.10: Total investment cost, annualised operating cost and first-year cost calculations

Parameter	**ICLWS (a)**	**ICLWS (b)**	**SMR_m/ATR (one train)**	**SMR1**	**TRCLR (one train)**
Total investment cost (US$, M)	394.0	394.0	154.2-430.3	749.0	174.5
Total operating cost (US$/yr, M)	246.5	289.0	92.2-104	265.4	87.5
Hydrogen produced (Mt/yr)	0.20	0.20	0.07	0.20	0.055
Interest rate (%)	10	10	10	10	N/A
Plant lifetime (yr)	25	25	25	25	30
Total annual cost (US$, M)	287.2	329.7	123.6-148.4	347.9	92.4
H_2 production cost (US$/kg H_2)	1.42	1.62	1.63-2.0	1.71	1.68

- ICLWS (a) = ICLWS process with $MgAl_2O_4$ support material
- ICLWS (b) = ICLWS process with ZrO_2 support material

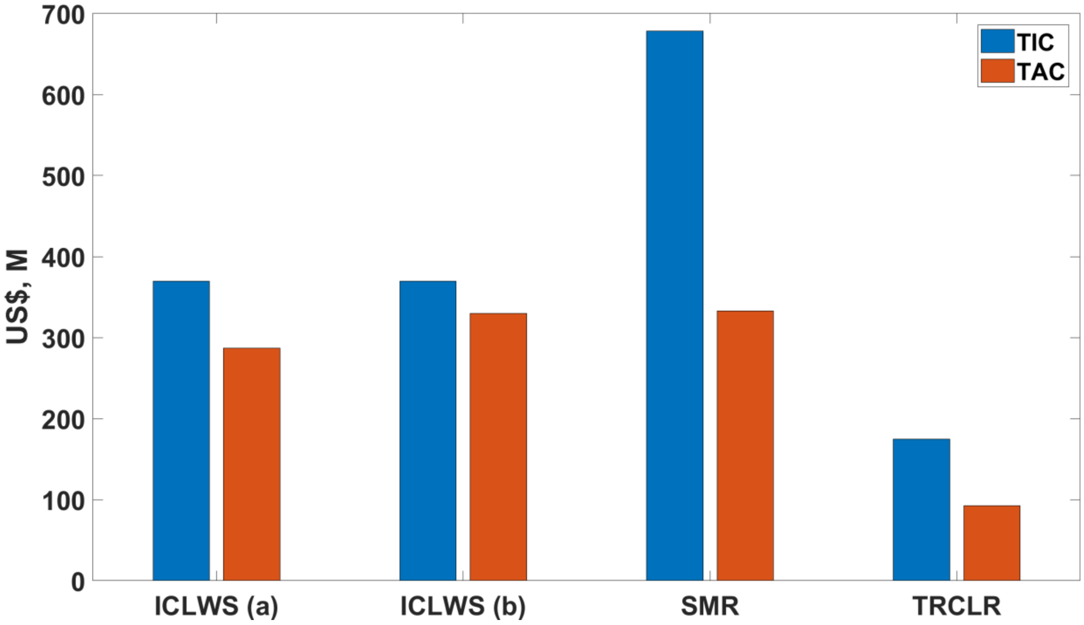

Figure 6.1: Comparison between the SMR1, ICLWS and TRCLR processes by total investment cost (TIC) and annualised operating cost (TAC)

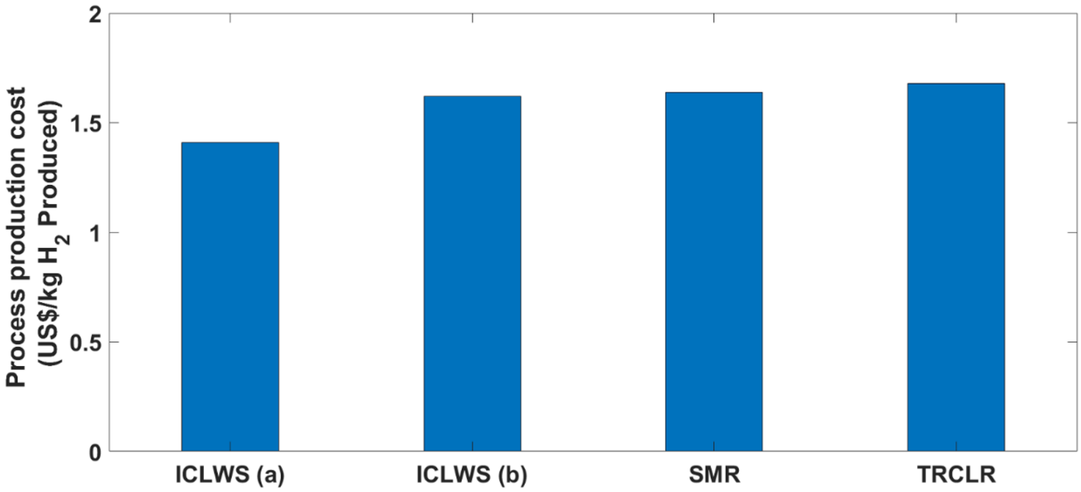

Figure 6.2: Comparison between the SMR, ICLWS and TRCLR processes hydrogen production cost

6.4 Economic evaluation of the CLWSFe process

The CLWSFe process was evaluated following the methodology presented in section 6.1. All the results are listed in Tables 6.11 to 6.14.

Table 6.11: Operating parameters assumed in this study

Parameter	Value	Reference
Fuel (natural gas)	US$0.17 /kg	[47]
Iron oxide	US$0.07 /kg	[48]
Iron selling price	US$0.3 /kg	[48]
Iron oxide make-up percentage required	7 %/15 h	[15]
Power consumption of iron oxide manufacturing	22 kWh/t	[48]
Plant operating time in a year	328 days	[28]
Electricity (selling price)	US$0.07 /kWh	[51]
Cooling water	US$1.03 /m^3	[52]

Table 6.12: Operating cost parameter calculations

Operating cost parameter	Total consumption	Cost (US$/year, M)
Electricity	-88.7 MW	-43.6
Cooling water	1.4×10^8 m^3/year	146.3
Fuel	9.0×10^5 ton/year	147.7
Iron oxide make-up	1.2×10^5 ton/year	141.8
	Total	435.8

Table 6.13: List of equipment unit prices assumed in this work

Equipment	Purchase price (US$, M)
Reducer-1	0.51
Reducer-2	0.52
Oxidiser	7.80
Air-reactor	0.55
Heat exchangers	3.9
HRSGs	26.7
Gas-solid cooler	0.37
LP + HP turbines	25.0
CO_2 compressors	13.1
H_2 compressors	9.29
Separation vessels	2.41
Surface condensers	1.6
Pumps	0.028
Total	**91.9**

Table 6.14: Total investment cost, annualised operating cost and production calculations

Parameter	**CLWSFe**	**SMR$_m$/ATR**	**SMR1**
Total investment cost (US$, M)	536.4	154.2-430.3	749.0
Total operating cost excluding the effect of selling iron (US$/yr, M)	435.8	92.2-104	265.4
Total operating cost including the effect of selling iron (US$/ yr, M)	222.8	92.2-104	265.4
Hydrogen produced (Mton/yr)	0.22	0.07	0.20
Iron produced (Mton/yr)	0.71	-	-
Interest rate (%)	10	10	10
Plant lifetime (yr)	25	25	25
Total annual cost excluding the effect of selling iron (US$/yr, M)	491.3	123.6-148.4	347.9
Total annual cost including the effect of selling iron (US$/yr, M)	275.1	123.6-148.4	347.9
H_2 production cost excluding the effect of selling iron (US$/kg H_2)	2.2	1.63-2.0	1.71
H_2 production cost including the effect of selling iron (US$/kg H_2)	1.25	1.63-2.0	1.71

As shown in Table 6.14, the total investment cost is 28.4% lower than that for the SMR1 process due to the inherent CO_2 capture and H_2 production that minimise the amount of equipment required. Also, the CAPEX of the CLWSFe process is 27.5% lower than the values reported for the MIDREX process in the literature [81]. The total annual cost of the CLWSFe process, taking into account the effect of production of a saleable DRI co-product, is 20.9% lower than that of the benchmark SMR1 process with CO_2 capture. As with the ICLWS process, the CLWSFe process capacity is 3.1 times that of the modern SMR/ATR processes. Thus, the CAPEX for the scaled up SMR$_m$/ATR process is 478 –

1333.9 US$,M. The lowest CAPEX for the modern SMR/ATR processes included in this study were developed by Wood [80]. The CAPEX for this SMR_m/ATR process is 12.2% lower compared with the CLWSFe process. However, the modern SMR_m/ATR with highest CAPEX developed by IEAGHG is 59.8% higher compared with the CLWSFe process [18]. Regarding the OPEX, the CLWSFe process is 22 – 30.9% lower compared with the SMR_m/ATR including the effect of saleable iron product. In contrast, the SMR_m/ATR OPEX is 35.2 – 52.5% lower compared with the CLWSFe when the effect of saleable iron product is excluded. The H_2 production cost is also 26.9% and 23.3 – 37.5% lower than those of both the conventional and the modern SMR processes, respectively. These values were determined considering the CO_2 capture in the SMR processes and the effect of saleable DRI co-product. This is shown in Figure 6.3. However, Table 6.14 indicates that the H_2 production cost is 28.6% and 10 – 35% higher for the SMR1 and SMR_m processes, respectively, compared with that of the CLWSFe method if the effect of the saleable DRI co-product is ignored.

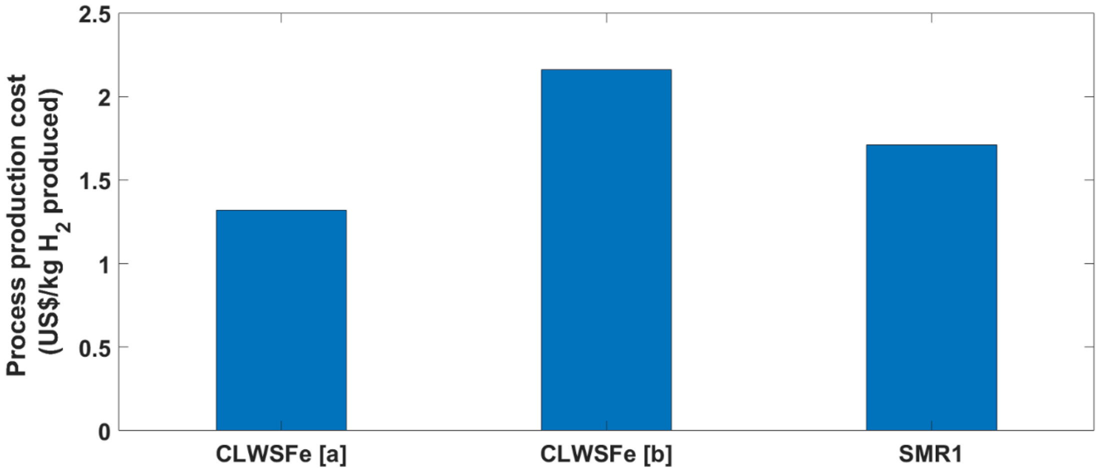

Figure 6.3: H_2 production cost by: CLWSFe [a] (including iron sales), CLWSFe [b] (excluding iron sales) and SMR1 processes

6.5 Concluding remarks

The hydrogen production processes that were described in Chapter 3, i.e. ICLWS and SMR, were economically assessed to calculate their feasibilities. In addition, the economics of the hydrogen plus DRI process CLWSFe, the development of which was described in Chapter 4, were considered. The economic analyses for the SMR process described in Chapter 3 were compared with those for the SMR process reported in the literature. Results showed differences between the economic parameters calculated for the simulated SMR process and those reported in the literature for SMR. Differences were observed in the parameters CAPEX, OPEX and P_c. The CAPEX for the simulated process was found to be 4.8% lower than the values recorded in the literature process. However, the OPEX was 9.3% higher compared with that reported in the literature. These differences led to a 4.9% difference between the production cost of H_2 for the simulated SMR and the analogous value listed in the literature.

The economic analyses of the ICLWS process indicated promising results. The CAPEX was 50.7% lower compared with the CAPEX for the SMR1 process. Regarding the OPEX, the figure calculated for the ICLWS with $MgAl_2O_4$ as oxygen carrier support material (a) was 7.1% lower than that found for the SMR1 process; however, the SMR1 process OPEX was 8.9% lower than that calculated for the ICLWS with ZrO_2 as oxygen carrier support material (b). Both the CAPEX and the OPEX for the modern SMR/ATR processes were significantly lower than those calculated for the ICLWS due to the difference in the capacities of both processes. As a consequence, the hydrogen production cost was 17.5% and 5.3% lower in the ICLWS process with (a) and (b) support materials respectively than the cost for SMR1. Also, it was 12.9 – 29% and 0.6 – 19% lower compared with the costs of modern SMR_m/ATR processes that were reported in the literature.

The CLWSFe economic parameters resulted in a CAPEX value that was 28.4% lower than that of the SMR1. In addition, it was 25.7% lower compared with values for the MIDREX process reported in the literature. The total annual cost was 20.9% lower than that of the conventional SMR1 process when a saleable DRI product was considered. These values led to a 26.9% and 23.3 – 37.5% lower hydrogen production cost for the CLWSFe process compared with that of SMR1 and modern SMR_m/ATR processes. However, if the saleable DRI product was not taken into account, the total annual cost was 41.2% higher compared with SMR1. Also, the hydrogen production cost was 28.6% and 10 – 35% higher for the CLWSFe process compared with the corresponding costs for the SMR1 and SMR_m/ATR processes.

The economic investigation has proved that both ICLWS and CLWSFe processes were able to produce decarbonised hydrogen and steel products at costs compatible with those of the benchmark processes i.e. steam methane reforming and a blast furnace currently used for the production of hydrogen and steel.

Chapter 7 : ***Pumped thermal energy storage integrated with chemical looping technology***

This chapter discusses the synergy between power production through chemical-looping technology and storing it via pumped thermal-energy storage systems (PTES). The first section of the chapter introduces the PTES system and includes details regarding previous work conducted on this technology. The second section explains the development in this project of the energy production and storage cycle, and the integration of the chemical looping water splitting process developed earlier with PTES. The thermodynamic and economic assessments of the energy cycle developed are contained in the third and fourth sections. A novel technique is introduced in the fifth section that uses the hydrogen fuel from the ICLWS process in a gas turbine and integrates it with the energy cycle, the development of which is described previously in this chapter. The last section discusses the viability of this integration and the economic sensitivity analysis performed to determine the conditions required to economically viable the cycle of gas turbine plus ICLWS integrated with PTES.

7.1 Literature review: pumped thermal energy storage systems

Energy demand is growing due to the global rise in population and increased industrialisation [107]. Fossil fuels remain the dominant source of energy globally [108], and this has led to a rapid acceleration in their prices. However, there are many environmental concerns, including global warming, that are related to the usage of fossil fuels. Therefore, regulations have been set by many organisations such as the United Nations Intergovernmental Panel on Climate Change (IPCC) to limit their utilisation worldwide and transfer dependence towards renewable sources [2]. There are many challenges associated with large-scale production of renewable energy, one of which is its dependence on natural power sources such as the sun, wind or water, which are unpredictable and fluctuate. Hence, power output from these sources may not meet power demand. Therefore, integration of energy storage systems (ESSs) with these sources is essential to improve their reliability. In addition, energy storage is necessary to manage the peak demand from the power network. It enables transmission and distribution to operate at full capacity, reducing the need to fit new lines and hence increasing the overall plant efficiency [109, 110]. Several EESs have been proposed such as: pumped hydro storage (PHS), flywheels, super capacitors, batteries and flow batteries, compressed air energy storage (CAES), pumped thermal energy storage (PTES) and hydrogen storage. A comprehensive overview of these technologies has been published in the literature [110]. Moreover, some articles present the role of energy storage with renewable sources of energy in the power grid from an economics point of view [111-113]. Chen et al. reviewed cutting-edge EESs [114]. Table 7.1 summarises these technologies based on energy density, cycle lifetimes, discharge times and costs, while Figure 7.1 shows the maturity of each ESS [114].

According to the published review, PHS leads the EES technologies, while CAES and flow batteries are developing rapidly and may be commercially available soon [110].

Table 7.1: Comparison of technical characteristics of EES systems [114]

Parameter	**PHS**	**CAES**	**ZnBr Batteries**	**Lead-acid batteries**	**PTES**
Power rating (MW)	100-500	5-300	0.05 – 2	0 – 20	0 – 60
Discharge time	1-24 h	1-24 h	s – 10 h	s – h	1 – 24 h
Storage duration	h - m	h – m	h – m	min – d	Min – m
Capital Cost ($/kWh)	5 - 100	2 – 50	150 – 1000	200 – 400	30 – 60
Energy density (Wh/L)	0.5 - 1.5	3 – 6	30 – 60	50 – 80	50 – 500
Lifetime (yr)	40 - 60	20 – 40	5 – 10	5 – 15	5 – 15
Impact on environment	Negative	Negative	Negative	Negative	Positive
Description of the impact	Green land destruction	Hydrocarbon emissions	Toxic remains	Toxic remains	removing contaminates

- h = hours, m = months, min = minutes, d = days

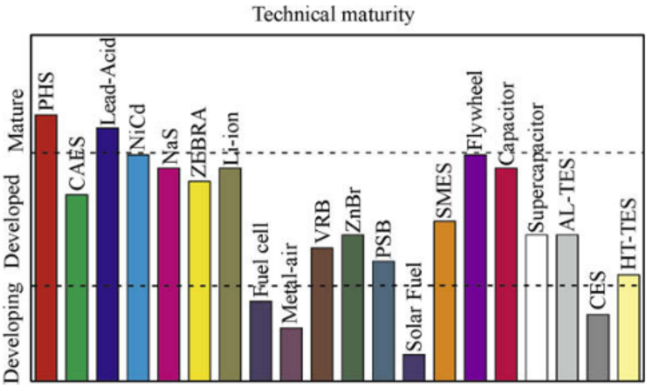

Figure 7.1: Technical maturity of EES systems [114]

Despite these findings, geographical constraints are one of the main challenges and drawbacks for use of PHS, as well as the high capital cost of flow batteries and limited power output of CAES [109, 115]. Therefore, an energy-storage technology with high energy density is necessary, i.e. plant with a small footprint and high power output (long cycle life), in addition to a competitive cost. PTES technology exhibits high energy density resulting in low cost per unit of energy stored [115]. Furthermore, it has no geographical limitations. As a conclusion, it has the potential of rapid development and commercialisation, and could play a crucial role among EES technologies in the near future.

7.2 Pumped thermal energy storage

The pumped thermal energy storage (PTES) technique was first proposed by Weissenbach in 1959 [116]. This technology transforms electric power to thermal energy and stores it as heat in hot and cold storage tanks. An engine cycle retrieves the thermal energy to return it to electrical energy [109]. The basic design comprises two turbomachinery devices i.e. a compressor and an expander, two heat exchangers, two thermal storage tanks and a working fluid (gas) as shown in Figure 7.2 [117]. The PTES operating cycle is summarised as follows [115, 118]:

Charging:

1) The gas is introduced to the compressor driven by electric power $W_{c,ch}$ received from the power grid at initial temperature T_a. As a result, it is compressed and gains heat to reach a maximum temperature of T_H.
2) The gas at temperature T_H is fed to the hot storage tank where it passes through a solid material. Consequently, its thermal energy is transferred to the solid, which is initially at temperature T_a, and stored there.
3) The gas is discharged at temperature T_a and passed to the expander where it expands to generate a power $W_{T,ch}$.
4) The effluent gas from the expander with minimum cold temperature T_c is fed to a cold tank where it gains heat from the solid storage material there. The gas exits at temperature T_a and the cycle resumes.

Discharging

1) The gas at temperature T_a is fed to the hot tank where it passes through the hot storage material. Heat is transferred to the gas and it is discharged at a maximum temperature of T_H.
2) The gas at T_H is introduced to the expander where power $W_{T,d}$ is produced and the gas exits at temperature T_a.

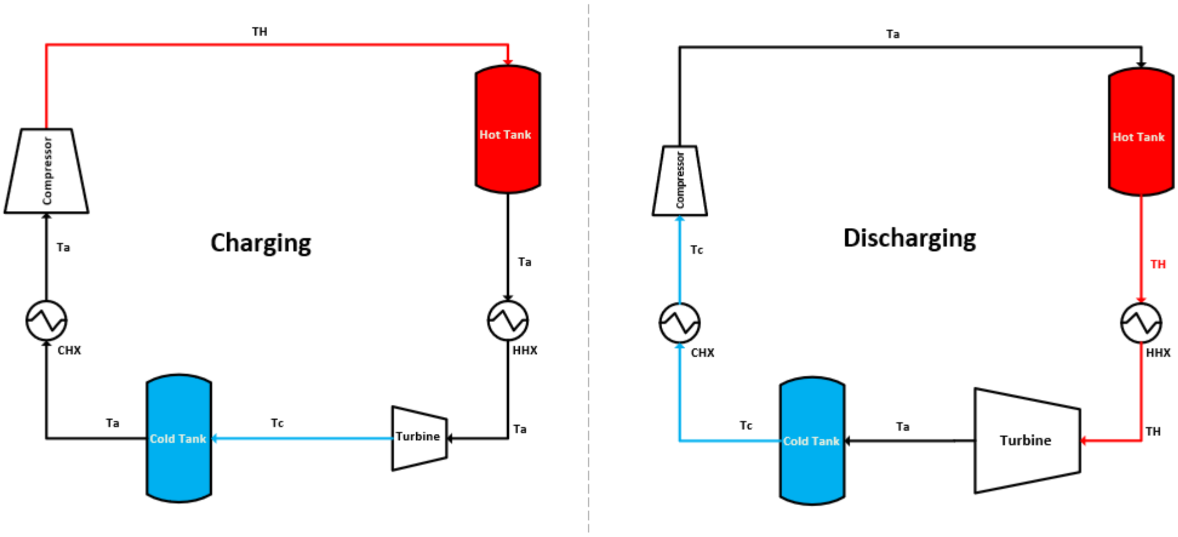

Figure 7.2: Schematic diagram of the PTES system

3) The effluent gas at temperature T_a is fed to the cold tank, where it passes via the cold solid material. The gas temperature drops to T_c at discharge.
4) The discharged gas at temperature T_c is compressed and gains thermal energy to exit at temperature T_a and the cycle continues.

As illustrated above, this system is time dependent. Thermal losses occur in both hot and cold tanks. At the beginning of the charging period, all the solid bed material in the storage tanks is at initial temperature T_i. As the charging progresses, and the hot gas flows through the bed, most of the heat transfer takes place at the upper zone of the tank. This upper zone where most of the heat transfer takes place is called the thermal layer. Consequently, axial temperature profiles for both the gas and the solids are created in the tank in addition to the transient temperature behaviour for both. After a certain time, a thermal equilibrium is reached at the upper part of the tank and heat moves downward. As a result, the gas discharged from the hot tank will have a temperature higher than T_a at the end of the charging time. Therefore, a heat exchanger is installed downstream to maintain the inlet temperature to the expander as T_a. This is considered as a thermal loss from the cycle. Similarly, thermal losses take place in the cold tank during the charging phase. Thus, another heat exchanger is placed between the cold tank and the compressor to raise the temperature of the gas that exits from the cold tank to T_a. Thermal losses also happen during the discharge period, and hence heat exchangers (labelled as HHX and CHX in Figure 7.2) are included in the cycle to maintain the inlet temperatures to the turbomachinery devices at T_H and T_c, respectively. In addition to the thermal losses of the tanks, mechanical losses are experienced in the compressor or turbine and electrical losses occur in the generator that delivers power to the compressor during the charging period. McTigue et al. conducted a study that quantified these losses and their effect on the system efficiency [118].

7.3 Integrating the pumped thermal energy storage system with the chemical looping water splitting process

Comparison of the pumped thermal energy storage cycle (PTES) process shown in Figure 7.2 with the flow diagram of the integrated chemical looping water splitting process shown in Figure 3.6, Chapter 3, indicates possible integration of the two systems. Figure 3.6 shows that the depleted air stream (stream 73) is effluent to the atmosphere. Therefore, this stream can be retrofitted to the PTES system as the working fluid of the cycle. In addition, 15 MW of the power generated from the steam cycle in the ICLWS can be introduced to the PTES cycle to drive the compressor. This produces the integrated cycle named “IPTES”, which can be represented as in Figure 7.3 during the charging and discharging periods.

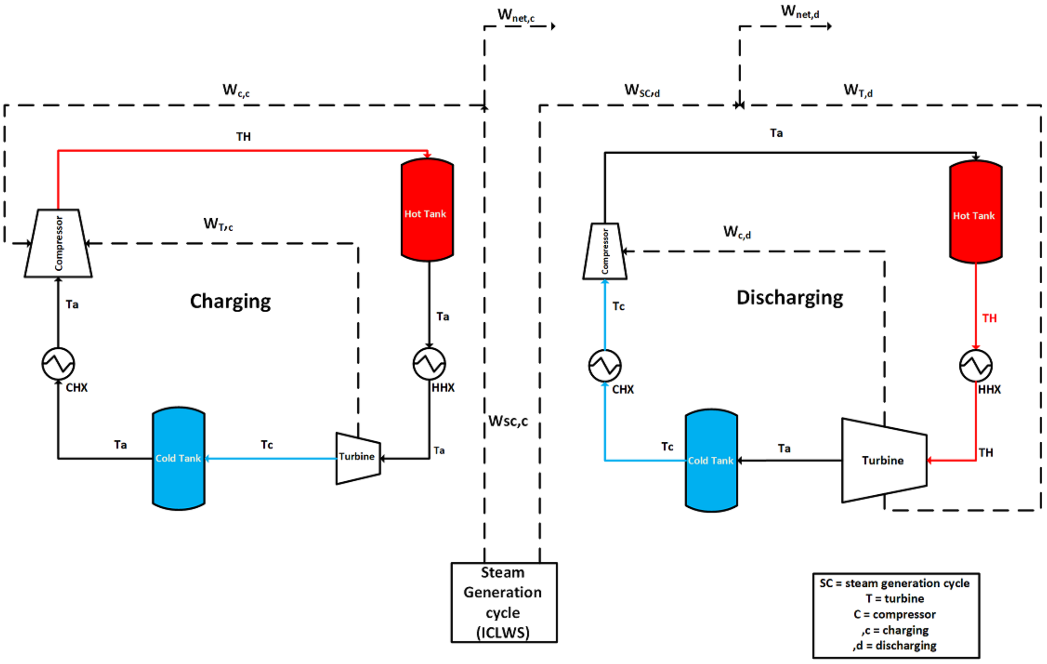

Figure 7.3: Schematic diagram for the IPTES energy storage system

The methodology used to model each piece of equipment in the cycle is illustrated in the following subsections.

7.3.1 Turbomachinery

Both the compressor and the expander were computationally modelled using Aspen Plus v.9. The outlet temperature was determined from the simulator using polytropic compression or expansion and setting the compression ratio to 16 bar. The expander was modelled as a gas turbine with polytropic efficiency of 76%. This technique was employed in studies published in the literature [119]. Also, the compressor showed a polytropic efficiency of 76%, similar to that of the turbine.

7.3.2 Hot and cold energy storage tanks

Section 7.2 explains that the pumped thermal-energy storage technology is a time-dependent process. Also, the temperatures of the discharged gas from both the hot and cold energy storage tanks influence the heat load of the hot and cold heat exchangers downstream. Therefore, accurate modelling of the axial and transient temperatures in both storage tanks is important. Several models are proposed in the literature [109, 118, 120]. We selected the discretised model due to its simplicity and the excellent approximation it provided for the partial differential equation (PDE) system, as indicated in the literature [109]. Thus, the axial gas temperature of any layer m in the tank, in addition to the solids bed temperature of layer m at any time t, are given by Eqs. (7.1) and (7.2) as follows [115]:

$$T_{a,m+1} = T_{b,m} + \left(T_{a,m} - T_{b,m}\right)^{-\emptyset_1} \quad (7.1)$$

Whereas the temperature of the solid bed at layer m can be represented as:

$$T_{b,m\,(t+\Delta t)} = T_{b,m\,(t)} + \left[\emptyset_2\left(T_{a,m+1} - T_{a,m}\right) + \emptyset_3\left(T_{b,m} - T_{amb}\right)\right]\Delta t \quad 7.2)$$

Where:

$$\emptyset_1 = \frac{h_v AL}{N m_a Cp_a},\ \emptyset_2 = \frac{N\, m\, Cp_a}{\rho_s ALCp_s(1-\varepsilon)},\ \emptyset_3 = \frac{U_m \Delta A_m}{m_a Cp_a} \quad (7.3)\text{ (a-c)}$$

h_v = The heat transfer coefficient per volume (W/m^3.K) and is calculated via the following equation:

$$\frac{Nu\, k_a}{d_e^2} \quad (7.4)$$

A = Surface area of the tank (m^2)

L= Tank height (m)

m_a = Mass flow rate of the working fluid of the PTES cycle (kg/s)

N = Number of discretised layers in the bed $i.e$ 50 layer.

Cp_a= Heat capacity of the gas at layer m (J/kg.K)

k_a = Thermal conductivity of the gas (W/m.K)

$d_e =$ Effective diameter of the solids particle (m)

G_a = Gas mass flow per area (kg/s.m^2)

$\rho_s =$ Solids particle density (kg/m^3)

Cp_s = Heat capacity of the solids. (J/kg.K)

ε = Bed void fraction

U_m = Overall heat loss coefficient (W/m^2.K)

ΔA_m = surface area of one layer (m).

ψ = Sphericity of the solid particles.

7.3.3 Hot and cold heat exchangers

Based on the temperatures of the gas discharged from the hot and cold energy storage tanks at time t, the heat loads from the hot and cold heat exchangers are determined, respectively. During the charging, the hot heat exchanger (HHX$_1$) acts as a cooler whereas the cold heat exchanger (CHX$_1$) acts as a heater to maintain the inlet temperatures to both pieces of turbomachinery at T_a. In contrast, HHX$_2$ acts as a heater maintaining the inlet temperature to the turbine at T_H while CHX$_2$ mainly functions as a cooler to set the inlet temperature to the compressor at T_c during the discharging period. For HHX$_1$, water is used as a coolant, while liquid nitrogen is the coolant chosen for CHX$_2$ since phase change limits the ability of water to maintain the inlet gas temperature to CHX$_2$ at T_c. An electric heater is used for both CHX$_1$ and HHX$_2$. The expressions that represent the heat load for both exchangers are summarised through Eqs. (7.5) and (7.6).

$$\text{Hot heat exchanger } (HHX): Q_{HHX} = m_a Cp_a \left(T_{ho,t} - T_{ah,s}\right) \quad (7.5)$$

Cold heat exchanger (CHX): $Q_{CHX} = m_a Cp_a \left(T_{co,t} - T_{ac,s}\right)$ (7.6)

In these equations:

$T_{ho,t}$ = The temperature of the discharged gas from the hot storage tank at time t (ºC)

$T_{ah,s}$= The temperature of the discharged gas from the hot storage tank at steady state (ºC)

$T_{co,t}$ = The temperature of the discharged gas from the cold storage tank at time t (ºC)

$T_{ac,s}$ = The temperature of the discharged gas from the cold storage tank at steady state (ºC)

7.4 Operating conditions of the PTES cycle and the operating hours schedule

Since the PTES system is a time-dependent process, an operating schedule must be proposed for the time between charging and discharging periods. Switching between the charging and discharging periods depends on the daily variable electricity price. Also, the lengths of the charging and discharging periods affect the total efficiency of the PTES system, as indicated by Eq. (7.14). Therefore, the selection of an operating schedule is of significant importance. The electricity prices used in this study were block auction prices, which varied daily according to three price blocks as follows: a) peak price, b) overnight price and c) the base or average price. The time period for each block was selected based upon an earlier study in the literature. The block auction electricity prices for several days in the year were employed in this study to provide a representative economic evaluation of the PTES system throughout the year, in which a significant variation occurs in the electricity prices as shown by Table 7.2 [121]. Based on these data, the operating schedule is specified and listed in Table 7.3. The day-ahead electricity price for day1 is represented in Figure 7.4 [121, 122]

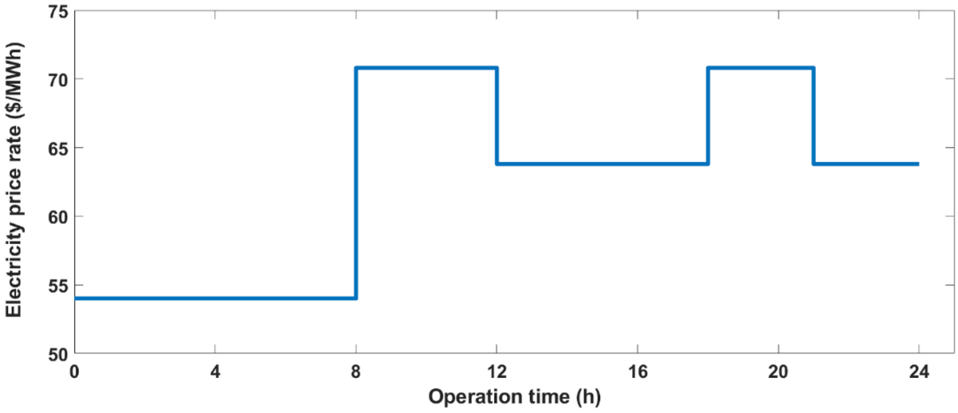

Figure 7.4: Variable electricity price for 24h period for day$_1$ [121, 122]

Table 7.2: Block auction electricity prices for various days in the year representing the variation in the prices

Days	Date	Base	Overnight	Peak
Day$_1$	10/01/2019	63.8	54.0	70.8
Day$_2$	13/02/2019	49.4	43.5	52.5
Day$_3$	16/03/2019	44.9	41.0	46.3
Day$_4$	11/06/2019	39.8	33.1	43.7
Day$_5$	18/10/2019	37.9	32.3	41.4
Day$_{max}$	24/01/2019	75.3	56.3	90.9
Day$_{min}$	08/12/2019	26.5	5.5	36.9

Table 7.3: Operating schedule for IPTES energy storage cycle

Time of operation (h)	Mode of operation	Stage of operation
0-8	Charging	First
8-14	Discharging	
14-18	Charging	Second
18-24	Discharging	

7.5 Temperature transient behaviour in the hot and cold tank for the IPTES energy storage cycle

The variations of the axial temperatures inside the tank are illustrated by representing the first and last layer temperatures in the tank. The operating conditions for the IPTES energy storage cycle are summarised in Table 7.4.

Therefore, the temperature transient behaviour for the first and last layers during the operating schedule mentioned in section 7.4 for both tanks is represented in Figures 7.5 and 7.6. Note that this temperature behaviour is recorded after the bed reaches steady periodic state after many operating cycles over 24 hours. In other words, for each operating cycle (24 hr), the bed temperature response must be the same i.e. the bed temperature for any layer at the end of the cycle must be the same as the temperature at the start of the cycle.

For the hot tank (Figure 7.5) during the first charging period (0-8 h), the temperature of the first layer rises exponentially to achieve the maximum hot temperature i.e. 525 ºC after 2 h. This behaviour is attributed to the high rate of heat transfer at the first layer due to the high temperature difference between the gas fed to the tank and the bed initial temperature. However, the temperature of the last layer remains constant for the first 2 h since the hot gas i.e. working fluid of the cycle loses most of its enthalpy in the upper layers of the bed. For $t > 2$ h, the bed temperature for the last layer increases linearly until the end of the first charging period.

During the first discharge period ($8 < t < 14$ h), the gas is fed at ambient condition from the bottom of the hot tank, hence it will gain most of the heat stored in the solids during the charging period. As a result, the bed temperature drops significantly for the last layer of the bed and attains the ambient gas temperature i.e. 40 ºC at $t = 11.8$ h as shown by Figure 7.5. On the other hand, the bed temperature for the first layer starts to decrease at $t = 11.8$ h until it achieves a final steady value of 394 ºC. This indicates that at this time the thermal layer of the hot tank starts to ascend upward.

Table 7.4: Operating conditions for the IPTES energy storage cycle

Parameter	Value
Gas mass flow rate (kg/s)	28.05
Solid storage density (kg/m^3)	9990
Power supplied to the compressor during the charging period (MW)	15
Storage material	Fe_2O_3+$MgAl_2O_4$
Pressure compression ratio	16
Compressor polytropic efficiency (%)	76
Turbine polytropic efficiency (%)	76
Tank volume (m^3)	220
Tank length (m)	10
Gas nominal temperature (°C)	40
Initial bed temperature (°C)	25
Maximum gas temperature (°C)	525
Minimum temperature (°C)	-154

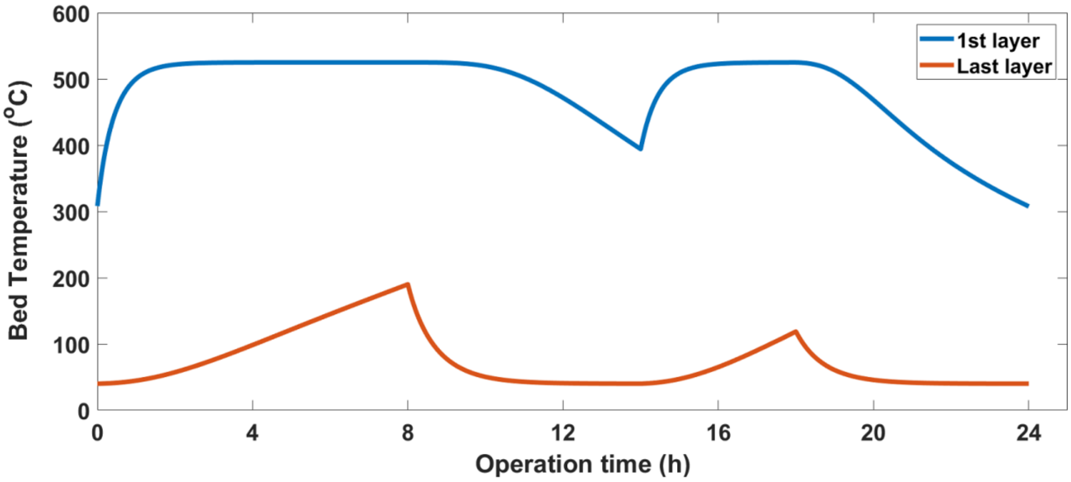

Figure 7.5: Transient behaviour for bed temperature in the hot tank during 24 hr operation time

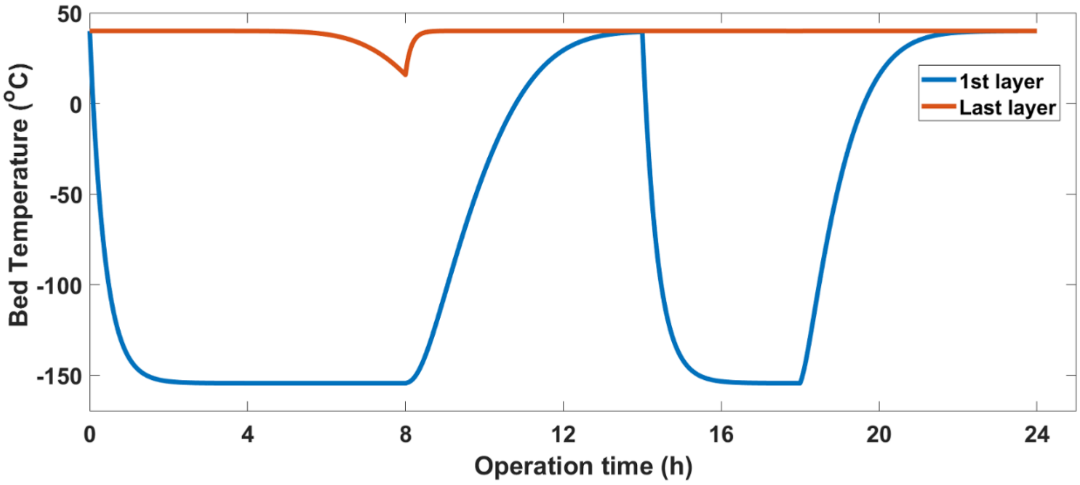

Figure 7.6: Transient behaviour for the bed temperature in the cold tank during 24 hr operation time

The curvature trend for the bed temperature is repeated in the second charging and discharging stage, but there is a difference in the time required for the bed temperature in both layers to hit the steady-state value. The bed temperature of the first layer in the cold tank decreases rapidly and attains the minimum cold temperature at t = 2 h during the first charging period (0-8 h). The reason for this behaviour is similar to the reason for the changes in the hot tank, since this zone contains most of the heat transfer between the solid storage material and the gas. Analogously to the hot tank, the bed temperature of the last layer remains constant during the first six hours of the charging period. Then, the thermal layer moves downward due to the thermal equilibrium that occurs between the gas and the solid materials for most of the upper layers of the bed. It reaches 8 ºC at t = 8 h. Similarly to the hot tank, the gas is fed at the bottom of the cold tank during the discharge period. Thus, the solid materials gain most of the thermal energy from the ambient gas at the first layer of the bed. Therefore, the temperature of the bed at the first layer rises rapidly for $8 < t < 12$ hr, then it increases gradually to achieve the gas ambient temperature i.e. 40 ºC. For the last layer of the bed, the solid temperature increases rapidly and achieves the gas ambient temperature during the first hour of discharge (t = 9 h). As opposed to the hot tank, during the second charging and discharge period, the bed temperature of both the first and last layers follows the same trend as is seen in the first cycle. It should be noted that, relative to the last layer in the solid bed for the second cycle, the variation in its temperature is insignificant.

7.6 Development of the IPTES energy storage cycle integrated with open cycle gas turbine (OIPTES)

A novel pumped-thermal energy-storage cycle was implemented by merging the open cycle gas turbine technology with PTES. This energy storage cycle was beyond the state of the art with respect to the pumped thermal technology. This energy storage cycle is referred as "OIPTES".

The system comprised three modes of operation: charging, discharging and the open cycle gas turbine (OCGT) energy production. The charging and discharging phases were similar to those of the IPTES cycle presented above. Yet, the discharging period was shorter. For the OCGT, hydrogen from the ICLWS plant was combusted with compressed air and fed to a turbine at high temperature and pressure to produce power. The discharged flue gas from the turbine was recycled back in the steam generation cycle of the ICLWS to utilise its excess heat to generate more power through the steam turbine. The process flow diagram of the cycle is represented by Figure 7.7.

The Aspen plus V.9 simulator was employed to determine the work generated by the gas and steam turbines. In addition, it was used to evaluate the heat load supplied to the steam generation cycle from the gas turbine discharged gas. The operating conditions for the OCGT process are shown in Figure 7.7. The amount of work generated by the gas and steam turbines varied according to the amount of H_2 fuel fed to the OCGT process.

Control valves V-(1-3) were mainly responsible for the switch between the discharging and the OCGT modes of operation, as shown in Table 7.5.

Table 7.5: Illustration for the control valves used to switch between OCGT and discharge mode of operation

Mode of operation	Valves open	Valves closed
Discharge	V-3	V-1&V-2
Open cycle gas turbine	V-1&V-2	V-3

Therefore, the discharge and OCGT modes of operation cannot take place at the same time. Based on that, the 6 h discharge period indicated in the operating schedule listed in Table 7.2 was segmented between discharge and OCGT. Four hours were designated as the period for the discharging mode and the remaining before hours were used for the OCGT operation. The operating schedule for the OIPTES energy storage system is summarised in Table 7.6.

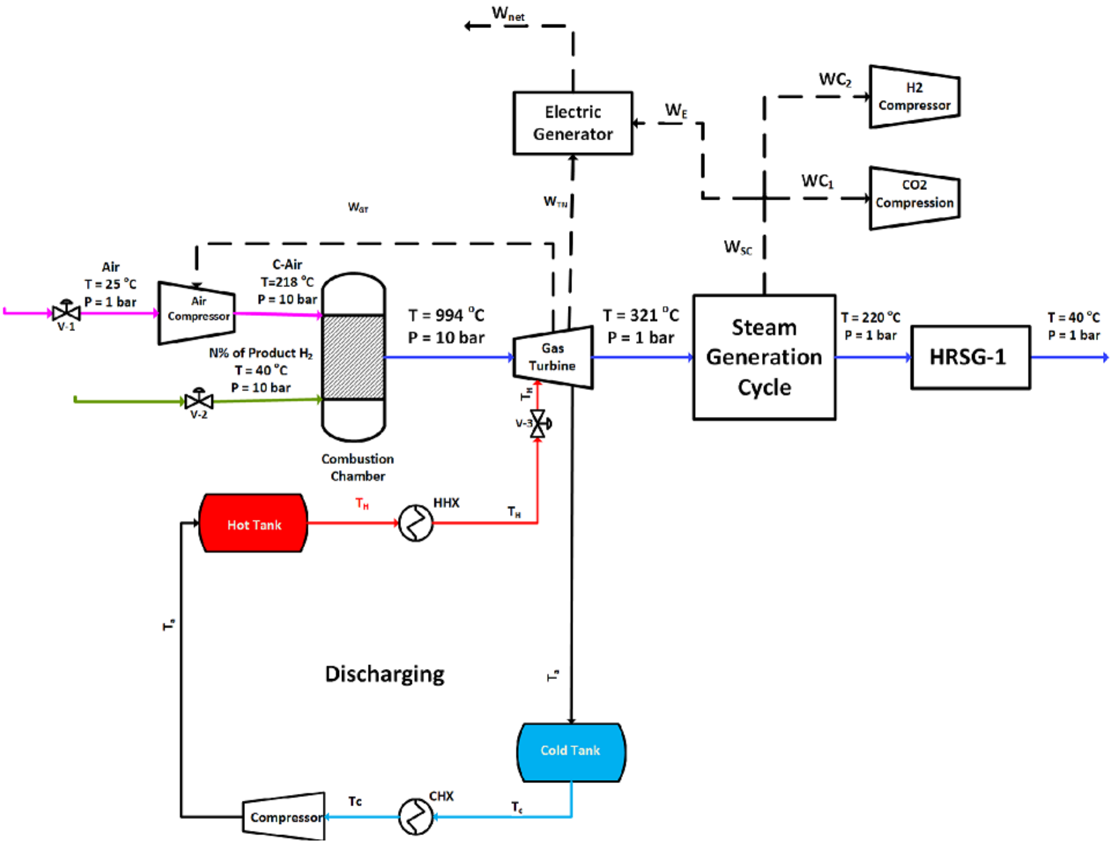

Figure 7.7: Process flow diagram of ICLWS process integrated OCGT

7.7 Bed temperature transient behaviour for OIPTES system

The transient behaviour of the bed temperatures in the hot and cold energy storage tank OIPTES system is illustrated in Figures 7.8 and 7.9. In this case 5% of the H_2 produced through the ICLWS process was fed to the OCGT system. The transient temperature responses shown were obtained once the steady-periodic state had been achieved after several operating cycles. The bed temperature of the first layer in the hot tank varied insignificantly during the 24 h period of operation (Figure 7.8). This was an expected trend since the initial temperature of this layer equalled the maximum temperature of the gas. Consequently, the thermal front would transport downward toward the bed layers, which exhibited lower temperatures. During the charging period, the temperature of the last layer exhibited an approximate linear increase to achieve 463 ºC at the end of the charging period.

Table 7.6: Operating schedule for the OIPTES energy storage system

Time of operation (h)	**Mode of operation**	**Stage of operation**
0-8	Charging	First
8-12	Discharging	
12-14	OCGT	
14-18	Charging	Second
18-22	Discharging	
22-24	OCGT	

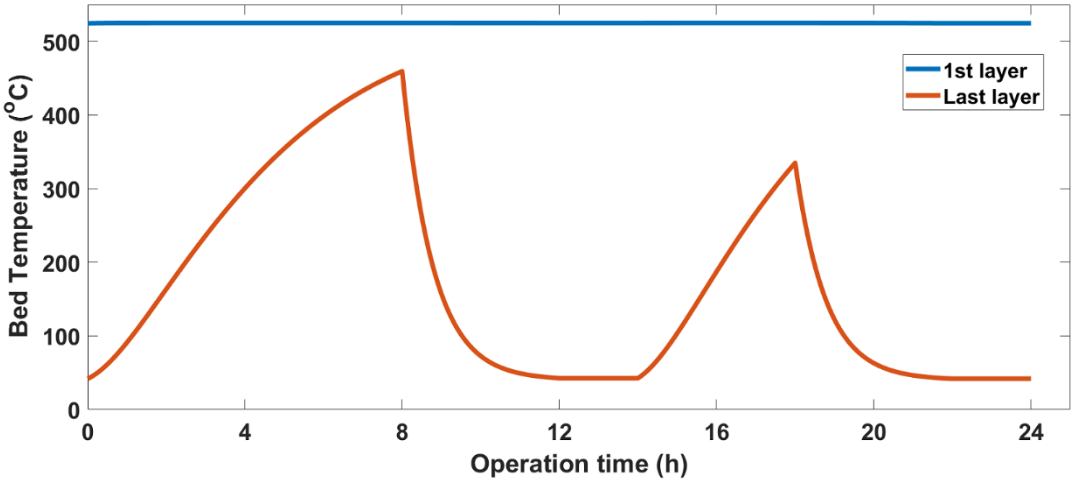

Figure 7.8: Transient behaviour for the 1st and last bed temperature for the hot tank in the OIPTES system

During the discharge mode, the temperature of the last layer in the bed reduces rapidly and reaches a final value of 49 ºC at t = 12 h. This behaviour is due to the thermal front which is concentrated in this area of the bed, hence most of the heat transfer between the gas and the solids in the bed occurs in this zone. During the second stage of operation, i.e. from t = 14 h upward, the bed temperature at the last layer exhibits similar behaviour to that observed in the first stage. For the cold tank, the bed temperature of the last layer begins to decrease after 5 h of operation, when the thermal front reaches this layer.

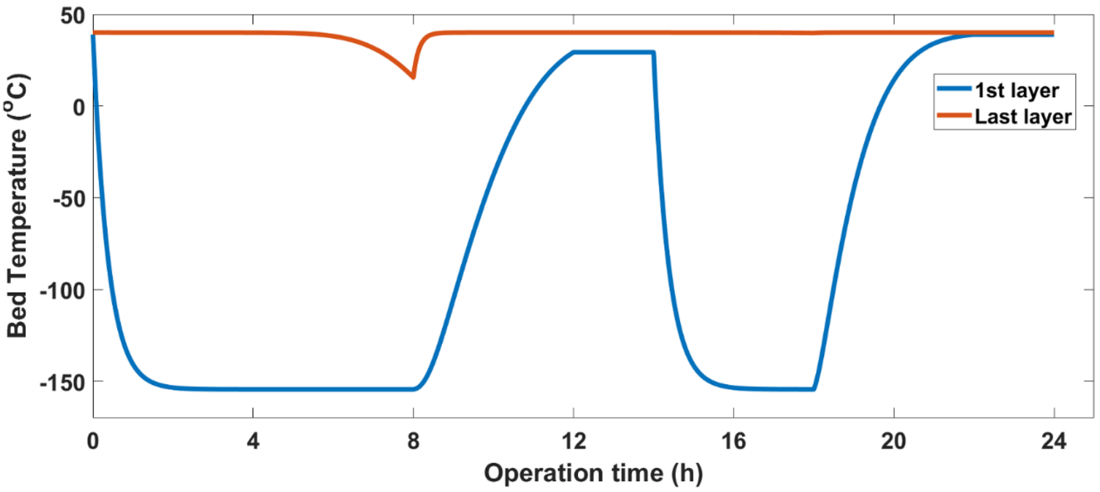

Figure 7.9: Transient temperature behaviour for the 1st and last layer of the bed temperature for the cold tank in the OIPTES system

During the charging period, the temperature of the last layer drops by 34.5% from its initial temperature. Also, during this period, the temperature of the first layer of the bed decreases at a very fast rate to attain the minimum cold temperature after only 2 h of operation. During the discharge phase, i.e. ($8 < t < 12$ h), the bed temperatures at both the first and last layers exhibit steep increases. The temperature of the first layer reaches a thermal equilibrium with the gas temperature at $t = 9$ h, whereas the last layer temperature achieves 11 ºC at the end of the discharging phase. This bed temperature behaviour is repeated for the second stage of operation. Yet, the final temperatures reached for the first and last layers of the bed at both charging and discharging phases are different to those obtained during the first stage, as shown in Figure 7.9.

7.8 Daily electricity generation from IPTES and OIPTES energy storage systems

The electricity generation for 24 h operation of IPTES energy storage systems can be calculated through Eq.(7.7) to (7.10) as follows:

$$E_{gI=}E_{gI,Ch} + E_{gI,d} + E_{SCI} \tag{7.7}$$

$$E_{gI,Ch} = W_C \, . t_{ch} - W_T \, . t_{ch} + \int_0^{t_{Ch}} Q_{CHX1} dt \tag{7.8}$$

$$E_{gI,d} = W_T \, . t_d - W_C \, . t_d - \int_0^{t_d} Q_{HHX2} dt \tag{7.9}$$

$$E_{SCI} = W_{SC} \cdot t \tag{7.10}$$

$$W_{SCI} = 29.5\ MW \tag{7.11}$$

For the OIPTES the energy generation is represented by:

$$E_{gO=}E_{gO,Ch} + E_{gO,d} + E_{OCGT} \tag{7.12}$$

$$E_{OCGT} = \ (W_{OCGT} + \ W_{SCO}) \cdot t_{OCGT} \tag{7.13}$$

Where:

E_g = Electrical energy produced in the cycle (MWh)

W = Work delivered or needed from the turbomachinery equipment (MW)

t = time (h)

Subscript:

I = IPTES system

O = OIPTES system

OCGT = Open cycle gas turbine

SCO = steam cycle of ICLWS process when integrated with open cycle gas turbine.

T = Turbine.

C = Compressor.

d= Discharge period.

ch = Charging period.

The electricity generation of both IPTES and OIPTES systems for 24 h operation is illustrated in Figure 7.10 (a&b). As shown in this figure, the energy generation profiles for both systems are linear with different slopes according to the mode of operation. The slope is relatively steep during the discharge, whereas it is shallow during the charging period. However, in the time period 12-14 h, the incremental rate for OIPTES is higher than that of the IPTES due to the usage of OCGT. As a result, the daily rate of energy generation for OIPTES is 11.5% higher than that produced by IPTES.

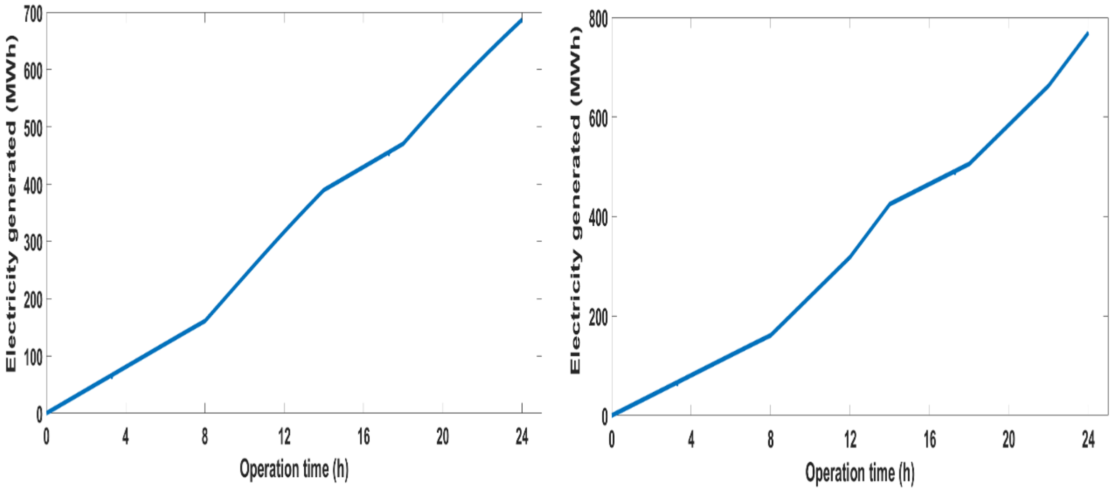

(a) (b)

Figure 7.10: The electricity generation for 24 h operation for: (a) IPTES process; (b) OIPTES process

7.9 The thermodynamic evaluation for the IPTES and OIPTES energy storage cycles

Furthermore, the energy storage systems developed in this study, i.e. the IPTES and OIPTES processes, both affect the efficiency of the ICLWS process. Therefore, the effective efficiency (η_{eff}) defined earlier in Eq. (3.14) in section 3.7 was used in addition to the round trip efficiency to evaluate the thermodynamic efficiencies of the energy storage systems. The round trip efficiency for one stage of operation of the IPTES and OIPTES systems is defined as:

$$\eta_{rt} = \frac{Net\ energy\ retrived\ during\ the\ discharge\ or\ OCGT\ period}{Net\ energy\ supplied\ during\ the\ charge\ period}$$

$$= \frac{E_{g,d}\ or\ E_{OCGT} + E_{SC}}{E_{g,Ch} + E_{SC}} \qquad (7.14)$$

An arithmetic average is calculated between both stages to obtain the round trip efficiency for 24 h operation. The values of the round trip efficiency as well as the effective efficiency for both IPTES and OIPTES systems at each mode of operation during 24 h operation time is summarised in Table 7.7.

The average round trip efficiency for both systems is 5% higher than that of the conventional PTES as quoted in the literature [123]. The main reason for this improvement in round trip efficiency is due to the long period of discharge time during the second stage of operation. Moreover, the solid storage material used for the ICLWS process has high heat capacity and diameter, which enables greater storage of the energy than is possible in the PTES system. As a result, the temperature of the discharged gas from both tanks will not differ significantly from the value set when introduced to the turbomachinery equipment. Therefore, the losses in the both HHX and CHX are minimised.

Table 7.7: Summary of the thermodynamic evaluation for IPTES and OIPTES energy storage systems

Mode of operation	Round trip efficiency		Effective Efficiency	
	IPTES	**OIPTES**	**IPTES**	**OIPTES**
Charging, 1st stage	61.8	61.7	80.8	80.9
Discharging, 1st stage			82.3	82.4
OCGT, 1st stage			-	80.0
Charging, 2nd stage	92.1	92.4	80.9	80.8
Discharging, 2nd stage			82.1	82.4
OCGT, 2nd stage			-	80.0
Average over 24 h	77.0	77.1	81.5	81.1

7.10 Economic assessment for the IPTES and OIPTES energy storage systems

7.10.1 Methodology

The methodology followed for the economic assessment of both energy-storage systems developed in this study was similar to the methodology introduced in Chapter 6. However, since electricity is the main product of these systems, only the units used for electricity generation are accounted for in the CAPEX analysis. For the OPEX analysis, electricity production, consumption of cooling water in the HHX during the charging phase, use of liquid nitrogen i.e. coolant in the CHX during the discharging phase and the use of hydrogen fuel during the OCGT mode of operation were all considered in the analysis. Finally the levelised electricity cost via Eq. (7.15) was utilised. Table 7.8 lists the units involved in the CAPEX analysis for both the developed systems. The equations employed for the economic assessment shown in Chapter 6 were:

$$A_c = CAPEX \times (1 + i)^n \left[\frac{\mathrm{i}}{(1+\mathrm{i})^n - 1}\right] \tag{6.1}$$

$$CAPEX = Total\,purchased\,cost\,of\,equipment\ \times total\,capital\,invesment\,factor\ \times plant\,cost\,index \tag{6.2}$$

where A_c is the annual value of the total investment cost of the plant divided by the number of operating days in a year (US$/d);

i is the interest rate (%); and

n is the project lifetime (year).

The levelised cost function therefore is as follows:

$$LEC = \frac{Total\,annual\,cost\,or\,profits\,for\,electricyproduction}{Annual\,electricity\,production} = \frac{P_A}{E_A} \tag{7.15}$$

$$P_A = \frac{A_c}{N_d} + OPEX \tag{7.16}$$

The OPEX of the energy storage system is calculated via the following equation:

$$OPEX = C_E - C_f - C_U \tag{7.17}$$

$$C_E = E_g \cdot E_p \tag{7.18}$$

$$E_p = \begin{bmatrix} P_1 & t_{chi} \leq t \leq t_{chf} \\ P_2 & t_{di} \leq t = t_{df} \end{bmatrix} \tag{7.19}$$

$$C_f = \dot{m}_f P_f t_{OCGT} \tag{7.20}$$

$$C_U = C_w + C_r \tag{7.21}$$

$$C_{cw} = \dot{m}_{cw} t_{ch} P_w \tag{7.22}$$

$$C_r = \dot{m}_r t_d P_r \tag{7.23}$$

In these equations

C_E = Revenues earned due to selling the electricity generated (US$/d)

E_p = Electricity unit price rate (US$/MWh)

P_1 = unit price rate of electricity during the charging time (US$/MWh)

P_2 = unit price rate of electricity during the discharging time (US$/MWh)

Both $P_1$and P_2 can be obtained from Figure 7.4

C_f = Daily cost associated with fuel consumption during the OCGT mode of operation (\$/d)

$\dot{m}_f$ = mass flow rate of the hydrogen fuel utilised in the OCGT per year (kg/d)

Table 7.8: List of the equipment used in the CAPEX analysis for both IPTES and OIPTES energy storage systems

Energy storage system	Equipment involved in CAPEX
IPTES	Hot and Cold heat exchangers (HHX& CHX)
	Cold and Hot electric heaters
	Hot and cold tanks + storage material
	Gas turbine
	Compressor
OIPTES	Combustion chamber
	Air compressor
	Hot and Cold heat exchangers (HHX& CHX)
	Cold and Hot electric heaters
	Hot and cold tanks + storage material
	Gas turbine
	Compressor
	Difference in size of the steam generation (SGC) unit from ICLWS process used for IPTES cycle

N_d = Number of operating days in the year (328 days)

P_f = unit price rate of hydrogen fuel used (US$/kg)

C_U = Daily cost associated with utilities consumption (US$/d)

C_{cw}= Daily cost associated with cooling water consumption. (US$/d)

$\dot{m}_{cw}$ = Mass flow rate of the cooling water utilised in heat exchangers during the charging period in both cycle stages per day (kg/d)

P_w= Unit price rate of the cooling water used (US$/m^3)

C_r= Daily cost of the refrigerant (Liquid nitrogen) used in the heat exchangers during the discharging mode (US$/kg)

P_r = Unit price rate of the refrigerant used (US$/m^3)

7.10.2 Economic evaluation for the IPTES and OIPTES energy storage systems

The costs of equipment purchased and the utilities are listed in Tables 7.11 and 7.10. Also, the economic assessment is fully summarised in Tables 7.12 – 7.15.

Table 7.9: Price rates of the utilities used for CHX and HHX in the IPTES system

Parameter	**Price rate**	**Ref**
Cooling water	1.03 $/m^3	[104]
Liquid nitrogen	16 $/100 Nm^3	[124]

Table 7.10: Determination of the operating cost used for CHX and HHX

Parameter	**Consumption rate (kg/d)**		**Annual cost (US$/d)**	
	IPTES	OIPTES	IPTES	OIPTES
Cooling water	6.6x10^5	6.0x10^6	-2,093	-5,285
Liquid nitrogen	1.7x10^6	3.0x10^6	-852	-544
H_2 fuel	-	3.1x10^4	-	-6,559

The IPTES and the OIPTES systems produced daily revenues of US$22,385 and US$62,783 respectively for day$_1$, as shown in Figure 7.11. The revenues for the other simulated days are represented in Tables 7.13 – 7.15. The daily revenues ranged between US$22,385 and US$67,173 for the IPTES. For the OIPTES, the daily electricity revenues were US$25,218 to US$75,142. The revenues grew linearly at different rates between the charging and discharging periods as well as between the days simulated due to the variation of the electricity produced (Figure 7.10) and the price of the electricity (Table 7.2). This means that the electricity revenues that were produced by the OIPTES process were 11.9 – 12.6% higher than those produced by IPTES for the several days simulated. However, the daily utility and fuel costs for the OIPTES system were US$9,444, which was 320.7% higher than the comparable costs for the IPTES system. This led to a calculation of US$53,126 per day gross revenue after taking into account the OPEX for IPTES.

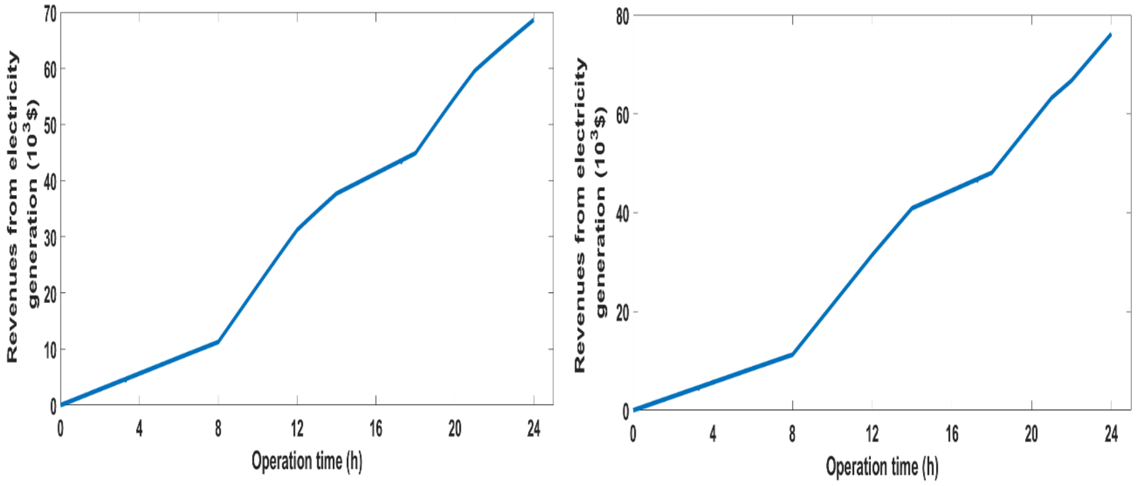

(a) *(b)*

Figure 7.11: Revenue obtained from electricity generation during 24 h for (a) IPTES and (b) OIPTES energy storage systems

The dominant parameters that affected the CAPEX of the IPTES system (Table 7.11) were the costs of the electric heater and gas turbine. These accounted for 62% of the total CAPEX. This was not the case for the OIPTES system, in which the air compressor and gas turbine were the main cost generators as they required 58% of the overall cost. Therefore, the CAPEX for the IPTES was 14.4% lower than that of the OIPTES. Regarding the OPEX, the OIPTES system was 5.1% higher than that of the IPTES for day$_1$ and it was 2.2 – 34.0% higher for the rest of the days that were simulated. This can be attributed to the utility and fuel costs, which were higher for the OIPTES system compared with the IPTES. Considering the annual value of the CAPEX, the total profit due to electricity generation was US$ 44,518 for the IPTES system for day$_1$, which was 11.0% higher than the profit generated by the OIPTES system (Table 7.12) for the same day. In addition, the total electricity profits were in the range of US$2,966/d – US$52,899/d for the OIPTES system, which was 4.9 – 72.6% less than the profit generated by the IPTES system. Consequently, the levelised electricity cost was 16.2 – 81.5% higher for the IPTES compared with the OIPTES system.

The economic assessment results for both systems indicate that the IPTES system is more feasible than the OIPTES system for the operating conditions mentioned in Table 7.4 and Figure 7.7.

Table 7.11: Purchased cost for the equipment involved in the IPTES and OIPTES systems

Equipment	**Purchased Cost (US$,M)**	
	IPTES	OIPTES
Energy storage tank + bed material	1.3	1.4
Hot electric heater	2.06	0.0
Cold electric heater	0.11	0.13
Hot and cold heat exchangers	0.06	0.16
Gas turbine	0.67	1.2
Compressor	0.15	0.15
Combustion Chamber	-	0.11
Air compressor	-	1.7
Difference in SGC size	-	0.2
Total	-4.4	-5.0

Table 7.12: Summary of the economic analysis main parameter for both the IPTES and OIPTES systems (a)

	Day$_1$		**Day$_2$**	
Parameter	**Value**		**Value**	
	IPTES	OIPTES	IPTES	OIPTES
CAPEX (U$, M)	-25.6	-29.3	-25.6	-29.3
Daily electricity revenue (US$/d)	56,071	62,783	42,931	48,129
Total electricity Produced per year (MWh/d)	687.2	769.2	687.2	769.2
OPEX (US$/d)	53,126	50,394	39,987	35,740
Total annual profits {P_A} (US$/d)	44,518	40,530	31,378	25,149
Levelised annual cost {LEC} ($/MWh)	64.8	52.7	45.7	33.6

Table 7.13:Summary of the economic analysis main parameter for both the IPTES and OIPTES systems (b)

	Day$_3$		**Day$_4$**	
Parameter	**Value**		**Value**	
	IPTES	OIPTES	IPTES	OIPTES
CAPEX (U$, M)	-25.6	-29.3	-25.6	-29.3
Daily electricity revenue (US$/d)	38,831	43,529	34,699	38,882
Total electricity Produced per year (MWh/d)	687.2	769.2	687.2	769.2
OPEX (US$/d)	35,886	30,409	31,754	26,494
Total annual profits {P_A} (US$/d)	27,278	20,549	23,146	15,902
Levelised annual cost {LEC} ($/MWh)	39.7	26.7	22.7	21.6

Table 7.14:Summary of the economic analysis main parameter for both the IPTES and OIPTES systems (c)

	Day$_5$	
Parameter	**Value**	
	IPTES	OIPTES
CAPEX (U$, M)	-25.6	-29.3
Daily electricity revenue (US$/d)	33,096	37,092
Total electricity Produced per year (MWh/d)	687.2	769.2
OPEX (US$/d)	30,151	23,971
Total annual profits {P_A} (US$/d)	21,543	14,112
Levelised annual cost {LEC} ($/MWh)	31.5	18.3

Table 7.15: Summary of the economic analysis main parameter for both the IPTES and OIPTES systems (d)

	Day$_{max}$		**Day$_{min}$**	
Parameter	**Value**		**Value**	
	IPTES	OIPTES	IPTES	OIPTES
CAPEX (U$, M)	-25.6	-29.3	-25.6	-29.3
Daily electricity revenue (US$/d)	67,173	75,142	22,385	25,218
Total electricity Produced per year (MWh/d)	687.2	769.2	687.2	769.2
OPEX (US$/d)	64,228	62,021	19,441	12,098
Total annual profits {P_A} (US$/d)	55,620	52,162	10,832	2,239
Levelised annual cost {LEC} ($/MWh)	80.9	67.8	15.8	2.9

7.11 Feasibility equation and economic sensitivity analysis for OIPTES system

In this section, the aim is to investigate the conditions or operating parameters that enable the integration of the open cycle gas turbine operation with a pumped thermal energy storage system to be more economically viable than the original PTES system. Thus, in this section some of the operating parameters for OIPTES system are manipulated to improve the economic evaluation of the system presented in section 7.10.

7.11.1 Feasibility Equation

To achieve this objective, initially we applied the annual profit equation for both systems as follows:

$$P_{AI} = A_{cI} + OPEX_I \tag{7.24}$$

$$P_{AO} = A_{cO} + OPEX_O \tag{7.25}$$

In these equations, subscript "I" denotes the IPTES system and subscript "O" denotes the OIPTES system.

In order for the OIPTES system to be economically more attractive than IPTES system, this condition must be satisfied:

$$P_{AO} > P_{AI} \tag{7.26}$$

Breaking down the parameters of Eq.(7.25) leads to

$$C_{EO} - C_{UO} - C_{fO} - A_{cO} > C_{EI} - C_{UI} - C_{fI} - A_{cI} \tag{7.27}$$

Since no fuel is utilised in the IPTES system, $C_{fI} = 0$. Representing each parameter in Eq. (7.26) with its relative equation yields to:

$$E_{gO,C}(P_1 + \eta_{rtO}P_2) + W_{OCGT}t_{OCGT}P_2 + (A_{cO} - A_{cI}) > E_{gI,C}(P_1 + \eta_{rtI}P_2) + \dot{m}_f t_{OCGT}P_f - (C_{UI} - C_{UO}) \tag{7.28}$$

Eq.(7.28) can be rearranged to the following:

$$P_1(E_{gI,C} - E_{gO,C}) + P_2(E_{gO,C}\eta_{rtO} - E_{gI,C}\eta_{rtI}) + t_{OCGT}(W_{OCGT}P_2 - \dot{m}_f P_f) + (C_{UI} - C_{UO}) + (A_{cO} - A_{cI}) > 0 \tag{7.29}$$

Eq. (7.28) is called the feasibility equation for the OIPTES system. This equation informs us how to improve the profitability of OIPTES to be greater than that of the IPTES system. To fulfil this criterion, the following considerations should be taken into account:

1- $P_1(E_{gI,C} - E_{gO,C})$ the adjustment of this term has insignificant effect on Eq. (7.29). This is due to the tiny difference between the electricity generated from both systems as a result of the similarity of the charging times and conditions for both systems.

2- $P_2(E_{gO,C}\eta_{rtO} - E_{gI,C}\eta_{rtI})$ this term depends on the round trip efficiency, which in turn relies on the discharge time. In most cases, a small difference does occur between the systems based on the change of discharge time, which is discussed in more detail in the next section.

3- $t_{OCGT}(W_{OCGT}P_2 - \dot{m}_f P_f)$ this term depends on the fuel price, which is a critical parameter to satisfy Eq. (7.29). Hence, the selection of inexpensive fuel plays a key role here in order to maximise this term.

4- $(C_{UI} - C_{UO})$ this term is usually negative; therefore, it should be minimised. The reason for this is attributed to the shorter discharge time in the OIPTES system. Consequently, the temperature of the gas effluent from the hot tank during the charging period in the second stage is higher than is the case for IPTES. As a result, more consumption of cooling water is required in the HHX.

5- $(A_{cO} - A_{cI})$ this term is negative, since the OIPTES comprises more equipment than the IPTES. Therefore, it should be minimised.

7.11.2 The influence of varying the discharge time on the OIPTES annual profits

The operation times for the discharge and the open cycle gas turbine modes were manipulated via four different scenarios presented in Table 7.16. It was only simulated for day$_1$ since the main aim here was to investigate the scenario with highest daily profits. Notice that scenario 2 is the one evaluated in section 7.8. Based on the information in Tables 7.2&7.9, the electricity generation as well as the utilities and fuel consumption were calculated in order to evaluate economically each individual operation scenario. The CAPEX of the OIPTES system was similar to the value obtained in section 7.8 since the equipment sizes were not varied.

Table 7.17 shows that the highest electricity revenue was obtained in scenario 3, since this scenario produced the greatest electricity generation. Nevertheless, the total daily profit was US$36,221/d, which was the lowest among the four scenarios. The reason for this can be understood to be the significantly high cost relative to the fuel and utility obtained through this scenario.

Table 7.16: Different operation scenarios for discharge and OCGT modes

Scenario (Sc)	**Mode of operation**	**Operation time (h)**
1,2,3,4	Charging	0-8, 14-18
1	Discharging	8-12, 18-21
	OCGT	12-14, 21-24
2	Discharging	8-12, 18-22
	OCGT	12-14, 22-24
3	Discharging	8-11, 18-21
	OCGT	11-14, 21-24
4	Discharging	8-11, 18-22
	OCGT	11-14, 22-24

Table 7.17: Summary for the Economic evaluation for the four different scenarios

Parameter	**IPTES**	**OIPTES**			
		SC$_1$	SC$_2$	SC$_3$	SC$_4$
CAPEX (U$, M)	-25.6	-29.3			
Utility cost (US$/d)	-2,945	-6,081	-5,829	-6,402	-6,098
Electricity Revenue (US$/d)	56,071	63,283	62,783	63,463	62,387
Fuel Cost (US$/d)	-	-9,114	-6,559	-10,976	-9,146
OPEX (US$/d)	53,126	48,087	50,394	46,085	47,143
Electricity generation (MWh/d)	687.2	775.3	769.2	776.2	763.1
Total Annual Profits (US/d)	44,518	38,223	40,530	36,221	37,279

The lowest utility and fuel costs were obtained from the second scenario. Eq. (7.29) shows that the discharge time and the OCGT affect the second, third and fourth terms of the equation. Therefore, increasing the period of discharge minimised these terms and resulted in the highest daily profit of all the scenarios; the daily profit was 6% higher than that of the scenario in second place (SC1). Despite that, the OIPTES (SC2) daily profit was lower than that of the IPTES by 14.1%.

From Eq. (7.29), it can be seen that the feed rate of the fuel could be an important factor to enhance the daily profit. Therefore, this factor is investigated in the next section.

7.11.3 The effect of H_2 feed rate on the economic evaluation of the OIPTES

According to the third term in the feasibility equation (7.29), the effect of the feed rate of H_2 to the OCGT is critical. Increasing this feed rate results in the generation of more power from the OCGT mode. However, it can also reverse the positive third term to negative, which consequently leads to failure of satisfaction of Eq. (7.29).Therefore, the H_2 feed rate must be optimised so that Eq. (7.29) is fulfilled and hence the daily profitability of the OIPTES is improved compared with that of the IPTES. To achieve this, the H_2 feed rate to the OCGT was manipulated from 0% (IPTES system) to 100% from the ICLWS process product, as shown in Figures 7.12 – 7.16. Consequently, the CAPEX, OPEX and daily profits for the OIPTES system were determined for each feed rate and for days 1, 2, min and max.

The percentage differences in daily profits for the OIPTES system ($\%P_A$) between variable H_2 feed rates and the base case (IPTES) were obtained and are presented in Figures 7.17 – 7.18. These figures enable us to decide which energy storage system is feasible based on the OCGT fuel rate.

The CAPEX for the OIPTES system increases as the flow rate of H_2 fed to the OCGT increases. This is a logical trend due to the larger size of equipment required to handle the high fuel flow rate in the OCGT cycle. The highest growth in CAPEX was 56% for increases of between 40% and 60% in H_2 feed rate. As a consequence, the annual value relative to CAPEX increased.

For the OPEX, the utility cost remained constant since the same operating schedule was fixed for all different H_2 feed rates. Thus, the outlet gas temperature from the hot and cold tanks during the charging and discharging periods were the same for all H_2 feed rates studied.

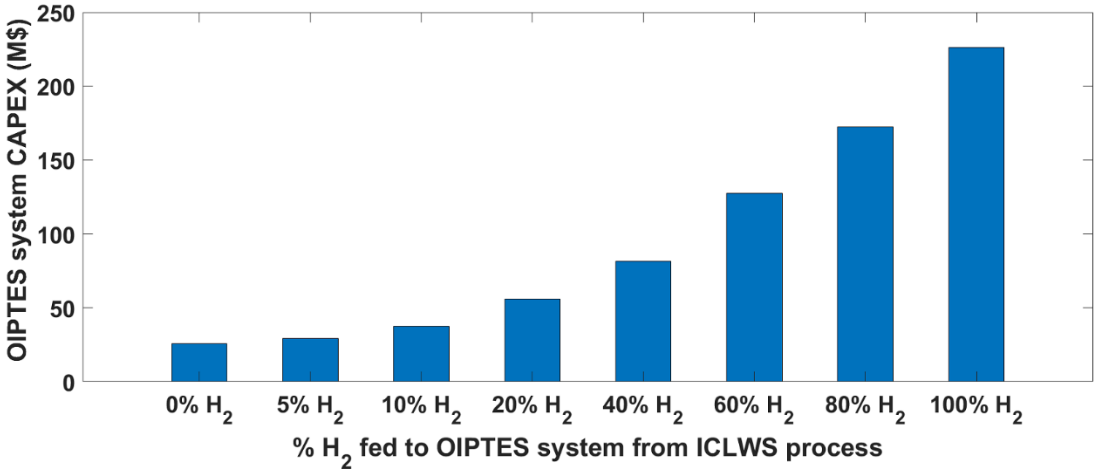

Figure 7.12: CAPEX for OIPTES at different fuel feed rates

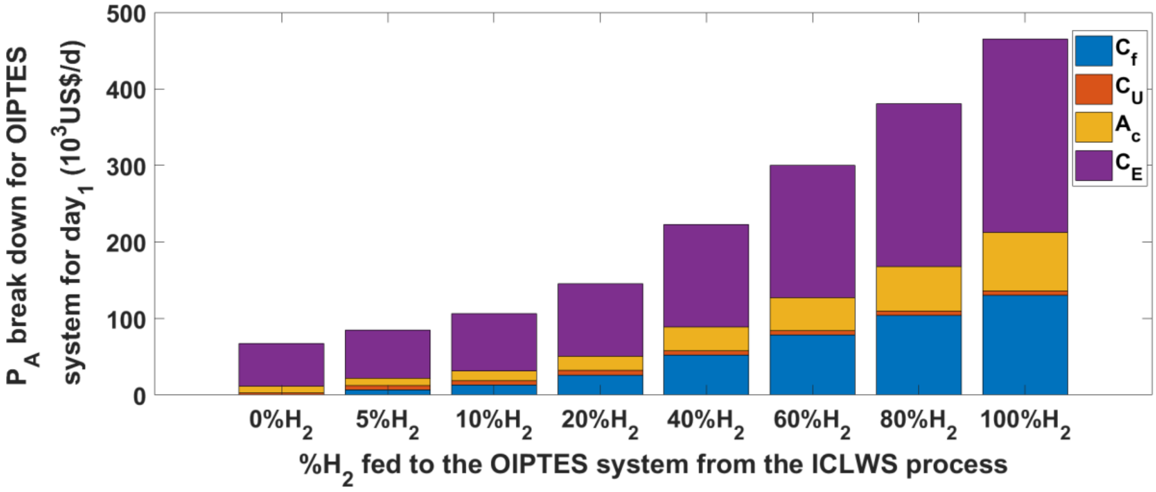

Figure 7.13: Economic evaluation for OIPTES system at different fuel feed rates

The fuel cost rose by 300% for 5% $<H_2<$ 20%, then the incremental percentage decreased to 25% for 80% $<H_2<$100%. The electricity revenues varied significantly with the variation of the operating days due to the non-trivial change in the electricity prices, as represented by Table 7.18. However, they followed the same trend relative to the change in the hydrogen feed rate to the OIPTES system. The maximum incremental percentage of 114% occurred when the hydrogen feed rate was increased to 40% relative to 5% for all the operating days. After this, the electricity revenues incremental percentage decreased to attain 19% for 8% $<H_2<$ 100%. For day_1 and day_{max}, the OIPTES system was gaining profits regardless of the amount of hydrogen fed to the OCGT.

Table 7.18: P_A breakdown for the rest of the operating days simulated for the OIPTES system

Days	H_2%	C_f (US$/d)	C_U (US$/d)	A_c (US$/d)	C_E (US$/d)	P_{A0} (US$/d)
1	0	0	2,945	8,608	56,071	44,518
	5	6,559	5,829	9,864	62,783	40,530
	10	13,198	5,829	12,677	74,417	42,713
	20	26,208	5,829	18,830	94,404	43,536
	40	52,127	5,829	30,896	133,766	44,915
	60	78,190	5,829	42,830	173,424	46,574
	80	104,143	5,829	57,951	213,136	45,213
	100	130,317	5,829	76,059	253,131	40,925
2	0	0	2,945	8,608	42,931	31,378
	5	6,559	5,829	9,864	48,129	25,876
	10	13,198	5,829	12,677	56,554	24,850
	20	26,208	5,829	18,830	72,630	21,763
	40	52,127	5,829	30,896	103,108	14,257
	60	78,190	5,829	42,830	133,797	6,948
	80	104,143	5,829	57,951	164,564	-3,359
	100	130,317	5,829	76,059	195,532	-16,674
Min	0	0	2,945	8,608	22,385	10,832
	5	6,559	5,829	9,864	25,218	2,966
	10	13,198	5,829	12,677	30,058	-1,646
	20	26,208	5,829	18,830	38,360	-12,508
	40	52,127	5,829	30,896	54,709	-34,143
	60	78,190	5,829	42,830	71,181	-55,668
	80	104,143	5,829	57,951	87,676	-80,247
	100	130,317	5,829	76,059	104,288	-107,918
Max	0	0	2,945	8,608	67,173	55,620
	5	6,559	5,829	9,864	75,142	52,889
	10	13,198	5,829	12,677	88,885	57,181
	20	26,208	5,829	18,830	112,475	61,607
	40	52,127	5,829	30,896	158,932	70,081
	60	78,190	5,829	42,830	207,507	80,657
	80	104,143	5,829	57,951	252,621	84,698
	100	130,317	5,829	76,059	299,812	87,606

The maximum profit earned for day_1 was US$46,574 at 40% H_2 feed rate, whereas it was US$87,606 for day_{max} at 100% H_2 feed rate, as indicated by Table 7.18. However, for day_2 and day_{min}, the operating expenditures were greater than the revenues associated with selling electricity at a certain range of H_2 percentage fed to the OIPTES system. The OIPTES system made profits when the H_2 feed rate fell in the range $5\% < H_2 < 60\%$ and $H_2 = 5\%$ for day_2 and day_{min}. In contrast, the OIPTES made a loss when the H_2 feed rate was outside this range. The maximum losses were US$16.674 for day_2 and US$107,918 for day_{min}; for a H_2 feed rate in both cases of 100%.

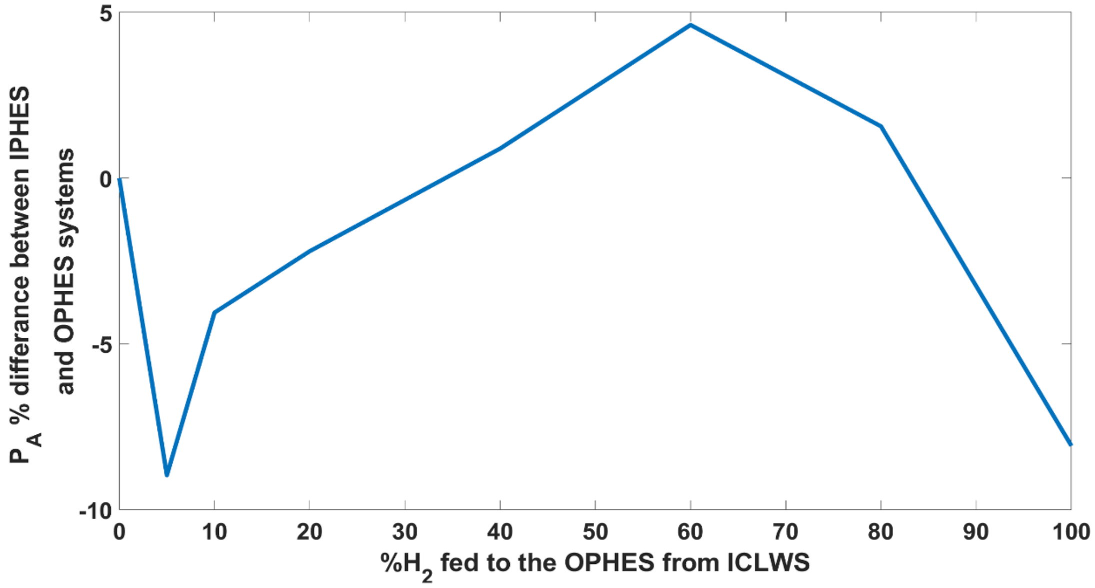

Figure 7.14: % difference in total daily profits for OIPTES relative to IPTES energy storage systems for day_1

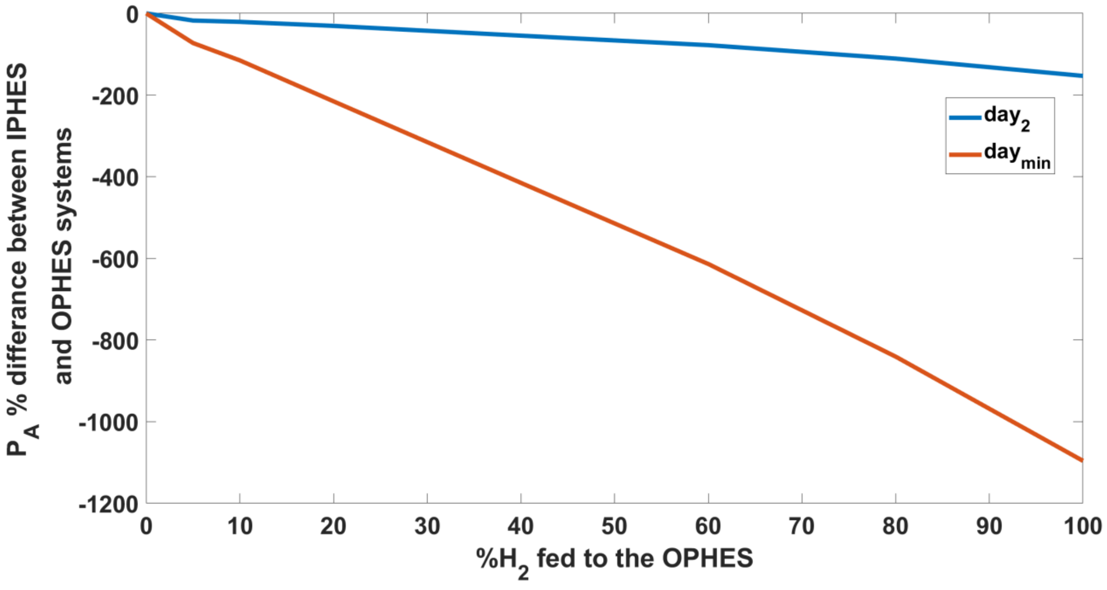

Figure 7.15: *% difference in total daily profits for OIPTES relative to IPTES energy storage systems for day_2 and day_{min}*

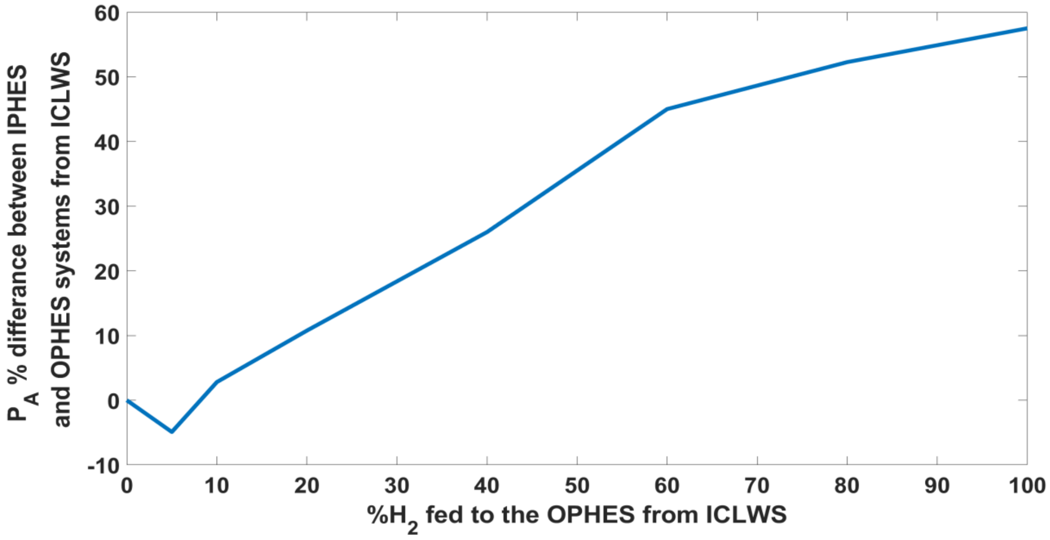

Figure 7.16: % difference in total daily profits for OIPTES relative to IPTES energy storage systems for day$_{max}$

Figures 7.14 – 7.16 show the final results obtained from Figure 7.12 and Table 7.18 by providing a decision criterion of whether the integration of OCGT to IPTES is feasible or not based on the values of H_2 fed to the OCGT cycle. For day$_1$, operating at a H_2 feed rate of above 37% results in a positive value of P_A%. Therefore, for this range of H_2 feed rate to the OCGT, OIPTES is more economically viable than the IPTES system. However, for a H_2 feed rate of less than 37%, it is not feasible to integrate the IPTES with OCGT, as indicated by Figure 7.14. The IPTES system is the feasible choice for the electricity prices selected in day$_2$ and day$_{min}$. This is concluded from the negative values of P_A% determined for all the H_2 feed rates as shown by Figure 7.15. For day$_{max}$, operation at H_2 feed rates above 7% results in positive values of P_A%. Therefore, it can be concluded that the OIPTES is the more economically feasible method for H_2 feed rates greater than 7%. Table 7.19 summarises the range of H_2 feed rates at which each system is more feasible for every day simulated.

Table 7.19: Summary of H_2 feed rate at which operation of each system is more feasible

Days	H_2% feed rate at which OIPTES is feasible	H_2% feed rate at which IPTES is feasible
1	>37%	<37%
2	-	All
Min	-	All
Max	>7%	<7%

7.12 Concluding remarks

Pumped thermal energy storage was coupled with the ICLWS hydrogen production process to investigate its thermodynamic and economic effects on the process due to the production and storage of electricity. A model was developed for the integrated energy storage cycle (IPTES) to determine the transient behaviour of the temperature of the solid storage material as well as the electricity produced per year.

The IPTES system was also economically assessed via determination of its CAPEX and OPEX, and the daily profits generated by selling electricity. The OPEX and the daily profits were determined over several days in a year with significant fluctuation in electricity prices. In addition, a novel energy storage cycle was proposed that combined the integrated cycle developed in this study (IPTES) with the open cycle gas turbine (OIPTES). This novel energy storage system was thermodynamically and economically assessed and compared with the IPTES system. First results have shown that there is negligible difference between the thermodynamic performances represented by the round trip efficiencies of both systems. However, the IPTES method is more economically viable than the OIPTES for the operating conditions used and the days simulated in the elementary analysis. Therefore, economic sensitivity analysis was performed for the OIPTES system to enhance its economic performance.

A feasibility equation was derived to represent the factors that affected the economic performance of the OIPTES system and to find ways to enhance it over the IPTES system. The H_2 fuel feed rate from the ICLWS was observed to play a key role in improving the daily profits of the OIPTES system. Sensitivity analysis results show that, for the day_1 and day_{max} simulated, when the H_2 feed rate was greater than 37% and 7% respectively, the OIPTES was more economically viable than the IPTES, i.e. more daily profits were earned from sales of electricity than through use of the IPTES system. In contrast, the IPTES system was more economically feasible for the day_2 and day_{min} simulated for the whole range of H_2 feed rates used.

Chapter 8 : *Conclusions and future work*

8.1 Conclusions

In this thesis, two novel processes for hydrogen and iron production in-situ with CO_2 capture via chemical looping technology were described and techno-economically evaluated. Furthermore, the developed hydrogen production process was integrated with pumped heat energy storage and open cycle gas turbine processes for electricity production and storage. In the first chapter, the topic was outlined by introducing the topic of global warming and its main causes, including the anthropogenic emissions of CO_2 produced by the combustion of fossil fuels in power plants and other industries. Therefore, CO_2 capture technologies (CCS) would be required to mitigate CO_2 emissions in order to attain the IPCC Paris agreement.

Hydrogen is a potentially environmentally benign source of fuel with steam as the only combustion product; therefore use of hydrogen fuel can reduce dependence on fossil fuels in the future. A review of the literature assessed the routes for hydrogen production, the main reactions that govern each technology, their advantages and disadvantages, their levels of maturity and their thermodynamic and economic performances. The technologies reviewed were steam methane reforming, partial oxidation of hydrocarbons, light hydrocarbon splitting, electrolysis and photolysis and chemical looping.

Steam methane reforming (SMR) is considered as the dominant process due to its economic attractiveness, and it is the most mature system. However, it is an intensive CO_2 emission source. Other close to emissionless sources such as electrolysis and photolysis are still in their development phases and not economically feasible. Hydrogen production via chemical looping with water splitting (CLWS) is a potentially promising future technology with inherent CO_2 capture and low energy penalty, which has the potential to substitute for SMR in the future. The scope of this thesis was about this technology. The work performed on this technology and the important findings obtained are summarised in the following paragraphs.

Development of a novel hydrogen production process based on three-stage chemical looping technology

An integrated hydrogen production process via three-stage chemical looping water splitting (ICLWS) technology using moving-bed reactors was developed and simulated through use of the Aspen Plus V.8.8 simulator. Thermal energy integration following pinch-point analysis and sensitivity analysis was applied to the baseline process in order to optimise the integrated version (ICLWS). Then, the thermodynamic performance of the integrated process (ICLWS) represented by the effective and hydrogen production efficiencies was assessed and compared with the benchmark hydrogen production process, i.e. SMR system developed in this study and other modern SMR or auto-thermal reforming (ATR) processes reported in the literature. It was also compared with other CLWS processes as described in the literature, such as the CLWS process developed by Ohio State University (OSU) and the Three Reactor Chemical Looping Reforming (TRCLR) process proposed by the Centre for Energy in Abu Dhabi.

Heat integration improved the ICLWS performance via a developed optimised heat exchanger network and the minimisation of utility usage. This can be observed through the 23.7 percentage point and 41.3 percentage point improvements in the effective and hydrogen efficiencies, respectively, compared with the baseline process. In addition, the effective efficiency of the optimised process (ICLWS) was improved by 12.3 percentage points, 2 – 11.1 percentage points and 4.1 – 10.8 percentage points compared with the efficiencies of the SMR, modern SMR_m and ATR processes, respectively. Also, the effective efficiency of the ICLWS showed an improvement by 6.5 percentage points and 10.8 percentage points over the OSU and TRCLR processes, respectively. Furthermore, it showed the greatest hydrogen efficiency among all the comparable SMR/ATR and CLWS processes. The hydrogen efficiency was 11.7 percentage points, 6.8 – 13.5 percentage points and 6.5 – 12.7 percentage points greater than those obtained in the SMR, modern SMR_m and ATR processes. In addition, the hydrogen production efficiency was improved by 6.3 and 13.4 percentage points compared with the OSU and (TRCLR) processes, respectively.

The sensitivity analysis for the fuel reactor indicated that the conversion of the discharged gas increased as the ratio of oxygen carrier to fuel increased until a complete conversion was achieved. Similar behaviour was observed for the conversion of the discharged gas when the discharged gas temperature was increased. In contrast, the conversion of the discharged solids decreased as the oxygen carrier to methane ratio increased. However, the conversion of the discharged solids increased to 66% as the temperature increased. At this temperature of the discharged solids, the carbon deposition inside the reducer was zero.

For the oxidiser, the steam outlet conversion remained constant for a certain range of the ratio of oxygen carrier to methane feed. Beyond this range, it began to decrease when all the $Fe_{0.947}O$ was fully converted to magnetite. As the ratio increased, the conversion of the discharged solids decreased until all the $Fe_{0.947}O$ was fully oxidised.

Development of a state-of-the-art decarbonised iron and hydrogen production system via a four-stage chemical looping water splitting process

The integrated chemical looping process developed earlier (ICLWS) was adjusted to produce decarbonised iron in addition to hydrogen. The new emerging process was referred to as chemical looping water splitting plus iron production “CLWSFe”. It was simulated using the Aspen Plus V.9 simulator. The main motive for development of such a process was to mitigate the CO_2 emissions that form a by-product of the iron and steel industry. These emissions constitute 30% of the global industrial emissions. The "CLWSFe" process that was developed in this study comprised of four stages: in the first, metallic iron Fe^0 was produced via the complete reduction of iron ore oxygen carrier by the pre-heated natural gas fuel. The fuel was partially combusted to syngas, which was fed to the second stage where it was completely converted via its reaction with iron ore to a mixture of CO_2 and steam. The CO_2 was then separated from steam and captured. Part of the iron produced at stage one was stored as a co-product while the other part was introduced to the third stage, where it was partially oxidised with steam to produce blue hydrogen as a main product from the process. The partially oxidised oxygen carriers were fully regenerated in the fourth stage of the process through their reaction with pre-heated air.

The CLWSFe process was thermally optimised in a similar way to the ICLWS process by the application of of pinch-point analysis. The heat integration of the process consisting of a heat exchanger network, an HRSG unit, was intended to generate the steam required for the oxidiser while excess steam was utilised through another HRSG unit to generate power.

The thermodynamic performance of the process was assessed through the determination of the hydrogen and effective efficiencies and compared with those of the SMR and OSU processes mentioned earlier. Also, the iron effective efficiency was a measure of the thermodynamic performance of the CLWSFe process against that of the MIDREX process, which was considered as the benchmark process for the production of DRI. The results of the thermodynamic analysis of the CLWSFe process revealed an improvement in the effective efficiency of 20.8 percentage points and 10.9 – 20.9 percentage points compared with the figures for the SMR and modern SMR_m/ATR processes, respectively. However, the hydrogen production efficiency of the CLWSFe process was 1.6 percentage points, 6.8 percentage points and 7.0 percentage points lower than the comparable data for the SMR, modern SMR_m/ATR and OSU processes. This was due to the amount of Fe^0 stored as a by-product and therefore not available to be sent to the oxidiser to produce H_2. Furthermore, the iron effective efficiency for the CLWSFe process was 0.7 – 6.6 percentage points greater than the corresponding values recorded for the MIDREX process in the literature.

Mathematical modelling of the reactors involved in both the developed ICLWS and CLWSFe processes

A steady-state one-dimensional mathematical model was derived for all the moving-bed reactors involved in the ICLWS and CLWSFe processes developed earlier. The main purpose of the developed model was to obtain the axial conversion and temperature profiles of the gas and solids for each reactor in each process that had been developed. These profiles enabled the determination of the length of the reactor needed to achieve the required conversion. Hence, the size of the reactor was obtained, which was mandatory for the economic evaluation of both ICLWS and CLWSFe processes. In addition, the rate of conversion and temperatures of the gases and solids fed into and discharged from each reactor were compared with the values obtain by the Aspen Plus simulator. The percentage errors in gas and solid conversion and temperatures were less than 5% with a maximum error of 4.8% in the solid temperature for reducer-2. These values indicate that the polymath model shows good agreement with the Aspen simulation.

Economic evaluations of the developed ICLWS and CLWSFe processes

The hydrogen (ICLWS) and hydrogen plus iron (CLWSFe) production processes via chemical looping, the development of which was described in Chapters 3 and 4, were assessed for their economic validity. The economic assessment was based on the total investment value of the process (CAPEX), operating cost (OPEX) and the hydrogen production cost P_c. In addition, economic evaluation of the SMR process developed (SMR1) in Chapter 3 was conducted and compared with the values reported in the literature. Also, the effect of implementing CCS on the CAPEX, OPEX and P_c for the SMR process was determined.

Results indicated that a 4.9% difference was obtained in H_2 production cost between the developed SMR and the value published for an analogous SMR process in the literature. Furthermore, it was shown that P_c became 5.5 percentage points higher when CCS was integrated with the SMR process.

The economic analysis for ICLWS showed an encouraging result. The CAPEX for the ICLWS process was 47.4% lower than that for the SMR1 process. This was as a result of the inherent CO_2 capture in the ICLWS system, which led to a requirement for less equipment in the ICLWS system than in the SMR1 process. Regarding the OPEX, the figure calculated for ICLWS with $MgAl_2O_4$ as oxygen-carrier support was 7.1% lower than the corresponding value in the SMR1 process. This clearly indicates that the thermal optimisation of the process helps to reduce the energy penalty, resulting in a lower operating cost. However, the OPEX for the SMR1 process was 8.9% lower than that for the ICLWS process with ZrO_2 as support material for the oxygen carrier, since the ZrO_2 support material was expensive. Summing this up, the hydrogen production cost was 17.5%, 12.9 – 29% and 19.1% lower for ICLWS with $MgAl_2O_4$ as support material compared with the SMR1, SMR_m/ATR and TRCLR processes reported in the literature, respectively. Moreover, P_c was 5.3%, 0.6 – 19% and 3.6% lower for ICLWS with ZrO_2 as support material compared with the SMR1, SMR_m/ATR and TRCLR processes, respectively. The CAPEX and OPEX values for the ICLWS process were not compared with that of the modern SMR_m/ATR and TRCLR process, since the capacity of the TRCLR process was 3.5 and 2.9 times lower than that of the ICLWS process developed for this study. Hence both processes were scaled up linearly to compare their CAPEX and OPEX with the ICLWS process. The CAPEX for the ICLWS was 11.8 – 65.8% and 37.3%

compared with SMR_m/ATR and TRCLR processes, respectively. The OPEX for ICLWS (a) process is 6.4 – 17% lower compared with SMR_m/ATR. In addition, it is 22.4% less than the TRCLR process.

The economic evaluation of the CLWSFe process indicated a CAPEX value that was 28.4% lower than that of the SMR1. The reason for this significant difference was as described for the ICLWS process. In addition, it was 25.7% lower than the corresponding values for the MIDREX process reported in the literature. The total annual cost (TAC) was 20.9% lower than that of the SMR1 when a saleable product, direct reduced iron (DRI), was considered. As a result, the hydrogen production cost was 26.9% and 23.3 – 37.5% down on the comparable cost of the conventional (SMR1) and modern (SMR_m/ATR) steam methane/auto-thermal reforming processes. In contrast, if the effect of saleable DRI was excluded, the total annual cost for the CLWSFe process was 41.2% higher than that of the SMR1 process. This led to a hydrogen production cost that was 28.6% and 10 – 35% higher than the hydrogen production cost through the SMR1 and SMR_m/ATR processes.

The economic investigation of the ICLWS and CLWSFe methods has proved that both processes are potentially economically viable and can produce decarbonised hydrogen and iron with comparable cost to those produced from benchmark processes, i.e. steam methane reforming and a blast furnace. This provides a promising future for these two processes.

Development of an energy storage system through the merging of pumped heat energy storage with chemical looping and an open cycle gas turbine

An energy storage system was developed by integrating the pumped heat energy storage (PHES) technology with the ICLWS process, the development of which was described in Chapter 3. The electric power that drove the system, the solid storage material and the working fluid cycled through the system were supplied from the ICLWS process. Also, a novel energy storage system (OIPHES) was developed by coupling the IPHES system to an open cycle gas turbine.

The transient behaviour of the temperature for both energy storage tanks in both systems was obtained for 24 h of operation. Also, the daily energy generation from both energy storage systems was reported. In addition, both systems were thermodynamically assessed via the determination of their round trip efficiencies. Results showed that the round trip efficiency for both systems was 77%, which was five percentage points higher than the efficiency of a conventional PHES system reported in the literature. In addition, the effect of integrating both energy storage systems on the ICLWS thermodynamic performance was measured as a function of the effective efficiency. Both systems showed negligible influence on the effective efficiency.

Both systems were economically analysed by calculating their total investment costs (CAPEX), operating costs (OPEX), daily profits from selling the electricity (P_A) and the levelised profits (LEC) over several days in the year that showed significant fluctuations in the electricity prices. Initial results indicate that the IPHES system was economically more viable than the OIPHES, with lower values for both CAPEX and OPEX for all the days selected. The daily profits were 4.9 – 72.6% higher for the IPHES system compared with the OIPHES for all the days simulated. Also, the LEC value for the IPHES system was higher by between 16.2% and 81.6% compared with the OIPHES. Therefore, an economic sensitivity analysis was performed to detect the main parameters that affected the annual profits of both systems, in order to attempt to improve the economic performance of the OIPHES system.

For this analysis, a feasibility equation was derived that summarised all the factors affecting the economic assessment of both systems that had been developed during this study. This equation provided a criterion on which to decide the feasibility of the systems, based on the operating conditions used in each energy storage system that was developed. The percentage of H_2 fuel used in the open cycle gas turbine (OCGT) from ICLWS was a crucial factor that affected the economic analysis performed on the OIPHES system. Also, the discharging period of the system was an important factor. Thus, the effect of both parameters was incorporated into the economic analysis of the OIPHES process. The results showed that once the percentage of H_2 from the plant fed to OIPHES system became greater than 37%, and 7% for day_1 and day_{max} respectively, the latter system became more economically feasible than the IPHES system. However, for day_2 and day_{min}, the IPTES was more economically viable for the whole range of H_2 feed rates. The highest percentage difference in the daily profits for OIPHES relative to IPHES was obtained at a H_2 feed rate of 60% and 100% for day_1 and day_{max}, respectively.

8.2 Future Work

The future work proposed in this section could not be performed either because it was outside the scope of this thesis or because it did not match the assumptions made for the work conducted for this thesis. Such work ideas are as follows:

Biomass could be substituted for the natural gas fuel used in both ICLWS and CLWSFe processes

The emphasis of the work performed for this thesis was on using natural gas as the main fuel for ICLWS and CLWSFe processes, since it was more widely used and would remain so for the near future. However, these two processes can be retrofitted to use biomass as the source of fuel. Such a process would enable achievement of negative emissions which would have a positive effect toward the efforts made to meet the targets of the IPCC Paris agreement. The effect of this change on the thermal optimisation of both ICLWS and CLWSFe processes could be studied, as could their thermodynamic and economic performance. Based on the results of these studies, the feasibility of such a substitution could be determined.

The kinetics of the oxygen carrier used in this study could be studied with biomass as fuel and the result could be incorporated into the reactor modelling

In this work, the kinetics of all the reactions that govern the ICLWS and CLWSFe processes, except for methane reduction using pure iron ore, were obtained from the literature. Kinetics of such reactions with biomass as fuel would be required to be known in order to perform the economic evaluation of the ICLWS and CLWSFe processes with biomass as fuel.

The integration of the OIPHES system with the CLWSFe process should be investigated

The results of this study have shown that integration of an open system gas turbine coupled with pumped heat energy storage enhance the round trip efficiency of the PHES system by five percentage points and provide more annual profits than the PHES process. Integration of such a system into the CLWSFe system could increase profits since the CLWSFe process produces more power than the ICLWS process. Thus, the temperature behaviour of the bed material inside the storage tanks should be obtained and the losses from the cycle calculated so that the system could be thermodynamically and economically assessed similarly to OIPHES.

Sensitivity analysis of the CLWSFe process should be performed

CLWSFe provides a promising economic and thermodynamic performance as indicated by the results obtained. Sensitivity analysis would provide us with information regarding the conditions that affect the process performance. As an example, the results of sensitivity analysis might enable us to switch the main product of CLWSFe process to be iron instead of hydrogen.

Nomenclature

Roman Letters

A = The area of the reactor (m^2).

A_c = The total annual cost of the plant divided by the operation days per year. (US$/d)

A_i = Pre-exponential factor for reaction rate *i.*

A_P = The area of the solid particle (m^2).

b = stoichiometric parameter of solid B.

C_{Ag} = concentration of gaseous reactant A in the bulk gas (mol/m^3).

C_{As} = Concentration of A at the solid surface (mol/m^3).

CAPEX = The total investment cost of the plant. (US$,M).

C_{cw} = Daily cost associated with cooling water consumption. (US$/d).

C_E = Revenues earned due to selling the electricity generated (US$/d).

C_f = Daily cost associated with fuel consumption during the OCGT mode of operation ($/d).

C_r= Daily cost of the refrigerant (Liquid nitrogen) used in the heat exchangers during the discharging mode (US$/kg)

C_U = Daily cost associated with utilities consumption (US$/d).

Cp_a= Heat capacity of the gas at layer m (J/kg.K).

$Cp_{\bar{A}}$ = The average heat capacity of component A over the reactor temperature range (J/mol.K).

Cp_s = Heat capacity of the solids. (J/kg.K).

D_e = effective diffusivity of reactant A in the ash layer (in m^2/s).

$d_e =$ Effective diameter of the solids particle (m).

d_P = The diameter of the solid particle (µm).

E_a = The activation energy of the reaction (kJ/mol).

E_{gI} = Total electrical energy produced in the IPTES system (MWh).

$E_{gI,Ch}$ = Electrical energy produced in the IPTES system during charging period (MWh).

$E_{gI,d}$ = Electrical energy produced in the IPTES system during discharging period (MWh).

E_{gO} = Total electrical energy produced in the OIPTES system (MWh)

$E_{gO,Ch}$ = Electrical energy produced in the OIPTES system during charging period (MWh)

$E_{gO,d}$ = Electrical energy produced in the OIPTES system during discharging period (MWh)

E_{OCGT} = Electrical energy produced in the OIPTES system during open cycle gas turbine period (MWh)

E_p = Electricity unit price rate (US$/MWh)

E_{SCI} = Electrical energy generated via steam cycle from the ICLWS process (MWh)

F_{CO_2} = The molar flow rate of CO_2 captured through the process (kmol/h).

F_{Fe} = The molar flow rate of metallic iron (kmol/h).

F_{gi} = is the inlet molar flow rate of the gas to the reactor (mol/time);

F_{gf}= is the outlet molar flow rate of the gas discharged from the reactor (mol/time);

F_{H_2} = The molar flow rate of H_2 produced (kmol/h).

F_{NG} = The molar flow rate of natural gas consumed by the process (kmol/h).

F_{oc} = The molar flow rate for the oxygen carrier fed to the reducer in ICLWS process (kmol/h).

F_{oc_d} = The molar flow rate of discharged oxygen carrier from reducer in ICLWS process (kmol/h).

F_{sti} = The molar flow rate for the steam fed to the oxidiser in ICLWS process (kmol/h).

F_{si} = the inlet molar flow rate of the solid to the reactor (mol/time);

F_{sf} = the molar flow rate of the solid discharged from the reactor (mol/time);

F_T = The total molar flow rate of the gaseous mixture (kmol/h).

F_{tCO_2} = The molar flow rate of the total CO_2 produced through the process (kmol/h).

G = Gibbs free energy of reaction (kJ/mol).

G_a = Gas mass flow per area (kg/s.m^2).

h = Heat-transfer coefficient between the gas and solid mixtures (W/m^2.K).

H_A = The enthalpy of component A (J/mol).

HHV_{H_2}= The higher heating value of hydrogen fuel (MJ/kg).

HHV_{NG}= The higher heating value of natural gas fuel (MJ/kg).

i = Interest rate (%).

k = The intrinsic reaction rate constant.

k_a = Thermal conductivity of the gas (W/m.K).

K_e = The equilibrium constant of the chemical reaction.

k_g = mass transfer coefficient through the gas film (m/s).

L = The length of the reactor or the vessel (m).

m_a = Mass flow rate of the working fluid of the Pumped thermal energy storage cycle (kg/s).

$\dot{m}_{cw}$ = Mass flow rate of the cooling water utilised in heat exchangers during the charging period in both cycle stages per year (kg/yr).

$\dot{m}_f$ = mass flow rate of the hydrogen fuel utilised in the OCGT per year (kg/d).

$\dot{m}_{Fe}$ = The mass flow rate of the direct reduced iron product from CLWSFe process (kg/s).

$\dot{m}_{H_2}$ = The mass flow rate of H_2 produced from the process (kg/s).

$\dot{m}_{H_2y}$ = annual production rate of the hydrogen product (ton/yr).

$\dot{m}_{NG}$ = The mass flow rate of natural gas consumed by the process (kg/s).

N = Number of discretised layers in the bed *i.e.* 50 layer.

N_A = Number of moles of gas component A (moles)

N_B = Number of moles of solid component B (moles)

n = Plant lifetime (years).

n_i = The order of the reaction rate.

$OPEX$ = The operating cost of the plant (US$/yr,M).

P = The pressure of the gas (bar).

P_A = The annual profits of selling electricity (US$/yr, M).

P_{AI} = The annual profits of selling electricity for IPHES system (US$/yr, M).

P_{Ao} = The annual profits of selling electricity for OIPHES system (US$/yr, M).

P_C = production cost of hydrogen product (US$/kg).

$P_{c/g}$ = The power generated (-ve) through turbines or consumed (+ve) through pumps and compressors in the process (MW).

P_f = Unit price rate of hydrogen fuel used (US$/kg).

P_r = Unit price rate of the refrigerant used (US$/m^3).

P_w= Unit price rate of the cooling water used (US$/m^3).

P_1 = Unit price rate of electricity during the charging time (US$/MWh).

P_2 = Unit price rate of electricity during the discharging time (US$/MWh).

Q = The amount of heat added of removed of the reactor (MW).

Q_{As} = The flux of A within the ash layer (mol/m^2.s).

Q_{CHX} = The heat load of the cold heat exchanger in the pumped thermal energy storage (MW).

$\dot{Q}_f$ = Thermal energy of the fuel input to the process (MW).

Q_{fs} = The specific rate of fuel consumed in iron production process (GJ/tDRI)

Q_{HHX} = The heat load of the hot heat exchanger in the pumped thermal energy storage (MW).

$\dot{Q}_i$ = The total thermal energy input to the process (MW).

Q_{Is}= The specific rate of thermal energy input to the iron production process (GJ/tDRI)

$\dot{Q}_{MH}$ = The net heating utility supplied to the process (MW).

$\dot{Q}_o$ = The total thermal energy output from the process (MW).

Q_{0s}= The total rate of thermal energy produced by an iron production process (GJ/tDRI)

R = radius of the solid particle S (m^2).

Re = Reynolds number.

R_1 = Oxygen carrier-to-methane feed ratio for ICLWS process.

R_2 = Oxygen carrier-to-steam feed ratio for ICLWS process.

r = The reaction rate of gas solid reaction (mol/vol.time).

r_c = radius of the unreacted core of the solid particle B (m).

S_m = Surface area per volume of heat transfer related to solid particle (m^{-1}).

T_a = The ambient temperature of the working fluid for the pumped heat energy storage cycle (°C).

$T_{ac,s}$ = The temperature of the discharged gas from the cold storage tank at steady state (ºC).

$T_{ah,s}$= The temperature of the discharged gas from the hot storage tank at steady state (ºC).

T_c = The cold temperature of the working fluid for the pumped thermal energy storage cycle (°C).

$T_{co,t}$ = The temperature of the discharged gas from the cold storage tank at time t (ºC).

T_{gi} = the inlet temperature of the gaseous mixture to the reactor (K);

T_{gf} = the temperature of the gaseous mixture discharged from the reactor (K).

T_{go} = Temperature of oxidiser's discharged gas for ICLWS process (℃).

T_{gr} = Temperature of reducer's discharged gas for ICLWS process (℃).

T_H = The hot temperature of the working fluid for the pumped thermal energy storage cycle (℃).

$T_{ho,t}$ = The temperature of the discharged gas from the hot storage tank at time t (ºC).

T_{sf} = the temperature of the solid mixture discharged from the reactor (K).

T_{si} = the inlet temperature of the solid mixture to the reactor (K).

T_{so} = Temperature of oxidiser's discharged solids for ICLWS process (℃).

T_{sr} = Temperature of reducer's discharged solids for ICLWS process (℃).

t = time (h)

t_{Ch} = Charging period of the pumped thermal energy storage cycle (h).

t_d = Discharging period of the pumped thermal energy storage cycle (h).

t_{OCGT} = Open cycle gas turbine period (h).

U_m = Overall heat loss coefficient (W/m^2.K).

V_P = Volume of one solid particle (m^3).

W_C = The work required by compressor (MW).

$W_{c,ch}$ = The work supplied to compressor of the pumped thermal energy storage cycle during the charging period (MW).

W_{OCGT} = Work delivered by the open cycle gas turbine (MW).

W_{SC} = The work generated by the steam cycle (MW).

W_{SCO} = Work delivered by the steam cycle of ICLWS process during open cycle gas turbine period (MW).

W_T = The work delivered by turbine (MW).

$W_{T,ch}$ = The work delivered by the turbine of the pumped thermal energy storage cycle during the charging period (MW).

X_B = fractional conversion of solid particle B.

X_{gf}= is the conversion of the discharged gas at the reactor outlet;

X_{gi} = is the conversion of the gas at the reactor inlet;

X_{go} = Gas outlet conversion in the oxidiser for ICLWS process.

X_{gr} = Gas outlet conversion in the reducer for ICLWS process.

X_{si} = the conversion of the solid at the reactor inlet.

X_{sf}= the conversion of the solid discharged from the reactor.

X_{so} = Discharged solid conversion in the oxidiser for ICLWS process.

X_{sr} = Discharged solid conversion in the reducer for ICLWS process.

y_{Fe} = The yield of metallic iron produced in CLWSFe process (mol/mol).

y_{H_2} = The hydrogen yield (mol/mol).

Z = Axial direction through the reactor length (m).

Greek letters:

α = The degree of solid reduction, i.e. conversion.

ΔA_m = surface area of one layer (m).

ΔH_{cFe} = The heat of formation of Fe_2O_3 or heat of combustion of metallic iron at standard condition (MJ/kg).

ΔH_{rxi} = The heat of reaction i taking place in the solid phase (J/mol).

ε = Bed void fraction.

η_{eff} = The effective efficiency of the process.

η_{Ieff} = The iron effective efficiency of the process.

η_{H_2}= The hydrogen efficiency of the process.

η_{rt} = Roundtrip efficiency.

η_{th}= The thermal efficiency of the process.

$\dot{v}$ = The volumetric flow rate of the gas (m^3/h).

υ_A = The stoichiometric coefficient of component A.

ρ_B = molar density of solid particle B (mol/m^3).

ρ_b = The bulk density of the solid moving particles inside the reactor (kg/m^3).

ρ_p = The mass density of solid particle (kg/m^3).

ρ_s = Solids particle density in the storage tanks of pumped thermal energy storage (kg/m^3).

ρ_{sm} = The molar density of solid particle (kmol/m^3).

τ = Time for complete conversion (s).

ψ = Sphericity of the solid particles.

Abbreviations:

BCLWS = Baseline chemical looping water splitting process.

CAES = Compressed air energy storage.

CCS = Carbon capture and storage.

CDLC = Coal direct chemical looping.

CHX = cold heat exchanger.

CLC = Chemical looping combustion.

CLR = Chemical looping reforming.

CLRa = Chemical looping reforming for syngas

CLRS = Steam reforming integrated with chemical looping.

CLRw = Chemical looping reforming integrated with oxidation for hydrogen and syngas

CLWS = Chemical looping water splitting.

CLWS(a) = chemical looping water splitting with no syngas split from fuel reactor.

CLWSFe = Chemical looping water splitting with iron co-production process.

DRI = direct reduced iron.

EES = energy storage system.

HE = Heat exchanger.

HHX = hot heat exchanger.

HRSG = Heat recovery steam generation unit.

HTS = High water gas shift reactor.

GHG = Greenhouse gases.

ICLWS = Integrated chemical looping water splitting process.

IEAGHG = International Energy Agency's Greenhouse Gas.

IPCC = Intergovernmental Panel on Climate Change.

IPTES = Integrated pumped thermal energy storage system developed.

LTS = Low water gas shift reactor.

MDEA = Methyldiethanolamine.

MEA = Monoethanolamine.

OCGT = Open cycle gas turbine.

OIPHES = Open cycle gas turbine merged with integrated pumped thermal energy storage system.

OSU = Ohio state university process.

PHS = Pumped hydro storage.

PSA = pressure swing adsorption.

PTES = Pumped Thermal energy storage system.

SCL = Syngas chemical looping.

SCO = Steam cycle of ICLWS process when integrated with open cycle gas turbine.

SE-CLSR = Sorbent-enhanced steam reforming integrated with chemical looping.

SMR = Steam methane reforming.

TRCLR = Three reactor chemical looping reforming.

VL = Valves.

WGS = Water gas shift reaction.

Publication List

The following list shows the work which has been considered for publication during the PhD program.

1. Bahzad, H., et al., Iron-based chemical-looping technology for decarbonising iron and steel production. *International Journal of Greenhouse Gas Control*, 2019. **91**. **(Journal paper, published)**
2. Bahzad, H., et al., Development and techno-economic analyses of a novel hydrogen production process via chemical looping. *International Journal of Hydrogen Energy*, 2019. **(Journal Paper, published)**
3. Patzschke, C.F., Bahzad, H., Boot-Handford, M.E. et al. Simulation of a 100-MW solar-powered thermo-chemical air separation system combined with an oxy-fuel power plant for bio-energy with carbon capture and storage (BECCS). *Mitig Adapt Strateg Glob Change (2019)*. **(Journal paper, published)**
4. Katayamaa, K., Bahzad, H., Boot-Handford, M.E. et al. Process Integration of Chemical Looping Water Splitting with the Sinter Plant for Iron Making. **(Journal Paper, published)**.
5. Patzschke, C., Wenzhao, X., Bahzad, H. et al. The economic and environmental impact of oxygen carriers in a natural gas-fuelled chemical looping combustion process. **(Journal Paper, Submitted)**.

References

1. IPCC, Climate Change 2007: Synthesis Report. Contribution of Working Groups I, II and III to the Fourth Assessment Report of the Intergovernmental Panel on Climate Change. 2007, IPCC: Geneva, Switzerland.

2. IPCC, Synthesis Report. Contribution of Working Groups I, II and III to the Fifth Assessment Report of the Intergovernmental Panel on Climate Change [R.K. Pachauri and L.A. Meyer (eds.)] 2014, IPCC: Geneva, Switzerland. p. 151.

3. Jansen, D., et al., Pre-combustion CO_2 capture. *International Journal of Greenhouse Gas Control*, 2015. **40**: p. 167-187.

4. MacDowell, N., et al., An overview of CO_2 capture technologies. *Energy & Environmental Science*, 2010. **3**(11): p. 1645.

5. Ball, M. and M. Weeda, The hydrogen economy – Vision or reality? *International Journal of Hydrogen Energy*, 2015. **40**(25): p. 7903-7919.

6. Fan, L.-S., et al., Chemical looping processes for CO_2 capture and carbonaceous fuel conversion – prospect and opportunity. *Energy & Environmental Science*, 2012. **5**(6): p. 7254-7280.

7. Bohn, C., The production of pure hydrogen with simultaneous capture of carbon dioxide. 2010.

8. Kathe, M.V., et al., Hydrogen production from natural gas using an iron-based chemical looping technology: Thermodynamic simulations and process system analysis. *Applied Energy*, 2016. **165**: p. 183-201.

9. International Energy Agency, CO_2 Capture and Storage: A Key Carbon Abatement Option. 2008.

10. Fennell, P. and B. Anthony, *Calcium and chemical looping technology for power generation and carbon dioxide (CO_2) capture*. **2015**.

11. Zeng, L., Multiscale Study of Chemical Looping Technology and Its Applications for Low Carbon Energy Conversions, L.-S. Fan, A. Asthagiri, and W. Ho, Editors. 2012.

12. Rath, L.K., Assessment Of Hydrogen Production With CO_2 Capture Volume 1: Baseline State-Of-The-Art Plants. 2010, US department of energy: United States.

13. Borlée, J., Low CO_2 Steels – ULCOS Project ETP 2008 Workshop on Deploying Demand Side Energy Technologies. 2007, OECD/IEA: Paris.

14. Zeng, L., et al., Iron oxide looping for natural gas conversion in a counter-current moving bed reactor. *Applied Energy*, 2015. **157**: p. 338-347.

15. Bahzad, H., et al., Iron-based chemical-looping technology for decarbonising iron and steel production. *International Journal of Greenhouse Gas Control*, 2019. **91**.

16. IEAGHG, Reference Data and Supporting Literature Review for SMR Based Hydrogen Production with CCS 2017.

17. Committee on Alternatives and Strategies for Future Hydrogen Production and use, The Hydrogen Economy: Opportunities, Costs, Barriers, and R&D Needs, E. United States. Department Of Energy. Office Of Energy and E. Renewable, Editors. 2004.

18. IEAGHG, Techno-Economic Evaluation of SMR Based Standalone (Merchant) Plant with CCS. 2017.

19. Nikolaidis, P. and A. Poullikkas, A comparative overview of hydrogen production processes. *Renewable and Sustainable Energy Reviews*, 2017. **67**: p. 597-611.

20. Kothari, R., D. Buddhi, and R.L. Sawhney, Comparison of environmental and economic aspects of various hydrogen production methods. *Renewable and Sustainable Energy Reviews*, 2008. **12**(2): p. 553-563.

21. Muradov, N., Hydrogen via methane decomposition: an application for decarbonization of fossil fuels. *International Journal of Hydrogen Energy*, 2001. **26**(11): p. 1165-1175.

22. Muradov, N., How to produce hydrogen from fossil fuels without CO_2 emission. *International Journal of Hydrogen Energy*, 1993. **18**(3): p. 211-215.

23. Carmo, M., et al., A comprehensive review on PEM water electrolysis. *International Journal of Hydrogen Energy*, 2013. **38**(12): p. 4901-4934.

24. Ursua, A., L.M. Gandia, and P. Sanchis, Hydrogen Production From Water Electrolysis: Current Status and Future Trends. *Proceedings of the IEEE*, 2012. **100**(2): p. 410-426.

25. Yao, J., et al., Techno-economic assessment of hydrogen production based on dual fluidized bed biomass steam gasification, biogas steam reforming, and alkaline water electrolysis processes. *Energy Conversion and Management*, 2017. **145**: p. 278-292.

26. Russell JH, N.L., Fickett AP, Hydrogen generation by solid polymer electrolyte water electrolysis. *American Chemical Society Division of Fuel Chemistry Preprints*, 1973. **18**(3): p. 24-40.

27. Shiva Kumar, S. and V. Himabindu, Hydrogen production by PEM water electrolysis – A review. *Materials Science for Energy Technologies*, 2019. **2**(3): p. 442-454.

28. Barbir, F., PEM electrolysis for production of hydrogen from renewable energy sources. *Solar Energy*, 2005. **78**(5): p. 661-669.

29. Medina, P. and M. Santarelli, Analysis of water transport in a high pressure PEM electrolyzer. *International Journal of Hydrogen Energy*, 2010. **35**(11): p. 5173-5186.

30. Grigor'ev, S., et al., Electrolysis of Water in a System with a Solid Polymer Electrolyte at Elevated Pressure. *Russian Journal of Electrochemistry*, 2001. **37**(8): p. 819-822.

31. Bak, T., Photo-electrochemical properties of the TiO_2-Pt system in aqueous solutions. *International Journal of Hydrogen Energy*, 2002. **27**(1): p. 19-26.

32. Turner, J., et al., Renewable hydrogen production. *International Journal of Energy Research*, 2008. **32**(5): p. 379-407.

33. Bohn, C.D., et al., Production of Very Pure Hydrogen with Simultaneous Capture of Carbon Dioxide using the Redox Reactions of Iron Oxides in Packed Beds. *Industrial and Engineering Chemistry Research*, 2008. **47**(20).

34. Dou, B., et al., Hydrogen production and reduction of Ni-based oxygen carriers during chemical looping steam reforming of ethanol in a fixed-bed reactor. *International Journal of Hydrogen Energy*, 2017. **42**(42): p. 26217-26230.

35. Dou, B., et al., Hydrogen production from the thermochemical conversion of biomass: issues and challenges. *Sustainable Energy Fuels*, 2019. **3**(2): p. 314-342.

36. Johansson, M., T. Mattisson, and A. Lyngfelt, Comparison of oxygen carriers for chemical-looping combustion. *Thermal Science*, 2006. **10**(3): p. 93-107.

37. Rydén, M., A. Lyngfelt, and T. Mattisson, Synthesis gas generation by chemical-looping reforming in a continuously operating laboratory reactor. *Fuel*, 2006. **85**(12): p. 1631-1641.

38. Luo, M., et al., Review of hydrogen production using chemical-looping technology. *Renewable and Sustainable Energy Reviews*, 2018. **81**(P2): p. 3186-3214.

39. Dou, B., et al., Hydrogen production by sorption-enhanced steam reforming of glycerol. *Bioresource Technology*, 2009. **100**(14): p. 3540-3547.

40. Rydén, M. and P. Ramos, H_2 production with CO_2 capture by sorption enhanced chemical-looping reforming using NiO as oxygen carrier and CaO as CO_2 sorbent. *Fuel Processing Technology*, 2012. **96**: p. 27-36.

41. Bahzad, H., et al., Development and techno-economic analyses of a novel hydrogen production process via chemical looping. *International Journal of Hydrogen Energy*, 2019.

42. Kang, K.-S., et al., Reduction and oxidation properties of Fe_2O_3/ZrO_2 oxygen carrier for hydrogen production. *Chemical Engineering Research and Design*, 2014. **92**(11): p. 2584-2597.

43. Moghtaderi, B., Review of the Recent Chemical Looping Process Developments for Novel Energy and Fuel Applications. *Energy & Fuels*, 2012. **26**(1): p. 15-40.

44. Chen, S., et al., Hydrogen and electricity co-production plant integrating steam-iron process and chemical looping combustion. *International Journal of Hydrogen Energy*, 2012. **37**(10): p. 8204-8216.

45. Kang, K.-S., et al., Modelling a counter-current moving bed for fuel and steam reactors in the TRCL process. *International Journal of Hydrogen Energy*, 2012. **37**(4): p. 3251-3260.

46. Kang, K.-S., et al., Oxygen-carrier selection and thermal analysis of the chemical-looping process for hydrogen production. *International Journal of Hydrogen Energy*, 2010. **35**(22): p. 12246-12254.

47. Cormos, C.-C., Hydrogen production from fossil fuels with carbon capture and storage based on chemical looping systems. *International Journal of Hydrogen Energy*, 2011. **36**(10): p. 5960-5971.

48. Edrisi, A., et al., Hydrogen, nitrogen and carbon dioxide production through chemical looping using iron-based oxygen carrier – A Green plant for H_2 and N_2 production. *International Journal of Hydrogen Energy*, 2014. **39**(20): p. 10380-10391.

49. Khan, M.N. and T. Shamim, Techno-economic assessment of a plant based on a three reactor chemical looping reforming system. *International Journal of Hydrogen Energy*, 2016. **41**(48): p. 22677-22688.

50. Li, F., Chemical looping gasification processes, L.-S. Fan, Editor. 2009.

51. Cormos, C.C., Biomass direct chemical looping for hydrogen and power co-production: Process configuration, simulation, thermal integration and techno-economic assessment. *Fuel Processing Technology*, 2015. **137**: p. 16-23.

52. Gnanapragasam, N.V., B.V. Reddy, and M.A. Rosen, Hydrogen production from coal using coal direct chemical looping and syngas chemical looping combustion systems: Assessment of system operation and resource requirements. *International Journal of Hydrogen Energy*, 2009. **34**(6): p. 2606-2615.

53. Yan, L., et al., Design and comparisons of three biomass based hydrogen generation systems with chemical looping process. *International Journal of Hydrogen Energy*, 2014. **39**(31): p. 17540-17553.

54. Aziz, M., et al., Energy conservative brown coal conversion to hydrogen and power based on enhanced process integration: Integrated drying, coal direct chemical looping, combined cycle and hydrogenation. *International Journal of Hydrogen Energy*, 2017. **42**(5): p. 2904-2913.

55. He, F., N. Galinsky, and F. Li, Chemical looping gasification of solid fuels using bimetallic oxygen carrier particles – Feasibility assessment and process simulations. *International Journal of Hydrogen Energy*, 2013. **38**(19): p. 7839-7854.

56. Heng, L., H. Zhang, and R. Xiao, Hydrogen production from heavy fraction of bio-oil using iron-based chemical looping process: Thermodynamic simulation and performance analysis. *International Journal of Hydrogen Energy*, 2016. **41**(40): p. 17771-17783.

57. Sohn, H.Y. and J. Szekely, A structural model for gas-solid reactions with a moving boundary—III: A general dimensionless representation of the irreversible reaction between a porous solid and a reactant gas. *Chemical Engineering Science*, 1972. **27**(4): p. 763-778.

58. Richardson, J.T., B. Turk, and M.V. Twigg, Reduction of model steam reforming catalysts: effect of oxide additives. *Applied Catalysis A, General*, 1996. **148**(1): p. 97-112.

59. Hossain, M.M. and H.I. de Lasa, Chemical-looping combustion (CLC) for inherent separations—a review. *Chemical Engineering Science*, 2008. **63**(18): p. 4433-4451.

60. Levenspiel, O., *Chemical reaction engineering*. 3rd ed. **1999**, New York, Chichester: Wiley.

61. Richardson, J., X-ray diffraction study of nickel oxide reduction by hydrogen. *Applied Catalysis A: General*, 2003. **246**(1): p. 137-150.

62. Hossain, M., Fluidized bed chemical -looping combustion: Development of a bimetallic oxygen carrier and kinetic modeling. 2007.

63. Avrami, M., Kinetics of phase change III. *Journal of Chemical Physics 9*, 1941: p. 177–184.

64. Hancock, J.D. and J.H. Sharp, Method of Comparing Solid State Kinetic Data and Its Application to the Decomposition of Kaolinite, Brucite, and $BaCO_3$. *Journal of the American Ceramic Society*, 1972. **55**(2): p. 74-77.

65. Abad, A., et al., Mapping of the range of operational conditions for Cu-, Fe-, and Ni-based oxygen carriers in chemical-looping combustion. *Chemical Engineering Science*, 2007. **62**(1): p. 533-549.

66. Adekoya, T., Optimal Design of Heat Integration Strategies for Hydrogen Production, in Chemical Engineering. 2015, Imperial College London: London.

67. Douglas, J.M., *Conceptual design of chemical processes*. International ed. **2008**, New York, London: McGraw-Hill.

68. Andrews, W.G. *Apparatus for the purification of gas*. U.S. Patent 426,092, 1890.

69. Shirzad, M., et al., Moving Bed Reactors: Challenges and Progress of Experimental and Theoretical Studies in a Century of Research. *Industrial & Engineering Chemistry Research*, 2019. **58**(22): p. 9179-9198.

70. Rotating Bed Reactor Applications and Products; *SpinChem AB*: Umea, Sweden; Available from: http://www.spinchem.com.

71. Pivem, A.C. and M.J.S. de Lemos, Laminar heat transfer in a moving porous bed reactor simulated with a macroscopic two-energy equation model. *International Journal of Heat and Mass Transfer*, 2012. **55**(7-8): p. 1922-1930.

72. Bassin, J.P. and M. Dezotti, *Moving Bed Biofilm Reactor (MBBR), in Advanced Biological Processes for Wastewater Treatment*. **2018**. p. 37-74.

73. Dautzenberg, F.M. and M. Mukherjee, Process intensification using multifunctional reactors. *Chemical Engineering Science*, 2001. **56**(2): p. 251-267.

74. Yang, M., S. Banerjee, and R.K. Agarwal, Transient Cold Flow Simulation of Fast Fluidized Bed Fuel Reactors for Chemical-Looping Combustion. *Journal of Energy Resources Technology*, 2018. **140**(11).

75. Fogler, H.S., *Elements of chemical reaction engineering*. Pearson international, 4th ed. **2006**, Upper Saddle River, N.J.: Pearson Education International.

76. Direct vs. indirect heating technology; *Solex thermal science*: 2016; Calgary, Canada; Available from: https://www.solexthermal.com/products-solutions/heating/

77. Miller, J., *The combined cycle and variations that use HRSGs, in Heat Recovery Steam Generator Technology*. **2017**. p. 17-43.

78. U.S Energy Information Administration, International Energy Outlook 2016 With Projections to 2040. 2016, U.S. Department of Energy: Washington, DC.

79. Smith, J.M., *Introduction to chemical engineering thermodynamics*. 6th / ed. Chemical engineering thermodynamics, ed. H.C. Van Ness and M.M. Abbott. **2001**, Boston, London: McGraw-Hill.

80. Callum, E., et al., *Novel Steam Methane / Gas Heated Reformer Phase 1 Final Study Report*. 2020, Wood Group UK Limited: UK. p. 22.

81. Cavaliere, P., *Direct Reduced Iron: Most Efficient Technologies for Greenhouse Emissions Abatement, in Clean Ironmaking and Steelmaking Processes: Efficient Technologies for Greenhouse Emissions Abatement, P. Cavaliere*, Editor. **2019**, Springer International Publishing: Cham. p. 419-484.

82. Muscolino F, M.A., Ghiglione M, Duarte P, Introduction to direct reduction technology and outlook for its use. *Metallurgia Ital*, 2016. **108**(4): p. 25–31.

83. Jiang, X., L. Wang, and F.M. Shen, Shaft Furnace Direct Reduction Technology - Midrex and Energiron. *Advanced Materials Research*, 2013. 805-806: p. 654-659.

84. Smil, V., *Modern Ironmaking and Steelmaking, in Still the Iron Age*. **2016**. p. 87-114.

85. Mizutani N, K.T., Maeda N, Application of coke oven gas to MIDREX process. *R and D: Res Develop Kobe Steel Eng Rep*, 2014. **64**(1): p. 14-19.

86. Huitu, K., et al., Optimization of Midrex Direct Reduced Iron Use in Ore-Based Steelmaking. *Steel research international*, 2015. **86**(5): p. 456-465.

87. Sarkar, S., et al., Modeling MIDREX Based Process Configurations for Energy and Emission Analysis. *Steel research international*, 2018. **89**(2).

88. Liu, B.N., et al., Discussion on chemical energy utilisation of reducing gas in reduction shaft furnace. *Ironmaking & Steelmaking*, 2013. **41**(8): p. 568-574.

89. Cavaliere, P., *Ironmaking and Steelmaking Processes*. **2016**

90. Kemp, I.C., *Pinch Analysis and Process Integration: A User Guide on Process Integration for the Efficient Use of Energy*. 2 ed. **2007**.

91. Piotrowski, K., et al., Effect of gas composition on the kinetics of iron oxide reduction in a hydrogen production process. *International Journal of Hydrogen Energy*, 2005. **30**(15): p. 1543-1554.

92. Sastri, M.V.C., R.P. Viswanath, and B. Viswanathan, Studies on the reduction of iron oxide with hydrogen. *International Journal of Hydrogen Energy*, 1982. **7**(12): p. 951-955.

93. Piotrowski, K., et al., Topochemical approach of kinetics of the reduction of hematite to wüstite. *Chemical Engineering Journal*, 2007. **131**(1): p. 73-82.

94. Go, K.S., S.R. Son, and S.D. Kim, Reaction kinetics of reduction and oxidation of metal oxides for hydrogen production. *International Journal of Hydrogen Energy*, 2008. **33**(21): p. 5986-5995.

95. Moghtaderi, B. and H. Song, Reduction properties of physically mixed metallic oxide oxygen carriers in chemical looping combustion. *Energy and Fuels*, 2010. **24**(10): p. 5359-5368.

96. Son, S.R. and S.D. Kim, Chemical-looping combustion with NiO and Fe_2O_3 in a thermo-balance and circulating fluidized bed reactor with double loops. *Industrial and Engineering Chemistry Research*, 2006. **45**(8): p. 2689-2696.

97. Nam, H.W., et al., Kinetics study on the reduction with methane, oxidation with water and oxidation with air of Fe_2O_3/ZrO_2 using TGA. Trans. *Korean Hydrogen New Energy Soc*, 2011. **22**(2): p. 168-177.

98. Wen, F., H. Wang, and Z. Tang, Kinetic study of the redox process of iron oxide for hydrogen production at oxidation step. *Thermo-chimica Acta*, 2011. **520**(1): p. 55-60.

99. Sinnott, R.K., *Chemical engineering design*, J.M. Coulson and J.F. Richardson, Editors. **2005**, Elsevier Butterworth-Heinemann: Oxford.

100. Couper, J.R., et al., *Chemical Process Equipment*: Selection and Design. **2013**.

101. Garrett, D.E., *Chemical Engineering Economics*. **1989**.

102. Chemical Engineering Plant Cost Index, in PCI. Chemical Engineering: S.l.

103. Department for Business, Energy and Industrial Strategy, Industrial electricity prices in the IEA. 2016: UK.

104. Thames Water Utilities Limited, Charges Schedule For the Supply of Water and Wastewater Services. 2017.

105. Werkheiser, W.H., Mineral Commodity Summaries 2018. 2016.

106. Survey, U.G., Mineral Commodities Summaries. 2016: Washington DC: United States.

107. Balta, M.O. and F. Eke, Spatial Reflection of Urban Planning in Metropolitan Areas and Urban Rent a Case Study of Cayyolu, Ankara. *European Planning Studies*, 2011. **19**(10): p. 1817-1838.

108. Dincer, I., Renewable energy and sustainable development: A crucial review. *Renewable & sustainable energy reviews*, 2000. **4**(2): p. 157-175.

109. Benato, A., Performance and cost evaluation of an innovative Pumped Thermal Electricity Storage power system. *Energy*, 2017. **138**: p. 419-436.

110. Hadjipaschalis, I., A. Poullikkas, and V. Efthimiou, Overview of current and future energy storage technologies for electric power applications. *Renewable and Sustainable Energy Reviews*, 2009. **13**(6-7): p. 1513-1522.

111. Daim, T.U., et al., Evaluation of energy storage technologies for integration with renewable electricity: Quantifying expert opinions. *Environmental Innovation and Societal Transitions*, 2012. **3**: p. 29-49.

112. Koohi-Kamali, S., et al., Emergence of energy storage technologies as the solution for reliable operation of smart power systems: A review. *Renewable and Sustainable Energy Reviews*, 2013. **25**: p. 135-165.

113. Pearre, N.S. and L.G. Swan, Technoeconomic feasibility of grid storage: Mapping electrical services and energy storage technologies. *Applied Energy*, 2015. **137**: p. 501-510.

114. Chen, H., et al., Progress in electrical energy storage system: A critical review. *Progress in Natural Science*, 2009. **19**(3): p. 291-312.

115. Benato, A. and A. Stoppato, Heat transfer fluid and material selection for an innovative Pumped Thermal Electricity Storage system. *Energy*, 2018. 147: p. 155-168.

116. Weissenbach, B., Thermischer kraftspeicher thermal power storage, D.P. App, Editor. 1979.

117. White, A., G. Parks, and C.N. Markides, Thermodynamic analysis of pumped thermal electricity storage. *Applied Thermal Engineering*, 2013. **53**(2): p. 291-298.

118. McTigue, J.D., A.J. White, and C.N. Markides, Parametric studies and optimisation of pumped thermal electricity storage. *Applied Energy*, 2015. **137**: p. 800-811.

119. Deligant, M., et al., Performance assessment of a standard radial turbine as turbo expander for an adapted solar concentration ORC. *Renewable Energy*, 2018.

120. Desrues, T., et al., A thermal energy storage process for large scale electric applications. *Applied Thermal Engineering*, 2010. **30**(5): p. 425-432.

121. Nord Pool AS, *N2X Block Auction Prices in GBP/MWh*. 2019.

122. Mechleri, E., P.S. Fennell, and N.M. Dowell, Optimisation and evaluation of flexible operation strategies for coal- and gas-CCS power stations with a multi-period design approach. *International Journal of Greenhouse Gas Control*, 2017. **59**: p. 24-39.

123. Smallbone, A., et al., Levelised Cost of Storage for Pumped Heat Energy Storage in comparison with other energy storage technologies. *Energy Conversion and Management*, 2017. **152**: p. 221-228.

124. BOC - A member of Linde Group, Pricing Schedule for Industrial Gases. 2018.

Appendices

Appendix A: Supplementary figures

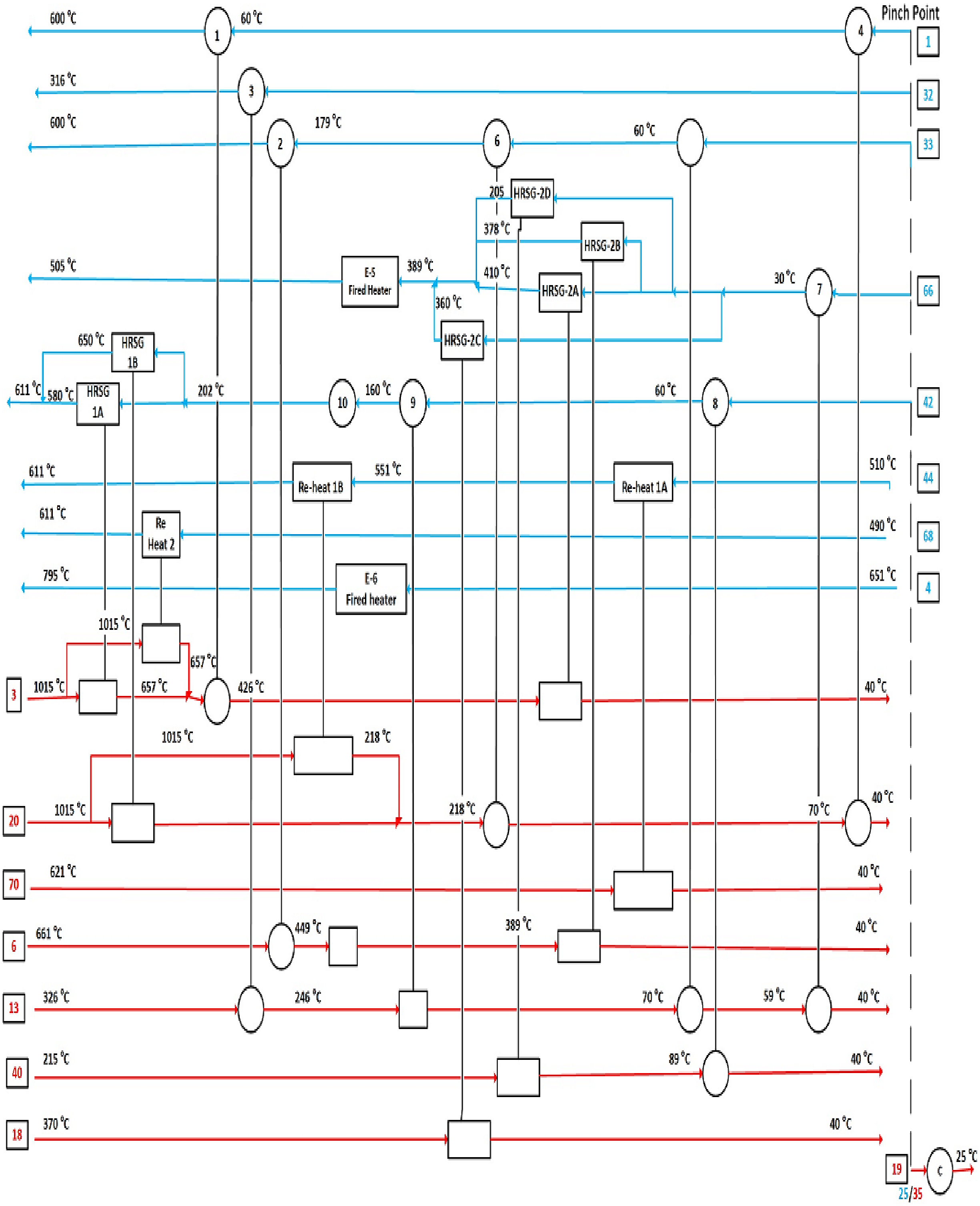

Figure. A1: The heat exchanger network for the ICLWS Process

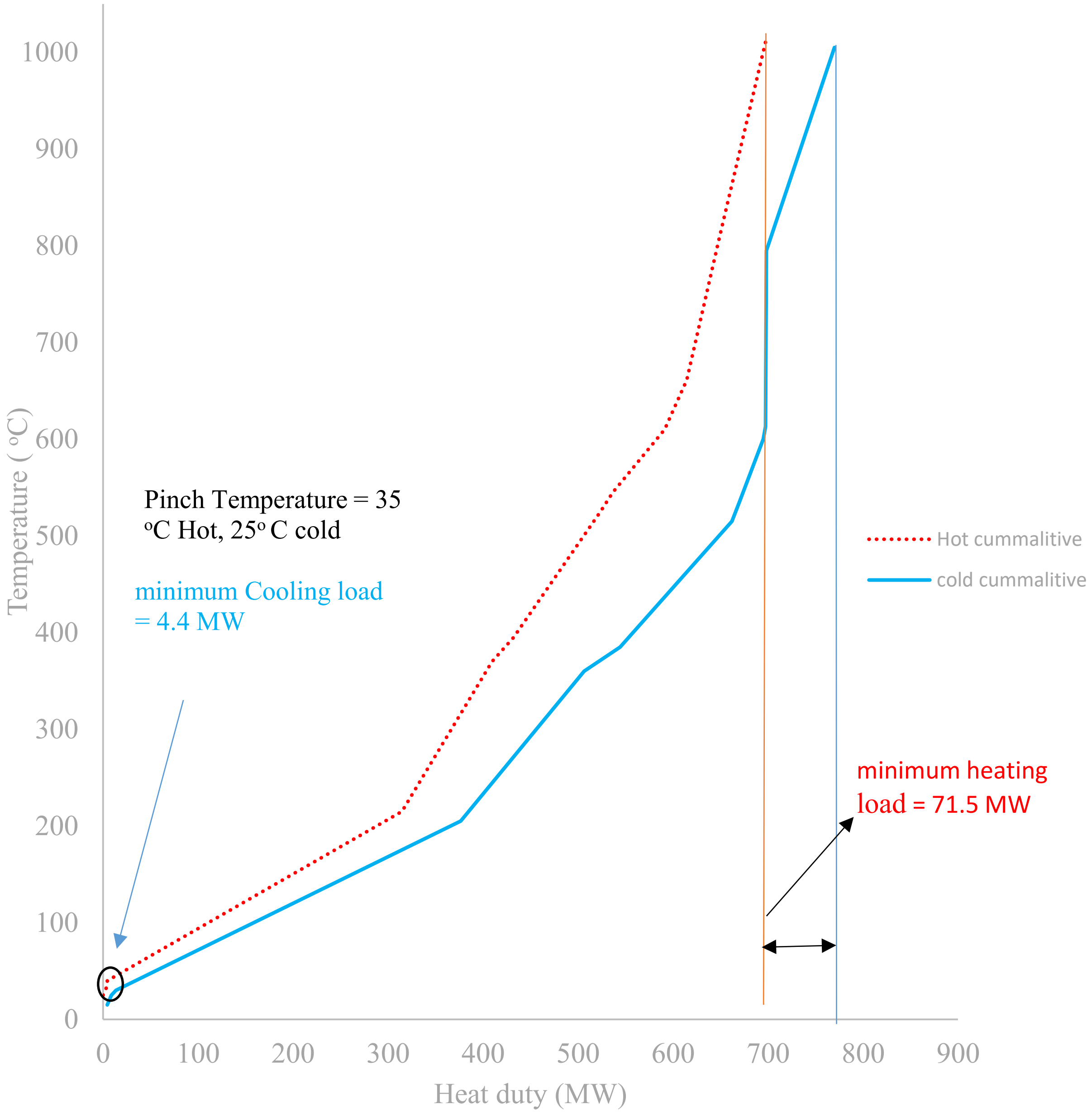

Figure. A2: Cumulative curves for the heat integration analysis performed on the BCLWS process

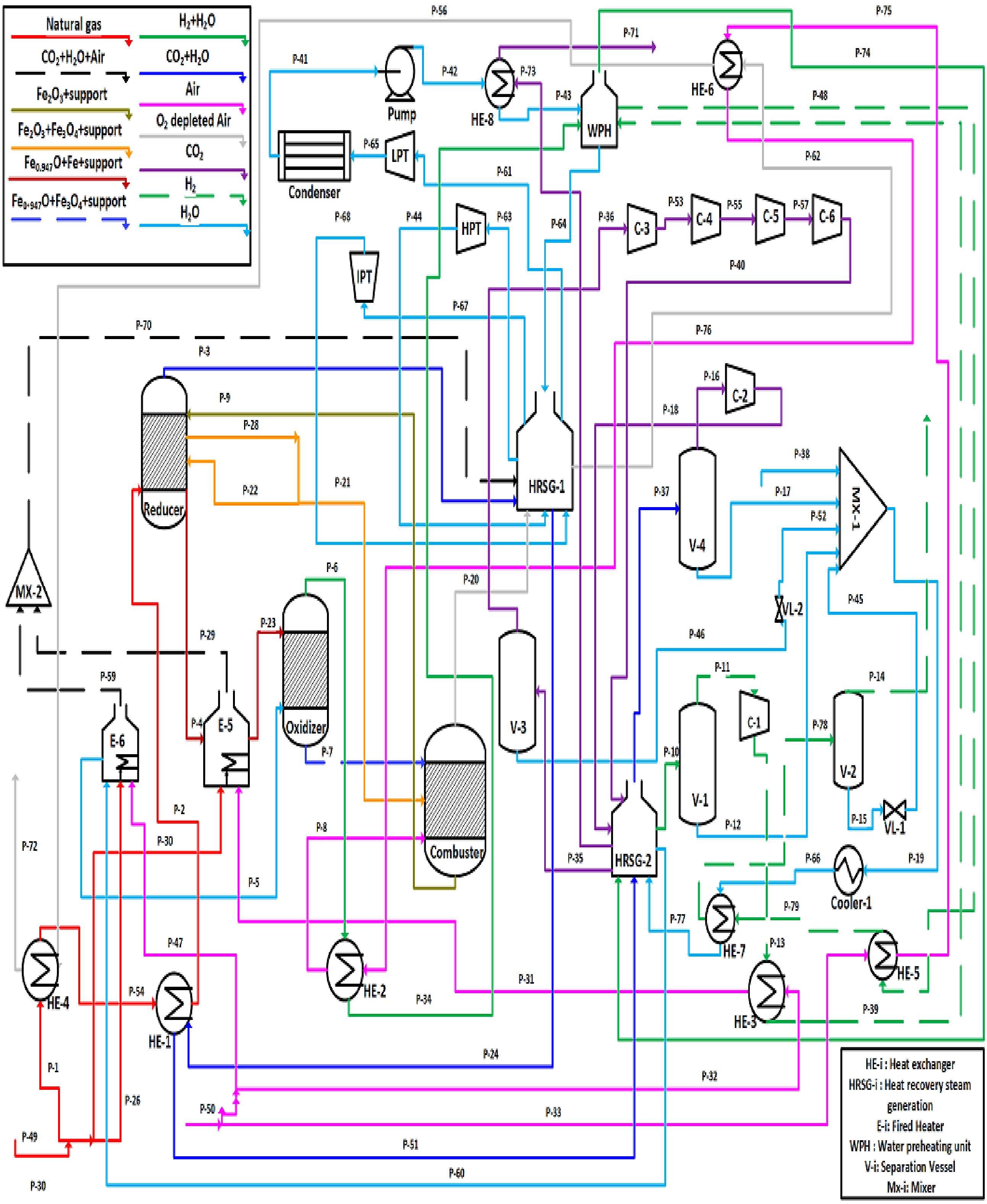

Figure. A3: Process flow diagram for the ICLWS(a) process

Appendix B: Supplementary data:

Energy Balance Tables for ICLWS process

Table B.1: Energy balance for the main units involved in the ICLWSIC process (a)

Equipment symbol	Identification	Streams In	Streams out	T_{in}(°C)	T_{out} (°C)	P_{in} (bar)	P_{out} (bar)	Energy Associated (MW)
R1	Reducer	2	3	600	1015	1.0	1.2	103.7
		9	4	1015	651	1.2		
R2	Oxidiser	23	7	805	820	1.2	1.2	-43.7
		5	6	505	656	1.2		
R3	Combustor	7	20	820	1015	1.2	1.2	-60.4
		8		600		1.2		
			9		1015			
		21		1015		1.2		
HE-1	Heat exchanger	24	51	657	426	1.0	1.0	34.9
		54	2	55	600	1.2	1.2	
HE-2	Heat exchanger	6	34	661	449	1.2	1.2	38.3
		76	8	179	600	1.0	1.0	
HE-3	Heat exchanger	32	31	25	316	1.0	1.0	9.0
		13	39	326	246	10.0	10.0	
HE-4	Heat exchanger	1	54	25	60	1.0	1.0	1.5
		56	72	70	40	1.2	1.2	

Table B.2: Energy balance for the main units involved in the ICLWSIC process (b)

Equipment symbol	**Identification**	**Streams In**	**Streams out**	**T_{in}(°C)**	**T_{out} (°C)**	**P_{in} (bar)**	**P_{out} (bar)**	**Energy Associated (MW)**	
HE-5	Heat exchanger	48	79	71	59	10.0	10.0	3.1	
		33	75	25	61	1.0	1.0		
HE-6	Heat exchanger	75	76	60	179	1.0	1.0	10.2	
		62	56	218	70	1.2	1.2		
HE-7	Heat exchanger	79	78	59	40	10.0	10.0	3.2	
		66	77	25	30	1.2	1.2		
HE-8	Heat Exchanger	73	71	89	40	110	110	7.8	
		42	43	27	60	260	260		
HRSG-1 (A-B)	Heat recovery steam generation	64	63	208	612	260	260	Total	136.1
		3	24	1015	657	1.2	1.2	A	42.1
		20	62	1015	218	1.2	1.2	B	51.8
		44	67	510	612	150	150	Reheat1	14
		68	61	480	612	70	70	Reheat2	16.5
WPH (A-B)	Water Pre-Heating	39	48	246	70	10	10	A	23.4
		34	74	461	389	1.2	1.2	B	12.7
		58	64	55	215	260	260	36.1	
Condenser	Condenser	65	41	25	25	0.026	0.026	-119.7	
Cooler-1	Cooler	19	66	35	25	1.2	1.2	-4.4	

Table B.3: Energy balance for the main units involved in the ICLWSIC process (c)

Equipment symbol	**Identification**	**Streams In**	**Streams out**	**T_{in}(°C)**	**T_{out} (°C)**	**P_{in} (bar)**	**P_{out} (bar)**	**Energy Associated (MW)**
E-5	Indirect fired heater (Combustion heating)	4	23	651	795	1.2	1.2	71.5
		30	29	25	661	1.0	1.0	
		31		360				
E-6	Fired heater	26	59	651	560	1.2	1.2	24.1
		47		25		1.0		
		60	5	395	505	1.2		
V-1	Separation vessel	10	11	40	40	1.2	1.2	0.0
			12					
V-2	Separation vessel	78	14	40	40	10.0	10.0	0.0
			15					
V-3	Separation vessel	35	36	40	40	21.2	21.2	0.0
			46					
V-4	Separation vessel	37	16	40	40	1.2	1.2	0.0
			17					

Table B.4: Energy balance for the main units involved in the ICLWSIC process (d)

MX-1	Mixer	38	19	20	35	1.2	1.2	0.0
		17		40				
		52		40				
		12		40				
		45		40				
MX-2	Mixer	29	70	661	622	1.2	1.2	0.0
		59		560				
C-1	Compressor	11	13	40	396	1.2	10.0	31.8
C-2	Compressor	16	18	40	370	1.2	21.2	16.9
C-3	Compressor	36	53	40	107	21.2	41.2	2.9
C-4	Compressor	54	55	40	68	41.2	61.2	2.7
C-5	Compressor	56	57	40	55	61.2	81.2	1.7
C-6	Compressor	58	40	30	36	81.2	101.2	1.1
HPT	Turbine	63	44	612	510	260	150	-8.0
IPT	Turbine	67	68	612	480	150	70	-11.6
LPT	Turbine	61	65	612	25	70	0.026	-67.4
P-1	Pump	41	42	25	27	1.0	260	1.6
VL-1	Valve	15	45	40	40	10.0	1.2	0.0
VL-2	Valve	46	52	40	40	21.2	1.2	0.0

Main specifications for the equipment used in both ICLWS and CLWSFe processes

Table B.5: Heat transfer areas for the heat exchangers utilised in the ICLWS process

Heat exchanger title	Heat exchanger heat transfer Area (m^2)
HE-1	247
HE-2 (A&B)	297
HE-3	102
HE-4	210
HE-5 (A&B)	424
HE-6 (A&B)	538
HE-7	158
HE-8 (A&B)	430

Table B.6: Heat transfer areas for the heat exchangers utilised in the CLWSFe process

Heat exchanger title	Heat exchanger heat transfer Area (m^2)
HE-1 (A&B)	652
HE-2 (A&B)	497
HE-3 (Condenser)	5402
HE-4	108
HE-5	82
HE-6	22.4
HE-7 (A-E)	1516

Table B.7: The size of the gas-liquid separation vessels utilised in the ICLWS process

Separation vessel title	Size (m^3)	Orientation
V-1	108	Vertical
V-2	16	Vertical
V-3	15	Vertical
V-4	153	Vertical

Table B.8: The size of the gas-liquid separation vessels utilised in the CLWSFe process

Separation vessel title	Size (m^3)	Orientation
V-1	49	Horizontal
V-2	4	Horizontal
V-3	19	Horizontal
V-4	3	Horizontal

Table B.9: The size of the reactors used in the ICLWS and CLWSFe processes

Process	Reactor title	Diameter (m^2)	Length (m)
ICLWS	Reducer	1.3	7.0
	Oxidiser	2.6	11.0
	Air reactor	1.0	6.0
CLWSFe	Reducer-1	1.2	10.0
	Reducer-2	1.5	6.5
	Oxidiser	3.0	18.0
	Air reactor	1.5	7.0

Table B.10: Material of construction for the main units in the ICLWS process

Equipment	Material of construction	Equipment	Material of construction
Reducer	Stainless steel 316	HE-8	Stainless steel 304/stainless steel 304
Oxidiser	Stainless steel 316	HRSG-1	Stainless steel 316
Air reactor	Stainless steel 304	HRSG-2	Stainless steel 316
HE-1	Carbon steel/stainless steel 304	Condenser	Stainless steel 304
HE-2	Carbon steel/stainless steel 304	Cooler	Stainless steel 304
HE-3	Carbon steel/stainless steel 304	Heater E-5	Stainless steel 316
HE-4	Carbon steel/carbon steel	Heater E-6	Stainless steel 316
HE-5	Carbon steel/stainless steel 304	Vessels (V1-V4)	Stainless steel 304
HE-6	Carbon steel/carbon steel	Compressors	Stainless steel 316
HE-7	Stainless steel 304/stainless steel 304	Turbines	Stainless steel 316

Table B.11: Material of construction for the main units in the CLWSFe process

Equipment	Material of construction	Equipment	Material of construction
Reducer-1	Stainless steel 316	Cooler (E-4)	Stainless steel 304/stainless steel 304
Reducer-2	Stainless steel 316	H-1	Carbon steel
Oxidiser	Stainless steel 316	HRSG-1	Stainless steel 316
Air reactor	Stainless steel 304	HRSG-2	Stainless steel 316
HE-1	Carbon steel/stainless steel 304	HRSG-3	Stainless steel 316
HE-2	Carbon steel/stainless steel 304	HRSG-4	Stainless steel 316
HE-3	Stainless steel 304/stainless steel 304	Condensers	Stainless steel 304
HE-4	Carbon steel/stainless steel 316	Vessels (V1-V4)	Stainless steel 304
HE-5	Stainless steel 304/stainless steel 304	Compressors	Stainless steel 316
HE-6	Carbon steel/Stainless steel 304	Turbines	Stainless steel 316
HE-7	Carbon steel/carbon steel		